UNIVERSITY OF CALIFORNIA, SAN DIEGO

Analytical and Experimental Study of Seismic Performance of Reinforced Concrete Frames Infilled with Masonry Walls

A dissertation submitted in partial satisfaction of the requirements for the degree Doctor of Philosophy

in

Structural Engineering

by

Andreas Stavridis

Committee in charge:

Professor P. Benson Shing, Chair
Professor Joel Conte
Professor Vlado Lubarda
Professor Hidenori Murakami
Professor Jose Restrepo

2009

The dissertation of Andreas Stavridis is approved and it is acceptable in quality and form for publication on microfilm and electronically:

_____

_____

_____

_____

_____

_____

Chair

University of California, San Diego

2009

To my Parents,

Niko and Voula

EPIGRAPH

When you set out on your journey to Ithaca,
pray that the road is long,
full of adventure, full of knowledge.
The Lestrygonians and the Cyclops,
the angry Poseidon -- do not fear them:
You will never find such as these on your path,
if your thoughts remain lofty, if a fine
emotion touches your spirit and your body.
The Lestrygonians and the Cyclops,
the fierce Poseidon you will never encounter,
if you do not carry them within your soul,
if your soul does not set them up before you.

Pray that the road is long.
That the summer mornings are many, when,
with such pleasure, with such joy
you will enter ports seen for the first time;
stop at Phoenician markets,
and purchase fine merchandise,
mother-of-pearl and coral, amber, and ebony,
and sensual perfumes of all kinds,
as many sensual perfumes as you can;
visit many Egyptian cities,
to learn and learn from scholars.

Always keep Ithaca on your mind.
To arrive there is your ultimate goal.
But do not hurry the voyage at all.
It is better to let it last for many years;
and to anchor at the island when you are old,
rich with all you have gained on the way,
not expecting that Ithaca will offer you riches.

Ithaca has given you the beautiful voyage.
Without her you would have never set out on the road.
She has nothing more to give you.

And if you find her poor, Ithaca has not deceived you.
Wise as you have become, with so much experience,
you must already have understood what these Ithacas mean.

Constantine P. Cavafy

TABLE OF CONTENTS

LIST OF FIGURES

LIST OF TABLES

LIST OF ABBREVIATIONS

ACI	American Concrete Institute
ASCE	American Society of Civil Engineers
ASTM	American Society for Testing and Materials
CU	University of Colorado, Boulder
ec	Eurocode
EERI	Earthquake Engineering Research Institute
FAS	Fourier Amplitude Spectrum
FEMA	Federal Emergency Agency
LHPOST	Large High Performance Outdoor Shake Table in UCSD
MSJC	Masonry Standards Joint Committee
NEES	Network for Earthquake Engineering Simulation
NSF	National Science Foundation
OLI	OnLine Iteration
PAP	Professional Advisory Panel
RC	Reinforced Concrete
SDC	Seismic Design Category
SEI	Structural Engineering Institute of ASCE
SU	Stanford University
UCSD	University of California, San Diego

LIST OF SYMBOLS

A_g	gross area of the column
A_{op}	area of opening area
A_{Wtot}	total area of the bay
A_w	cross-sectional area of the masonry wall
c	cohesive strength
c_o	cohesion strength of mortar joints
$C_{Y,P}$	the maximum percentage change of a response quantity "Y" when the value of parameter "P" is changes
D_n	normal stiffness of interface elements
D_t	shear stiffness of interface elements
d_n	normal displacement across a crack
d_t	shear displacement across a crack
d_w	width of the masonry wall
E	modulus of elasticity
E_c	modulus of elasticity of concrete
E_m	modulus of elasticity of masonry
$E_{Y,P}$	sensitivity of a response quantity "Y" to parameter "P"
E_w	modulus of elasticity of the masonry wall

f	frequency
$f_c^{'}$	compressive strength of concrete
$f_m^{'}$	compressive strength of masonry
f_0	compressive stress at first yielding of the uncracked material
f_s	nominal working stress of the longitudinal column reinforcement
f_t'	the tensile strength
f_y	yield stress
G_f^I	mode-I fracture energy
G_f^{II}	mode-II fracture energy
G_w	shear modulus of masonry wall
h	height of the mortar joints
h_a	height of masonry wall above the door or window
h_b	height door or window
h_c	height of masonry wall below the window
h_{cb}	height of the composite column
h_w	height of the masonry wall
I_{ce}	equivalent moment of inertia of the transformed section with respect to concrete
J_2	second invariant of the deviatoric stress
K_2	secondary stiffness

K_{60}	secant stiffness between zero load and 60% of the peak load
K_{ini}	initial stiffness of the uncracked infilled frame
K_{fl}	flexural stiffness
K_{res}	stiffness defining the residual strength.
K_{sh}	shear stiffness
L_a	length of windward masonry pier
L_b	length of door or window
L_c	length of leeward masonry pier
l_w	length of masonry panel
M_{prot}^{grav}	gravity mass carried by the external frame of the prototype structure
M_{spec}	mass of the shake-table specimen
N_{lc}	axial force in the left column
N_{rc}	axial force in the right column
N_w	axial force in the infill wall
P	compressive capacity of reinforced concrete columns
P_w	vertical load applied on the infill
Q	plastic potential
R_A	ratio of the opening area with respect to the area of a solid panel
r	radius of the yield surface at the vertex of the hyperbola
r_o	initial radius of the yield surface at the vertex of the hyperbola

r_p	ratio of residual to peak compressive strength
r_r	residual radius of the yield surface at the vertex of the hyperbola
r_t	ratio of residual to peak tensile strength
S_{A}	area scaling factor
S_E	scaling factor for elastic moduli
S_F	scaling factor for forces
S_{I}	moment of inertia
S_L	length scaling factor
S_{M}	moment scaling factor
S_a	spectral acceleration
$S_a^{i^{recorded}}$	spectral acceleration of i$^{\mathrm{th}}$ recorded base motion
S_a^{MCE}	spectral acceleration of MCE
S_a^{grav}	scaling factor for gravitational acceleration
S_a^{seis}	scaling factor for seismic acceleration
S_m^{grav}	scaling factor for gravitational mass
S_m^{seis}	scaling factor for seismic mass
S_t	time scaling factor
S_ε	strain scaling factor
S_k	curvature scaling factor
S_σ	stress scaling factor

s	tensile strength
s_o	initial tensile strength
T_1	fundamental structural period
$V_{\delta=1\%}$	shear force at 1.00% drift
$V_{c,res}$	residual shear strength of a concrete column
V_E	strength after major drop of lateral load
V_{lc}	shear force in the left column
$V_{\max}$	maximum lateral resistance
V_{res}	residual lateral strength
V_{rc}	shear force in the right column
V_{tot}	total shear force
V_y	yield strength
V_w	shear force in the infill wall
$V_{w,res}$	residual shear strength of the masonry panel
α	material parameter controlling the rate of reduction of μ
α_1	shape factor governing the tensile stress-strain relation
α_d	shape factor for infills with doors
α_i	shape factor
α_w	shape factor for infills with windows
β	material parameter controlling the rate of reduction of r

β_d	ratio of the secondary to the initial stiffness for infills with doors
β_i	ratio of the secondary to the initial stiffness
β_w	ratio of the secondary to the initial stiffness for infills with windows
γ	strength reduction factor
γ_{res}	strength reduction factor
δ_{90}	drift ratio at which the resistance drops to 90% of the peak strength
δ_E	drift after the major drop of lateral load
$\delta_{V_{res}}$	drift at which the residual strength is reached
δ_y	drift at the yield point
ε_1	strain at the peak compressive stress for the cracked material
ε_{1p}	strain at the peak compressive stress for the uncracked material
ε_2	strain at the transition point between the parabola and the exponential function for the cracked material
ε_{2p}	strain at the transition point between the parabola and the exponential function for the uncracked material
ε_{cr}	cracking strain
ε_{ij}^{p}	plastic strain tensor
ε_p	effective plastic strain
η	scalar parameter controlling shear dilatation
θ	angle of interface elements in mesh for concrete elements

θ_{res}	slope of force-vs.-drift relation after the major load drop
κ_i	plastic work that governs the strength degradation
λ	plastic multiplier
μ	slope of the asymptotes
μ_o	initial slope of the asymptotes
μ_r	residual slope of the asymptotes
ξ	damping ratio
ρ_g	ratio of longitudinal reinforcement
σ	normal stress
σ_e	effective stress
σ_{cr}	normal to the crack stress
σ_t	tangential normal to the crack stress
τ	shear stress
ψ	reduction factor for the shear strength of the columns

ACKNOWLEDGMENTS

The research presented in this dissertation has been a long journey. This journey was supported by the NSF Grant No. 0530709 and a graduate fellowship generously awarded by the Department of Structural Engineering at the University of California San Diego for three years of my doctoral studies. However, the assistance I received from the Department has been far and beyond the financial aid and the monthly stipends. All the staff, the personnel in the labs, the students, and the faculty I met throughout the years of my study have made this trip to Ithaca a unique experience. It has been an honor and great pleasure to be part of this community.

I am grateful to all the people I worked with in the laboratories. I consider myself fortunate to have collaborated with such skillful and knowledgeable technicians who supported my experimental endeavors through unexpected difficulties while chasing tough-to-meet deadlines. Whether this was in Colorado or UCSD's Powel Laboratories and the Englekirk Center, their willingness to assist me was remarkable. I truly appreciate their help and friendship.

During my doctoral studies, I also collaborated with a team of knowledgeable engineers and academics. I benefited a lot from working and exchanging ideas with the great researchers like Marios Kyriakidis and Dr Sarah Billington in Stanford University, Ben Blackard and Dr Kaspar Willam in University of Colorado at Boulder, whose help I greatly appreciate. Thanks to the fact that they hosted me in their laboratory facilities and allowed me to actively participate in the tests, I had the chance to observe and better

understand the behavior of the structures I was analyzing and to efficiently design and prepare the large-scale shake-table tests presented in this dissertation. Furthermore, I am grateful for the input I received from a professional advisory panel which consisted of experienced engineers. Discussing the research dilemmas and findings with Joe Maffei, John Kariotis, Mike Valley, Dave Breiholz, Greg Kingsley, Ron Mayes, Tony Court, and Mike Braund offered me different perspectives and helped me to meet successfully the challenges I was facing. From this great group of engineers, I would like to especially thank John Kariotis for his advice over the course of this study. His devotion to this research subject is beyond doubt inspirational. I am also grateful to Dr Thalia Anagnos for sharing valuable data regarding existing RC structures in the city of Los Angeles.

I am also thankful to my all my professors for the knowledge and guidance that they gracefully offered me throughout the years. Dr Joel Conte's classes have been extremely organized and stimulating; I am sure my notes from his classes will be valuable for years to come! Not to mention the example he sets with his pursuit of perfection. Dr Jose Restrepo has been a very inspirational figure for his passion and ability to tackle challenging problems with innovative solutions and for his desire to help people which are simply unmatched. These two professors are merely responsible for the fact that I continued my graduate studies in UCSD after the completion of my M.Sc. research. I would also like to thank professors Murakami and Lubarda for all that I learnt in their classes as their student and as their teaching assistant, and for the help they offered me as my dissertation committee members.

However, the most influential figure throughout my doctoral studies has been my advisor, Dr Benson Shing. With his patience, cool temper, and positive thinking he helped me overcome the various hurdles that I came across. I would like to thank him for offering me all the resources I needed to conduct my doctoral research, for his trust and his exceptional guidance. Thanks to him I learnt how to approach challenging problems with an open mind and resolve them with analytical thinking. Most importantly though, he taught me to trust my reasoning and make important decisions with confidence.

I firmly believe that like Homer's hero I could not have made this trip by myself. I was fortunate that during my PhD I met and worked with people from all over the world. Making friends with such different cultures and backgrounds has made me, I believe, a more rounded person and a more resourceful engineer. Among them, dr-to-be Matthew Schoettler, whom I met during my first week on campus, has been an amazing friend and a great colleague. With Matt we went through all the steps of grad school together and he was always there willing to help me and make things easier. Matt was not the only friend and fellow student whom I would like to thank. Yannis, Hussein, Bobak, Yohsuke, JongKook, Ozgur, George, Giusi, Goran, Bruno, Andre, Juan, Marios, Bernd, Andrea, Kevin, Marianna, Thanos, Stavros et al. are just some of my fellow students and friends who helped me at different times and situations during my graduate studies in San Diego.

I would like to thank Zoe. Had it not been for her, I would have probably never have begun this journey. Not only did she inspired me to embark on this intellectual quest several years ago, but has always led the way in a wise and affectionate manner. And I

am confident there is no other person happier and prouder that this dissertation is completed than her.

Finally, I would like to thank my parents for everything they have done for me. My mother has been throughout the years a low profile hero who always made sure I had everything needed to focus on my studies. The sacrifices she has made are a priceless lesson for life. My father, an engineer himself, not only encouraged me to follow his steps but made sure to train me very early on by posing questions and problems. His goal was to teach me to seek for the reasoning behind what was happening around me. Moreover, it was during his inspections of damaged structures after the 1999 earthquake in Athens that I decided to study structural engineering and focus on the seismic performance of structures. My parents will always be two great examples to follow and two sources of wisdom and ethos to learn from.

This dissertation signifies the end of a trip. It was not the first one I ever took, but it was certainly the most challenging and adventurous. As Cavafy mentions with regards to Odysseus' quest of Ithaca, the Ph.D. was my motivation for this amazing trip. Getting there can only be the starting point for new voyages to other destinations. The experience I got from this journey will be very helpful, no matter which the new Ithacas will be. I only hope the trips to come will be as fulfilling and rewarding as this one.

VITA

2002	Diploma in Civil Engineering, National Technical University of Athens
2004	Master of Science, University of California, San Diego
2009	Doctor of Philosophy, University of California, San Diego

ABSTRACT OF THE DISSERTATION

Analytical and Experimental Study of Seismic Performance of Reinforced Concrete Frames Infilled with Masonry Walls

by

Andreas Stavridis

Doctor of Philosophy in Structural Engineering

University of California, San Diego, 2009

Professor P. Benson Shing, Chair

Unreinforced masonry panels are often used as interior or exterior partitions in reinforced concrete frames. How infills affect the seismic performance of an RC building is an intricate issue since their exact role in the seismic load resistance is not yet clearly understood due to the interaction with the bounding frame. Assessing this role presents a challenge for structural engineers due to the variety and complexity of observed failure mechanisms and the lack of reliable methods able to capture these mechanisms.

Furthermore, there is a lack of experimental data from large-scale dynamic tests of multi-story, multi-bay infilled frames to validate the analytical tools.

This dissertation addresses this intricate issue with extensive analytical and experimental studies. The testing program involved quasistatic tests of small and large-scale specimens with and without openings and shake-table tests of a large-scale, three-story, two-bay, RC frame. This frame, which had a non-ductile design and was infilled with unreinforced masonry panels with openings, was the largest structure of this type tested on a shake table. The design of the specimens, the testing procedures, and the obtained results are discussed in this dissertation as they enhanced the understanding of the structural behavior.

The experimental data has been used to validate the proposed analytical tools. These include a nonlinear finite element methodology and a simplified assessment tool for the engineering practice. The finite element modeling methodology combines the smeared and discrete crack approaches to capture the shear and flexural failure of RC members, crushing and splitting of brick units and the mixed-mode fracture of mortar joints. A systematic approach has been developed to calibrate the material parameters, and the comparison with the experimental results indicates it can successfully capture the nonlinear behavior of the physical specimens.

The validated models have been used in parametric studies to identify the critical material parameters and assess the influence of design parameters and variations of the geometrical configurations to the structural response. The parametric studies and

experimental findings have been used to develop a simplified method for the structural assessment of infilled frames. The proposed approach can estimate the structural performance, including the stiffness and strength and can be used for the construction of simple strut models for an entire structure.

CHAPTER 1

INTRODUCTION

1.1 Background

Unreinforced masonry walls are often used as interior and exterior partitions in reinforced concrete (RC) frames. The infill walls are typically considered as non-structural elements and are often overlooked in the structural analysis and design. However, they can interact with the bounding frames under seismic loads and alter the load resisting mechanism and failure pattern of the RC frame. The issue as to how infills affect the seismic performance of an RC building is intricate as the exact role of the masonry walls during an earthquake is complex and not yet clearly understood.

In many cases, masonry infills have proven to increase the lateral in-plane stiffness and strength of an RC frame (EERI 1996). However, in some cases, the interaction of infill walls with the bounding frames induced the brittle shear failure in the RC columns and, thereby, led to catastrophic failures and undesired soft-story mechanisms (e.g., EERI 2000). Often, the structural failures can be attributed to the poor quality of the construction, inferior design, torsional irregularities, and irregularities in stiffness and strength distribution along the height of the structure, including the absence of infill walls in critical locations such as the first story. Due to the considerable number of existing buildings with this type of structural systems, it is important to be able to

assess their seismic performance in a reliable manner. However, such analysis presents a major challenge since the frame-infill interaction can result in a number of possible failure mechanisms including the cracking and crushing of the infill walls and the shear failure of the columns. Nonetheless, the exact failure mechanism is often unknown since variations of material properties, design details, and geometric configurations can influence the seismic response of these structures.

Guidelines for the evaluation of infilled frames have been provided in reports published by FEMA (1998 and 2000), International Existing Building Codes (ICBO 2001), and ASCE/SEI 41-06 (ACSE/SEI 2007), but they are far from satisfactory in terms of completeness and reliability. The aim of this study is to experimentally and analytically investigate the seismic behavior of such structures, and to provide guidance for the development and calibration of analytical tools to assess the seismic performance of masonry infilled RC frames. To this end, two analytical approaches have been developed; a detailed finite element modeling scheme which can capture the frame-infill interaction and the failure mechanisms and a simplified methodology which aims to provide basic information on the behavior of these structures. The analytical approaches have been validated with the results of an extensive experimental program which included large-scale quasistatic and dynamic tests. The latter were conducted on a 2/3-scale, three-story, two-bay frame, which was the largest structure of this type tested on a shake-table.

1.2 A Widespread Problem

Reinforced concrete frames infilled with unreinforced masonry walls can be found in many areas of high seismicity around the world. This is the most common structural system for new and existing buildings in many areas including the Mediterranean and Latin American countries, which have suffered the results of destructive earthquakes as seen in Figure 1.1. Moreover, infilled frames can be found in earthquake prone countries like China and Iran. In most of these cases, the design considerations for the infilled frames have evolved over the years, as a result of damages suffered during earthquakes and also due to the research that has been conducted world wide to improve the understanding of their behavior. However, a number of the existing structures have been designed with older design approaches, which did not appropriately address the seismic threat.

Examples of such structures exist in crowded downtown areas in California as well, even though unreinforced masonry has been disallowed in California since the 1933 Long Beach Earthquake. Anagnos et al. (2010) have conducted an extensive study to identify and catalogue older reinforced concrete structures in California and their current structural condition. So far, 594 such older buildings have been identified only in the City of Los Angeles, excluding schools and hospitals (Anagnos 2009). As presented in Figure 1.2, most of these structures were built in the 1920s, and only 5% of them have been retrofitted. The majority of these structures are low-rise structures of five or less stories as illustrated in Figure 1.3, with an average floor area of 6050 m^2 (65024 ft^2). Some of these structures are churches, hospitals, and movie theaters and 17% are residential

buildings, as summarized in Figure 1.3(b). The vast majority however, is used for offices, and commercial and industrial activities. Severe damage to these structures in a major earthquake could result in considerable economic losses even if the structures can avoid collapse. Moreover, these structures can generate significant hazard due to the falling debris of damaged masonry walls. Hence, it is important to have reliable analytical tools to assess their seismic performance so that vulnerable structures can be identified and retrofitted.

1.3 Experimental Investigations

The seismic performance of masonry-infilled RC frames has intrigued the interest of many researchers worldwide and has been the subject of a large number of experimental studies. The experimental research efforts have included studies of non-ductile RC frames infilled with unreinforced masonry (Fiorato et al. 1970; Al-Chaar et al. 2003; Mehrabi et al. 1994, Centeno et al. 2008), as well as ductile RC frames designed according to current code provisions (Fardis et al. 1999; Zarnic et al. 2001; Calvi et al. 2004; Hashemi and Mosalam 2006). These studies have indicated the importance of the interaction between the infill panel and the bounding frame that can change the load resisting mechanism of either component. In most cases, the in-plane lateral resistance of an infilled frame is not equal to a simple summation of the resistance of the masonry wall and the bare frame. For low levels of lateral load, an infilled frame acts as a monolithic load-resisting system. As the load increases, the infill tends to partially separate from the

frame and form a compression strut mechanism as postulated by Stafford Smith (1962). However, the compression strut may or may not evolve into a governing load resisting mechanism depending on the stiffness and strength of the infill with respect to those of the RC frame.

Mehrabi et al. (1994) examined the influence of various parameters on the structural performance of 14 half-scale, single-story RC frames tested under in-plane lateral loads. The RC frames had either a ductile or a non-ductile design according to the provisions of ACI 318-89. For the masonry walls, two types of infill panels were considered. One consisted of hollow concrete blocks (weak infill) and the other had solid concrete bricks (strong infills). In both cases, the infill panels tended to significantly increase the strength and stiffness of an RC frame.

The study has identified three main failure mechanisms that are shown in Figure 1.4. A frame with a weak infill panel tended to exhibit a relatively ductile behavior that was dominated by the sliding of the masonry bed joints over the height of the wall. This could sometimes lead to flexural yielding or shear cracks in the concrete columns and masonry crushing at the compression corners, as shown in Figure 1.4a. This mechanism could also occur in a strong infill bounded by a relatively strong and ductile RC frame. The second mechanism, illustrated in Figure 1.4b, was characterized by a diagonal crack initiating in the infill, near the top windward corner, and leading to a shear failure of the adjacent column. This mechanism occurred in non-ductile frames with strong infills. Such behavior was brittle and associated with a significant drop of the loading carrying capacity. In the case of a strong frame and a strong infill, a third mechanism

characterized by corner crushing, as shown in Figure 1.4c, can occur. The wide range of failure mechanisms indicates the importance of the interaction of the RC frame and the infill wall. The different possible failure mechanisms of infilled frames, such as the ones discussed above, can be captured with an appropriate finite-element modeling and discretization approach, and with the selection and calibration of appropriate constitutive models. These are discussed in the following chapters

.

1.4 Available Analytical Tools

Evaluating the seismic performance of infilled frames has been a challenging task for structural engineers. In practice, they commonly use simplified analytical methodologies such as the diagonal strut models (ASCE 41-06). Strut models have been used quite successfully (Stafford Smith 1966; Madan et al. 1997; Al-Chaar 2002); however, they are not accurate in representing some of the failure mechanisms exhibited by infilled frames. Moreover, the estimation of the effective strut width often relies on empirical formulas or case-specific experimental data. Hence, their usefulness as a predictive tool is limited. Alternatively, one can use limit analysis methods (Fiorato et al. 1970, Liauw and Kwan 1983, and Mehrabi et al. 1994). Nonetheless, the information they can provide is limited to the maximum resistance of the structure according to predefined failure mechanisms. Hence, they should be used with extreme caution and examined all possible failure mechanisms to ensure that the actual failure mechanism is included in the considered mechanisms.

The most powerful analysis tool is the nonlinear finite element modeling. Lotfi (1992), Lourenco (1996) and Attard et al. (2007) modeled masonry walls with a combination of continuum elements and interface elements to simulate the brick units and the mortar joints. Mehrabi and Shing (1997) simulated the behavior of masonry infilled RC frames using a combination of discrete and smeared crack elements for the RC frame and the infill panel. Their models showed some success in capturing the nonlinear behavior of the infilled frames but failed to capture some of the failure mechanisms observed in their tests. This is probably attributed to issues related to the finite element discretization and model calibration. Chiou et al. (1999) modeled infilled RC frames by discretizing the brick elements and concrete members into blocks interconnected with contact springs able to simulate the tensile and shear failure.

ASCE 41-06 recognizes the recent advancements in computational modeling and permits the analysis of such structures with nonlinear finite element methods. Nevertheless, aside from a general statement, it does not provide further information or guidance to ensure the accuracy of the analyses. The document also includes guidelines for the assessment of infilled frames based on the equivalent strut approach. The guidelines, however, are not satisfactory in terms of completeness and have not been fully validated.

1.5 Dissertation Outline

This dissertation consists of three main parts: i) finite element modeling of RC frames with brick infills, ii) experimental evaluation of the performance of these structures under seismic loads, and iii) simplified analytical tools that can be used to assess existing structures.

Chapter 2 introduces a finite element modeling methodology for the assessment of the performance of RC members and masonry walls under in-plane loads. The methodology incorporates a non-linear finite element scheme and a systematic calibration approach for masonry infilled RC frames. The modeling scheme combines the advantages of the smeared and discrete crack approaches to circumvent the inadequacy of the smeared crack elements to simulate the brittle shear behavior of RC members and the mixed-mode fracture of masonry mortar joints. Hence, if appropriately calibrated, it is able to reproduce the different failure modes of infilled frames, including the flexural and shear cracking of the RC members, the crushing of concrete and brick units, and the fracture of mortar joints.

Chapter 3 presents the validation of the finite element modeling approach developed in Chapter 2 with experimental data from quasistatic tests on a bare RC frame and two infilled RC frames. The three frames were tested by Mehrabi et al. (1994) and had the same non-ductile design, while for the infills solid concrete units and hollow concrete blocks were used corresponding to a strong and a weak infill, respectively. The comparison of the numerical and laboratory data indicates that the numerical models

successfully capture the highly nonlinear behavior of the physical specimens and their distinct failure mechanisms as they are able to capture the nonlinear material behavior and the interaction of the infill wall with the bounding RC frame. The validated models have been used to assess the sensitivity of the numerical results to the modeling parameters and to identify the critical material parameters through a parametric study which considered all the modeling parameters for concrete, steel rebars, masonry units and mortar.

Chapter 4 presents the design of a prototype RC building with the approach used in the 1920s in California. The design approach is similar to the allowable stress design philosophy. It only considered gravity loads, and resulted in non-ductile detailing of the RC members that do not meet the current standards. The prototype structure designed in this chapter is the focal point of the analytical and experimental studies presented in the subsequent chapters.

Chapter 5 discusses the results from an experimental program of quasi-static tests of singe-bay, single-story, masonry-infilled, non-ductile RC frames, which were scaled subassemblages of the prototype structure designed in Chapter 4. The specimens were infilled with solid masonry walls and walls with three different opening configurations. The test results provide useful information on the scaling effect and also on the effect that doors and windows have on the lateral strength and load resisting mechanism of infilled frames. The physical specimens have been modeled with the nonlinear finite element modeling scheme developed in Chapter 2, and the comparison of the analytical and

experimental results demonstrates the capabilities of the modeling scheme, and provides insight into the behavior of these structures.

Chapter 6 examines the influence of a number of design parameters on the behavior of the RC frames with solid panels. To this end, frames with different aspect ratios, different amounts of longitudinal and transverse reinforcement, as well as different amounts of vertical load have been analyzed with the finite element modeling approach validated in Chapter 5. The results of this study are used to develop a simplified analytical approach for RC frames with solid infills.

Chapter 7 considers the effect of openings on the structural performance of infilled frames. The study extends the experimental results presented in Chapter 5, by considering five different opening geometries: four different window sizes and a door, and five different locations of each opening type with respect to the RC frame. The scope of the study is to provide insight as to the mechanism which transfers the seismic loads and can lead to the failure of such structures. Based on the results of the parametric study, the simplified analytical tool developed in Chapter 6 has been extended to account for the effect of the openings.

Chapter 8 discusses the specimen design, test setup, material properties, and instrumentation for the shake-table tests of a three-story, two-bay infilled RC frame. The specimen was a 2/3-scale model of the external frame of the prototype structure and was the largest structure of this type ever tested on a shake table. The challenges associated with the design of the test specimen involved the incorporation of different gravity and

inertia masses, appropriate scaling of the prototype, and the prevention of unrealistic failure modes such as rocking, twisting, and out-of-plane collapse of the frame. Moreover, the chapter presents an extensive testing program conducted to obtain the properties of the materials used for the construction of the specimen. The material tests included special test setups which were built to measure the tensile and shear properties of the brick-mortar interface. The specimen was instrumented with an array of 285 sensors used to monitor its performance during the shake-table tests.

Chapter 9 presents the results of the shake-table tests conducted on the three-story, two-bay infilled frame RC frame. The frame was tested on the outdoor shake table at the Englekirk Center of UCSD in the fall of 2008 and was subjected to a sequence of 44 dynamic tests, of which 14 were scaled earthquake records. The goal of the testing protocol was to gradually damage the structure by subjecting it to ground motions of increasing intensity, which eventually brought the structure to a state of impending collapse. The structural performance and the induced damage at every stage of the testing sequence are presented in detail in this chapter.

Chapter 10 presents an overview of the study and summarizes the major findings conclusions. The appendices included at the end of this dissertation provide additional data and information that were generated in this study.

Figures of Chapter 1

(a) Kocaeli, 1999 (EERI 2000)

(b) Mexico city, 1985 (photo courtesy of Zeris 2006)

Figure 1.1: Historic failures of infilled RC frames.

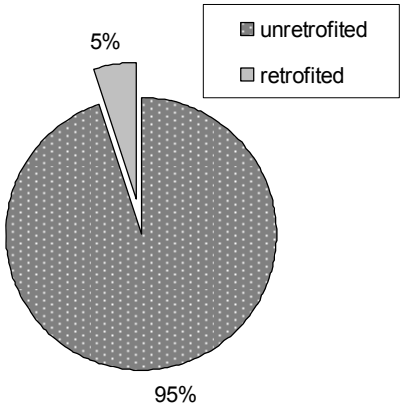

(a) current condition

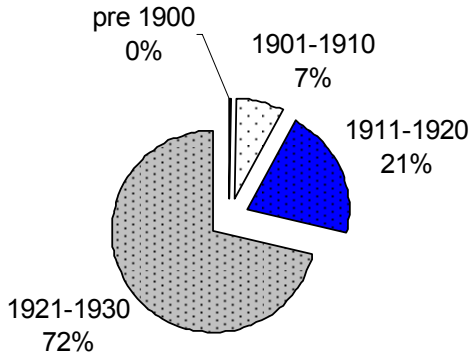

(b) year built

Figure 1.2: Statistics of the 595 structures found in the City of Los Angeles (data courtesy of Anagnos 2009).

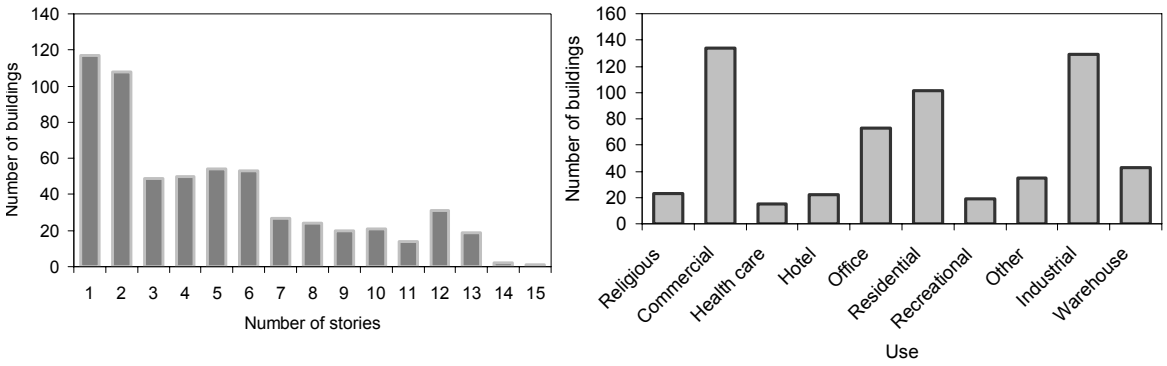

(a) number of stories (b) current use

Figure 1.3: Distribution of existing structures in the City of Los Angeles in terms of the number of stories and current use (data courtesy of Anagnos 2009).

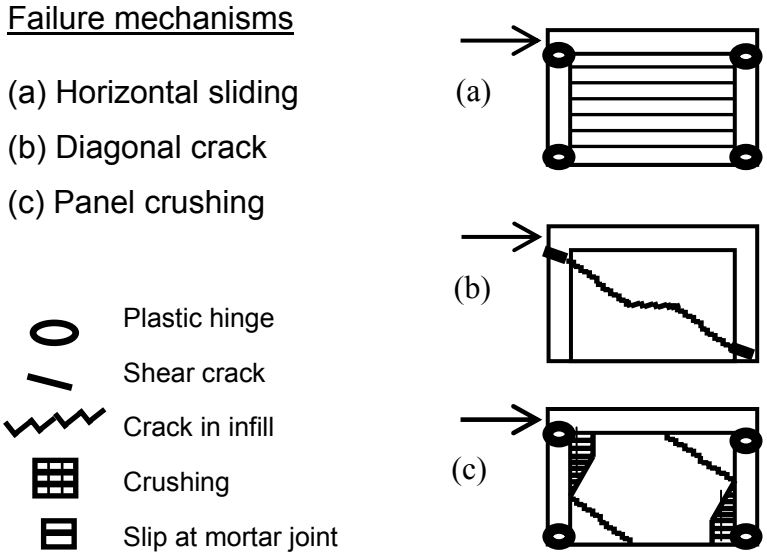

Figure 1.4: Failure mechanisms of infilled frames observed by Mehrabi et al. (1994).

CHAPTER 2

FINITE ELEMENT MODELING SCHEME

2.1 Introduction

The failure pattern of an infilled RC frame may be characterized by diffused flexural cracks and dominant shear cracks in the RC members, tensile and shear fracture of mortar joints, and compressive failure of concrete and masonry units. To capture the possible failure mechanisms of RC members and masonry panels with a finite element model, two main considerations are essential: the first is the modeling and discretization approach, and the second is the selection and calibration of appropriate constitutive models. These issues are addressed with a general modeling scheme and the calibration methods which are presented in this chapter.

2.2 Background

The different failure modes exhibited by RC frames can be captured in an accurate manner with the combination of the smeared and discrete crack approaches. The smeared crack approach is an efficient way to model diffused cracks and compression failure in concrete and masonry. However, this approach suffers from some inherent

problems including the inability to capture the brittle behavior associated with the opening of diagonal shear cracks (Lotfi and Shing 1991; Shing and Spencer 2001). This is caused by the kinematic constraint introduced in a smeared crack formulation and is sometimes referred to as stress locking (Rots 1988). Similarly, a smeared crack model cannot adequately capture the sliding shear failure of masonry mortar joints. Nevertheless, these are common failure mechanisms encountered in masonry-infilled RC frames.

To overcome this inherent limitation of smeared-crack elements, Mehrabi and Shing (1997), and Shing and Spencer (2001) supplemented the smeared crack models with zero-thickness interface elements to model shear cracks in a discrete fashion. However, this requires that the location and orientation of potential cracks be known *a priori*. In the masonry infill, the mortar joints introduce weak planes at known locations and do not present a problem for the discrete crack approach. The issue is more complicated for RC members in which brittle shear failure can occur in various locations and orientations. Mehrabi and Shing (1997); and Shing and Spencer (2001) introduced interface elements at selected locations in RC columns to model shear behavior. Figure 2.1(a) illustrates the difficulty in capturing the shear failure of a column with smeared crack elements, while Figure 2.1(b) presents the model of the same column using zero thickness interface elements (Shing and Spencer 2001). This was possible due to laboratory observations that provided information regarding the crack locations. For complicated structures, though, adequate information may not be available *a priori*. Moreover, the interface elements complicate the connectivity of the truss elements

simulating the reinforcing bars, which is crucial for capturing the behavior of an RC member.

2.3 Discretization scheme for reinforced concrete members

Reinforced concrete members are often discretized with a rectangular grid of nodes connected with quadrilateral smeared-crack elements. The reinforcing steel can be modeled as a smeared overlay or with discrete truss bars. While the former is more efficient, the latter is often preferred when the mesh for the concrete member is fine enough to allow the positioning of the steel bars at proper locations. To model shear cracks in a discrete fashion without the prior knowledge of their locations and orientations, each quadrilateral element can be replaced with a module of smeared-crack and interface elements. Each module consists of four triangular smeared-crack elements connected with four, diagonally placed, double-noded, zero-thickness interface elements, as illustrated in Figure 2.2. Each module is connected to the adjacent modules with horizontal and vertical interface elements. With the proposed mesh topology, discrete cracks can develop at angles of 0^o, 90^o and $\pm \theta$, where θ can be close to 45^o to represent diagonal shear cracks. This scheme allows for the propagation of cracks with a combination of the above orientations depending on the stress distribution. Flexural cracks in concrete can be captured in either a smeared or a discrete fashion, while the smeared-crack elements can model the compressive failure. The introduction of discrete cracks not only removes the undesired stress locking under shear but also alleviates the mesh-size sensitivity problem, which is well known for smeared-crack models (Bazant

and Oh 1983). To model the nonlinear behavior of concrete members in a refined manner, they can be discretized with as many modules as needed in either direction to obtain an accurate solution. In general, it is desirable that the size of an element be close to the expected compressive failure zone in the concrete member.

With the aforementioned discretization scheme, each interior node of the initial orthogonal mesh is replaced by eight nodes which have the exact same coordinates. Each node is associated with one triangular element and two interface elements, as shown in Figure 2.2. Consequently, the steel bars can be connected to the concrete elements in a number of ways. One should consider though, that the bars, when strategically placed, can enhance the numerical robustness of a finite element model for quasi-brittle materials. Therefore, it is desirable to have as many nodes of a smeared-crack element connected to steel bars as possible. Furthermore, it is important that a potential discrete crack will cross the same quantity of flexural and shear steel as in reality.

A scheme illustrated in Figure 2.2 has been proposed for the flexural and shear reinforcement in light of the above considerations. As shown, the flexural steel at each interior location is equally divided into eight truss elements so that every triangular element is attached to flexural steel at two of its nodes. Along the external edges of an RC member there are four nodes with the same coordinates at each location. Therefore, the flexural steel is divided into four truss elements. This arrangement is repeated in the longitudinal direction and provides a degree of restraint to the triangular elements when the tensile strength of the adjacent interface elements has been exhausted. For the shear reinforcement, the number of parallel bars can be reduced for computational efficiency

since the arrangement of the longitudinal reinforcement provides the desired restraint to the triangular smeared-crack elements. The total shear steel area at each location can be divided in two bars placed in a zigzag pattern, as shown in Figure 2.2. The zigzag pattern is selected to prevent the horizontal sliding along the horizontal surfaces, because this is not a realistic mechanism. In this case, the transverse reinforcement provides the resistance which the longitudinal reinforcement would provide in an actual RC member due to the dowel action.

With the proposed modeling scheme, every potential horizontal and diagonal crack would cross the proper quantity of flexural and shear steel. This is illustrated in Figures 2.3 and 2.4 for a concrete member modeled with three modules of smeared and discrete crack elements along its width. Figure 2.3 shows the development of a horizontal flexural crack, while in Figure 2.4, the development of a discrete diagonal crack is shown for the same RC member. In members discretized with a large number of modules, discrete cracks can propagate as a combination of horizontal and diagonal cracks. In all cases, the total amount of longitudinal and transverse reinforcement resisting a crack would correspond to the reinforcement amount that an actual crack would cross.

2.4 Discretization scheme for masonry infill

In a masonry assembly, the mortar is normally much weaker and softer than the brick. However, the failure pattern of the assembly may involve crushing and tensile fracturing of masonry units, fracturing of mortar joints, and tensile or shear fracturing of

the interface between mortar joints and masonry units. When a masonry assembly is under compression, the lateral expansion of the mortar introduces a lateral tensile stress on the brick, which in turn provides a confining stress on the mortar (Hilsdorf 1969). This lowers the compressive strength of the brick as it often leads to a tensile splitting crack parallel to the compression force. Due to the brick-mortar interaction, the stiffness and compressive strength of the masonry assembly are lower than those of the brick but higher than those of the mortar. Under tension or shear, field and laboratory evidence has indicated that the fracture of a masonry assembly normally occurs at a brick-mortar interface. Owing to a kinematic constraint introduced by the continuum approach (Lotfi and Shing 1991), which contributes to the stress-locking problem, a smeared-crack model cannot capture the sliding failure of a mortar joint. Hence, a precise simulation would require the detailed modeling of the brick units and the mortar joints with continuum elements and their inter-connection with cohesive interface elements. However, this will result in a rather computationally intensive model.

For the modeling of a masonry wall, one can make a significant simplification and represent an entire mortar joint with a zero-thickness cohesive interface model (Lotfi and Shing 1994). In this case, the dimensions of the masonry units need to be modified in the finite element model to maintain the same overall dimensions of a brick-mortar assembly when a mortar joint is replaced by a zero-thickness line element as shown in Figure 2.5. Clearly, with this approach, the failure of a brick-mortar interface is not distinguished from that of the mortar layer itself. Furthermore, the brick-mortar interaction in a masonry assembly and the tensile splitting of the brick units under compression can not

be simulated. Hence, with this modeling approach, it is evident that some of the material properties of the continuum elements representing the brick should reflect those of a masonry assembly rather than those of the brick itself. This is discussed further in the calibration procedure in the following section.

A discretization scheme based on the above discussion is presented in Figure 2.6, in which each masonry unit is modeled with two rectangular continuum elements that are inter-connected with a vertical interface element. The latter allows for the tensile splitting of the brick units and the relative rotational or sliding motion within a fractured unit, which can occur when the mortar is sufficiently strong as compared to the brick. Since masonry crushing is simulated with smeared-crack elements the size of the half-brick elements influences the localization of compressive failure. As a result, for larger masonry units, finer discretization may improve the numerical accuracy.

2.5 Constitutive models

The finite element discretization schemes discussed above require a smeared-crack constitutive model to represent the nonlinear behavior of concrete and masonry with a continuum approach. In addition, a cohesive crack model is required to capture cracks in the concrete members, brick units, and mortar joints in a discrete manner. While a number of different models are available in the literature and commercial programs, the smeared and the interface cohesive crack models described below are used in this study. These models have the essential features to capture the quasi-brittle behavior of concrete

and masonry in a satisfactory manner, and are general enough to cover broad modeling issues.

2.5.1 Smeared-crack model

From the theoretical standpoint, a plasticity-based model is preferable for simulating the compressive failure of a quasi-brittle material. However, because of the computational efficiency, simple nonlinear orthotropic material laws are most attractive for simulating the tensile fracture process and the behavior of a fractured material. The smeared-crack model used in this study takes advantage of both model types. The model was originally developed by Lotfi and Shing (1991) and incorporated in the finite element analysis program FEAP (Taylor 2007).

In this model, the tensile fracture is governed by a tension cutoff criterion, while the compressive behavior of the uncracked material is governed by the von-Mises failure criterion. When the von Mises yield surface is reached, the plastic behavior is represented by a J_2-plasticity model. Between the initial yield surface and final failure surface, the material exhibits a strain-hardening behavior, followed by a strain-softening behavior after the final failure surface is reached. The von Mises criterion is expressed as

$$f = J_2 - \frac{1}{3}\sigma_e^2\left(\varepsilon_p\right) = 0 \tag{2.1}$$

in which J_2 is the second invariant of the deviatoric stress, σ_e is the effective stress, and ε_p is the effective plastic strain computed from the plastic strain tensor ε_{ij}^p as $\varepsilon_p = \int \sqrt{(2/3) d\varepsilon_{ij}^p d\varepsilon_{ij}^p}$. For modeling the strain-hardening/softening behavior of concrete, the effective stress is expressed as a parabolic function of the effective plastic strain followed by an exponential tail. As shown in Figure 2.7(a), this relation is defined by the following parameters: the compressive stress f_0 at first yielding, the compressive strength of the material $f_c^{'}$, the strain at the peak stress ε_{1p}, and the strain ε_{2p} at the transition point between the parabola and the exponential function.

In tension, the material is initially linearly elastic and when the maximum principal stress reaches the tensile strength f_t' of the material, cracks initiate in a direction normal to the direction of the maximum principal stress. The cracked material is considered as orthotropic with the axes of orthotropy, *n*-*t*, normal and tangential to the direction of the crack as illustrated in Figure 2.7(b). In this study, the crack orientation and axes of orthotropy are assumed to remain constant. After cracking, the tensile stress becomes an exponentially decaying function of the strain as shown in Figure 2.7(c). The brittleness of the fracture is controlled by parameters r_t and α_1 that govern the shape of the exponential decay function. A residual strength $r_t f_t'$ is introduced to enhance the numerical stability. The assumed residual tensile strength should be minimal, since uniaxial tensile tests of concrete and masonry materials indicate brittle behavior and total loss of the tensile load resistance. The initial modulus of elasticity, *E*, tensile strength, f_t' ,

and the shape factor, α_1, which controls the brittleness of the material, define the tensile stress-strain relation.

The compressive stress-strain behavior for the cracked material is depicted in Figure 2.7(d), and is similar in shape to the effective stress-strain relation of the plasticity model. It is parabolic with an exponential tail and is defined by the following three parameters: the compressive strength of the material $f_c^{'}$, the strain at the peak stress ε_1, and the strain ε_2 at the transition point between the parabola and the exponential function. The orthotropic model can be calibrated with data from uniaxial compression tests of the material. The plasticity model should be consistently calibrated so that the compressive stress-strain behaviors represented by the two models match each other to provide a smooth transition at crack initiation.

2.5.2 Interface model

The interface model used in this study is implemented in FEAP as a 4-noded, zero-thickness, isopararametric, line element as shown in Figure 2.8(a). The constitutive model adopts a cohesive crack formulation to simulate mode-I, mode-II, and mixed-mode fracture (Lotfi and Shing 1994). It also accounts for the shear dilatation which is often observed in reality and can be important for simulating the shear response of a confined crack. The model follows a classical elastic-plastic formulation.

$$\dot{\boldsymbol{\sigma}} = D\left(\dot{\mathbf{d}} - \dot{\mathbf{d}}^{\,p}\right) \tag{2.2}$$

in which $\boldsymbol{\sigma} = \{\sigma \quad \tau\}^T$, with σ and τ being the normal and shear stresses at the interface, and $\mathbf{d} = \{d_n \quad d_t\}^T$, with d_n and d_t being the relative normal and shear displacements across a crack, the superposed dot represents the rate form, and **D** is a diagonal matrix with elastic constants D_n and D_t.

The following hyperbolic yield surface, as shown in Figure 2.8(b), is used to model fracture.

$$F(\boldsymbol{\sigma}, \mathbf{q}) = \tau^2 - \mu\left(\sigma - s\right)^2 + 2r\left(\sigma - s\right) = 0 \tag{2.3}$$

in which μ is the slope of the asymptotes of the hyperbola, s is the tensile strength, and r is the radius of the yield surface at the vertex of the hyperbola. It can be shown that $r=(c^2-\mu^2 s^2)/2s$, where c represents cohesion. This surface reduces to the Mohr-Coulomb criterion when r is equal to zero or to a tension-cutoff criterion for infinitely large values of r and μ. The internal variables $\mathbf{q} = \{s \quad r \quad \mu\}^{\mathrm{T}}$ control the evolution of the yield surface with $\mathbf{q}_0 = \{s_0 \quad r_0 \quad \mu_0\}^{\mathrm{T}}$ characterizing the initial surface and s_o being equal to the tensile strength f_t', while $\mathbf{q}_r = \{0 \quad r_r \quad \mu_r\}^{\mathrm{T}}$ characterizes the final state. The following softening rules govern the evolution.

$$
\begin{aligned}
s &= s_0\left(1-\frac{\kappa_1}{G_f^{I}}-\frac{\kappa_2}{G_f^{II}}\right)\geq 0\\
r &= r_r+\left(r_0-r_r\right)e^{-\beta\kappa_3}\\
\mu &= \mu_r+\left(\mu_0-\mu_r\right)e^{-\alpha\kappa_3}
\end{aligned}
\tag{2.4}
$$

in which G_f^{I} and G_f^{II} are the mode-I and mode-II fracture energies, α and β are material parameters controlling the rate of reduction of μ and r, and the κ_i's represent the plastic work that governs the strength degradation. A non-associated flow rule with the following plastic potential is used.

$$
Q(\sigma,q)=\eta\tau^2+\left(r-r_r\right)\left(\sigma-s\right) \tag{2.5}
$$

in which η is a scalar parameter controlling shear dilatation. The direction of plastic relative displacements is governed by the flow rule, i.e. $\dot{\mathbf{d}}=\dot{\lambda}\dfrac{\partial Q}{\partial\boldsymbol{\sigma}}=\dot{\lambda}\,\mathbf{m}$, where λ is the plastic multiplier. With the above plastic potential, the rate of shear dilatation decreases as the plastic work or the compressive stress increases; however, the cumulative dilation is irreversible upon the reversal of shear displacement, which is not realistic for cracks in concrete and masonry. Therefore, this model is not suitable for simulating the crack behavior under cyclic loading when shear dilatation has a significant influence on the shear strength.

2.6 Calibration of Material Models

A systematic calibration approach for the smeared-crack and interface elements is discussed here. This approach considers the modeling assumptions and finite element schemes presented in this study. While one should calibrate the models with relevant material test data, some of the modeling parameters cannot be easily quantified with standard tests and may have to be calibrated with assumptions based on information available in the literature. The implications of these assumptions are assessed with available experimental data in Chapter 3 and a sensitivity study estimates the sensitivity of the numerical results to these modeling parameters.

2.6.1 Calibration of concrete model

As mentioned previously, cohesive interface models can be used to compensate for the deficiency of smeared-crack models in capturing the brittle shear behavior of a concrete member. When both models are employed, they should be calibrated in a consistent manner. To this end, one can calibrate the interface model first as it is a more direct representation of an actual crack.

In theory, one can obtain the tensile behavior of concrete by conducting direct tension tests. However, these tests are generally difficult to conduct and indirect laboratory methods, such as the modulus of rupture and split cylinder tests, are often employed to extract the tensile strength, f_t'. For flexural cracks, the modulus of rupture

can be used for the tensile strength of concrete model, while the split-cylinder strength is more appropriate for shear cracks. However, such considerations will complicate the model calibration. In general, the use of the split-cylinder strength for all the interface elements in a model should be sufficiently accurate, as the tensile strength of concrete does not have a significant influence on the flexural behavior of a reinforced concrete member. Finally, if none of the aforementioned test methods is available, one can estimate the tensile strength of concrete from its compressive strength using well-known empirical formulas available in design codes and the literature (MacGregor and Wight 2005). The methods mentioned above can only provide information on f_t'. The pre-peak behavior is usually assumed to be linearly elastic before fracture, and the elastic modulus can be obtained from compressive tests. The post-peak tensile behavior can be determined with mode-I fracture tests, which are generally difficult to conduct. However, the mode-I fracture energy and thereby the post-peak behavior can be often estimated with test data and formulas available in the literature (e.g. Bazant and Becq-Giraudon 2002). Information on the mode-II (shear) fracture energy is more difficult to obtain. In the absence of such data, one can assume that $G_f^{II} = 10G_f^I$, which has been demonstrated to provide satisfactory numerical results (Lotfi 1992).

The modeling scheme proposed here uses zero-thickness interface elements to capture dominant shear cracks in a concrete member in a more accurate manner. These elements are not supposed to influence the stiffness of the member before fracture. Therefore, their elastic stiffness should be high but not too high to make the model numerically ill-conditioned. Besides the tensile strength, the cohesive crack model used

in this study allows one to specify the mode-I and mode-II fracture energies directly in terms of work per unit area. Information on the former is available in the literature and the latter can be estimated as discussed above. The fracture energies govern the evolution of the failure surface (see Figure 2.8(b)) related to the fracture (de-cohesion) process. The change of the shape of the failure surface signifying the smoothening of a fractured interface under frictional work is governed by α and β, the material parameters controlling the rate of reduction of μ and r, respectively. Information for the calibration of these parameters, as well as the dilatation parameter, η, is not readily available. Such properties depend considerably on the size of aggregates, the composition of the mixture and other factors. Hassanzadeh (1990) conducted mixed mode tests on concrete specimens. Such tests can be used to calibrate the fracture energy and some of the parameters discussed above such as the dilatancy parameter η.

For the calibration of the tensile behavior of the smeared-crack concrete elements, one can use the calibrated stress-displacement curve of the interface model as a reference. To match the tensile behavior of the smeared-crack and interface elements analytically, one should consider the stress-displacement relations for the two types of elements. To define the appropriate stress-strain relation for a smeared crack element, one way is to determine the stress-displacement curve and relate strains to nodal displacements by considering a characteristic length. For constant strain triangular elements, one can assume that the characteristic length be equal to the square root of the element area (Papadrakakis et al. 2005).

The smeared-crack elements have to be calibrated to simulate the compressive behavior of concrete as well. If the interface element, which is elastic in compression, has a high stiffness, its influence can be ignored; otherwise, its flexibility needs to be accounted for, so that the combined behavior matches the stress-strain relation obtained from compressive cylinder tests. One can first calibrate the compressive stress-strain relation of the orthotropic model in the smeared crack formulation. Then, one can calibrate the plasticity model accordingly to assure a smooth transition from one to the other as a crack develops. The slope of the post-peak softening branch should be calibrated with the consideration of the element size to avoid the mesh-size sensitivity problem and capture the localization of compressive failure in an accurate manner. However, this problem could be alleviated by the use of cohesive interfaces in the model in that the discretization shown in Figure 2 can simulate compressive failure with discrete shear fracture along the inclined interfaces.

2.6.2 Calibration of masonry model

While a variety of tests are available to characterize the masonry materials (ASTM 2004), the calibration of the finite elements used to represent the masonry assembly should use experimental data consistent with the simplifying modeling assumptions. To model a masonry infill, a zero-thickness interface, able to account for the mode-I, mode-II, and mix-mode fracture, is used to represent a mortar joint including the two interfaces between the mortar and the masonry unit. According to laboratory and

field evidence, the unit-mortar interface is the weakest link in a masonry assembly. Therefore, tests measuring its tensile (mode-I) and shear (mode-II) behavior can be used for the calibration of the mortar interface element.

For the calibration of the shear behavior of the mortar joints, triplet tests or shear tests of two brick units connected with a mortar joint can be used. In the field, shove tests can be conducted to measure the shear strength and the corresponding normal load. In such tests, one brick displaces laterally under a monitored, normal to the sliding surface, constant load exerted by a flat jack. In case a flat jack cannot be inserted to replace the existing bed joints, the vertical load can be estimated based on the weight of the masonry wall above the location of the shear test. An example of a test setup in an existing infill wall is presented in Figure 2.9. The shear test can be repeated for different values of the normal stress to provide information on the initial and final yield surfaces of the mortar interface element. Such tests can also measure the mode-II fracture energy. Results of such tests are reported by Tasios (1992), van der Pliujm (1992), Mehrabi (1994), Amadei (1989), and Manzouri (1995).

Direct tensile tests on mortar joints are difficult to conduct and may not yield good results. However, the tensile strength of a brick mortar interface can be obtained with beam tests or bond wrench tests. If shear test data is available, the mode-I fracture energy can be deduced from the mode-II fracture energy with the assumption that $G_f^{II} = 10G_f^{I}$. The Young's modulus of mortar can be determined with compression tests of mortar cylinders and the stiffness of the mortar interface elements can be approximated as $D_n=E/h$, in which h is the height of the mortar joints in the specimen.

Even though this assumption does not reflect the actual stiffness of a mortar joint as it ignores the confinement effect of the brick, the error can be compensated for by determining the brick element stiffness in such a way that the overall prism stiffness is matched.

The tensile and shear properties of the interface and smeared crack elements representing the brick can be calibrated in the same way as those simulating concrete. The tensile strength of the brick can be obtained with tensile splitting tests, while mode-I fracture tests can be used for the calibration of the post-peak behavior. Since mode-I fracture tests cannot be easily conducted, experimental data available in literature can be used to estimate the mode-I fracture energy (van der Pliujm 1992). However, one should be cautious about the possible differences due to variations in the geometry and material content of different bricks.

The smeared crack brick elements have to be so calibrated so that, combined with the mortar interface elements, they represent the compressive behavior of the masonry assembly. The interface element is elastic in compression and does not account for the Poisson effect of the mortar layer. To indirectly account for the three-dimensional brick-mortar interaction effect, the compressive behavior of the smeared crack elements modeling the brick should be calibrated with compression tests of masonry prisms rather than the compression tests of individual brick units. However, in the calibration of the masonry units the axial elastic stiffness of an interface element representing a mortar joint should be accounted for as well.

The modeling approach discussed here has an inherent assumption that the compressive behavior of a prism can be captured by a single element representing one course of brick and one zero thickness interface element representing a single mortar joint. This is approximately true if the failure of a prism is distributed along its height, which is often observed in clay brick prisms that exhibit tensile splitting failure under compression. However, stacking smeared-crack and interface elements to model the actual prism configuration will not lead to satisfactory results due to the localization of compressive softening in a single layer of elements. Hence, such a check is normally meaningless.

2.7 Summary and Conclusions

This chapter addresses the challenging issue of modeling the performance of existing masonry infilled RC frames under in-plane lateral loads with the finite element method. A finite element modeling scheme is developed together with consistent calibration guidelines based on the mechanics of concrete and masonry materials. This model combines the discrete and smeared-crack approaches to circumvent the inadequacy of the smeared-crack elements to simulate the brittle shear behavior of RC members and the mixed-mode fracture of masonry mortar joints. The developed models are validated with existing experimental data in Chapter 3 and are used in the following chapters to model laboratory specimens and provide insight to the experimental results obtained during this study.

Figures of Chapter 2

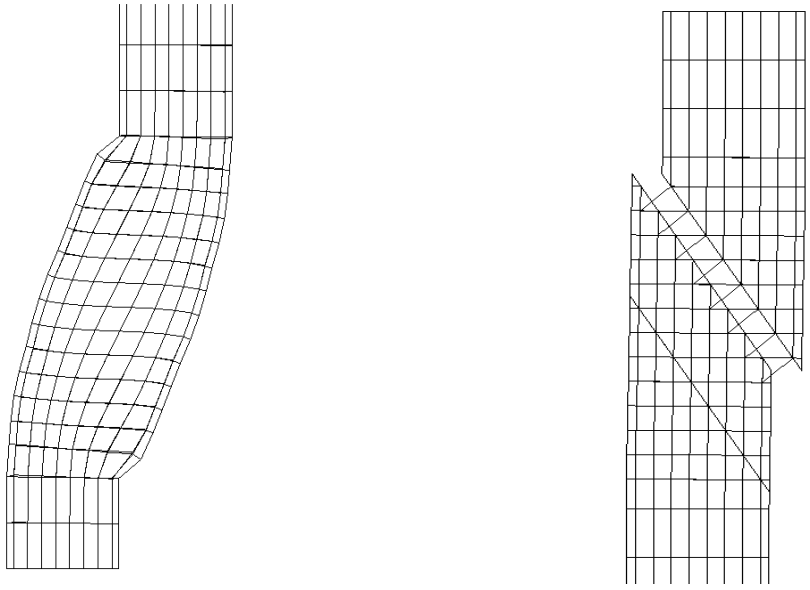

(a) Smeared-crack elements only (b) Smeared-crack and interface elements

Figure 2.1: Deformed messes for an RC column failing in shear (Shing and Spencer 2001).

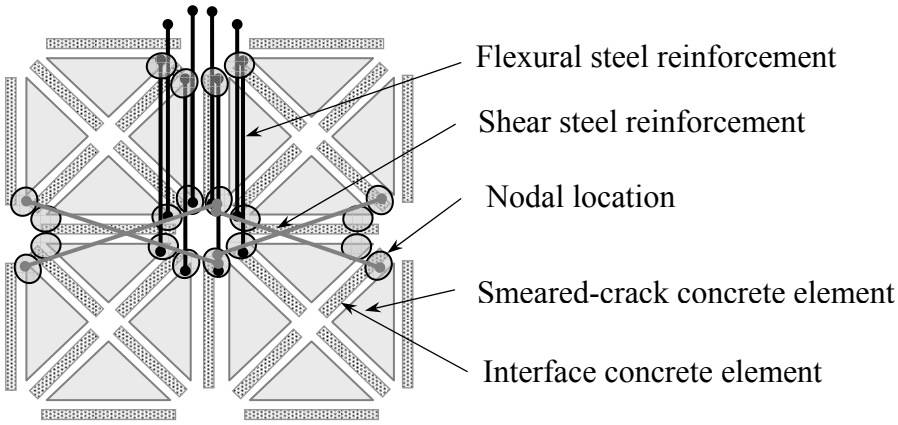

Figure 2.2: Finite element discretization of RC members.

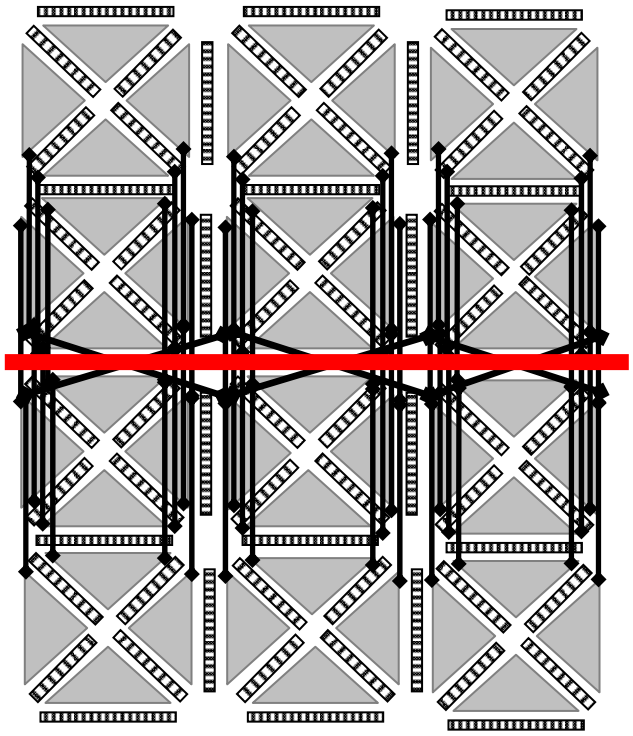

Figure 2.3: Potential flexural crack in reinforced concrete member.

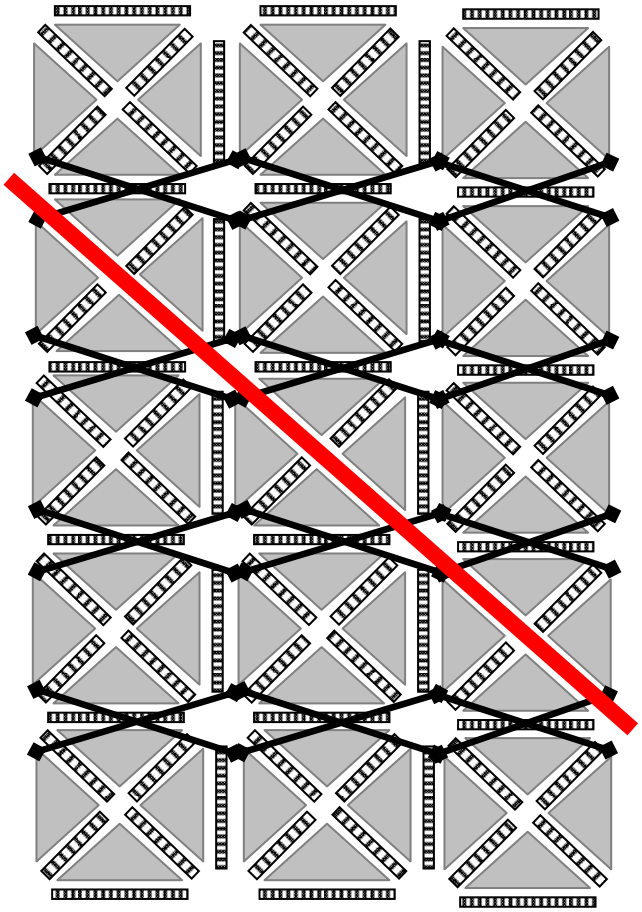

Figure 2.4: Potential discrete shear crack in reinforced concrete member.

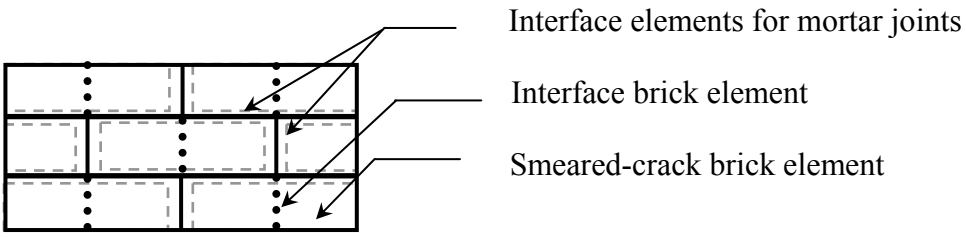

Figure 2.5: Finite element discretization of masonry infill.

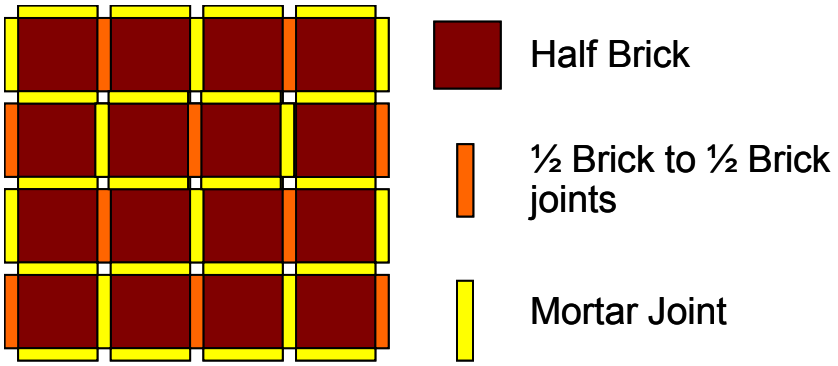

Figure 2.6: Finite element discretization of masonry infill.

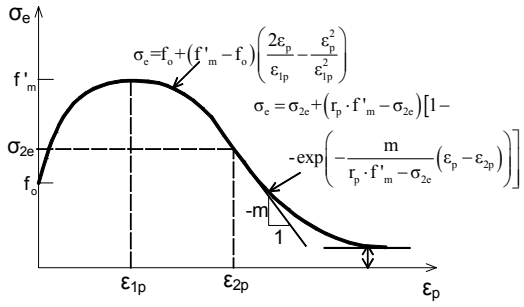

(a) Effective stress-effective plastic strain

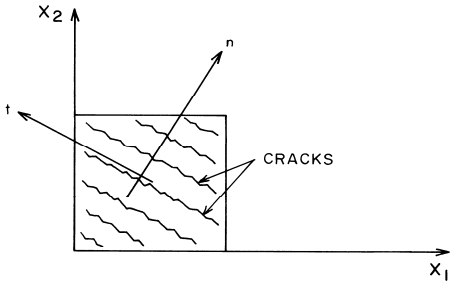

(b) Crack direction and axes of orthotropy

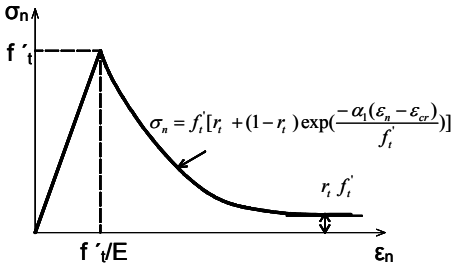

(c) Tension softening

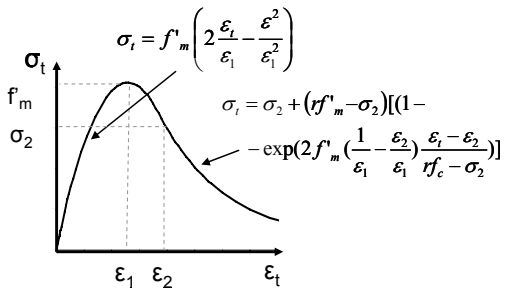

(d) Uniaxial behavior parallel to the crack

Figure 2.7: Smeared crack constitutive model.

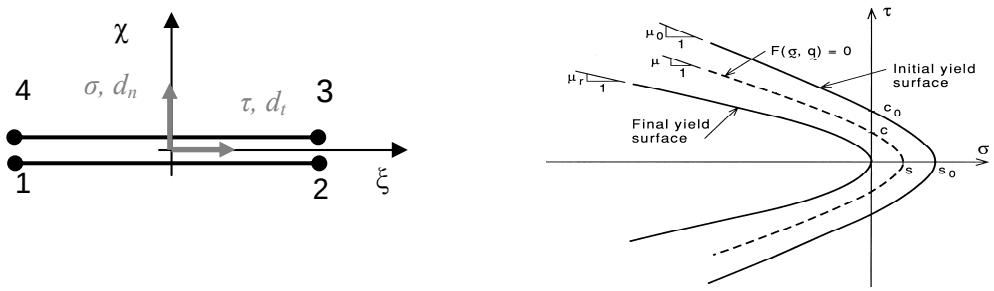

(a) Isoparametric interface element (b) Hyperbolic yield criterion

Figure 2.8: Interface element and constitutive model.

Figure 2.9: Setup for shear tests of existing bed joints exist masonry wall.

CHAPTER 3

EVALUATION OF FINITE ELEMENT MODELING SCHEME

3.1 Introduction

The capabilities of the modelling methodology proposed in Chapter 2 are evaluated in this chapter with the consideration of three infilled frames. These frames include a bare frame and two RC frames infilled with weak and strong masonry walls and have been selected due to the similar design of the RC members but very distinct failure mechanisms. The comparison of the numerical and experimental results indicates that the models can successfully capture the highly nonlinear behavior of the physical specimens and accurately predict their strength and failure mechanisms. The validated models are then used to conduct an extensive sensitivity study. The scope of this study is to assess the sensitivity of the numerical results to the modeling parameters and to identify the critical material parameters. The results of this study and recommendations for the material tests are discussed in this chapter.

3.2 Experimental Models

The proposed modeling method is evaluated in this chapter with three of the infilled frames tested by Mehrabi et al. (1994). They are Specimen 1, which was a bare frame, Specimen 8, which was infilled with hollow concrete blocks (weak infill), and Specimen 9, which had solid concrete bricks (strong infills). The frames were designed for moderate wind loads according to the provisions of ACI 318-89 without the consideration of seismic loads and represent older structures with weak RC frames that do not meet current seismic design requirements. The RC members had the same detailing for the three specimens, which is shown in Figure 3.1. For Specimens 8 and 9, the same concrete frame was used. The frame was repaired after the test of Specimen 8 and re-used for Specimen 9.

The frames were loaded laterally by an actuator moving in displacement control. The total gravity load applied was 66 kips. For Specimen 1, the load was distributed equally on the two columns. For Specimens 8 and 9, 98 kN (22 kips) were applied on each column and 98 kN (22 kips) were distributed along the infill on top of the concrete beam by a W5x16 steel beam. The units used in both specimens are illustrated in Figure 3.1 and the joints had an average thickness of 0.95 cm (0.375 inches) and a cement:lime:sand ratio of 1:0.5:4.5 by volume.

3.3 Numerical Models

The concrete columns are modeled with the scheme shown in Figure 2.2. The base slab and the beam are modeled with 4-node smeared crack elements only for computational efficiency since no shear cracks are expected to develop. The infill is simulated with the model shown in Figure 2.5. In the numerical model, the difference between the solid and hollow masonry units is reflected in the thickness and compressive behavior of the infill. The thickness of the infill in Specimen 8 is specified to be the total thickness of the face shells, which is 3.175 cm (1.25 inch). In terms of concrete properties, the same model is used for Specimens 8 and 9 since the same RC frame was used. Thus, the damage and subsequent repair have not been accounted for in the modeling of Specimen 9.

3.3.1 Material Properties

The material models for concrete have been calibrated according to the proposed approach with data from compression and split cylinder tests conducted by Mehrabi et al. (1994). The calibrated stress-strain/displacement curves are shown in Figure 3.2. In lack of relevant experimental data, the post-peak tensile behavior of concrete is determined with data from wedge-splitting tests conducted by Wittmann (2002). In this investigation of the fracture behavior of concrete, the obtained mode-I fracture energy ranges from 123

to 159 N/m (0.0007 to 0.0009 ksi-in) for tensile strength values varying from 1.9 to 3.8 MPa (0.28 to 0.55 ksi). Split cylinder tests of concrete conducted by Mehrabi et al. (1994) indicated a tensile strength of 2.76 MPa (0.40 ksi). Hence, the mode-I fracture energy of the concrete is assumed to be 140 N/m (0.0008 ksi-in). The values of the input parameters for the interface and smeared-crack elements modeling concrete fracture are summarized in Tables 3.1 and 3.2.

The data from shear tests of mortar joints conducted by Mehrabi et al. (1994) have been used to calibrate the interface elements in the masonry panel. The tests were conducted under constant compressive stresses of 345, 517, 689, and 1034 kPa (50, 75, 100, and 150 psi), and yielded similar results for the hollow and solid concrete units. Mode-II fracture energy was determined by adjusting the analytical shear stress-shear displacement curve to match the experimental, and mode-I fracture energy was assumed to be ten times that of mode-II fracture energy. The experimental and analytical shear stress-shear displacement relations for a normal stress of 1034 kPa (150 psi) are shown in Figure 3.3(a). Figure 3.3(b) shows the peak and residual shear stress values observed in the tests and the initial yield and final failure surfaces of the calibrated model. In the analyses, the same material parameters were assumed for the bed and head joints. The values of the mortar material parameters for each specimen are summarized in Table 3.1. The initial tensile strength for the wall-to-beam and wall-to-column interfaces is assumed to be 1.38 kPa (20 psi) and the corresponding mode-I fracture energy is 17.5 N/m (0.0008 ksi-in) because these joints are normally weaker than the bed joints.

The compressive behavior of the smeared-crack elements representing the masonry units has been calibrated with prism test data obtained for the infill walls (Mehrabi et al. 1994). The elastic modulus of these elements is estimated from the compressive strength of the brick itself in the same way as for concrete. Then, the stiffness of the interface elements representing the mortar joints is so determined that the combined stiffness of a smeared-crack element and mortar interface element matches the stiffness of a masonry prism. The tensile strength of masonry units is assumed to be 10% of its compressive strength (Drysdale et al. 1999). For the mode-I fracture energy of the masonry units, Van der Pluijm (1992) has found values ranging from 60 to 130 N/m (0.00034 to 0.00074 ksi-in) for tensile strength varying from 1.5 to 3.5 MPa (0.22 to 0.51 ksi). Based on this data, the mode-I fracture energy is assumed to be 105 N/m (0.0006 ksi-in) and the mode-II energy is calculated accordingly.

3.3.2 Numerical results

The load-displacement relations obtained from the finite element models are compared with the experimentally obtained responses in Figure 3.4. As shown, the strength and post-peak behavior of the three numerical models match the experimental results well. Initial stiffness is captured for specimen 8, although the numerical models for Specimens 1 and 9 overestimate the experimentally measured stiffness. For Specimen 1, the discrepancy could be caused by the fact that bond-slip between the steel and concrete is not accounted for in the model. Mehrabi et al. (1994) have shown that the pre-peak stiffness of a bare frame can be significantly influenced by bond-slip. However, the

influence of bond-slip is negligible for an infilled frame. Therefore, for Specimen 9, the discrepancy in stiffness is most likely caused by the fact that the model does not account for the pre-damage and repair of the RC frame that might lead to a lower stiffness. The experimental and numerical failure modes of each specimen are presented and discussed in the subsequent sections.

Specimen 1

The deformed shape of the finite element mesh of Specimen 1 at a displacement of 38.1 mm (1.5 inch) is presented in Figure 3.5. The crushing of a smeared-crack element is denoted by an 'X', and cracking by a line reflecting the crack orientation. The length of each line corresponds to the extent of crushing or crack opening. The opening of a gap between adjacent smeared-crack elements represents discrete cracks occurring in interface elements. The reinforcing bars are omitted from the deformed mesh for visual clarity. Figure 3.5(a) illustrates that the failure is dominated by flexural cracks. This is in agreement with the test observations (Mehrabi et al. 1994) and the ductile behavior indicated by the load-displacement curve of Specimen 1 which shown in Figure 3.4.

In Figure 3.5(b), the crushing of smeared crack elements associated with the formation of plastic hinges can be observed at the upper end of the leeward column. The compressive failure is more pronounced in the leeward column due to the axial forces developed in the two columns to resist the overturning moments due to the applied lateral load. Furthermore, the deformed mesh indicates that in the compression zone close to the bottom section of both columns, a triangular element slides downward, implying an

interface shear-sliding failure induced by compression. As the triangular element slides, it loses its compressive resistance signifying compressive failure. Thus, the model captures the compressive failure which is represented in both the smeared and discrete fashion.

Specimen 8

The RC frame of Specimen 8 had the same design as that of Specimen 1 but had slightly different material properties as indicated by the compression tests of concrete cylinders. With the addition of the infill, the structural behavior changed significantly and the lateral strength increased from 106 kN (23.9 kips) for the bare frame to 190 kN (42.7 kips) for the infilled frame. Figure 3.4 illustrates that the initial stiffness, strength and the ductile post-peak behavior are well reproduced by the numerical model.

Figure 3.6 presents the deformed mesh at three different displacement levels. The separation between the frame and infill and the first diagonal cracks shown in Figure 3.6(a), occur at a drift level of 0.17%, and a lateral load of 133 kN (30 kips). Prior to this, the frame and the infill behave as a monolithic system. In the actual test, such cracks were observed at the same load level and a drift of 0.23%. The peak load attained in the analysis is 201.5 kN (45.3 kips) and occurs at a drift of 0.82% while the physical specimen reached the peak load of 188.1 kN (42.3 kips) at a drift of 0.89%. In both the physical and numerical model, at this stage, horizontal sliding has occurred along the bed joints, as illustrated in Figure 3.6(b). The lateral load carried by the infilled frame does not drop significantly despite the cracking, crushing and rotation of some brick units in the infill. As the lateral drift increases further, there is a consistent drop in the resistance

in both the numerical model and test specimen. This is believed to be associated with the crushing of the masonry, which is shown in Figure 3.6(c) and significantly reduces the vertical load carried by the infill. The reduced vertical load reduces the lateral load capacity, which is provided by friction.

The failure pattern of the numerical model resembles that of the physical specimen, which is shown in Figure 3.7. In both cases, the damage is governed by severe slip along a large number of bed joints in the infill. Furthermore, the failure of Specimen 8 involves cracking and crushing of the masonry units; however, the crushing noted in the finite element model is more severe than in the specimen. In the numerical model, as well as in the test, the concrete columns demonstrate a flexural behavior, and only at a late stage of loading, diagonal cracks open at the top of the left column and the bottom of the right column. Therefore, the shear cracks have a limited impact on the load resistance and, are not of practical interest in this case.

Specimen 9

Specimen 9 had the same RC frame as Specimen 8, which was repaired and infilled with solid concrete bricks. As shown in Figure 3.4, the use of solid units (strong infill) leads to a very high strength and stiffness as compared to those of Specimen 8 which had hollow block infill. The peak load reaches 297 kN (66.7 kips), with a relatively steep post-peak slope. The failure of Specimen 9 initiated with the formation of a stair-stepped diagonal/sliding crack in the infill that was followed by a distinct diagonal shear crack at the top of the windward column. This failure sequence is accurately

reproduced with the finite element model, and the numerically obtained load-displacement curve matches the experimental result well, as shown in Figure 3.4.

Figure 3.8 presents the deformed mesh at three drift levels. At the low level of 0.17% and a lateral load of 250 kN (56.5 kips), a diagonal shear-sliding crack occurs in the masonry wall and is followed by minor flexural cracks in the windward column, as illustrated in Figure 3.8(a). The physical specimen yielded similar cracks at this load level but at a lateral drift of 0.30%. The numerical model reaches a load of 288 kN (64.8 kips) when a diagonal shear crack occurs at the top part of the windward column, as shown in Figure 3.8(b), causing a significant drop of the load carrying capacity. This behavior successfully represents the behavior of the test specimen (Mehrabi et al. 1994). At a drift of 2.80% the shear crack at the bottom of the leeward column is more severe in the model than in the test, as indicated in Figure 3.8(c).

3.4 Sensitivity Analysis

A parametric study has been conducted to investigate the sensitivity of the numerical results to the material parameters used to describe the behavior of the concrete, mortar and masonry units. The purpose of the study is to identify the most influential parameters and assess the reliability of nonlinear finite element modeling in view of the expected uncertainties in the material properties. This study considers all the material parameters of the constitutive models and uses the numerical models calibrated for Specimens 8 and 9 as baselines to cover two distinct failure scenarios. Some of the

modeling parameters are not explicitly discussed here because their influence was found to be insignificant or their values are dependent on those of the selected parameters to obtain meaningful material behavior. The selected parameters are varied, one at a time, to a lower and a higher value, and the range of variation reflects the level of uncertainty associated with the value of the respective parameter. However, for interface elements, to keep the same shear strength of a material under the initial normal stress when the tensile strength, $s_{o,}$ which is also denoted as f_t', is varied, the value of μ_0 is adjusted accordingly. The confidence level of each parameter depends on the expected variability in the value of the parameter, and the availability of standard and reliable material testing methods.

The tensile and shear behavior of the cohesive interface models simulating discrete cracks in RC members, brick units and mortar joints are controlled by 11 parameters. These include $\mathbf{q}_0 = \{s_0 \quad r_0 \quad \mu_0\}^{\mathrm{T}}$ and $\mathbf{q}_r = \{0 \quad r_r \quad \mu_r\}^{\mathrm{T}}$ which define the initial yield and final failure surfaces, parameters $\{\alpha, \beta, G_f^I, G_f^{II}\}$, which govern the evolution of the yield surface, the shear dilatancy parameter η, and the normal stiffness of an interface, D_n. For mortar joints, the normal stiffness is varied in conjunction with the stiffness of the brick elements so that the overall stiffness of a masonry assembly is not changed. The study has also included other parameters, such as the residual compressive strength and the Poisson's ratio of the concrete and brick. However, these have not shown significant influence on the response, and therefore the results are omitted. Consequently, 11 parameters are considered for the mortar joints while 14 parameters are studied for the concrete members and masonry units. The parameters considered and their bounds of

variation are summarized in Table 3.3 and 3.4, while the baseline values are shown in Tables 3.1 and 3.2.

The parameters for the tensile behavior of the smeared-crack models for the concrete and brick units are calibrated to match the corresponding behavior of the cohesive interface models. Therefore they are not independent. The compressive behavior of RC members and masonry panels is governed by the elastic modulus, the compressive strength, and post-peak softening behavior of the concrete and brick units. In the orthotropic model used here, these characteristics are controlled by the following three parameters: the compressive strengths $f_c^{'}$ and $f_m^{'}$, of concrete and masonry, respectively, and the strain values ε_1 and ε_2, as shown in Figure 2.7(d). These are explicitly considered in the sensitivity study, while the corresponding parameters for the plasticity model are calibrated to match the behavior of the orthotropic model. The parameters considered, their ID's and their variations are summarized in Tables 3.3 and 3.4, and Figure 3.10(a), while the baseline values are shown in Tables 3.1 and 3.2. Figure 3.10(a) shows large variations for η, α, and β (ID Nos. 12, 13, and 14), which reflect the fact that these parameters are in general more difficult to quantify.

To quantify the influence of each parameter on the structural response, four response quantities are selected to characterize the force-displacement relation of an infilled frame. They are the effective initial stiffness K_{60}, which is defined as the secant stiffness between zero load and 60% of the peak load, the maximum lateral resistance $V_{\max}$ and the corresponding drift ratio $\delta_{V_{\max}}$, and the drift ratio δ_{90} at which the resistance

drops to 90% of the peak strength. The influence of each parameter on a structural response quantity is assessed with two indices. One is $C_{Y,P}$, the maximum percentage change of a response quantity "*Y*" with respect to the baseline value when the value of a parameter "*P*" is increased or decreased according to the values shown in Tables 3.3 and 3.4. This can be expressed as

$$C_{Y,P} = \max \left| \frac{Y - Y^B}{Y^B} \right| \times 100\% \tag{3.1}$$

in which the superscript *B* denotes the respective value of the baseline model.

The sensitivity of a response quantity to each parameter is quantified in a similar way by the following index.

$$E_{Y,P} = \max \left| \frac{Y - Y^B}{Y^B} \frac{P^B}{P - P^B} \right| \tag{3.2}$$

in which *P* denotes the value of the parameter that is varied.

Figures 3.10 and 3.11 present the values of C_Y and E_Y obtained from the parametric study for the two frames with a weak and strong infill, respectively. The main observations are summarized below. However, these results should be interpreted with caution when the expected variation of a parameter is beyond the range considered here because of the nonlinearity of the models.

3.4.1 Effective initial stiffness

As shown in Figure 3.10(b), the percentage changes in the effective initial stiffness of the infilled frames are relatively small for the variations in the material parameters considered here. The results for Specimens 8 and 9 are different because of the different failure mechanisms which affect the relative importance of the parameters. However, it is interesting to note that for both models the material parameters for the concrete frames have little influence on the initial stiffness. For most parameters, the percentage change in stiffness is less than 5%, with a few cases lying between 10% and 16%. The interface parameters, f_t', r_o, and η, for the mortar joints, seem most influential. However, as it can be noted in Figure 12(a), the range of variation of η is also very large. For the weak infill, the variation of strain, ε_1, at peak compressive stress of the brick units shows a similar influence as it causes a stiffness change of 13%. This is expected as the bricks in the weak infill crush early due to their lower strength.

Figure 3.11(a) presents the sensitivity of the initial stiffness to the material parameters. The initial stiffness of both frames demonstrates relatively low sensitivity as the sensitivity index is, in most cases, below 0.4. The stiffness is most sensitive to the compressive behavior of the brick and therefore, that of the masonry. However, that can be relatively easily obtained with the prism tests.

3.4.2 Peak strength

As Figure 3.10(c) shows, the percentage change of the peak strength of the infilled frames is not significant for the range of the parameter values considered. The change is less than 5% for most cases with a few cases being around 15 to 17%. Except for the variation of the mortar dilatancy parameter η, the frame with the weak infill demonstrates negligible change in all cases considered here. The strength of the strong infill is mostly affected by some of the mortar parameters, such as the tensile strength and the dilatancy property of the mortar.

The sensitivity data shown in Figure 3.11(b) indicate that the most influential parameter for the peak strength for both frames is μ_o, which controls the peak shear strength of the mortar joints. This importance of μ_o for mortar can be expected as the shear sliding of the mortar joints initiates the failure of an infilled frame. However, even for this case, the sensitivity index $E_{V_{\max},\mu_o}$ is about 0.55 for the weak infill and 0.85 for the strong infill, and the corresponding changes in the strength are for both frames lower than 10%. It should be pointed out that the value of this parameter is not expected to vary considerably and can be measured with shear tests under different normal compressive stresses.

3.4.3 Drift at peak strength

As Figure 3.10(d) shows, the percentage change of the drift ratio at the peak strength of an infilled frame model is relatively significant for many of the parameters as compared to the change of the initial stiffness and peak strength. However, for most parameters, the change is less than 25% with only a couple of cases exceeding 50% for the model of Specimen 8 (weak infill). It is interesting to point out that in all cases which show considerable change in the drift, the drift increases due to the variation of the modeling parameter. For this frame the drift at peak strength is increased by 210% when the mode I fracture energy of the concrete is decreased by 50%, and by 90% when the dilatancy parameter for concrete is increased 10 times. To evaluate the implication of this large change, the numerical results are examined in further detail. Figure 3.12(a) presents the lateral force-vs.-drift curves obtained from the analyses with the different mode-I fracture energy values. It can be observed that even though the drifts at the peak strength are very different for the case of the weak infill, the overall responses are very similar for all three cases. Similar conclusions can be drawn on the influence of the dilatancy factor as shown in Figure 3.12(b). Hence, to quantify the drift property, one should exercise appropriate judgment and interpretation based on the load-vs.-drift response curve.

The sensitivity of the models in terms of the drift at the peak strength is presented in Figure 3.11(c). This figure indicates that the model with the weak infill is very sensitive to the mode-I fracture energy of concrete and the residual shear strength of the mortar joints. The sensitivity index for the drift at the peak strength with respect to the

variation of G_f^I and η is 4.2 and 4.6, respectively. For the model with the strong infill, the sensitivity is generally much lower except for the μ_o parameter for the concrete, brick, and mortar joint. The sensitivity to the parameter μ_o used for the mortar and brick interface elements is in about 2.5.

3.4.4 Drift at 90% of the peak strength

Figure 3.10(e) presents the percentage change of the drift ratio at which the load resistance of an infilled frame drops to 90% of its peak strength. The trends observed for this response quantity are very similar to those for the drift at the peak strength, although the actual values of the change in the drift may be different. Thus, the largest difference noticed is 117% for the mode-I fracture energy in the case of a weak infill, however, the difference in the actual response of the structure is not significant.

The sensitivity data shown in Figure 3.11(d) indicates that the drift at 90% of the peak load of the model with the weak infill is more sensitive compared to the frame with the strong infill. For the latter all sensitivity indices are less than 2.0. For the weak infill, the initial shear strength of the masonry and the concrete, governed by the parameter μ_o is the most influential parameter with the sensitivity index exceeding 3.0 in both cases.

3.4.5 General Remarks

The results of this study indicate that the μ_o values governing the initial shear strength for the concrete, brick, and mortar are the most influential parameters in the nonlinear finite element models. Of the three materials, the mortar properties appear to be the most influential for both the cases of a weak and a strong infill. Figure 3.13 presents the numerical results for different μ_o values for the mortar joints. Figure 3.13(a) shows the change of the yield surface as μ_o is varied by ±10% of the baseline value. The effect of this variation on the shear behavior of an interface element representing a mortar joint is illustrated in Figure 3.13(b). The impact on the response of the two frames is illustrated in Figure 3.14. The effect of this variation appears to be insignificant for the initial stiffness since at this load level the shear strength of the mortar elements has not been reached. However, when the lateral load increases beyond 50% of the peak strength of each structure, the deviation from performance of the respective reference model is more noticeable. Thus, experimental data on the shear behavior of the mortar joints is important for the calibration of a numerical model.

3.5 Summary and Conclusions

In the chapter, the finite element modeling methodology developed in Chapter 2 is validated with available experimental data. As shown by the numerical examples presented in this paper, the proposed modeling scheme is able to capture the different

failure mechanisms as well as the load-displacement responses exhibited by experimentally tested bare and infilled RC frames. A study has also been conducted to evaluate the sensitivity of the numerical results to the modeling parameters. It has been found that the initial stiffness and peak strength of an infilled frame can be estimated quite accurately as they are governed by material parameters that can be calibrated with relatively easy to obtain test data. Among all the material parameters, the μ_o values governing the initial shear strength of the concrete, brick, and mortar joints are the most important. Of the three materials, the mortar joint properties appear to be the most influential. In general, the μ_o value for mortar joints can be measured with shear tests or estimated with existing test data since it is not expected to vary significantly.

Tables of Chapter 3

Table 3.1: Material parameters for interface elements.

Material	Specimen(s)	D_n (GPa/m)	$f_t^{'}$ (MPa)	G_f^{I} (N/m)	G_f^{II} (N/m)	μ_0 -	μ_r -	r_0 (kPa)	r_r (kPa)	η -	α (m/N)	β (m/N)
Concrete	1, 8, 9	2443	2.75	140	1400	0.9	0.7	138	35	0.6	0.011	12.5
Brick	8	2443	1.72	105	1050	0.8	0.7	138	35	0.6	0.011	12.5
	9	2443	1.72	105	1050	0.8	0.7	138	35	0.6	0.011	12.5
Mortar	8	84.1	0.275	35	350	0.8	0.7	138	35	0.6	0.011	12.5
	9	146.6	0.275	35	350	0.8	0.7	138	35	0.6	0.011	12.5

Table 3.2: Material parameters for smeared-crack elements.

Material	Specimen(s)	$f_c^{'}$ or $f_m^{'}$ (MPa)	ε_1 -	ε_2 -
Concrete	1, 8, 9	26.9	0.0027	0.0043
Brick	8	9.5	0.0015	0.00165
	9	14.2	0.0017	0.0022

Table 3.3: Range of values for the material parameters considered in the parametric study for smeared crack elements modeling brick (B) and concrete (C).

Parameter	$f_c^{'}$ or $f_m^{'}$ (MPa)		ε_1 -		ε_2 -	
ID	1		2		3	
Material	B	C	B	C	B	C
Specimen 8	8.3-11.0	22.8-31.0	0.0023-0.0031	0.0020-0.0035	0.005-0.008	0.0035-0.0050
Specimen 9	11.7 - 17.9	22.8-31.0	0.0022-0.003	0.0020-0.0035	0.0037-0.0049	0.0035-0.0050

Table 3.4: Range of values for the material parameters considered in the parametric study for brick (B), concrete (C), and masonry (M).

Parameter	D_n (GPa/m)			$f_t^{'}$ (MPa)			G_f^{I} (N/m)			G_f^{II} (N/m)			μ_0 -			μ_r -			r_0 (MPa)			r_r (MPa)			η -			α (m/N)			β (m/N)		
ID	4			5			6			7			8			9			10			11			12			13			14		
Material	B	C	M	B	C	M	B	C	M	B	C	M	B	C	M	B	C	M	B	C	M	B	C	M	B	C	M	B	C	M	B	C	M
Specimen 8	814 - 4071	814 - 4071	67.8 - 100.4	1.03 - 2.41	1.38 - 4.14	0.13 - 0.55	52.5 - 157.6	70.0 - 215.2	17.5 - 52.5	525 - 1576	700 - 2101	175 - 525	0.72 - 0.88	0.81 - 0.99	0.72 - 0.88	0.63 - 0.77	0.63 - 0.77	0.63 - 0.77	0.07 - 0.28	0.034 - 0.34	0.034 - 0.34	0.003 - 0.070	0.0013 - 0.070	0.0034 - 0.070	0.06 - 6.0	0.035 - 3.5	0.06 - 6.0	0.0011 - 0.11	0.0011 - 0.11	0.0011 - 0.11	1.14 - 24.0	1.14 - 24.0	1.14 - 24.0
Specimen 9	814 - 4071	814 - 4071	117 - 176	1.03 - 2.41	1.38 - 4.14	0.13 - 0.55	52.5 - 157.6	70.0 - 215.2	17.5 - 52.5	525 - 1576	700 - 2101	175 - 525	0.72 - 0.88	0.81 - 0.99	0.72 - 0.88	0.63 - 0.77	0.63 - 0.77	0.63 - 0.77	0.07 - 0.28	0.034 - 0.34	0.034 - 0.34	0.003 - 0.070	0.0013 - 0.070	0.0034 - 0.070	0.06 - 6.0	0.035 - 3.5	0.06 - 6.0	0.0011 - 0.11	0.0011 - 0.11	0.0011 - 0.11	1.14 - 24.0	1.14 - 24.0	1.14 - 24.0

Figures of Chapter 3

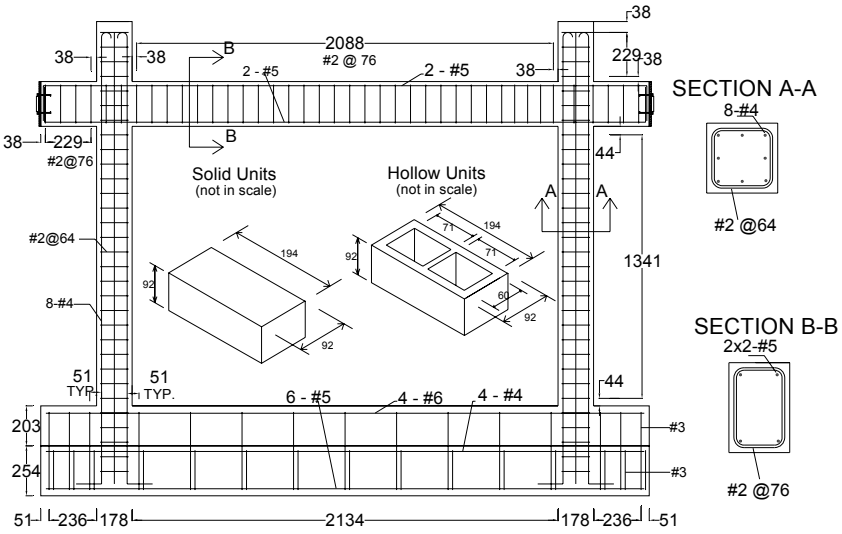

Figure 3.1: Design of concrete frame.

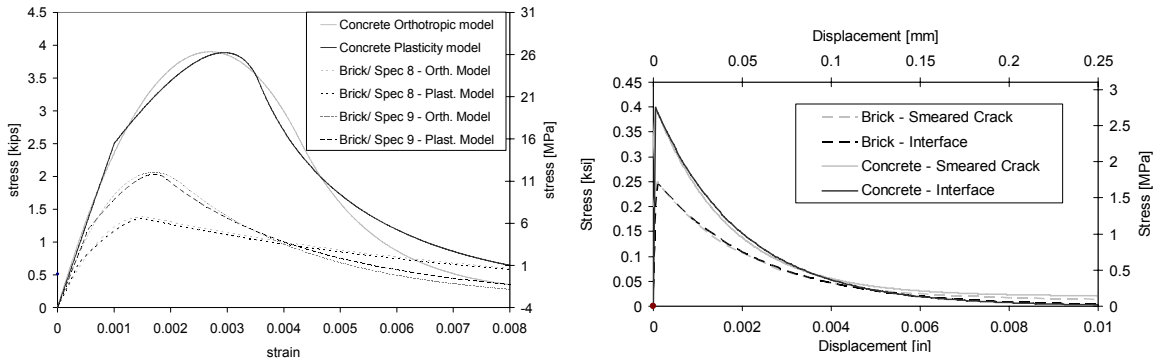

(a) Concrete and brick compressive behavior (b) Concrete and brick tensile behavior

Figure 3.2: Calibrated material models for concrete and brick elements.

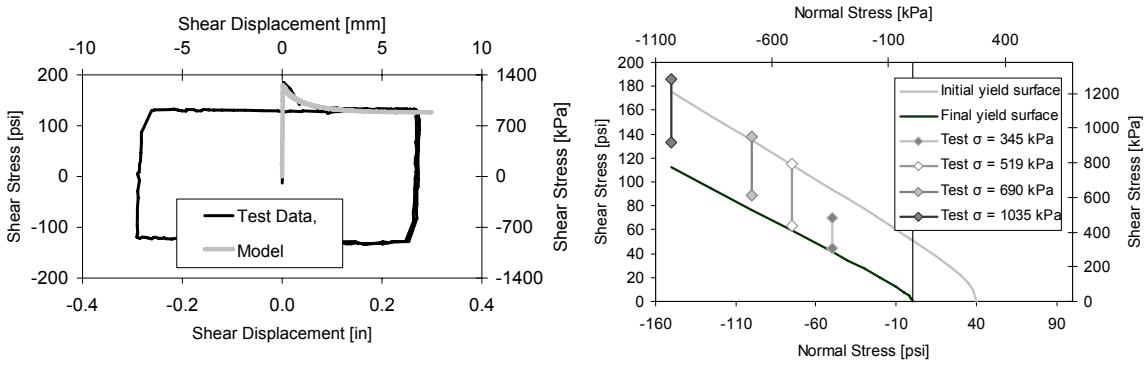

(a) shear test and numerical results for σ = 1034 kPa (150 ksi)

(b) initial and final yield surfaces

Figure 3.3: Calibration of interface model for mortar joints.

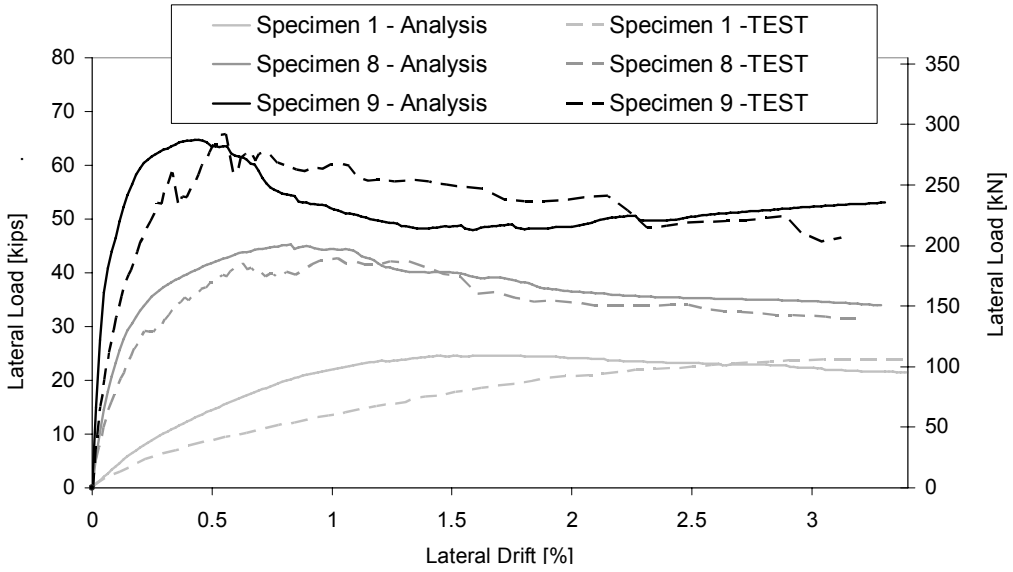

Figure 3.4: Lateral force-vs.-lateral displacement curves

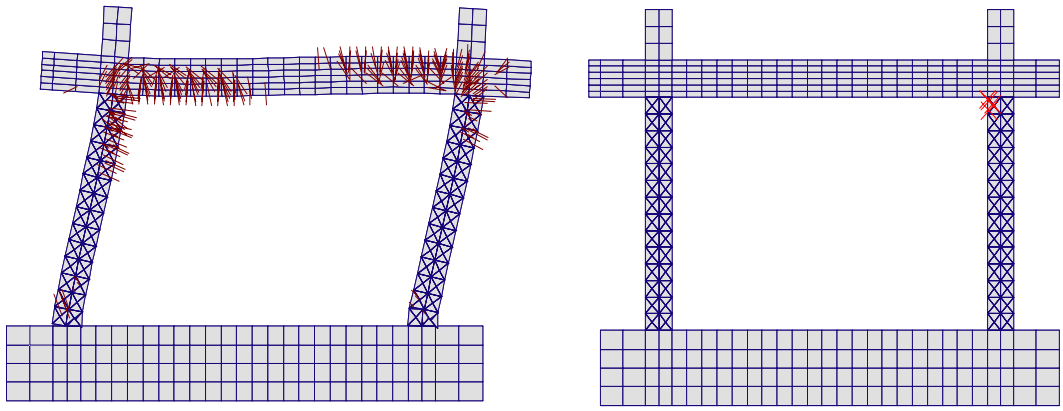

(a) Cracking pattern (b) Crushing pattern

Figure 3.5: Analytical failure pattern for Specimen 1.

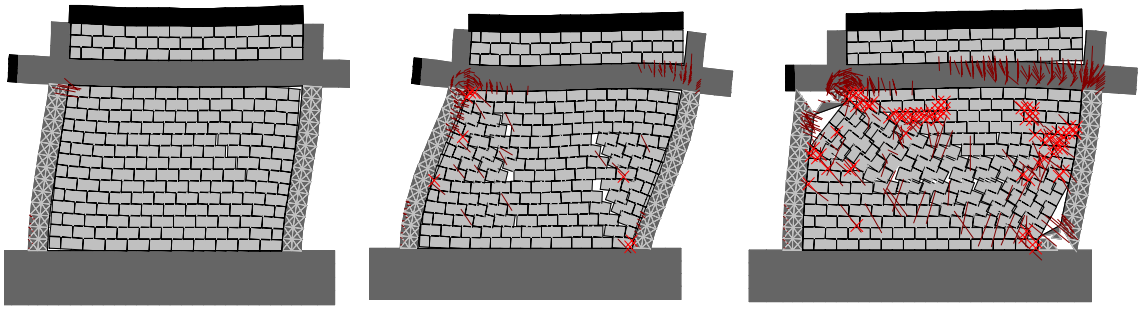

(a) drift of 0.17% (b) drift of (a) 0.82% (c) drift of 3.0%

Figure 3.6: Deformed meshes for model of Specimen 8.

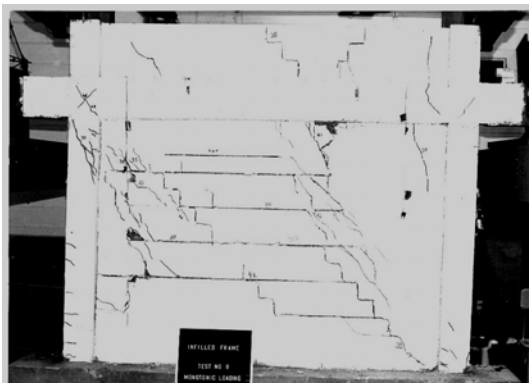

Figure 3.7: Experimental failure pattern of Specimen 8 at lateral drifts of 3.0%.

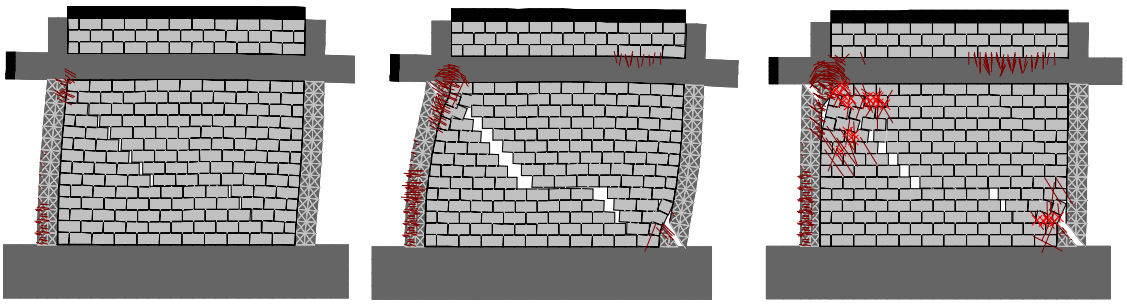

(a) drift of 0.17% (b) drift of (a) 0.46% (c) drift of 2.8%

Figure 3.8: Deformed meshes for model of Specimen 9.

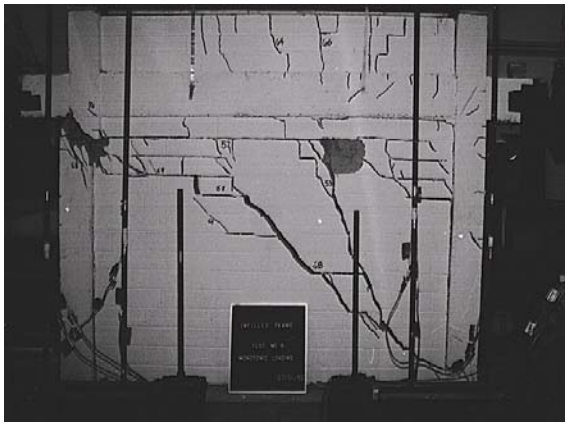

Figure 3.9: Experimental failure pattern of Specimen 9 at lateral drifts of 2.8%.

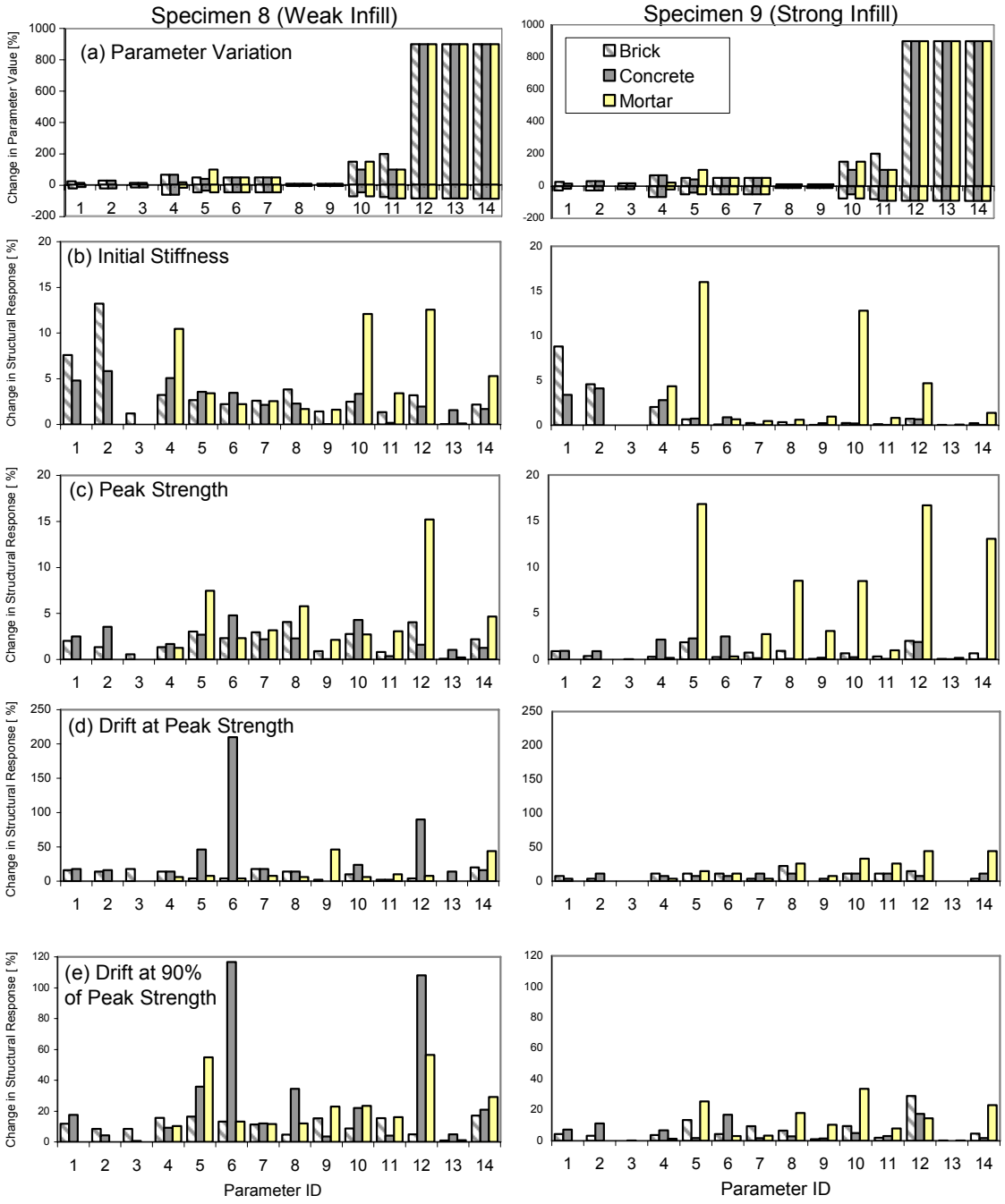

Figure 3.10: Change in material parameters and corresponding change in structural response. (see Tables 3 and 4 for Parameter ID).

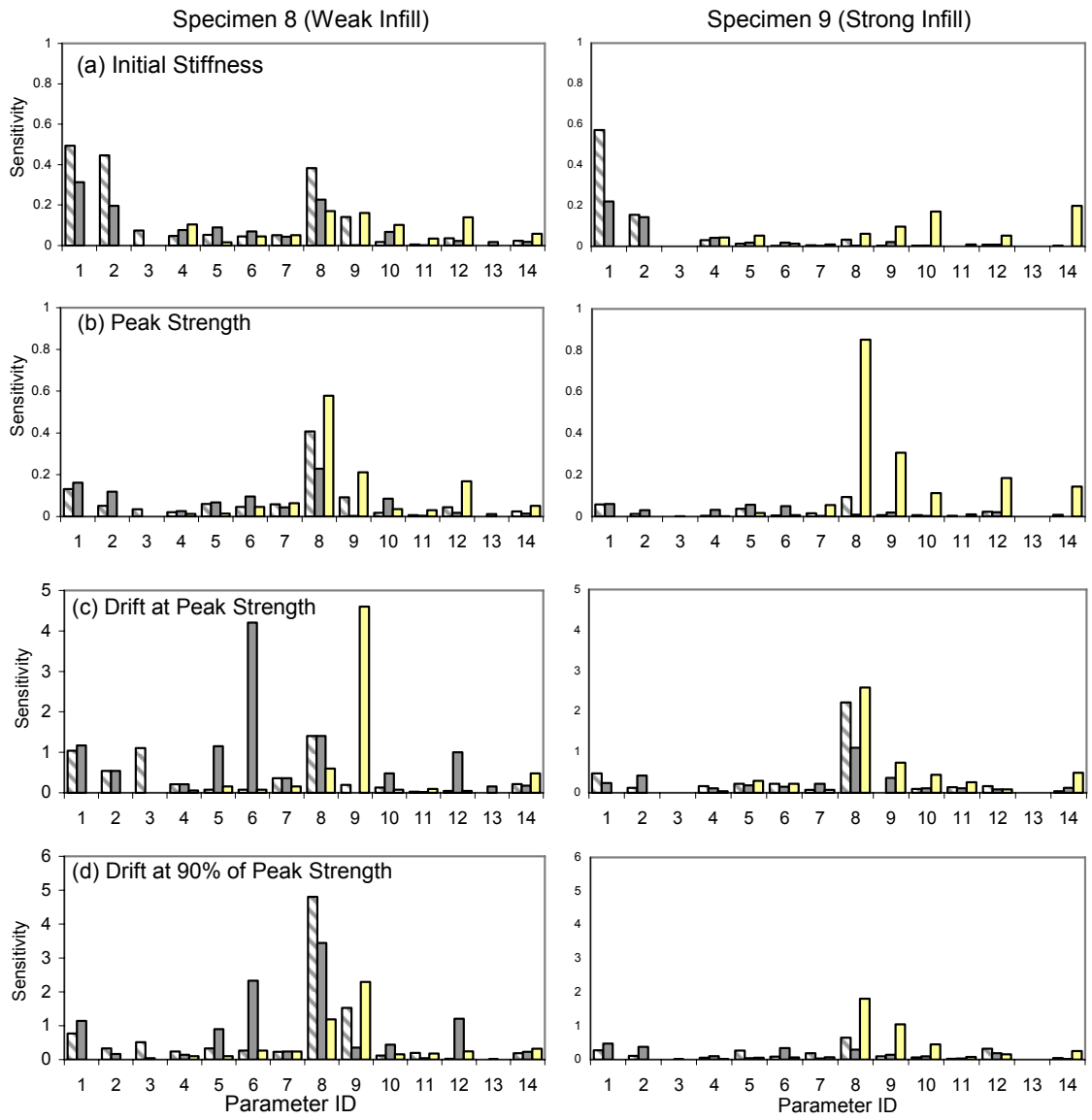

Figure 3.11: Sensitivity of structural response to material parameters. (see Tables 3 and 4 for Parameter ID)

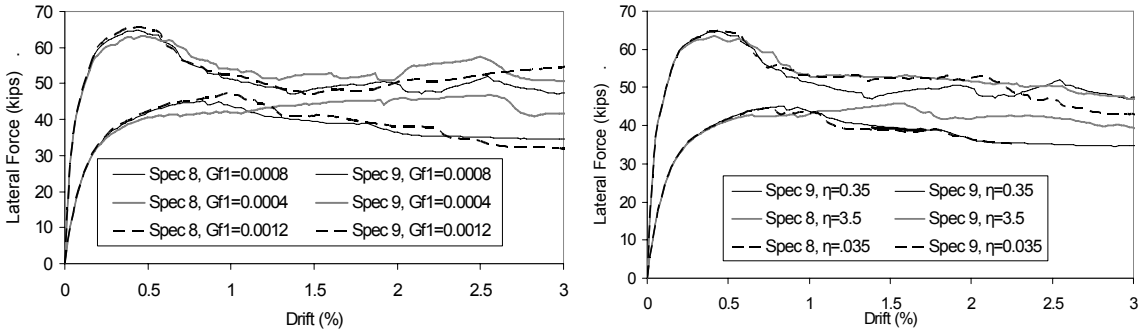

(a) Fracture energy of concrete

(b) Factor scaling the dilatancy of concrete joints

Figure 3.12: Lateral Load vs. lateral drift of the models resulting from the perturbation of different morel parameters.

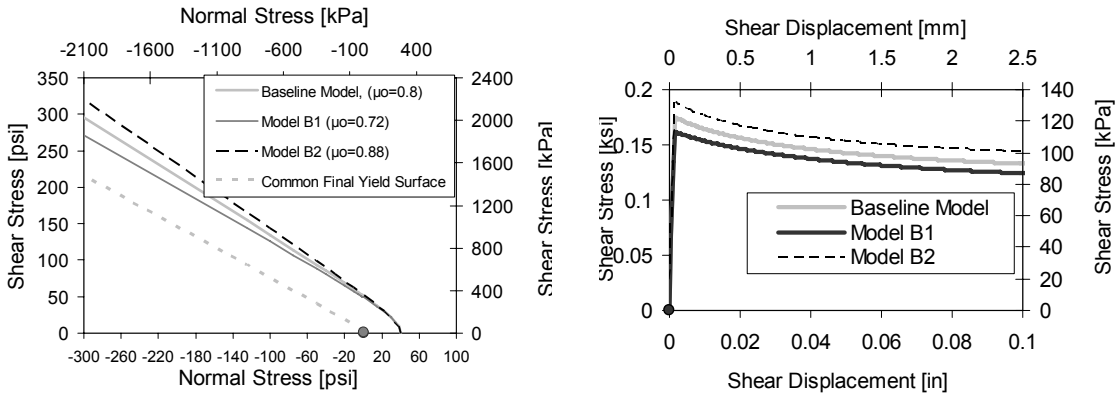

(a) Initial and final yield surfaces of interface element

(b) Shear stress vs Shear displacement for masonry joints under normal stress of 1034 kPa (150 psi),

Figure 3.13: Variation of mortar interface elements shear strength.

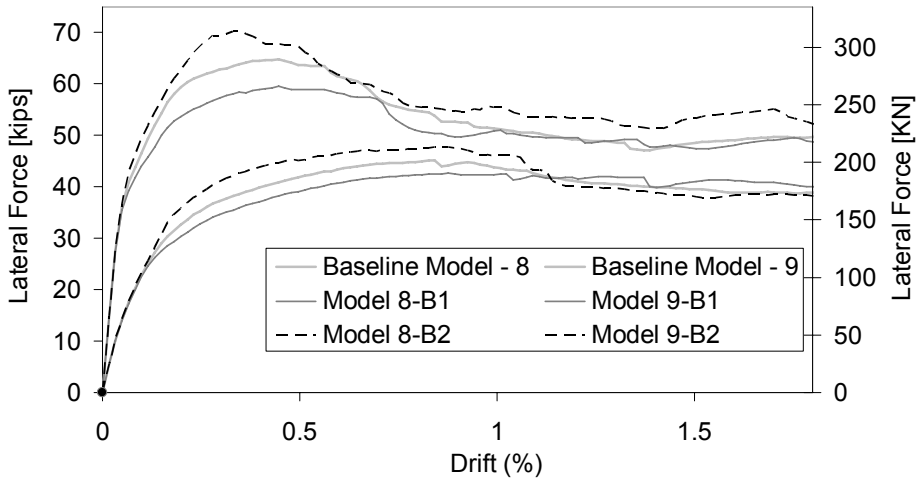

Figure 3.14: Sensitivity of the FE models to shear strength of mortar interface elements:

CHAPTER 4

PROTOTYPE BUILDING

4.1 Introduction

This chapter presents the design considerations and the final design of a non-ductile RC frame structure infilled with unreinforced masonry walls on its exterior frames. This structure represents existing older buildings and has been designed according to the engineering practice in California in the 1920s era. Structures with unreinforced masonry were disallowed in California after the 1933 Long Beach earthquake. However, there is a large inventory of such structures which were built prior to that event and need to be preserved due to their historical significance and economic importance. Infilled frames can be also found in many newer buildings in the midwestern and eastern parts of the United States. Moreover, RC frames with infilled masonry panels are a common construction practice in many regions of the world with high seismicity such as the Mediterranean and Latin American countries. Many of the existing buildings in those regions may have similar design details as the structure considered in this chapter.

From this point on, the structure designed in this chapter is referred to as the prototype structure and it is the focal point of the analytical and experimental study

presented in the following chapters. Subassemblages of this structure have been tested and analyzed under in-plane lateral loads simulating seismic forces.

4.2 Design Consideration

The scope of this design effort was to design a structure according to the engineering practice of the 1920s era. However, the earliest building code for reinforced concrete structures available by ACI was published in 1936 (ACI 1936). Therefore, valuable information on the design loads and philosophy was obtained from and Caughey (1936) and through interaction with practicing engineers (Maffei et al. 2006) who have significant experience on analyzing and retrofitting existing structures of that era. The loads typically used in the structural design of that era are summarized in Table 4.1. The full live load was considered for the design of the joists. However, it was reduced to 40% for the design of the columns, to 80% for the design of the exterior beams, and to 60% for the design of the interior beams.

The design provisions used in the 1920s era were similar to those of ACI 501-36T (ACI 1936) and Caughey (1936). According to these provisions, a working (allowable)-stress design approach was followed. The working stress for concrete was specified as a fraction of the expected compressive strength, based on the member and type of loading considered. In flexure, 40% or 45% of the estimated compressive strength was used, with the higher value used for cross-sections adjacent to the supports. For the shear design of beams, the allowable concrete stress ranged between 2 and 6% of the compressive

strength. The actual value was selected based on the anchoring conditions for the longitudinal steel and the use of shear reinforcement or not.

Three different grades of steel were used in the construction practice in the 1920s. Structural and intermediate grade steel was used for joists, beams and stirrups, and rail steel bars for the columns. The specified yield stresses were 228, 276 and 345 MPa (33, 40 and 50 ksi), respectively. The allowable tensile stress for steel was 45% of the specified yield stress. Furthermore, based on the grade, the lap-splice length was determined to be 30 bar diameters for rail steel bars and 24 diameters for intermediate steel. Moreover, square bars with minimal deformations were commonly used in the RC members in the 1920s, while deformed bars with a circular cross section are used in modern structures. This is a condition that cannot be replicated with modern building materials. Therefore, only circular deformed bars have been used for the design of the prototype.

For the beams, the quantity of the longitudinal steel was calculated at the mid-span and the supports based on simplified equations, as determined by prescribed continuity for the positive and negative moment, respectively. The engineers would decide on the appropriate equation for the moment demand based on the length and the number of spans. To achieve an economical design and provide anchorage for the longitudinal beam reinforcement, it was common practice to bend some of the longitudinal bars in the beams, as shown in Figure 4.1. The amount of shear reinforcement in the beams was based on the anchorage of beam reinforcement and the shear stress. There was no minimum requirement when the concrete shear stress was

equal to or less than that permitted for this condition. Consequently, in many cases, the beams were designed and constructed without stirrups.

For the columns, there were different design provisions for spirally confined and tied columns. The maximum quantity of the longitudinal reinforcement for the former was between 1% and 8% of the cross sectional area, while for the latter the bounds were 1% and 4%. The design only considered the axial load demand due to gravity loads which was compared to the axial force capacity. The latter was determined according to the following equations.

columns with spirals: $$P = A_g\left(0.22 f_c^{'} + f_s \rho_g\right) \tag{4.1a}$$

columns with ties: $$P = A_g\left(0.154 f_c^{'} + 0.70 f_s \rho_g\right) \tag{4.1b}$$

in which A_g is the gross area of the column, $f_c^{'}$ is the compressive strength of concrete, f_s is the nominal working stress of the longitudinal column reinforcement and ρ_g is the ratio of longitudinal reinforcement. A minimum of four bars with a diameter not less that 16.1 mm (0.625 in.) was specified for a rectangular column, with 38.1 mm (1.5 in.) concrete cover. The longitudinal bars were lap spliced at the base of the columns for a length equal to 30 bar diameters. For the lap splice, the bars from the column below the beam were offset into the core of the column above at a 1:6 inclination.

The lateral reinforcement in the columns normally consisted of ties with 90^o bends plus extension for tied columns or spirals made of hot-rolled steel for spirally

reinforced columns. Cross-ties with hooks were used to restrain interior column bars of tied columns. For the lateral reinforcement, the minimum quantity was 9.5 mm (0.375 in.) diameter bars spaced at a distance equal to the least dimension of the column. The minimum requirement for the lateral reinforcement was later revised in ACI 501-36T (1936), with the minimum bar diameter decreased to 6.4 mm (0.25 in.) and maximum spacing be the smallest of 16 longitudinal bar diameters, 48 tie diameters, and the least dimension of the column.

The concrete frames on the perimeter of such structures were typically infilled with three-wythe masonry walls. These walls were built with solid clay bricks and cement-lime mortar with properties similar to those of Type O (ACI 530.1-99, ASCE 6-99, TMS 602-99) or Type N (MSJC, 2008). The masonry walls were not considered as structural elements.

4.3 Prototype Structure

The prototype structure considered in this study is a three-story, non-ductile RC frame infilled with three-wythe masonry walls on the perimeter. The plan view of the building and the elevation view of an external frame are presented in Figure 4.2. The dimensions of the structure and the cross sections of the members were selected based on information provided by PAP (2006) on typical structures built in the 1920s and the capabilities of the laboratory facilities that would be used for the experimental investigation. The structural skeleton incorporates thin slabs supported by joists running

along the long direction of the structure. The joists are supported by beams and columns along lines A, B, C, and D shown in Figure 4.2 (a).

The design of the RC frame follows the design specifications described in the previous section but it is based on contemporary materials that would be available for the construction of the laboratory specimens. The moment demand for the joists and beams was based on the equations from Table 4.2, while the axial capacity of the columns was determined with equation 4.1b. The allowable stress used in the calculations has been calculated with the factors of safety used in the 1920s era. For Grade 60 steel which would be used in the experimental investigation, the allowable stress used in the design is 186 MPa (27 ksi). For concrete, a compressive strength of 20.7 MPa (3,000 psi) is considered representative of the current strength for existing structures. Consequently, this compressive strength is assumed in the design and has been the target value for all the concrete mixes used for the construction of the experimental models. A summary of the RC member design of the external frame along lines A and D is presented in Tables 4.3 and 4.4. The small quantity of shear reinforcement in the columns and the lack of any ties in the beams would violate the modern building codes (e.g. ACI 318 and Eurocodes 2 and 8).

4.4 Conclusions

This chapter summarizes the probable design requirements that were used in the 1920s era for RC frame structures that exist today in California. Typical design only

considered gravity loads and resulted in RC structures poorly detailed for seismic loading. Using the 1920 era design requirements and contemporary materials, a three-story structure was designed to serve as a prototype structure for this study. Scaled subassemblages of the prototype have been modeled with the finite element scheme presented in Chapter 2 and were tested in laboratory experiments. The test and analysis results are presented in the following chapters.

Tables of Chapter 4

Table 4.1: Design loads for exterior frames.

		2nd and 3rd Foor	Roof
Topping	[kPa] (psf)	86.2 (12.5)	34.5 (5)
Ceiling	[kPa] (psf)	82.7 (12)	82.7 (12)
Mechanical equipment	[kPa] (psf)	N/A	34.5 (5)
Live load	[kPa] (psf)	517 (75)	137.8 (20)
Infill	[kN/m^3] (pcf)	20.4 (130)	N/A
Parapet	[kN/m] (lbs/ft)	N/A	5.7 (390)

Table 4.2: Expressions for the moment and shear demand used in the design of beams.

	Length	Number of spans	Negative moment at the supports	Positive moment at mid-span	Shear
End span**	>3 m (10 ft)	2	$\frac{1}{8}wl^2$ *	$\frac{1}{10}wl^2$	$1.20\frac{1}{2}wl$
		>2	$\frac{1}{10}wl^2$		
	<3 m (10 ft)	2	$\frac{1}{10}wl^2$		
		>2	$\frac{1}{12}wl^2$		
Interior span	any	any	$\frac{1}{12}wl^2$	$\frac{1}{12}wl^2$	$\frac{1}{2}wl$

* w is the distributed design load per unit length of the beam and l is the length of the clear span for positive moments and the average of the two adjacent spans for negative moment.

** the formulas are applicable for the interior support of the end span.

Table 4.3: Design of exterior frame beams (the nominal geometry of the steel bars is shown in Table A.1).

	Width [cm] (in.)	Depth [cm] (in.)	Bent Bars	Straight Bars	Ties
1st Story	40.6 (16)	(22)	3#8	3#7	-
2nd Story	40.6 (16)	(22)	3#8	3#7	-
3rd Story	40.6 (16)	(18)	2#8	2#6	-

Table 4.4: Design of exterior frame columns (the nominal geometry of the steel bars is shown in Table A.1).

		Dimensions [cm x cm] (in. x in.)	Longitudinal Bars	Ties
Corner Column	1st Story	40.6 x 40.6 (16 x 16)	5#8	#3 at 16
	2nd Story	40.6 x 40.6 (16 x 16)	5#8	#3 at 16
	3rd Story	40.6 x 40.6 (16 x 16)	5#8	#3 at 16
Middle Column	1st Story	40.6 x 40.6 (16 x 16)	5#8	#3 at 16
	2nd Story	40.6 x 40.6 (16 x 16)	5#8	#3 at 16
	3rd Story	40.6 x 40.6 (16 x 16)	5#8	#3 at 16

Figures of Chapter 4

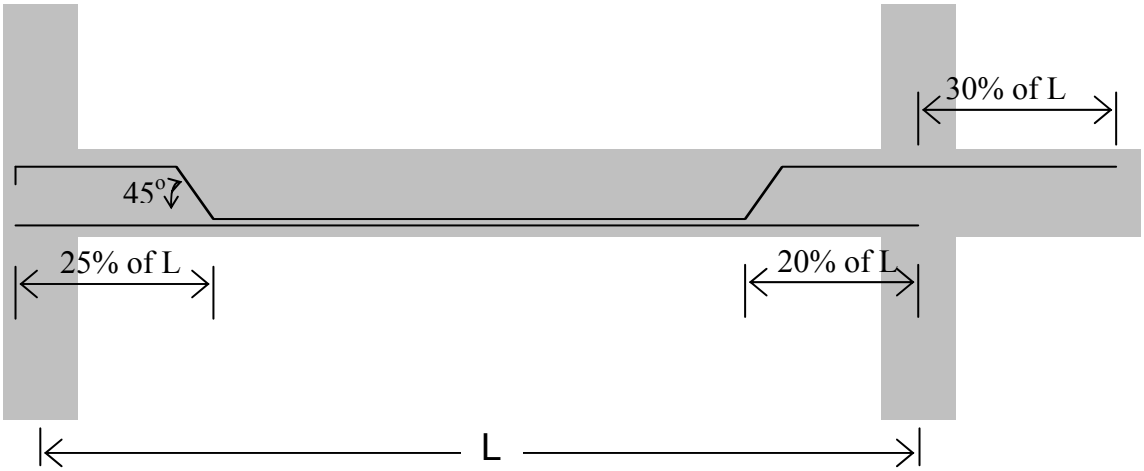

Figure 4.1: Typical detailing of beam flexural reinforcement.

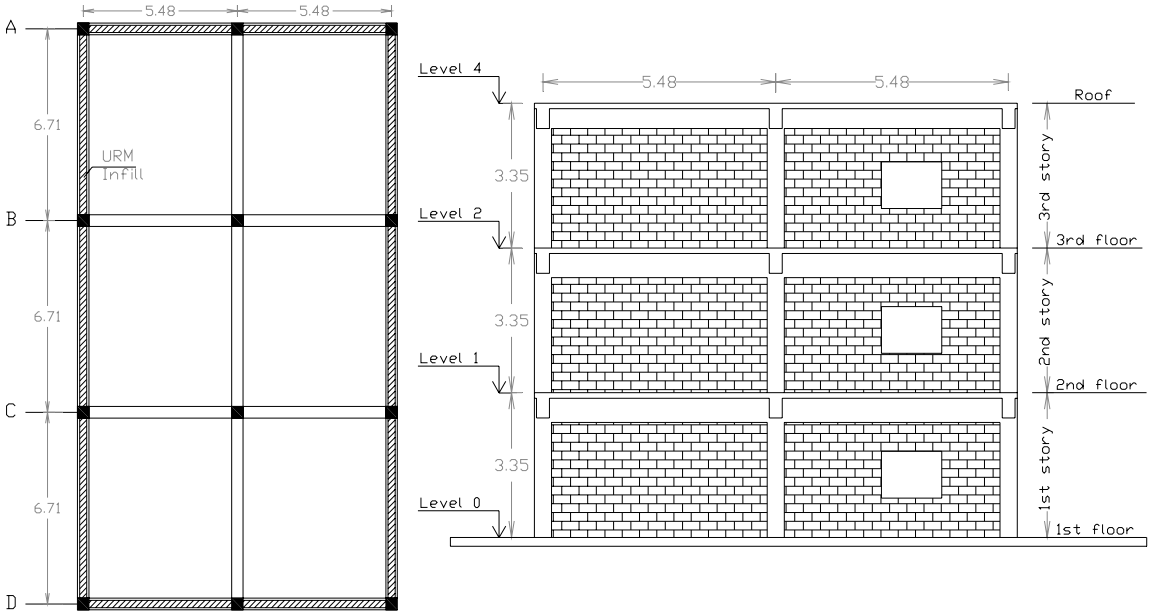

(a) plan view (b) elevation of an exterior frame along lines A and D

Figure 4.2: Prototype structure (dimensions in m).

CHAPTER 5

QUASI-STATIC TESTS AND ANALYSES OF INFILLED FRAMES WITH AND WITHOUT OPENINGS

5.1 Introduction

This chapter presents the results from an experimental program involving quasi-static tests of singe-bay, single-story, masonry-infilled, non-ductile RC frames. The specimens considered here represent scaled subassemblages of the prototype structure discussed in Chapter 4. They include a small-scale RC frame with a solid infill panel tested at the Blume Center in Stanford University (SU) and four large-scale specimens tested at the NEES facility at University of Colorado at Boulder (CU). The large-scale frames included a frame with solid infill and three infilled frames that had infill walls with different opening configurations. The comparison of the test results provides useful information on the scaling effect and also on the effect that doors and windows have on the lateral strength and load resisting mechanism of infills. To better understand the failure mechanisms, all the specimens have been modeled with the nonlinear finite element modeling scheme developed in Chapter 2 which combines the discrete and the smeared-crack approaches. The comparison of the analytical and experimental results demonstrates the capabilities of the modeling scheme, but also provides insight into the behavior of these structures. The analysis of the results indicates that the well-established

notion of the infill panels acting as struts along the two diagonals of the panels is not very precise and cannot explain the failure patterns exhibited by the frames.

5.2 Experimental Considerations

The specimens discussed in this chapter were extracted from the prototype structure presented in Chapter 4. The reinforcing details and vertical load of the specimens corresponded to the bottom story of the external frames along lines A and D, shown in Figure 4.2. The external frame was selected because the internal frames are not infilled; therefore, they do not contribute significantly to the lateral load resistance. From this frame, the bottom story would be subjected to the most severe seismic load.

Extracting single-bay specimens from the two-bay prototype structure is not straight-forward due to issues related to the vertical load distribution and the boundary conditions. In the prototype building, the two adjacent columns bounding a wall panel would include a corner and a middle column. Therefore, they would have different vertical loads due to the different tributary areas and different boundary conditions due to the restraints provided to a middle column by the infill walls on both of its sides. However, these conditions cannot be simulated in a single-bay test. Therefore, it was decided to treat both columns as if they were the external columns of the prototype structure and thus, the vertical load was calculated accordingly. Besides, reducing the vertical load was a conservative assumption as a higher axial compressive force would have increased the lateral load capacity of the structure. The scaling for the specimens

followed the similitude requirements (Harris and Sabnis 1999) after the length scaling factor was determined based on the testing capabilities of each laboratory facility. More details on the design of each specimen are provided in the sections that follow.

The brick units used in all specimens were not scaled for practical reasons; therefore the masonry walls consisted of solid clay bricks with dimensions of 95 x 57 x 197 mm (3.75 x 2.25 x 7.75 in.). The head and bed joints were not scaled as well and had an average thickness of 1 cm (0.375 inches). A cement:lime:sand ratio of 1:1:5 by volume was used according to the specifications for type N mortar because it is commonly found in buildings of the 1920s era. For the walls with openings, two L3x3x1/4 steel angles were used to build the lintel beams which had a bearing length of approximately 5 cm (2 in.) on both sides of the opening.

5.3 Numerical Models

Numerical models of the specimens have been created in FEAP. The models account for the differences in the infill geometry and the material properties. The concrete columns are modeled with the scheme shown in Figure 2.3. The foundations and beams are modeled with 4-node smeared-crack elements only for computational efficiency. These members were expected to remain elastic and no discrete dominant cracks were expected. The infill is modeled with the scheme shown in Figure 2.5. The lintel beams used in the specimens with openings are modeled with elastic quadrilateral elements. The beam elements are connected to the bottom of the first row of brick

elements over the opening and are appropriately calibrated to simulate the bending stiffness of the lintel beam. This connectivity scheme allows the simulation of the flexural resistance provided by the lintel beam without affecting the load transfer mechanism in the infill. The material parameters for the finite element models have been calibrated according to the procedure developed in Chapter 2 based on the material tests conduced at SU and CU and data from the literature.

5.4 Small-Scale Specimens

5.4.1 Specimen design

The laboratory facility at Stanford University could accommodate 1/5-scale specimens. This length scale factor would require a masonry panel with a width equal to 60% of a single-wythe. However, the need to consistently use the same brick units in all laboratory specimens combined with the difficulty to cut the bricks resulted in a single-wythe wall with a thickness that would correspond to 33% of that of the prototype. Furthermore, a minimum of a single-wythe was needed to have a reasonable scaling of the Engineered Cementitious Composite (ECC) overlay used in the retrofit the retrofit scheme that has been under investigation as part of the collaboratory research project. To accommodate the single-wythe wall and the ECC overlay, the width of the RC frame was increased by considering two parallel 1/5-scale frames built monolithically next to each other as a single frame.

Precisely scaling the prototype structure would require an unrealistically small amount of concrete cover for the reinforcement. The specimen design, illustrated in Figure 5.1, indicates that the dimensions of the columns were further expanded to provide sufficient cover for the reinforcement. This was taken into account in the design of the longitudinal reinforcement of the columns by selecting the required flexural reinforcement to have the same moment capacity as a precisely scaled doubled-up 1/5-scale frame. All these necessary adjustments resulted in a column cross sectional area 36.5% larger than what the precisely scaled area would be. Consequently, the applied vertical load was increased accordingly to obtain vertical stresses equal to those in the prototype structure. The increase of the column area also creates a mismatch between the scaling of the masonry wall and the RC frame, and this needs to be taken into account in the analyses of the specimen's performance.

The finite element analysis conducted with the scheme of Chapter 2 prior to the test indicated that exact scaling of the beam reinforcement would result in extensive cracking of the RC beam. This is not a realistic failure pattern since in a multi-story structure the in-plane rigidity of the infill wall in the upper story would not allow the development of such failure mode. Consequently, the beam reinforcement was significantly increased, as shown in Figure 5.1, to prevent this unrealistic failure mechanism.

A total of four small-scale RC frames with solid infill walls were tested in SU. The RC frame was the same in all cases; however, Specimens 2, 3 and 4 incorporated retrofit schemes ECC overlays (Billington et al. 2009, Kyriakides and Billington 2008)

which are examined in another doctoral dissertation (Kyriakides 2010). Therefore, only the test results from the first specimen are presented here. The basic material properties for this specimen are presented in Table 5.1.

5.4.2 Loading protocol and test set-up

The frames were loaded laterally in a cyclic fashion by an actuator. For the initial cycles, the actuator moved in load-control to avoid controlling a small displacement. The amplitude of these cycles was determined based on the finite element analysis so that the structure would remain in the elastic range. Displacement-control was used in the following cycles to apply the displacements corresponding to the predefined drift amplitudes shown in Figure 5.2. The drift levels were selected based on pre-test simulations, to have small increments initially to capture the initial stiffness, 'yield' point, and peak load. Beyond the peak load, the target drift amplitudes had larger increments so that larger drifts can be reached without over-testing the specimens. Two loading cycles were applied at each drift level so that the strength and stiffness degradation during the second cycle could be obtained as well as the backbone curve (FEMA 356). The total gravity load simulating the gravity loads from the rest of the structure was 77 kN (17.3 kips) according to the similitude requirement. The load was distributed along the top of the specimen by a steel beam made of two C6x8.2 channel sections. This load was controlled manually during the tests with an effort to maintain it within $\pm 10\%$ of the desired load.

5.4.3 Experimental results

The load-vs.-drift response of the small-scale specimen is presented in Figure 5.2. The load-vs.-drift relation indicates that the specimen behaved asymmetrically in the two loading directions. In the positive direction the specimen reached a peak load of 97.4 kN (21.9 kips) at a drift of 0.375%. At this drift level, a horizontal sliding crack along the top bed joint occurred. This crack was followed by a similar crack along the bed joint below and eventually let to a knee-brace mechanism and steep strength degradation. In the negative direction, the peak load was 87.6 kN (19.7 kips). The structure did not reach the same strength in this direction as it was pre-cracked upon the cycle initiation due to the positive loading cycle. In this direction of loading, the failure pattern involved sliding along the same horizontal crack, corner crushing occurring at the top left column of the infill, which limited the diagonal compressive force transferred by the infill, and a diagonal crack developed in the infill close to the leeward (right) column. This crack distributed the deformations and the damage along the height of the structure. The different mechanism formed in the negative direction allowed a more ductile behavior as the specimen was able to maintain more than 80% of the peak load until a drift of 2.00%. Beyond this point, a knee-brace mechanism similar to that in the positive direction developed and the load dropped to a residual strength of 53.4 kN (12 kips).

The failure pattern of the specimen is illustrated in Figure 5.4. The cracks are marked on the specimen with two different colors to identify the loading direction in

which each crack initiated. In Figure 5.4(a) the crack pattern at a drift of 1.00% is presented. The cracks are not symmetric due to the different failure patterns discussed previously. At a drift level of 3.00% the mechanisms developed in the two loading directions became similar and included corner crushing, diagonal and horizontal shear sliding cracks in the infill which eventually caused the shear cracks at the bottom of the leeward column for each loading direction, as shown in Figures 5.4(b) and (c). Thus, each column had flexural cracks along its height and a shear crack close to the bottom. However, the column shear cracks developed at large drifts and did not affect the maximum load capacity of the frame.

5.4.4 Finite element analysis results

Due to the symmetry in the specimen geometry, one monotonic analysis was conducted and the results are compared with the test results in both loading directions. As shown in Figure 5.5, the finite element model captures very well the behavior of the physical specimen. The model accurately predicts the initial stiffness and peak load. In terms of the strength degradation, the model matches the experimental behavior in the negative loading direction. The analysis is less brittle than the positive direction and predicts well the failure pattern which is presented in Figure 5.5 at 0.50% drift and at the end of the test. At 0.50% drift, which is right after the peak load, the crack pattern mainly involves flexural cracks in the columns and horizontal sliding in the infill. At the end of the test the horizontal cracks are complemented by corner crushing, diagonal cracks in

the infill, and a shear crack at the bottom of the leeward column at an angle smaller than 45^{o}. This behavior closely represents the experimentally observed behavior of the physical specimen.

5.5 Large-Scale Specimens

5.5.1 Specimen design

Six two-third scale, single-story, single-bay, infilled RC frames were quasistatically tested at the University of Colorado, Boulder between fall 2007 and summer 2009. The scaling of these specimens was more straight-forward than that of the small-scale specimens. The three-wythe masonry panel of the prototype was reduced to a two-wythe wall and the applied gravity load was calculated based on the load carried by the corner columns at the bottom story of the prototype. The column reinforcement was scaled considering not only the total area of the longitudinal bars, but also the need to maintain eight bars in each column as in the prototype structure. As shown in Figure 5.6, this consideration resulted in a scheme with four #4 and four #5 bars. The exact positioning of the bars was determined so that the moment capacity of the column would be close to the scaled moment capacity of the prototype according to the similitude law. In the calculation of the moment capacity the axial load was considered within a range of values which were expected to develop based pre-test finite element analyses. The only deviation from the similitude requirement in the design of these specimens was the reinforcement of the beam. As for the small-scale specimens, finite element analyses of

the frames were conducted prior to the tests with the modeling scheme presented in Chapter 2. The analyses indicated unrealistic cracking of the beam due to the absence of the confining effect of the masonry in the upper story. Therefore, the beam reinforcement was increased to prevent this failure pattern.

The six specimens incorporated different opening and retrofit configurations as summarized in Figure 5.7 and Table 5.2. The infill walls of Specimens 3 and 4 were retrofitted with Engineered Cementitious Composite (ECC) materials and their behavior is examined in another doctoral dissertation (Kyriakides 2010). This study considers the tests of the four unretrofitted specimens. These include a frame with a solid panel tested in Specimen 1, and infills with windows of different sizes tested in Specimens 2 and 6, and a door in Specimen 5. All openings were eccentrically located to represent realistic configurations and present a greater challenge for the finite element models. The location of the openings was determined so the centerline of the opening would be in all cases at the same location with respect to the columns. The basic material properties for the four specimens are presented in Table 5.1.

5.5.2 Test Set-up and loading protocol

The test set up and loading conditions for the large-scale specimens were similar to the conditions for the small-scale specimen, as shown in the test set-up presented in Figure 5.7. After two initial loading cycles in force control, the frames were loaded laterally in a cyclic fashion by an actuator moving in displacement control. As for the

small-scale specimens, two cycles were applied at each drift level as shown in Figure 5.2. However, the tests for the large scale specimens stopped at drift levels between 1.25% and 2.00% when the inspection of the specimens and the significant drop in their resistance indicated that they had practically failed. The total gravity load applied was 311 kN (70 kips) and it was distributed along the top of the concrete beam by a W8x31 steel beam. This load was manually controlled during the tests and an effort was made to maintain it within $\pm 10\%$ of the original load.

5.6 CU1: 2/3-Scale Specimen with Solid Panel

The unretrofitted frame with a solid infill was a control specimen so that the influence of the openings and/or the retrofit scheme in the subsequent specimens could be assessed. An extensive experimental program was carried out to obtain the properties of the materials used in Specimen 1 (Citto 2006).

5.6.1 Experimental results

The experimental load-drift relation is illustrated in Figure 5.8 and it is compared with the curve obtained from the finite element model. Although, the structure exhibited nonlinear behavior at a drift of 0.06% when the infill started to separate from the frame along the frame-infill interface, the lateral load continued to increase until a drift of

0.25% at which the peak resistance was reached and a dominant diagonal shear sliding crack developed in the infill. The peak strength reached was 685 kN (154 kips) for the positive direction of loading and 645 kN (145 kips) in the negative direction. After reaching the peak load, the specimen maintained a load capacity higher than 534 kN (120 kips) until diagonal shear cracks developed in the concrete columns as extensions of the dominant cracks in the infill. In the positive direction, a shear crack developed at the top of the windward at a drift of 0.55% and it was followed by a diagonal crack at the bottom of the leeward column at a drift of 0.75%. The same failure sequence was noted in the negative loading direction with the cracks opening at similar drift levels. After the columns failed in shear, the frame reached its residual capacity, which was 356 kN (80 kips) and it maintained that load up to 1.25% drift in both directions. Similarly to the small scale specimen, a higher load was reached in the positive loading direction which was followed by a more brittle failure compared to the behavior in the negative direction as indicated by the slope of the descending branch. The test was terminated at a drift of 1.25% since the load capacity of the structure had dropped at almost 50% of the peak strength. The final cracking pattern of Specimen 1 is presented in Figure 5.9(a) and it is symmetric for the two directions of loading.

5.6.2 Finite element analysis results

The nonlinear finite element model developed in FEAP was used to model the behavior of Specimen 1. The material properties used in the model are summarized in

Tables 5.3 and 5.4. Since the structure is symmetric and the analysis is monotonic, a single analysis can represent the structural performance in both loading directions. As Figure 5.8 indicates, the model accurately captures the experimental results in terms of the initial stiffness, failure mechanism and residual strength. Figure 5.9(b) presents the failure mechanism of the analytical structure which accurately captures the development of the cracking pattern that leads to the failure of the specimen. The analytical prediction for the strength is 582 kN (131 kips), which is 15% lower than the actual strength. The drift at which the peak strength develops is also lower than in the experiment. A shear-sliding crack develops in the infill at a drift of 0.19% and the shear cracks on the columns develop at 0.32% and 0.38% drift for the windward and the leeward column respectively. This discrepancy compared to the physical specimen can be attributed to the brittleness of the mortar joints in the analytical model. Furthermore, in the test, as the specimen deformed close to the peak value of the displacement trajectory for each cycle, the vertical load was increased at an average of 8%. This fluctuation of the vertical load would increase the lateral resistance of the specimen.

The force distribution along three cross sections of the structure at the instant of peak strength and at a drift of 1% is presented in Figure 5.10. The bottom cross section is right above the shear crack at the bottom of the leeward column, while the top cross section is right below shear crack at the top of the windward column. The third cross section is at the mid-height of the infill. For each cross section, the shear and normal forces on the columns and the infill are also shown in Figure 5.10. For the notations, N_{lc} and V_{lc} stand for the axial and shear forces in the left column, N_w and V_w stand for the

axial and shear forces in the infill wall, and N_{rc} and V_{rc} stand for the axial and shear forces in the right column. The total shear force along each cross section is noted in the figures as V_{tot}. Furthermore, the forces applied on the infill from the RC frame through the frame-wall interface are also plotted on the perimeter of the infill.

Figure 5.10(a) presents the force distribution at the instant of the peak load. As for the physical specimen, the load drops in a brittle manner due to the development of a shear crack at the top of the windward column. At this stage shear-sliding crack in the infill has fully developed and the leeward column has no shear cracks. The force distribution indicates the formation of two parallel, diagonal struts at an angle close to 45 degrees. This angle is close to the friction angle for the mortar joints. The first strut in the infill develops between the top third of the windward column and the foundation beam close to the centerline, while the second strut initiates at the top of the infill close to the centerline and ends at the bottom third of the leeward column. The force distribution changes drastically along the height of the structure, as the three cross sections indicate. At the top cross section, the windward column carries 30% of the lateral load and the infill wall carries the rest of the load. At the mid-height of the specimen, the lateral force has been transmitted to the infill and the two columns do not carry a significant portion of the vertical load, while at the bottom cross section the leeward column carries 43% of the load lateral load. After the shear cracks develop in the columns, their lateral load carrying capacity drops significantly and most of the load is carried by the infill. The forces are still transferred to the infill by two compressive struts as shown in Figure 5.10(b), although the strut orientation changes since the columns cannot carry lateral forces below

the shear crack for the windward column and above the shear crack for the leeward column. At this stage, the initiation point for the strut on the left moves above the shear crack in the windward column, towards the beam-column joint. At the same time, the strut on the right shifts below the shear crack in the leeward column towards the foundation beam.

5.7 CU2: 2/3-Scale Specimen with Regular Window

Specimen 2 incorporated a window with dimensions corresponding to a window size of 136 x 111 cm (54 x 43.5 in.) for the prototype structure. As noted in Table 1 this window is eccentrically located to represent a more general case compared to a concentric window. Moreover, the eccentric location presents a greater challenge for the finite element analysis.

5.7.1 Experimental results

The force-vs.-drift relation obtained from the test is shown in Figure 5.11. Specimen CU2 reached a peak load of 652 kN (146 kips) in the negative direction which is very similar to the strength obtained from the specimen with the solid infill. At that load level and a drift of 0.44%, a dominant diagonal shear crack developed in the windward (left) masonry pier initiating near the top of the windward column and caused a

load drop of 178 kN (40 kips). At a drift of 0.87%, this crack propagated as a diagonal shear crack at the bottom of the leeward (right) column causing a further load drop at 356 kN (80 kips).

In the positive direction, diagonal cracks developed in both piers of the wall at a drift level of 0.38% and limited the load capacity to 572 kN (128 kips). In the subsequent cycles of increased drift level, the structure maintained a load resistance greater than 83% of the peak load until a shear crack developed at the top of the windward (left) column at a drift of 0.88%. This crack was followed by a dominant diagonal crack in the windward (right) pier and a shear crack at mid-height of the leeward (right) column. The latter developed at mid-height because of a horizontal sliding crack at mid-height of the infill during the previous loading cycle in the opposite direction. The development of these cracks resulted in a significant load drop of 200 kN (45 kips).

The crack pattern at the end of the experiment is illustrated in Figure 5.12(a). The influence of the window in the cracking pattern can be observed from the triangular pieces of the masonry wall adjacent to the window that were detached from the wall due to diagonal cracks initiating at the window corners. These cracks developed at drift levels close to the drift at peak load and increased in width in the following cycles. In the earlier loading stages, however, radiating cracks initiated from the window corners but had the direction of the window diagonals. The early cracks reduced the stiffness of the structure. However, they did not cause any significant load drop and were inactive at larger drifts due to the redistribution of stresses. As a result, other cracks developed and dominated the behavior.

5.7.2 Finite element analysis results

To study the behavior of the infilled frame with the eccentric window, two monotonic analyses were conducted with the lateral load applied in opposite directions. The material properties of this specimen were not documented due to a malfunction of the data acquisition system which did not allow the recording of the material tests except for the concrete cylinders. The visual readings during the test indicated a stronger mortar and weaker prisms compared to Specimen CU1. However, this increase cannot be quantified due to the lack of data. Therefore, the prism properties used for the calibration of the model of Specimen CU1 are also used for Specimen CU2, while the concrete models are based on the values obtained from the material tests.

The force-vs.-drift curve presented in Figure 5.11 indicates that the model can accurately capture the initial stiffness and the 'yield' point at a drift of 0.07% in both loading directions. The peak strength is closely predicted in the positive direction, as the difference between the physical and the numerical model is less than 7%, while in the negative direction the difference is 18%. The post peak behavior in both cases is well represented by the finite element model which slightly underestimates the strength of the specimen for drifts between the drift at peak load and 1%. However the residual strength beyond 1% is precisely matched. Overall, the numerical model captures the experimental behavior reasonably well, especially if the lack of material data is considered.

The comparison of the experimental and analytical failure patterns shown in Figures 5.12(a), (b) and (c), indicates that the cracking pattern of the physical specimen is represented by the numerical model, as the latter captures the diagonal cracks in the infill, the shear cracks on the columns in the positive loading direction, and the flexural behavior of the left column in the negative direction. The only discrepancy between the experiment and the finite element model is the location of the shear failure in the left column. In the physical specimen, the crack developed at the mid-height of the column and it is likely caused by the cyclic load effect which the model does not account for. In the absence of the horizontal crack formed in the mid-height of the long masonry pier caused by loading in the other direction, the shear crack in the model develops at the bottom of the column.

The force distribution along five cross sections on the numerical model is presented in Figure 5.13 for the positive and in Figure 5.14 for the negative loading direction. In both cases the forces at the instant of peak load and at 1.00% drift are shown. To facilitate the comparison, both directions of loading have been plotted as if windward column is on the left and the force is applied towards the right. The window location signifies the loading condition according to the convention set for the physical models. In all cases, one can distinguish two diagonal struts forming around the window. However, the strut widths and lengths of the force vectors change for the different window locations and loading stages.

The force distribution can provide insight on the effect of the window location and how this affects the failure mechanism. At the instances of peak load, the total base

shear is slightly different in the two loading directions; however, the force distribution is quite different. In the positive direction, the windward column does not reach its strength at the top cross section and it carries 44.5 kN (10 kips) less than in the negative direction although the vertical load is the same. However, in the cross section at mid-height, the column carries 44.5 kN (10 kips) more load in the positive direction, indicating that the strut has shifted downwards due to the presence of the window close to the column. This strut develops through the infill wall below the window which is solid. The shifted strut creates a short column effect leading to a shear crack at the top of the windward column, as seen in Figure 5.12(b). In the case of the leeward column, the window is further from the column, allowing the full development of the diagonal strut starting at the bottom of the column and ending at the middle of the beam. This strut, similarly to the case of the solid panel leads to the shear failure of the column. Thus, at 1.00% drift, the capacity of the leeward column is limited due to the shear failure and the strut is redirected towards the RC joint and the foundation beam.

In the negative direction, the window is close to the leeward column and it changes drastically the geometry of the strut. The strut shifts to the left and has a reduced width and a steeper angle. Thus, this column does not reach its shear capacity. Instead, it is dominated by flexural bending as indicated by the deformed mesh of Figure 5.12(c). In the windward column the behavior is similar to the positive direction with a short column effect forming. However, due to the difference in the geometry, the column does not fail in shear until 1.00% drift.

5.8 CU5: 2/3-Scale Specimen with Door

The infill wall of Specimen 5 incorporated a door corresponding to an opening of 211 x 107 cm (74 x 42 in.) for the prototype structure. The door was not centered with respect to the concrete frame, as shown in Table 1, to represent a more general case. The material tests for Specimen 5 indicated that the concrete frame was weaker than all other specimens and the concrete strength was equal to only 60% of the strength of Specimen 1. Furthermore, the mortar and masonry strengths were considerably lower compared to the other specimens.

5.8.1 Experimental results

Figure 5.15 presents the experimental and analytical force-vs.-drift curves for Specimen CU5. The initial behavior was similar in the two directions of loading and was characterized by similar stiffness values and distinct yield points at a load level of 290 kN (65 kips) and drift of 0.06%. At this level, the infill separated from the frame and horizontal sliding occurred in the masonry above the lintel beam. In both directions, there was significant sliding of the infill along the foundation beam and the first few of mortar joints. Due to the sliding, the structure was more flexible than CU1 and could deform without developing diagonal cracks. As the imposed displacement increased, the behavior of the specimen became very different for the two loading directions. In the positive direction, the load carried by the specimen reached 591 kN (133 kips) at a drift level of

1.00% following a more or less bilinear envelope curve with a secondary slope equal to 9% of the initial elastic slope. At the point of peak load, a diagonal shear crack in the leeward (left) portion of the infill caused a brittle failure and a load drop of 294 kN (66 kips) to 50% of the peak strength. This crack is shown in Figure 5.16(a).

In the negative direction, the sliding at the base of the longer pier, on the left of the door, and the uplift of the shorter (right) pier drastically reduced the strength as opposed to the positive direction to only 383 kN (86 kips). The mechanism, shown in Figure 5.16(b), included the separation between the windward (left) column and the infill. Due to the separation, a part of the column was not supported by the infill and deformed in a flexural manner. As a consequence, the column could not carry enough load to cause a shear failure, leading to a reduced load capacity for the frame. Subsequently, the specimen was able to maintain more or less the peak load until it reached a drift of 1.25% forming an almost elastic-perfectly plastic backbone curve up to that point. At this level, a significant portion of the wall was detached from the frame due to a combination of vertical splitting cracks and horizontal sliding cracks along the base, as illustrated in Figure 5.16(c), and caused the reduction of the residual load to 267 kN (60 kips).

The final crack pattern of Specimen 5 is presented in Figure 5.16(c). As shown in the figure, fewer cracks developed in this specimen compared to Specimen CU2 which had a window. However, the behavior of the two specimens was similar in that two large pieces of the masonry wall on the two sides of the opening were separated from the panel at the end of the test. Thus, at the cycles beyond 1.00% drift these pieces did not move with the frame through the whole displacement trajectory, allowing the formation of a

few wide cracks. Due to partial contact with the rest of the infill, these pieces rotated within the frame and resulted in an interesting failure pattern. The pattern included crushing of the infill in the bottom left corner of the door and also some minor cracks in the beam. These observations are unique for this specimen among the tests conducted in CU and demonstrate the influence of the opening shape in the structural response.

5.8.2 Finite element analysis results

The comparison between the experimental and the finite element model for Specimen CU5 is presented in Figures 5.15, 5.16 and 5.17 in terms of the lateral load-vs.-drift curve and the crack pattern. The analysis results can accurately capture the response of the specimen except for the peak strength in the positive direction. The models predict accurately the initial stiffness, the yield point and the secondary stiffness for both loading directions. However, the finite element model underestimates the actual peak strength by 19%. In the analysis, the peak strength occurs at 0.50% drift, while the resistance of the specimen did not reach its peak value until 1% drift. In both cases, the load drop after the peak is very steep indicating a brittle behavior, although it occurs at an earlier drift level. The finite element model accurately estimates the residual strength of the structure reached at 1.05% drift. In the negative direction, the response is very well captured by the finite element model. The model predicts accurately the overall ductile behavior although it slightly overestimates the peak strength. The initial stiffness, the yield point and the residual strength are very close to the experimental values.

The deformed meshes, shown in Figure 5.17, reproduce the failure patterns of the specimen. In the positive direction, a major diagonal crack forms in the longer (left) pier and leads to the shear failure of the leeward (left) column, similarly to the behavior of the specimen shown in Figure 5.16(b). Moreover, the flexibility and the flexural cracks of the windward (right) column, caused by the proximity of the door to the column, is represented by the model. In the negative direction, the model captures the uplift of the short (right) pier, the crushing of the infill close to the door, and also the separation between the left column and the masonry wall at the upper half of the column. In the model the separation initiates at a lower level; however the difference is not significant. Finally, at a larger drift in the analysis, shear cracks formed in the bottom of the leeward (right) column and the top of the windward (left) column. Practically, these are not important though, as they occur late and do not affect the failure mechanism, similarly to the test.

The force distribution along three cross sections of the structure and the frame-infill interface is shown in Figure 5.18 at the instant of peak load and also at 1% lateral drift, when the residual strength has been reached in the positive loading direction. Initially, one can note that the shear forces at critical locations of the two columns are significantly lower than in the solid infill, with the different exceeding 89 kN (20 kips). The reason for the reduced forces is the existence of the door in the infill which limits the width of the strut and alters its angle. The low resistance of the infill prevents the shear failure of the columns which deform in a flexural manner. Eventually, as the drift increases, the strut on the longer masonry pier becomes significant and transfers a large

force to the bottom of the leeward column. Figure 5.18(b) presents the force distribution after the shear crack has developed in the column. One can notice that the shear force in the column is negligible, as is the force in the interface between the column and the wall. On the contrary, the forces between the infill and the horizontal RC members grow significantly as the orientation of the struts changes and the angle becomes closer to 90^{o}. The force orientation is also affected by the rotation of the two portions of the masonry wall which have separated from the infill on the two sides of the door.

Similar observations can be made for the negative direction which is presented in Figure 5.19. In this case, the shear force in the leeward column is even lower due to the small length of the adjacent pier. The reduced width of the strut on the leeward masonry pier limits the strength of the infilled frame, which reaches only 63% of the strength of Specimen CU1. In the positive direction, high normal forces develop at the base of the longer pier next to the door and this justifies the compressive failure of the masonry at that point observed in the experiment and the analysis, as shown in Figures 5.16 (c) and 5.17 (b).

5.9 CU6: 2/3-Scale Specimen with Large Window

The masonry panel of Specimen CU6 included a wide window while the concrete frame had the same geometry and design details as the previous specimens. The window of CU6 had the same height but it was 61 cm (24 in.) wider than the window in CU2, resulting in a 67% increase of the opening area. The exact dimensions of the window are

shown in Table 5.2. The location of the window was selected so that its center was as close as possible to the center of the openings of Specimens CU2 and CU5. This location resulted in a narrow pier on the right side of the opening that had a width of only 64 cm (25 in.). The material tests conducted on the concrete cylinders and masonry prisms obtained during the construction of this specimen indicated that their respective strengths were similar to the properties of CU5 but considerably inferior to those of CU1.

5.9.1 Experimental results

The force-vs.-drift response of Specimen 6 is presented in Figure 5.20. It indicates that this frame was significantly weaker in both loading directions but more ductile compared to the other three specimens. In more detail, the response demonstrated an initial yield point at a lateral load of around 200 kN (45 kips) caused by the separation between the frame and the masonry wall. After the yield point, the load increased until it reached the maximum resistance at 376 kN (84.5 kips) for the positive direction and 318 kN (71.6 kips) for the negative direction. In both directions, the specimen was able to sustain a load higher than 80% of the peak load until a drift of 1.5%. The ductile behavior was a result of the failure mechanisms that developed in the two loading directions.

At small drift levels in the positive direction, the masonry infill separated from the frame and then developed diagonal cracks radiating from the corners of the window, similarly to the CU2 which included a smaller size window. At drift levels beyond 0.5%, few dominant cracks formed in the longer masonry pier, while the cracks in the short pier,

on the right side of the window, were more diffused not allowing the formation of a dominant crack. The cracks in the masonry panel did not cause any brittle load drop but influenced the crack development in the RC frame as well. Consequently, diffused cracks developed along the height of the windward (right) column, while two shear cracks developed at the bottom of the leeward column as extensions of the dominant crack in the infill. The second of those cracks opened at a drift of 1.5% and caused a load drop of 70 kN (70 kips).

In the negative direction of loading, a prevailing diagonal crack developed at the longer (left) pier and at 0.22% drift and was followed by a shear crack at the top of the windward column at the following cycle. The shear crack in the column limited the capacity of the frame and resulted in a strength reduced by 15% in this direction of loading. The structure was able to maintain the load despite the increase of the imposed drift which caused the development of more cracks in the infill and the RC frame. During the cycles at 1.25% drift, the cracks in the infill grew larger and a shear crack developed at the bottom of the leeward (right) column, and reduced the load capacity of the infilled frame to 60% of the peak value. The final crack pattern of Specimen CU6 is illustrated in Figure 5.21(a).

5.9.2 Finite element analysis results

Figure 5.20 presents the response of the finite element model for Specimen CU6. The comparison of the responses indicates a very good match between the finite element

model and the experimental results. The calculated strength is very close to the test results in the positive direction and slightly overpredicts the test value in the negative direction. Also, as in all specimens, the initial stiffness, yield point and residual strength are well-captured. The only deviation compared to the tests is the fact that the model slightly underestimates the resistance in the positive direction between the drifts of 0.75 and 1.25%. However, the difference in the responses does not exceed 70 kN (15.7 kips) at any point.

The crack pattern is also well captured as shown in Figure 5.21. The model captures the dominant cracks in the longer pier that lead to shear cracks in the columns. As in the test, these shear cracks develop when drifts close to 1% are reached and after the column has deformed considerably due to flexure. Moreover, the cracks are more diffused in the shorter pier, allowing a more flexible behavior of pier and the adjacent (right) column for both loading directions. The flexibility of the specimen can be explained by the narrow struts developing in the masonry wall, as shown in Figures 5.22(a) and 5.23(a). The low resistance provided by the masonry limits the forces on the columns and thus reduces the peak load carried by the structure. The lower column forces prevent the shear failure of the columns allowing a more ductile behavior for the structure. The column forces remain practically constant at the top of the windward column and slightly decrease at the bottom of the leeward column at a drift of 1.00%.

5.10 Observations from the Experimental and Numerical Studies

5.10.1 Observations on the scaling effect

Interesting observations can be made when the behaviors of the small and large-scale specimens with solid infills are compared. The two specimens were scaled versions of the same prototype structure; however, their failure patterns are very different. The discrepancy can be attributed to three sources. One possible reason could be the different material properties; however, the differences are small. As the sensitivity analysis presented in Chapter 3 indicates, the frame behavior would not drastically change for the level of variation of the material properties encountered here.

Another possible reason for the different behavior is the distortion of the scaling law for the small-scale specimen. As explained in a previous section, the small-scale specimen can be considered as the combination of two parallel, 1/5-scale frames built monolithically. However, the infill width is 20% smaller compared to the width of an accurately scaled specimen, while the concrete columns have a cross sectional area that is 36% larger than an accurately scaled specimen. This deviation from the design weakens the infill and strengthens the columns pushing the structure towards the weak-infill, strong-column behavior that was also observed in Specimen 8 tested by Mehrabi (1994) which is discussed in Chapter 3. In fact, the failure patterns of the small-scale specimen and Specimen 8 tested by Mehrabi are similar.

To investigate the influence of the scaling discrepancy, a finite element model was created for a fictitious specimen that was accurately scaled. The failure pattern of

this model, as shown in Figure 5.24, is a combination of horizontal sliding cracks and with diagonal cracks leading to the shear failure of the columns. Hence, its behavior is closer to the large-scale specimen CU1. This is also indicated by the force-vs.-drift curves shown in Figure 5.25. In this figure, the responses of the small and large-scale specimens have been scaled-up to the prototype level. The comparison indicates that the three models reach comparable strengths and demonstrate similar post peak slopes. The exactly scaled specimen is slightly closer to the actual behavior in terms of the initial stiffness and post-peak behavior, and accurately matches the peak strength. However, the large-scale specimen demonstrates a significant load drop due to a shear crack around 0.36% drift. A similar drop is demonstrated by the exactly scaled specimen at a drift of 0.55%. The decline is not as steep though, because the failure is also governed by sliding along the bed joints. The latter is the dominant failure mode of the modified small-scaled specimen tested at Stanford.

Although the exact scaling improves the behavior, the small-scale specimen does not precisely match the large-scale specimen. The reason for this is the fact that the brick units and mortar joints have not been scaled. Thus, the 2/3-scale specimen includes 29 layers of bed joints along its height and the small scale specimen includes only nine layers. Given the strong brick units used in this study, reducing the number of mortar joints changes the stress field compared to prototype structure. Moreover, sliding along a bed joint has a larger impact on the small-scale structure, compared to the larger specimen which incorporates a number of them. The SU specimen also pronounces the cyclic loading effect as sliding along fewer mortar joints degrades them more rapidly,

causing a specimen with bed-joint sliding to demonstrate a brittle behavior. Finally, the fact that the mortar joints are not scaled in thickness, can account for the reduced initial stiffness of the small scale specimen.

Overall, this study shows that using small-scale specimens and modifying them to accommodate practical needs can result in specimens representing some features of the behavior of actual structures. A necessary condition for this is the careful scaling of the structure and the applied loads according to the similitude law. However, translating the results requires special attention since the small-scale structures may alter the load transfer mechanism and failure pattern. It is a good practice to check this possibility with reliable analytical tools like the finite element models used this study. Such check should be also made on the boundary conditions that can change when a subassemblage of a prototype is tested. One example in this study was the increase of the reinforcement needed to prevent the unrealistic cracking of the beam which was predicted by a finite element analysis.

5.10.2 Observations on the effect of openings

The envelopes of the experimental responses of the four tests conducted on large scale specimens in CU are presented in Figure 5.26. The response of a bare frame has been also estimated with finite element analysis and is included in the figure so that the effect of the infill panels can be better appreciated. The peak resistance of the bare frame is only 147 kN (33 kips) which is very low compared to the four specimens tested in CU.

Those had strengths ranging from 323 kN (72.6 kips) for CU6 to 680 kN (153 kips) for the solid infill. The difference introduced by the existence of the infill panels is even more significant for the stiffness which increases from 272 kN/cm (155 kips/in.) for the bare frame, to values between 3702 and 5987 kN/cm (2114 and 3419 kips/in.) for the four infilled frames.

Although the presence of the infills increases the strength and the stiffness of the frames in all cases, a general trend as to how the infills with openings influence the structural behavior cannot be easily deduced from the comparison of the test results shown in Figure 5.26. The specimen with the smaller window opening has the same strength as that with the solid panel in the negative direction which could not be anticipated according to the modeling method proposed by Al-Chaar (2002) and the current building codes (ASCE 41-06). Moreover, in the positive direction, the frame with a door exceeds the strength of the specimen with the regular window, while in the negative direction its strength only reaches 60% of CU2.

Figure 5.27 compares the responses obtained from each specimen for the two loading directions as they are plotted in the same quadrant. Although the specimens with the solid wall and the larger window demonstrated comparable responses in the two directions, it is evident that the specimens with the larger window and the door have very asymmetric load-vs.-drift relations in the two loading directions. The different responses in the two loading directions can be caused by the cyclic loading effect. However, it is not likely that this effect can cause such significant differences like that observed for Specimen 5. The most likely cause for the discrepancy is the effect of the location of the

openings. This is an important parameter that is often overlooked by engineers. However, the finite element analyse indicate that the location of the opening can favor one failure pattern over another and significantly influence the overall behavior of the infilled frame. This issue is addressed in detail in Chapter 7 with a parametric study which considers several different opening configurations.

5.10.3 Observations on the finite element modeling

The comparison of the analytical prediction with the experimental results that are presented in this chapter indicates that the modeling scheme developed in Chapter 2 can accurately capture the behavior of infilled RC frames. This is evident from the comparison of the predicted and measured force-vs.-drift curves of the five specimens considered here. Most importantly, though, the proposed modeling approach can accurately capture the variety of failure patterns exhibited by the physical specimens. In particular, the models simulate the sliding along the mortar joints in the small-scale specimen, as well as the dominant shear cracks in the infill and columns of the large-scale specimen with a solid panel. The models can also capture the combination of shear and flexural failure of the frames that include infill panels with openings. Moreover, the crushing of the masonry in Specimen CU6, and the distinct failure mechanism of CU5, which had a door, have been well represented, despite the fact that the cyclic loading effect is not accounted for.

The results of the finite element analysis also indicate that the models can estimate with good precision the initial stiffness, the initial yield point and the secondary stiffness of all specimens. For drifts between 0.5% and 1%, the models underpredict the actual behavior and the strength of the structure in some cases. However, the discrepancy is in all cases below 20%. A possible reason for this shortcoming can be the brittleness of the model caused by the tensile and shear failure of mortar and concrete. Conducting actual material tests for these parameters could improve the results of the analysis. In all cases, though, the models can precisely estimate the residual strength and represent the final cracking patterns.

5.11 Conclusions

This Chapter presents analytical and experimental studies on the behavior of scaled infilled RC frames. The structures were tested quasi-statically and involved two different length scales and also openings of various geometries and sizes. The outcome of the study is that small-scale specimens may have limitations in representing the full-scale structure, but can be used with caution as long as the scaling requirements need to be followed as close as possible. Moreover, the effect that openings in the masonry panel can have on the behavior of the frames has been pointed out. The cases examined, though, do not indicate a clear trend as to how the opening size and shape affect the strength of the structure. The notion that the size of an opening can determine the strength contribution of the infilled frame has proven to be inaccurate since the location of the

opening is also very important and can influence the load transfer mechanism. This is further examined in Chapter 7 which presents a parametric study on the effect opening sizes and locations. A necessary condition to conduct such a study is a tool able to capture the performance of these structures. The comparison of the analytical and experimental results indicates that the finite element modeling scheme developed in Chapter 2 is a reliable tool for this study.

Tables of Chapter 5

Table 5.1: Compressive strengths of building materials.

Material	Property		Small-scale	CU1	CU2**	CU5	CU6
Concrete*	Comp. Strength	kPa (ksi)	25.9 (3.76)	30.0 (4.36)	19.0 (2.76)	14.9 (2.16)	16.5 (2.40)
Brick Units	Comp. Strength	kPa (ksi)	49 (7.1)	49 (7.1)	49 (7.1)	49 (7.1)	49 (7.1)
Mortar	Comp. Strength	kPa (ksi)	7.65 (1.11)	9.2 (1.34)	-	4.5 (0.65)	5.4 (0.79)
Prism	Comp Strength	kPa (ksi)	20.1 (2.91)	24.3 (3.53)	-	14.5 (2.10)	13.8 (2.00)

* Sakrete was used instead of concrete for the frame small-scale specimens.
** An error of the data acquisition system did not allow the recording of the material testing.

Table 5.2: Summary of specimen configurations.

Specimen	Infill	Retrofit	l_a m (in)	l_b m (in)	l_c m (in)	h_a m (in)	h_b m (in)	h_c m (in)
CU1	Solid	N	-	-	-	-	-	-
CU2	Window	N	1.55 (61)	0.91 (36)	0.89 (35)	0.51 (20.25)	0.74 (29.25)	0.61 (24)
CU3	Solid	Y	-	-	-	-	-	-
CU4	Window	Y	1.55 (61)	0.91 (36)	0.89 (35)	0.51 (20.25)	0.74 (29.25)	0.61 (24)
CU5	Door	N	1.62 (64)	0.71 (28)	1.02 (40)	0.44 (17.5)	1.42 (56)	-
CU6	Window	N	1.22 (48)	1.52 (60)	0.64 (25)	0.51 (20.25)	0.74 (29.25)	0.61 (24)

Table 5.3: Material parameters for interface elements of CU1 model.

Specimen	Material	D_n (GPa/m)	$f_t^{'}$ (MPa)	G_f^{I} (N/m)	G_f^{II} (N/m)	μ_0	μ_r	r_0 (kPa)	r_r (kPa)	η	α (m/N)	β (m/N)
CU1	Concrete	2443	2.75	140	1400	0.9	0.7	138	35	0.6	0.011	12.5
	Brick	2443	1.72	105	1050	0.8	0.7	138	35	0.6	0.011	12.5
	Mortar	163	0.50	105	1050	0.8	0.7	138	35	0.6	0.011	12.5

Table 5.4: Material parameters for smeared-crack elements CU1 model.

Specimen	Material	$f_c^{'}$ or $f_m^{'}$ (MPa)	ε_1	ε_2
CU1	Concrete	30.0	0.0022	0.0027
	Brick	24.3	0.0014	0.0019

Figures of Chapter 5

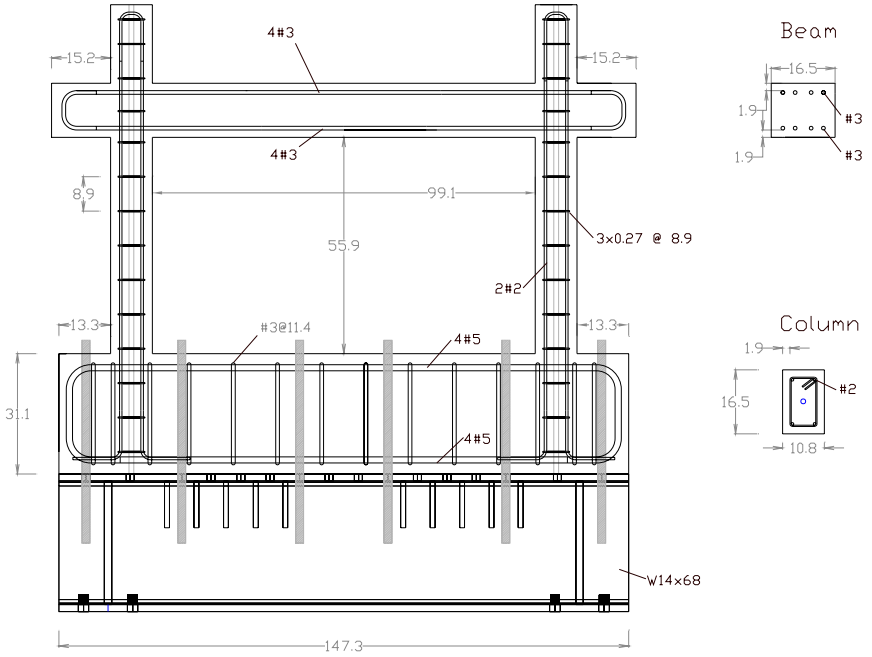

Figure 5.1: Design of small scale-specimen (units in cm, bar geometry can be found in Table A.1, Appendix A).

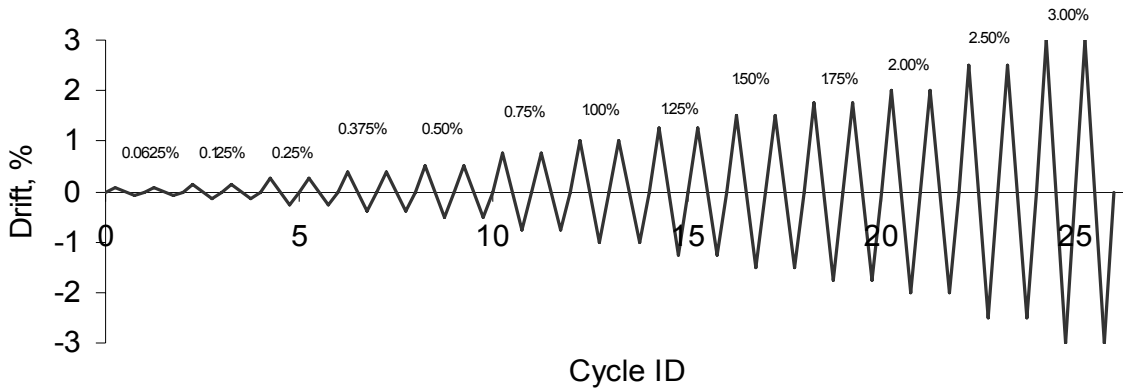

Figure 5.2: Loading protocol for quasi-static tests.

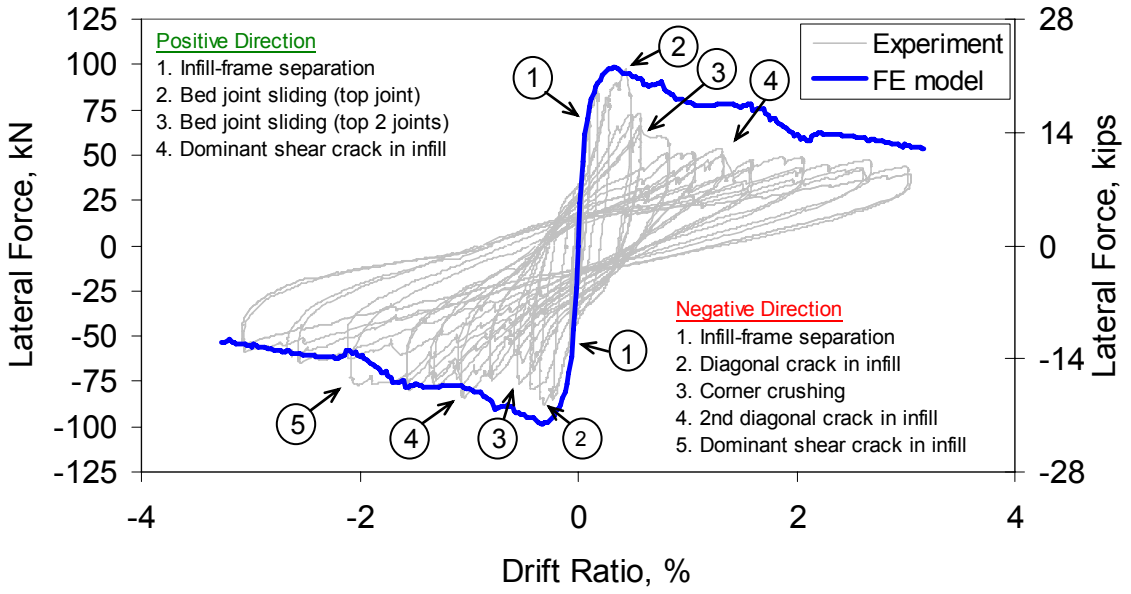

Figure 5.3: Analytical and experimental force-vs.-drift curves for small-scale specimen.

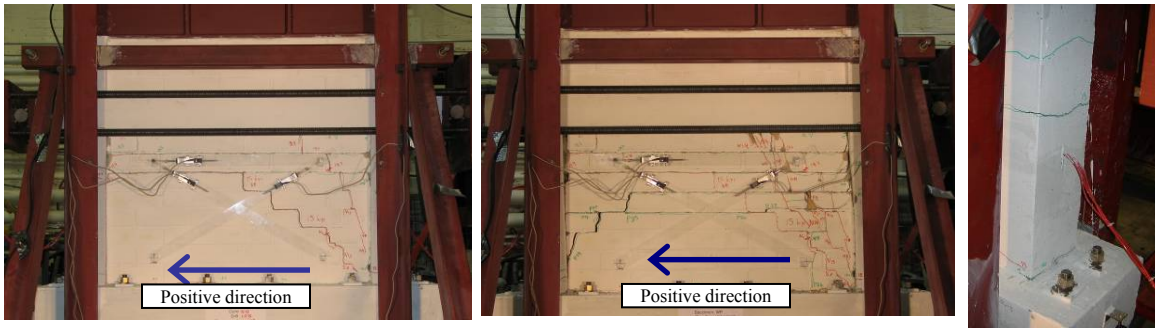

(a) 1.00% drift (b) 3.00% drift (c) 3.00% drift

Figure 5.4: Failure pattern of small scale specimen.

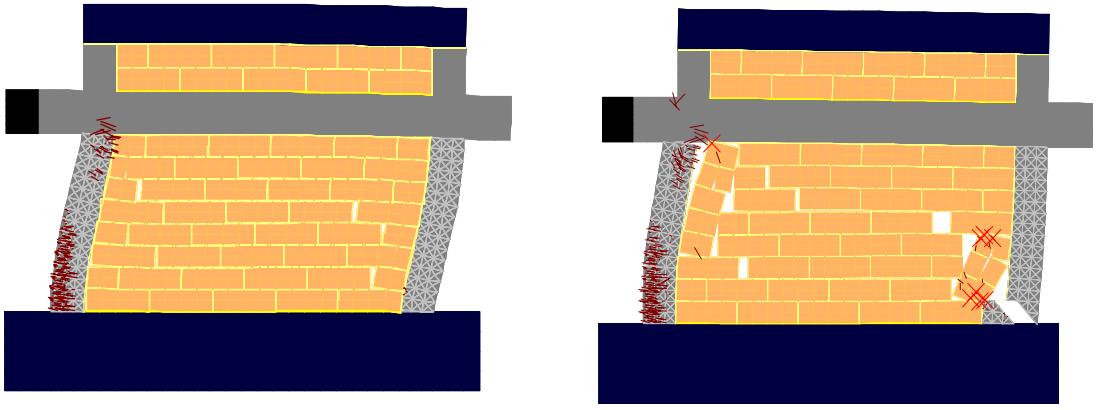

(a) at 0.50% drift (b) at 3.00% drift

Figure 5.5: Deformed mesh of numerical model.

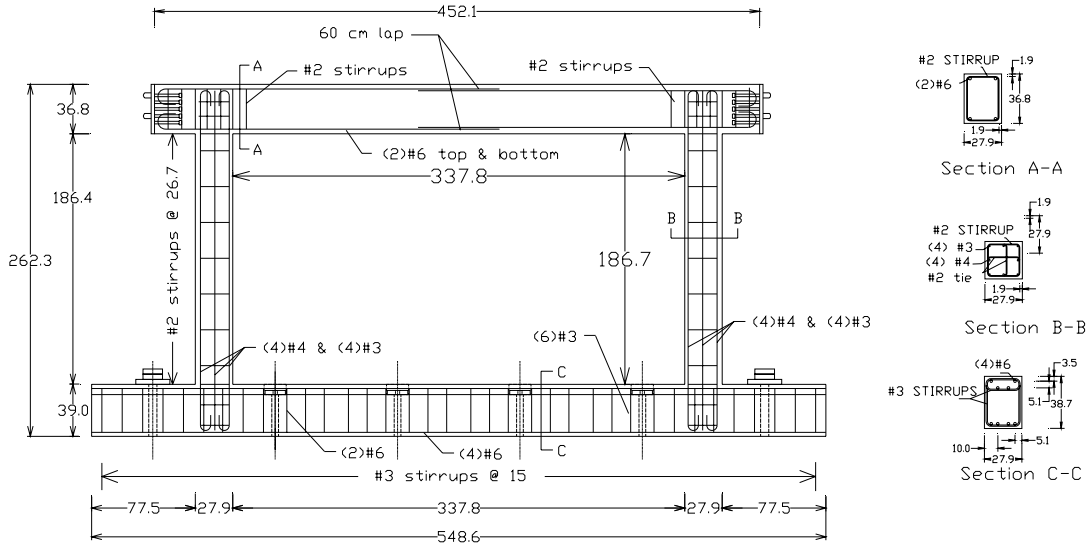

Figure 5.6: Design of RC frame for large-scale specimens (units in cm, bar geometry can be found in Table A.1, Appendix A).

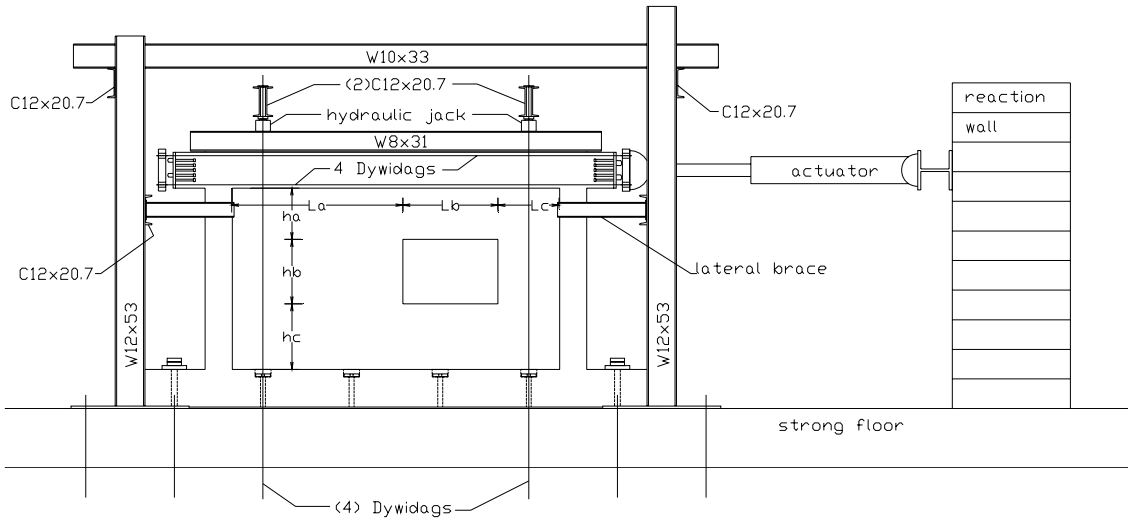

Figure 5.7: Test set-up and opening configurations (for the dimensions L_α, L_b, L_c, h_α, h_b, and h_c see Table 5.2).

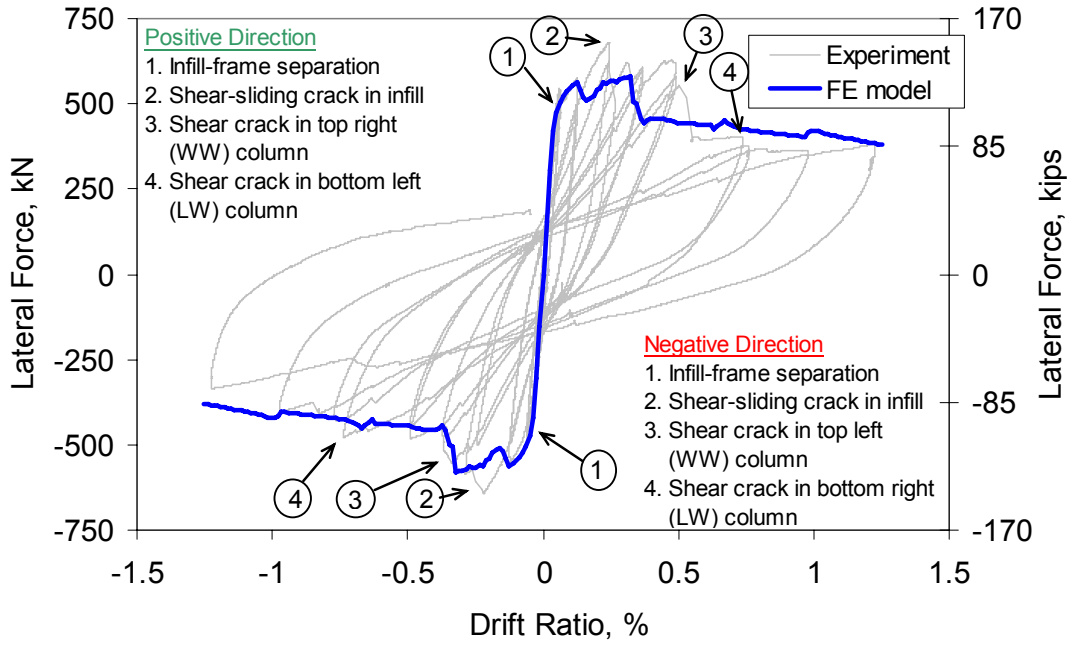

Figure 5.8: Analytical and experimental force-vs.-drift curves for Specimen CU1.

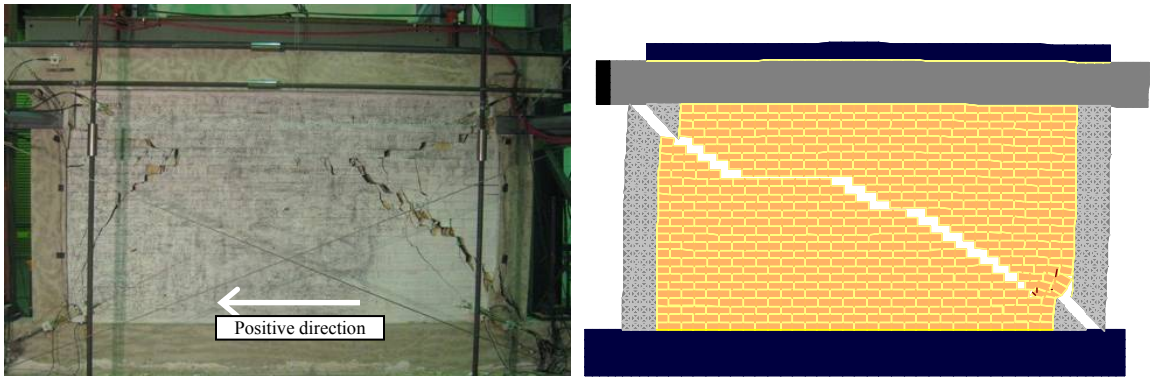

(a) Experimental (b) Analytical

Figure 5.9: Cracking pattern at 1% drift.

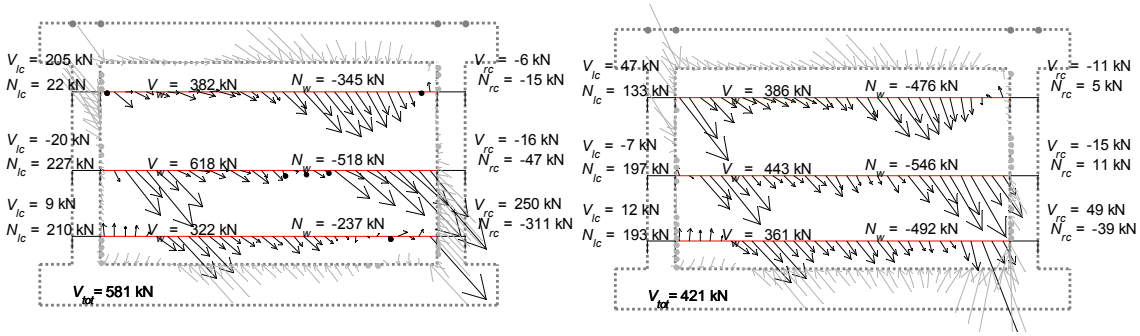

(a) at peak load (b) at 1.00% drift

Figure 5.10: Force distribution along five cross sections at two drift levels.

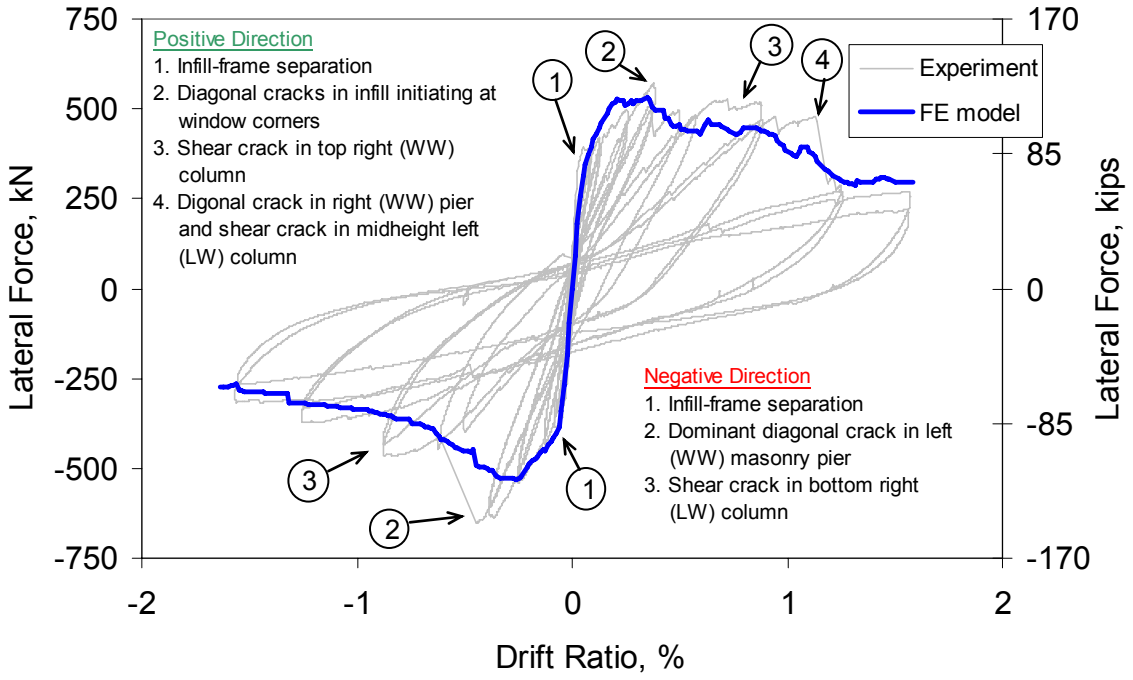

Figure 5.11: Analytical and experimental force-vs.-drift curves for Specimen CU2.

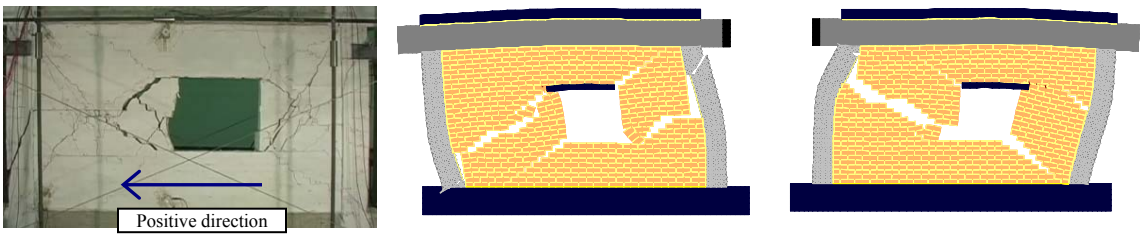

(a) Experiment (b) Positive direction (c) Negative direction

Figure 5.12: (a) Experimental and (b), (c) analytical failure mechanisms at 1% drift level.

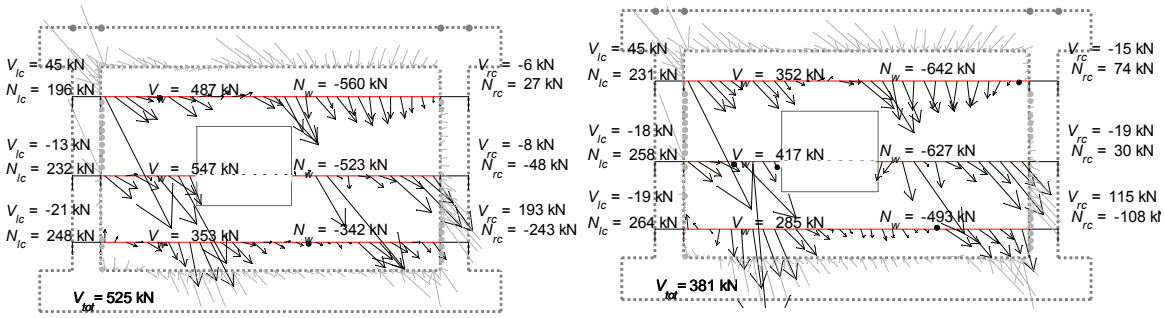

(a) at peak load (b) at 1.00% drift

Figure 5.13: Force distribution along five cross sections at two drift levels of the positive loading direction.

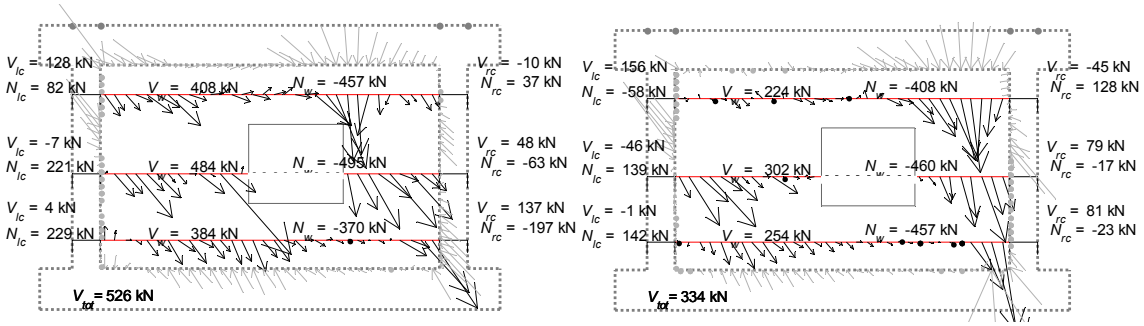

(a) at peak load (b) at 1.00% drift

Figure 5.14: Force distribution along five cross sections at two drift levels of the negative loading direction.

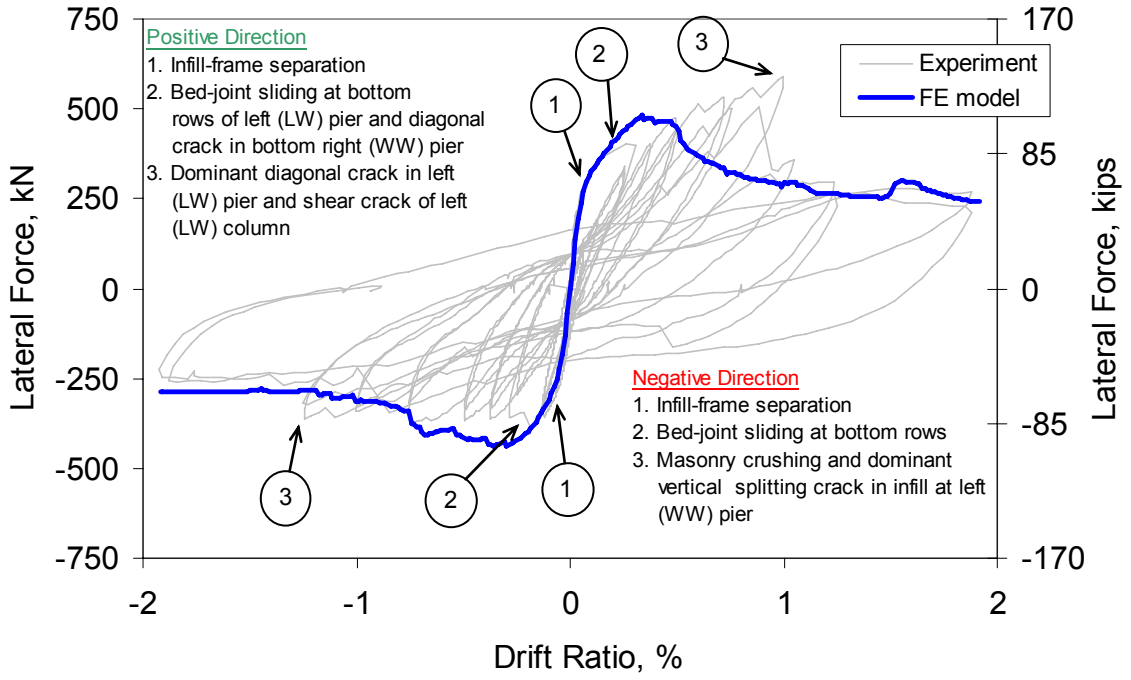

Figure 5.15: Analytical and experimental force-vs.-drift curve for Specimen CU5.

(a) at 1.00% drift

(b) Bottom left corner at 1.00% drift

(c) at 1.90% drift

Figure 5.16: Cracking patterns of physical specimen.

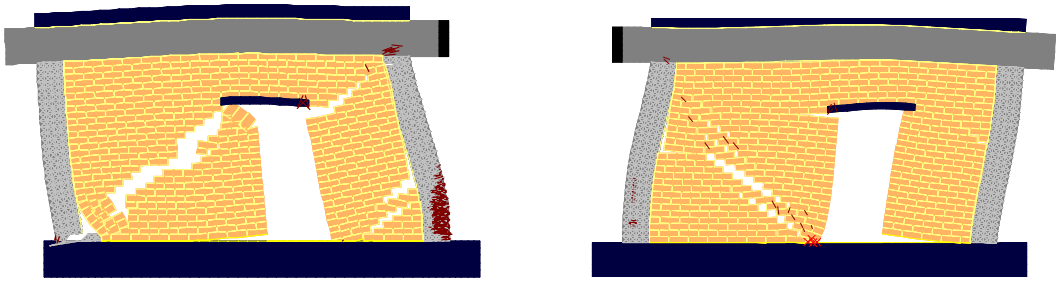

(a) Positive direction (b) Negative direction

Figure 5.17: Cracking patterns of finite element model at 1.00%.

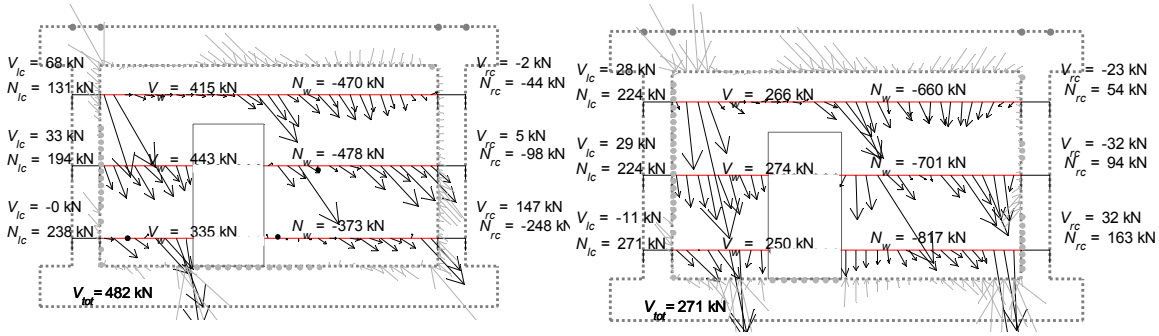

(a) at Peak load (b) at 1.10% drift

Figure 5.18: Force distribution along three cross sections for loading along the positive direction.

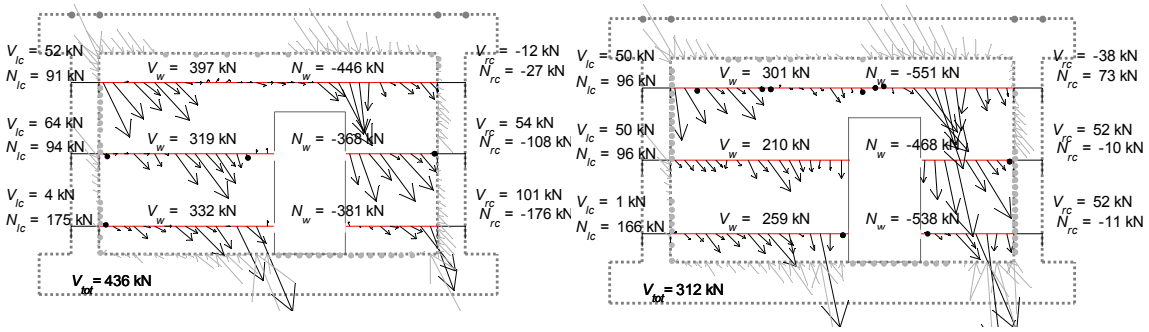

(a) at Peak load (b) at 1.00% drift

Figure 5.19: Force distribution along three cross sections for loading along the negative direction.

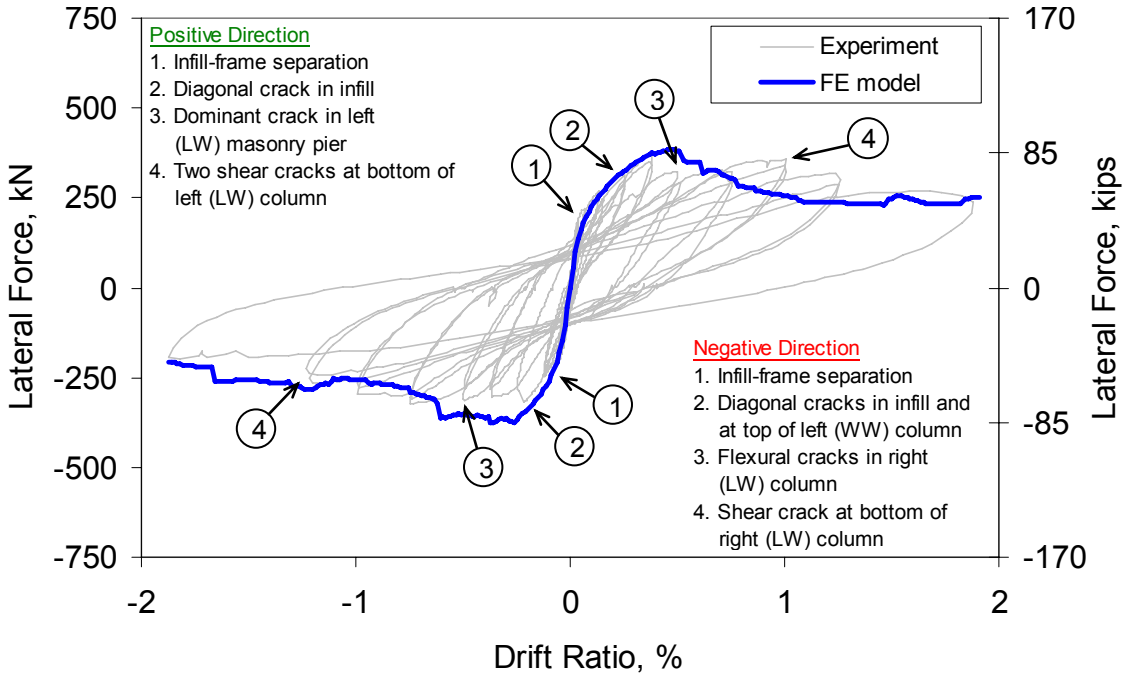

Figure 5.20: Analytical and experimental force-vs.-drift curves for Specimen CU6.

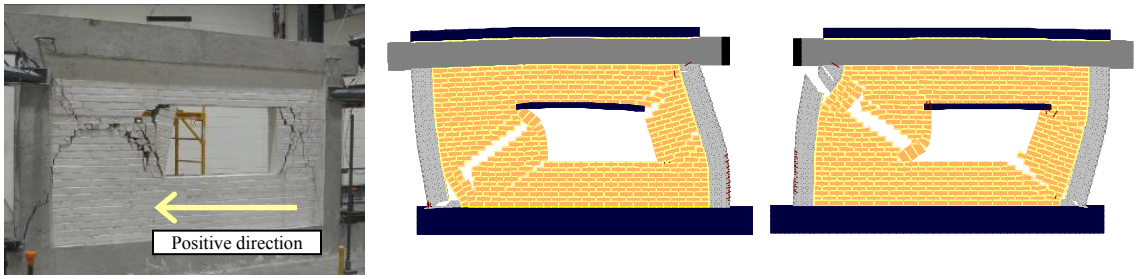

(a) Experiment (b) Positive direction (c) Negative direction

Figure 5.21: Cracking patterns at 1.00% drift.

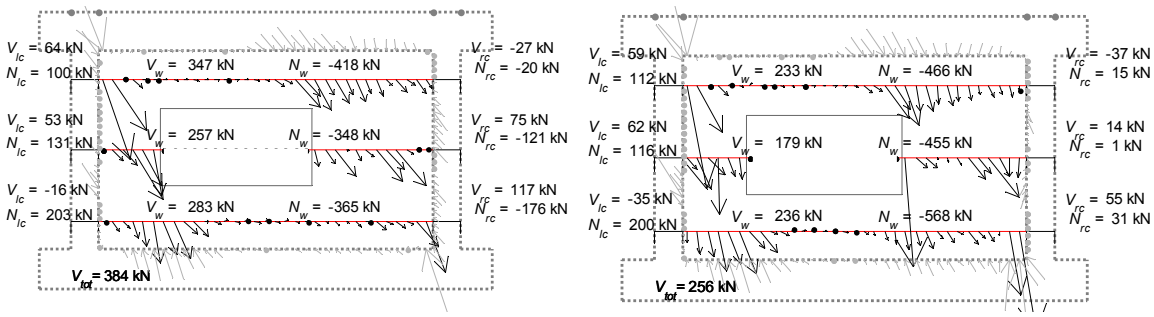

(a) at Peak load (b) at 1.00% drift

Figure 5.22: Force distribution along three cross sections for loading along the positive direction.

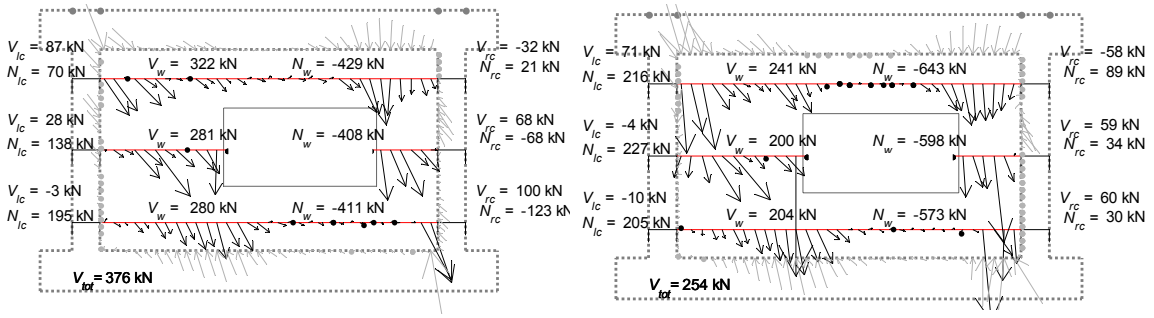

(a) at Peak load (b) at 1.00% drift

Figure 5.23: Force distribution along three cross sections for loading along the negative direction.

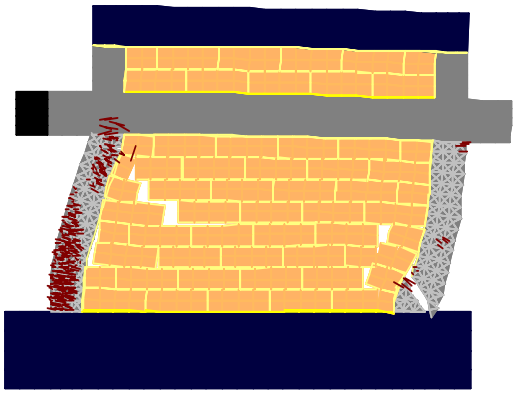

Figure 5.24: Deformed mesh at 0.60% drift,

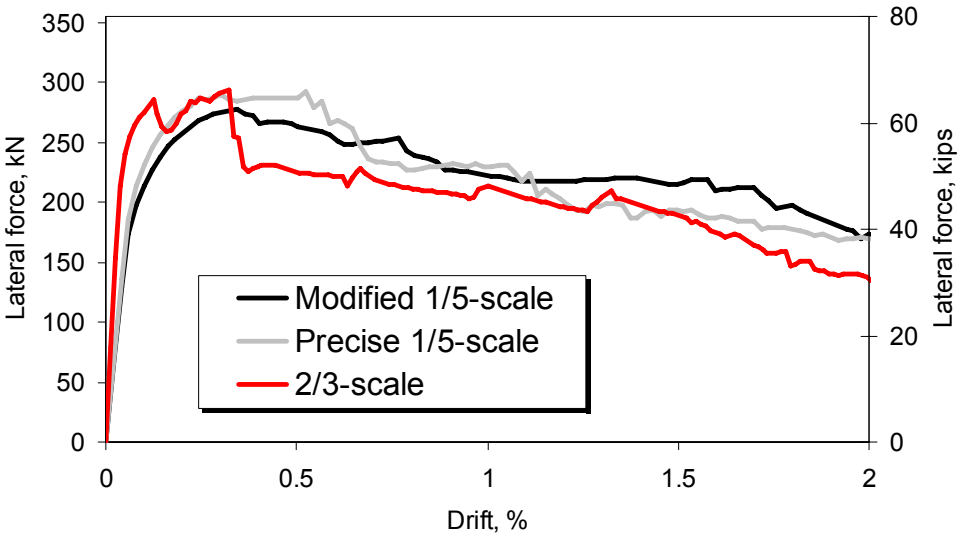

Figure 5.25: Analytical force-vs.-drift curves Scaled to the prototype.

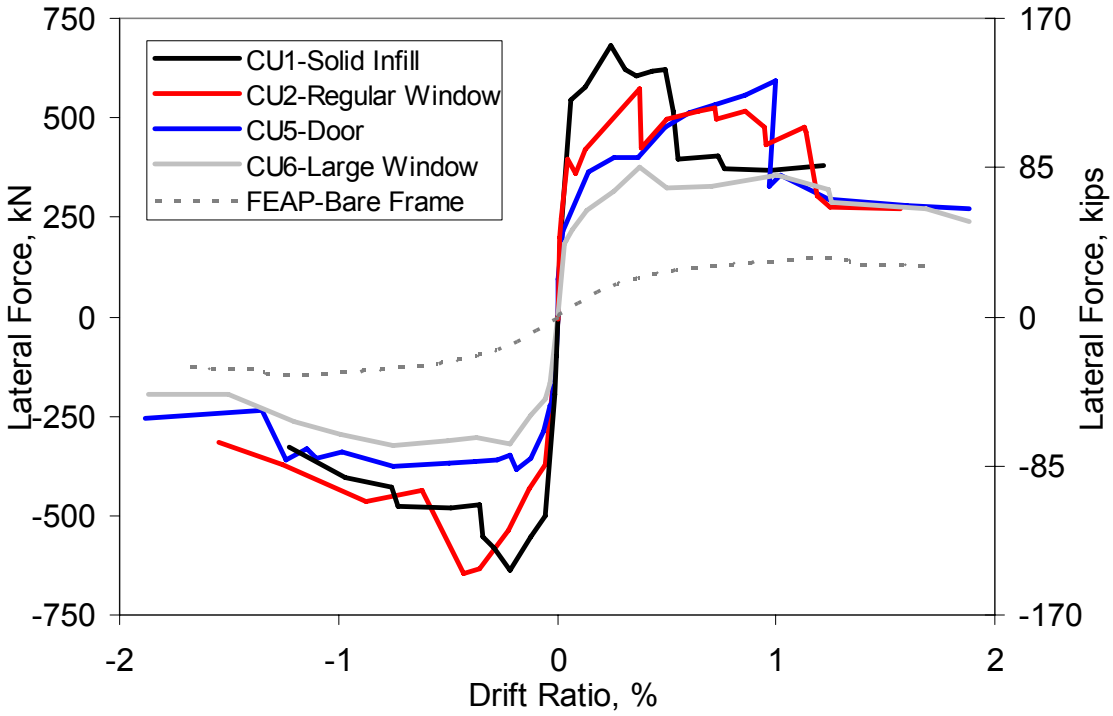

Figure 5.26: Backbone curves for the large scale specimens.

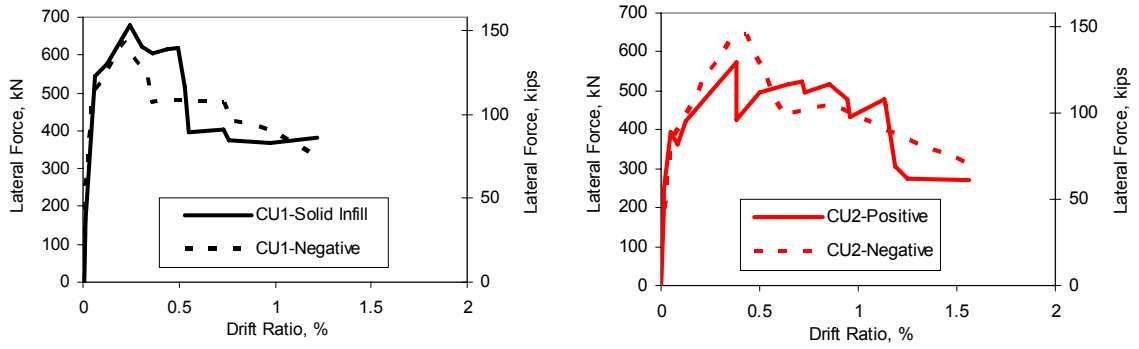

(a) CU1 - Solid Infill

(b) CU2 - Regular Window

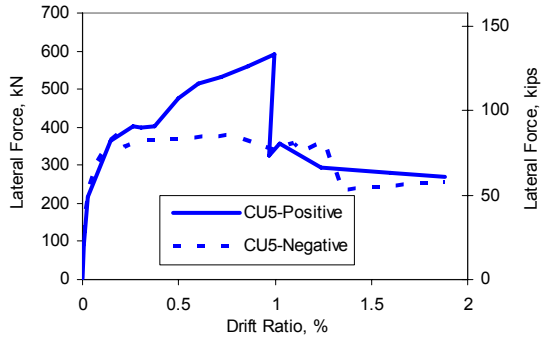

(c) CU5 - Door

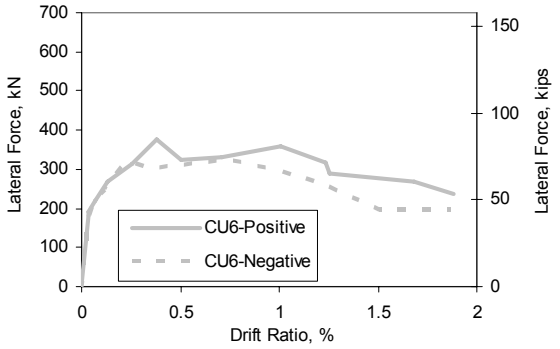

(d) CU6 - Large Window

Figure 5.27: Response envelopes of large-scale specimens in the two loading directions.

CHAPTER 6

PARAMETRIC STUDY ON INFILLED RC FRAMES WITH SOLID PANELS

6.1 Introduction

The tests and analyses presented in Chapter 5 provided valuable insight on the behavior of infilled RC frames subjected to in-plane lateral loads. However, for practical reasons, the study was limited to a single configuration in terms of the geometry of the frame, the reinforcement details, and the vertical load distribution. Hence, it is interesting to examine the influence of these parameters on the behavior of the RC frames with solid panels. This is addressed through a parametric study which is presented in this chapter. The study uses the validated model for the CU1 specimen discussed in Chapter 5 as a reference model. The scope of the study presented here was to assess the importance of each design parameter and develop a simplified approach for the derivation of the lateral force-lateral drift relation for infilled frames. Hence, the configurations considered in this study have been selected to identify the influence of each parameter in the structural response, rather than to represent actual cases.

A summary of the cases examined in this study is provided in Table 6.1. In all cases, one parameter is varied each time to facilitate the direct comparison between different configurations and the assessment of parameter's influence. To examine the

influence of the vertical load, four force levels have been considered including a case with zero load. The story height is not expected to vary drastically in real structures; therefore, the effect of the aspect ratio has been examined by varying the length of the frame. Furthermore, different reinforcing schemes have been considered for the RC columns since the reinforcing details of the beams are not expected to significantly affect the behavior of the infilled frame. Although the amounts of longitudinal and shear reinforcement used in the physical specimen tested at CU were the minimum amounts used in the 1920s, the study considered amounts equal to half of the minimum values. Finally, the transverse reinforcement was varied also in terms of the spacing of the stirrups with the spacing used in the physical specimen considered as a lower bound.

For consistency, the same material properties as for the model of specimen CU1 have been used. The results of this study are used to develop a simplified approach for the development of a simplified force-vs.-drift curve for reinforced concrete frames with solid infill panels.

6.2 Background

The effect of the aspect ratio of the infill panel and the differences in the reinforcement detailing were among the parameters studied experimentally by Mehrabi et al. (1994). In their study, Mehrabi et al. considered two aspect ratios for infill panels consisting of solid (strong infill) and hollow (weak infill) masonry units. The combinations considered resulted in four cyclically tested infilled frames tested as

Specimen 4, 5, 10, and 11. The design of the RC columns for these frames considered only wind load corresponding to a basic wind of 100 mph (UBC 1991) and resulted in a weak frame. A second design for the frames considered seismic loads corresponding to Seismic Zone 4 and resulted in a strong frame (UBC 1991). A summary of the tests with weak frames discussed here is provided in Table 6.2. The compressive strength of the masonry prisms also varied substantially; however, it is not included in the table as the crushing of the masonry occurred after the peak strength was reached. Table 6.3 presents a comparison of the tests considering different design requirements.

Specimens 4 and 10 had the same column design and infill, but different aspect ratios. Table 6.2 indicates that Specimen 10, with an aspect ratio of 0.48, had lower initial stiffness by 7.5% but higher strength by 17% compared to Specimen 4, which was shorter and had an aspect ratio of 0.67. These are contradictory results since the longer specimen is expected to have higher stiffness and strength. However, the material parameters indicate that the masonry panel of Specimen 4 was stiffer than the panel in Specimen 10, while its RC members were less stiff. Since the stiffness of an infilled frame is governed by the infill panel, the increased stiffness of the shorter frame can be explained by the stiffer masonry wall. Moreover, the respective gravity load carried by the infill and the columns can be calculated considering the material properties and the geometry. As indicated in Table 6.2, the differences in the geometry of the specimens and material properties resulted similar distribution of the vertical forces in the two frames. Therefore, the contribution of the infill to the lateral strength is expected to be the same for the two panels. The difference in the lateral strength can be explained by the difference in axial

forces in the RC columns. The shorter distance between the columns in Specimen 4, reduced the moment arm and caused a larger pair of axial forces in the columns that resisted the overturning moment induces by the lateral force. Therefore, the tensile axial force in the windward column was higher and allowed the shear failure at the of the column, while in Specimen 10 no shear cracks developed in the column due to the reduced tensile force.

In the case of Specimens 5 and 11, which had strong panels (solid masonry units), the infill carried the majority of the vertical load due to its higher stiffness compared to Specimen 4 and 10. The reduced compressive forces on the columns, compared to Specimens 4 and 10, resulted in lower resistance of the columns in shear as indicated by the shear cracks at the top and bottom cross-sections of the columns in Specimen 5 and 11 (Mehrabi 1994). The shear cracks near the top of the columns are of particular importance since they were more severe. These cracks occurred in the windward columns due to the tensile forces resisting the overturning moment. Although the two specimens had the same design, and similar material properties and failure mechanisms, they had different lateral load capacity. In this case, the higher strength of Specimen 11 can be attributed to the higher normal load in the masonry panel which resulted in higher lateral resistance due to friction along the bed joints. This is verified by the 26.8 kN (5.8 kips) increase of both the normal force in the infill and the lateral strength of the infilled frame which is consistent with the assumption made in Chapter 5 of a friction angle close to 45^{o}.

The tests of the frames with different design requirements are summarized in Table 6.3. The table indicates that Specimens 6 and 7, which had a strong-column design were considerably stiffer and stronger than Specimens 4 and 5 with a weak-column design which can be expected. However, it is relatively difficult to isolate the influence of each design parameter on the behavior of the specimens. For instance, it is not easy to justify that Specimen 6, which had a weak infill and strong frame, developed minimal masonry crushing compared to Specimen 4, which had a weak infill and weak frame.

Finally, Mehrabi et al. (1994) investigated the effect of the vertical load on the performance of infilled frames under lateral loads. The results indicate that increasing the vertical load increases the strength of the structure, which is expected. Comparing the values for Specimens 11 and 12, shown in Table 6.2, and if a 45^{o} friction angle is assumed, then 90% of the increase in lateral strength can be attributed to the increased vertical force on the infill. In that case, there would not be any considerable increase of the lateral capacity of the columns despite the increase by 82 kN (184 kips) of their total vertical load. This could be could be explained by the fact that the peak shear resistances of the infill and the RC columns do not occur at the same time, indicating that a more complex mechanism develops.

The experimental study of Mehrabi et al. (1994) is helpful as it provides useful information on the influence of a number of parameters on the structural response. Based on this information, the general trends of the effect of the panel's aspect ratio, the distribution of vertical forces, and the reinforcement detailing on the lateral strength can be observed. Nonetheless, it is not possible to quantify the influence of each parameter

due to a number of reasons. These include the variation of the material properties between the tests, the limited amount of configurations considered in the study, but also the fact that in some cases more than one parameter changed between the specimens. Finally, in some cases the RC frames were repaired after a test and retested with a new infill panel as a different specimen. This was done to maximize the test configurations; however, its effect on the test results cannot be determined.

To further investigate the influence of important parameters, a parametric study has been conducted. As shown in Table 6.1, this study has included the aspect ratio of the infill panel, the reinforcing details, and the vertical load applied on the frame. As a baseline model, the validated model used for CU1 Specimen presented in Chapter 5 has been used. In each model, only one of the parameters is varied so that its influence can be identified. The results of this study are discussed in the following sections.

6.3 Effect of Aspect Ratio of Infill Panel

The aspect ratio (h_w/L_w) of the masonry panels of the prototype structure and the CU specimens has been 0.55 which is in between the two values considered by Mehrabi et al. (1994). To investigate the influence of the aspect ratio of the infill panel, two configurations have been considered by changing the length of the frame since it is more likely for frames to have the same height and different lengths of bays than the opposite. Hence, models for the configurations illustrated in Figure 6.1 have been created with aspect ratios of 0.28 for AR-1 and 0.83 for AR-2. The force-vs.-drift relations for these

models are presented in Figure 6.2 together with the analysis for CU1 specimen. As shown in the figure, there are significant differences in the behavior of the specimens in terms of the initial stiffness, lateral strength, and drift at peak lateral force. The longer the masonry wall is, the stiffer and stronger the structure is. Moreover, for lower aspect ratios, the structure reaches its strength at a lower drift. Model AR-1 reached 524 kN (118 kips) of strength at a drift of 0.53%. For model CU1, the peak force was 577 kN (130) at 0.32% drift, while for AR-2, the respective values were 742 kN (167 kips) and 0.12%.

The difference in the strength is depicted in Figure 6.3, which presents the force distribution along three cross sections of the structures at the instant of peak strength. In model AR-1 due to the short length only one diagonal strut develops at an angle close to 45^{o} which is close to the angle of the diagonal of the concrete frame. Due to its dimensions, this frame deforms as shown in Figure 6.4(a). Contrary to the other cases, no shear crack develops near the top of the windward column despite the reduced resistance of the column caused by the increased axial tensile force. The latter is induced by the overturning moment and is higher than in the other structures due to the shorter distance between the columns. The reduced moment arm results in a high compressive force near the bottom of the leeward column which is part of the compressive zone due to bending. The compressive forces in the infill and the leeward column are higher than those in the other two models and increase the shear resistance of the column and the infill, despite the smaller cross sectional area of the latter.

In model AR-2 two struts develop near the columns. These struts are at 45^o and confirm the observation made in Chapter 5, according to which the struts do not develop along the diagonal of the panel as commonly perceived. Instead, if the geometry of the panel allows it, two diagonal struts develop and act against the columns. One strut initiates near the top of the windward column and the other near the bottom of the leeward column and they both develop inside the infill at 45^o. The strength of AR-2 is 742 kN (167 kips) and develops at a very small drift of 0.12% when a shear-sliding crack develops in the infill. At drifts of 0.22 and 0.40% the shear cracks occur at the top of the windward column and the bottom of the leeward column and cause load drops of 100 and 75 kN (22.5 and 17.1 kips) respectively. These cracks, however, do not affect the peak load since a load drop of 160 kN (36 kips) is caused when the crack in the infill develops.

Comparison of the two models with the CU1 model indicates that the behavior of AR-1 is dominated by bending and is significantly different from that of CU1. This can be expected due to the short masonry panel which changes the load transfer mechanism by only allowing the development of one strut in the entire panel. Model AR-2 however, has a similar behavior as CU1 with failure initiating at the same drift due to a similar shear sliding crack in the infill. The difference in the loads of the two models after the significant load drop is 165 kN (37 kips), which is equal to the difference in the cohesive force calculated from the following equation.

$$\Delta V = c d_w \Delta l_w \tag{6.1}$$

in which c is the cohesion coefficient, d_w is the width of the masonry wall, and Δl_w is the difference in the length of the two panels. This resistance due to cohesion gets mobilized when the panels are long enough to allow the development of a sliding shear dominated failure mechanism. In this case, the increased length of the panel affects its shear resistance due to the larger cross-sectional area which increases the resistance related to the cohesive force along the mortar joints.

6.4 Effect of Vertical Load

As indicated in a previous section, the initially applied vertical load can be an important factor in the resistance of infilled RC frames. The vertical load carried by the columns can affect their shear strength due to the interaction of axial and shear capacities (ACI 318 2008). In a masonry wall, the vertical load is directly related to its lateral resistance provided due to friction along the bed joints. In real structures, the vertical load exerted on the masonry wall depends on a number of parameters including the sequence in which the parts of the structure were built, the relative stiffness of the vertical RC members and the masonry walls, and the construction quality and condition of the joints along the interface between the RC beams and the walls. In many existing structures, a gap is introduced in this interface either due to shrinkage and creep of the mortar in the masonry, or due to poor quality construction since filling the top bed joint with mortar is not easily done in an existing RC frame. In this study, the effect of the variation of the externally applied vertical load on the structural performance is considered, with the

assumption of a good bond between the RC frame and the masonry wall. The effect of the relative stiffnesses between the infill panel and the frame has been indirectly addressed through the sensitivity analysis presented in Chapter 3, which considered different combinations of stiffnesses for the constitutive materials.

Five different load levels have been considered in the study presented here. The lower bound is a case with zero vertical load, and the upper bound is a total load of 534 kN (120 kips), which is 57% higher than the load applied in the quasistatic tests presented in Chapter 5. This study only addresses the effect of the increased of the gravity load to the capacity of the frames and not on the seismic demand. The lateral force-vs.-drift relations for the five cases are presented in Figure 6.5, while the force distributions at three cross sections along the height at the instant of peak strength and the deformed meshes at 1% drift are presented in Figures 6.6 and 6.7 respectively.

Figure 6.5 indicates that the increase of the vertical load in increments of 178 kN (40 kips), does not affect the initial stiffness of the structure as all models have more or less the same stiffness. However, the relative sliding between the frame and the wall, which signifies the onset of nonlinear behavior and the change of slope of the force-vs.-drift curves, occurs at different lateral loads due to the different pre-compression of the bed joints by the dissimilar external vertical loads. The force at which the yield point occurs increases in, more or less constant, increments of 77 kN (17.3 kips), as the vertical forces on the wall due to the externally applied vertical load increase in increments of 73.5 kN (16.5 kips). A close to one ratio of additional lateral yield strength to the

corresponding additional vertical forces justifies the assumption that the friction angle in the bed joints is close to 45^{o}.

Beyond the yield point, the lateral force-vs.-drift curves resemble one another in that they have the same peaks and troughs at similar drifts but different load levels. In all cases, there is a drop of lateral strength at around 0.15% drift due to the shear sliding crack in the infill and the loss of cohesion. This is followed by a shear crack or horizontal shear sliding near the top of the windward column which is in tension, and finally a shear crack occurs at the bottom of the leeward column. The only exception is the case of model Ng-1, in which the lack of initial compressive load in the columns results in horizontal sliding as indicated in Figure 6.7. In model Ng-1, the peak load coincides with the instant before the shear failure of the leeward column, while for models Ng-2, Ng-3, and Ng-4, the peak load occurs earlier and coincides with the shear failure near the top of the windward column.

The differences in resistance mechanisms developed in the models with different vertical loads can be explained considering the force distribution in the infill and RC columns at the instant of peak load for each model, which are presented in Figure 6.6. In model Ng-1, although no external load is applied, axial forces develop in the RC columns due to the interaction of the infill panel with the bounding frame. Hence, tensile forces develop at the top of the RC columns and lead to compressive vertical forces in the infill which result in the formation of a diagonal compressive strut resisted by the bottom of the leeward (right) column. A second strut does not develop due to the lack of shear resistance near the top of the windward column caused by the lack of initial compressive

load. Hence the column slides along the beam-column below the beam. In the other three models, the initial compressive load prevents the premature sliding failure at the top of the column. This leads to the development of a second compressive strut in the infill which causes the shear failure of the windward column. It is interesting to observe that the higher initial vertical load increases the shear resistance of the column, which in turn, increases the load carried by the second strut, resulting in a higher lateral strength for the structure. The failure mechanism for the three models is similar, as shown in Figure 6.7. The failure of Ng-1 is only similar in terms of the diagonal crack in the infill since the two columns develop shear sliding failures and the top beam cracks as well despite the excessive amount of longitudinal reinforcement described in Chapter 5. This failure mechanism is not likely to occur in a multistory structure with continuous lines of infill along the height since those exert vertical load on the beam and also prevent its bending due to their in-plane stiffness. However, it could occur in a single story structure with minimal load on the roof.

6.5 Effect of longitudinal reinforcement

The design approach used in the 1920s for the RC frames resulted in a weak RC frames vulnerable to shear failure as discussed in Chapters 4 and 5. Since the failure of the infilled frames is dominated by shear, it would be expected that the variation of the amount of longitudinal reinforcement would not alter the behavior of the frame drastically. The study here considered ratios ranging from 0.5% to 4%, while the

prototype structure had a reinforcement ratio of 1%. The force-vs.-drift curves shown in Figure 6.8 indicate that varying the amount of the reinforcement does not affect the initial stiffness and yield point of the structure, but it affects the peak strength. This behavior can be explained if the failure mechanism is considered. For models Ro-1, Ro-2, and Ro-3 the peak lateral load occurs at the instant before the shear failure of the windward column. As shown in Figure 6.9, the amount of longitudinal reinforcement increases the tensile resistance at the top cross section of the windward column before the shear failure. This allows the development of higher shear forces in the cross section which controls the peak strength of the structure. Hence, the three models have similar failure mechanisms which are shown in Figure 6.10 and resemble the failure pattern of the CU1 specimen discussed in Chapter 5.

The Ro-1 model is the only model that has a different failure mechanism. In this structure, the leeward column fails prematurely at mid-height due to bending as there is not sufficient reinforcement to carry the tensile forces. Hence, at the instant of peak load the leeward column is in compression, but can only carry a limited amount of shear load. The premature failure of the column alters the crack pattern in the infill as there is not enough resistance provided by the column for the development of a diagonal strut which would have led to the shear sliding crack of the infill. Although the 0.5% reinforcement ratio is beyond the lower bound of 1% used in the 1920s in California, it could possible represent structures built in other eras in other parts of the world.

6.6 Effect of Transverse Reinforcement

The effect of transverse reinforcement was studied by conducting two sets of analyses. Initially, for models St-1 through St-4, the area of the shear reinforcement was changed within a range of values with the lower bound being equal to half the area of used in the large-scale specimens discussed in Chapter 5 and the upper bound being four times the area of transverse reinforcement used in the large-scale specimens. The cases examined in this section should be considered together with those in the following section as in both cases the effect of the transverse reinforcement ratio is examined. Changing the spacing would be a more realistic approach to improve the detailing of the RC columns considered here; however, both cases are examined for the completeness of the study.

The lateral force-vs.-drift curves presented in Figure 6.11 indicate that the four models had the same initial behavior including the initial stiffness, yield point, and the load drop due to the opening of the shear sliding crack in the infill. Moreover, as shown in Figures 6.11, models CU1, St-2, St-3, and St-4 reached the same strength we well. This indicates that increasing the amount of transverse reinforcement does not increase the strength of the structure despite the fact that its failure is dominated by shear. The drift at which the peak strength occurs and the post peak behavior are significantly affected by the amount of lateral reinforcement. Hence, increasing the transverse reinforcement increases the ductility drift at which the peak strength occurs and therefore the ductility of the structure.

Figure 6.12 presents the force distributions at the instant of peak load, while Figure 6.13 illustrates the deformed meshes at a lateral drift of 1%. The peak load for models St-2, St-3, and St-4 occurs at the instant before the shear failure near the bottom of the leeward column, while for model St-1 it occurs before the shear sliding crack in the infill. This is depicted in Figure 6.13(a) which shows the highest forces at the top and bottom cross sections on the infill as the columns have not reached their strength. In the other three models similar forces are developed prior to the peak load; however, after the crack in the infill occurs, the additional lateral reinforcement increases the lateral strength by preventing the failure of the columns. Eventually, the leeward column reaches its capacity and fails in shear. Nonetheless, this does not signify a brittle load drop since the lateral reinforcement allows the structure to maintain its resistance. In the windward column, the additional transverse reinforcement prevents the shear failure and the column fails due to bending, which is a preferred failure mechanism.

6.7 Effect of Spacing of Transverse Reinforcement

The influence of transverse reinforcement was also investigated in terms of the distance between the stirrups. This distance was specified to be half of the distance used in CU1 for model Ds-1 and one quarter of that distance for model Ds-2. The results of the analysis are presented in Figures 6.14, 6.15, and 6.16. It is interesting to compare the performance of Ds-1 and Ds-2 to the results of the analysis for models St-2 and St-4 which incorporate the same overall amount of shear reinforcement distributed in a

different way. As expected the behavior is affected in a similar way as the amount of reinforcement increases. Hence, as shown in Figure 6.14, the initial behavior and peak strength of all models are not affected, while the drift at peak strength increases and the load drop is prevented when the amount of shear reinforcement increases. The load distributions and failure mechanisms are almost identical for the pairs with the same total amount of reinforcement. The only difference is the shear crack at the leeward column which has slightly lower strength which reduces the overall strength by 7 kN (1.6 kips). This difference is caused by the orientation of the shear crack which incorporates a horizontal part which reduces the amount of shear reinforcement crossed by the crack. However, the difference is insignificant and can be ignored.

6.8 General Observations

The analysis results presented in the previous sections reveal useful findings on the effect that geometric and design parameters have on the structural performance. This effect is summarized in Table 6.4 with respect to the initial stiffness, peak strength, and failure mechanism. It is interesting to observe that the initial stiffness is only affected by the aspect ratio of the infill wall. Moreover, the strength of an infill is mostly influenced by the aspect ratio and the vertical load, which are the parameters that affect the compressive load applied on the masonry wall, the frictional resistance of which governs the overall resistance. These are important findings which can lead to the development of simplified analytical tools for the assessment of the seismic resistance of infilled frames.

The failure mechanism of the RC columns is affected by a larger number of parameters. Especially the behavior of the windward column may change if any of the parameters considered here is altered, due to either the different axial load or the different detailing of the reinforcement. Hence the shear crack which causes a significant load drop in the case of CU1 can be prevented by an increase of the vertical load, decrease of the distance between the columns or increase of the amount of shear reinforcement. Any of these changes would lead to a bending of the column and a flexural failure mechanism which is more ductile. On the contrary, the behavior of the leeward column does not seem to be drastically affected by the changes introduced in the design, as in all cases this column fails in shear. Although its failure mechanism does not seem to change, its strength can increase if the compressive loads increase, while a more ductile behavior can be obtained if more transverse reinforcement is used.

The study of the failure sequence of the frames presented in this section provides valuable insight regarding the failure sequence of RC frames with solid masonry infills. In most cases considered here, the failure involves a dominant shear-sliding crack in the infill and diagonal shear cracks near the top of the windward column and the bottom of the leeward column. These initiate simultaneously, indicating that at the instant of peak capacity only one of the three components reaches its peak capacity, while the other two components may have not reached their peak strength yet, or might be in the post-peak regime. In both cases though, the load carried by the structures is less than the load corresponding to failure of the three at the same instant. Table 6.5 presents the mechanism that coincides with the peak load for each model. The table indicates that the

distribution is almost even among the failure mechanisms. Hence, adding the strengths of the three components would lead to unrealistic results. Moreover, the table indicates that for half of the models, a second peak occurring before or after the peak load due to the failure of another than the critical component has a load within 5% of the peak capacity.

An additional difficulty in the analysis of these frames is that the capacity of the infill and the columns depends on the vertical force. Therefore, for an accurate estimate, the load distribution would need to be considered. However, the vertical load is continuously re-distributed, while the wall-frame system is at all stages of lateral loading statically indeterminant. Consequently, the vertical loads carried by the three components cannot be accurately estimated which does not allow the calculation of the lateral load carried by each component at every loading step. This complex behavior is addressed in a following section through a simplified approach which allows the conservative estimate of the strength, based on the behavior of the infill.

6.9 Two-Bay Infilled Frames

The parametric study presented here was expanded to two-bay frames since this is an essential step to bridge the gap between the single-bay structures, which are commonly studied by researchers, and the multi-bay configurations, which are typically found in actual structures. The geometry and design details of a two-bay model can be assumed to result from the placement of two single-bay frames next to each other, with the resultant frame having three columns and two masonry walls. It is more difficult

however, to decide on the vertical load to be used for such a model. The cases considered here include model DB-1, which includes the same load as the single-bay specimens (338 kN or 76 kips), DB-2, which includes double the amount of that load, and DB-3, which includes a load of 597 kN (134 kips), which is the load corresponding to the prototype structure. DB-1 is considered only to facilitate the comparison with the single-bay specimens by only introducing the geometrical change. DB-2 represents an upper bound for the vertical force on the two-bay structure considering its almost double length, although the corresponding tributary area only increases by 50%. DB-3 incorporates the scaled load applied in the first-story columns and walls of the prototype structure.

Figure 6.17 presents the lateral force-vs.-drift curves of the models considered. For comparison the curve of the CU1 model is included as well as a curve equal to double the curve of CU1. The latter would be a rough way to estimate the behavior of the two-bay structure if that of the single-bay structure is known. The results indicate that the shape of the force-vs.-drift curve is the same in all cases considered due to the same more or less initial stiffness and drift at which the load drops. The structures yield at drifts lower than 0.1% when the crack between the infill and the frame develops, and they maintain the load until a drift of 0.3% at which the shear cracks develop in the columns. The peak load is affected by the vertical load as in the case of the single-bay models. It is interesting to note that model DB-2 and DB-3 reach higher strength than the consideration of two single-bay models would yield.

The force distribution at three cross sections at the instant before of peak load which occurs before the crack in the infills is shown in Figure 6.17. At this stage, the

infills of models DB-2 and DB-3 carry increased amounts of vertical load compared to the infill of the CU1 model shown in Figure 6.3 as there are two columns resisting the tensile forces. The increased vertical loads lead to increased lateral strength due to the frictional resistance along the mortar joints and an increased overall strength. Hence, the fact that the two-bay models have less one column less than the two CU1 models does not seem to affect their strength, and adding the capacities of adjacent frames can yield total capacity close to the strength of the two-bay frame. The failure patterns of the models, shown in Figure 6.19, strongly resemble the failure patterns of the single-bay models. Models DB-1 and DB-3 have essentially the same failure pattern with shear cracks in the three columns, a diagonal crack in the left panel, and a horizontal crack in the right panel. DB-2 model has a different mechanism triggered by the additional vertical load which prevents the shear failure of the windward column.

6.10 Simplified Backbone Curve for Infilled RC Frames

Based on the findings of the parametric study, a method to derive a simplified lateral force-vs.-drift behavior has been developed. The constructed curve is not a very accurate representation of the actual behavior and cannot provide the amount of information on the structural performance that a detailed finite element analysis can provide. However, it is a quick and simple way to conservatively estimate the basic features of the structural behavior in six steps. The skeleton of the curve which is similar

to that included in ASCE 41-04 and FEMA reports is presented in Figure 6.20. The curve is validated with experimental and analytical findings in Chapter 10.

Step 1: Initial Stiffness, K_{ini}

The initial stiffness of an uncracked infilled frame can be calculated with the consideration of a shear beam model with the following expression proposed by used by Fiorato et al. (1970).

$$K_{ini} = \frac{1}{\frac{1}{K_{fl}} + \frac{1}{K_{shl}}} \tag{6.1}$$

in which K_{fl} and K_{sh} represent the flexural and shear stiffness of an uncracked cantilever wall. With this approach, the structure is assumed to be a composite beam with the RC columns being the flanges and the masonry wall the web of the beam. Hence, for the flexural stiffness, K_{fl}, the equivalent properties of the composite beam should be considered, although for the shear stiffness only the contribution of the wall can be considered. The flexural stiffness can be calculated from the following expression.

$$K_{fl} = \frac{3E_c I_{ce}}{h_b^3} \tag{6.2}$$

in which h_b is the height of the composite wall measured from the top of the foundation to the mid-height of the RC beam, E_c is the modulus of elasticity of concrete, and I_{ce} is the moment of inertia of the transformed section with the masonry wall section replaced

by an equivalent concrete section. Hence, I_{ce} depends on the ratio of elastic moduli of concrete and masonry and geometry of the cross-section. Alternatively, the modulus of elasticity of masonry can be used in Equation 6.2, if the composite cross section is transformed to an equivalent masonry cross section. Assuming that the shear stress is uniform across the wall, the shear stiffness can be calculated from the following formula.

$$K_{sh} = \frac{A_w G_w}{h_w} \tag{6.3}$$

in which A_w, G_w, and h_w are the cross-sectional area, shear modulus and height of the infill wall. Masonry is not a homogeneous isotropic material. However, its effective shear modulus can be either measured or calculated from empirical formulas. For instance, it can be assumed that $G_w = 0.4E_w$ (MSJC 2008), in which E_w is the effective modulus of elasticity of the masonry wall, which is in term estimated from the compressive strength of masonry prisms.

Step 2: Yield strength, V_y

In the cases examined in the previous sections, the yield point which is defined as the point at which there is a distinct reduction in stiffness in the force-vs.-drift curve more or less coincides with the initiation of separation and sliding between the infill and the RC frame. The drift and force at which the separation occurs depend on the bond quality and cohesion between the two, as well as the vertical force. The frame-infill is a statically indeterminant system and the distribution of vertical forces changes as the structure

deforms. However, this study indicates that the yield force is in all cases between 65 and 80% of the peak force, $V_{\max}$, as shown by the force-vs.-displacement curves in Figures 6.2, 6.5, 6.8, 6.11, 6.14. Hence, a conservative estimate would be to calculate the yield force according to the following expression.

$$V_y = \frac{2}{3} V_{\max} \tag{6.4}$$

Step 3: Peak strength, $V_{\max}$

The majority of the frames considered in this parametric study reached their peak strength at the instant before the shear sliding cracks developed in the infill, or prior to the shear failure of one of the columns, as shown in Table 6.5. Knowing the failure mechanism *a priori* can help determine the strength of the structure. However, without conducting an experiment or a finite element analysis, there is no reliable tool able to predict the actual failure mechanism or strength. Moreover, even if the mechanism could be predicted, the distribution of vertical forces between the RC columns and the masonry wall remains unknown as the vertical forces change along the height of the wall and columns. Therefore, a precise calculation of the peak load with a simple model is not possible. However, the peak strength of an infilled frame can be estimated based on a number of simplification assumptions.

In the method proposed here, the load on the critical cross sections of the columns is considered. These are the top cross section of the windward column and bottom cross section of the leeward column. The externally applied vertical load can be distributed on

the columns and the masonry wall proportionally to their vertical stiffnesses. The lateral force carried by the infill can be estimated as the summation of the cohesive and frictional resistances of the mortar joints. The former can be estimated by the cohesion coefficient and the cross-sectional area of the wall, while the latter can be estimated by considering the initially applied vertical load on the infill and a friction coefficient of one. An accurate solution would include a fraction of the resistance of the column, which can be estimated based on the formulas provided by ACI 318. In this case, the lateral capacity of the infilled frame can be estimated with the following expression.

Single-bay: $$V_{\max} = \psi\left(V_{lc} + V_{rc}\right) + c_o A_w + \mu P_w \tag{6.5}$$

Multi-bay: $$V_{\max} = \psi\left(\sum V_{ic}\right) + c_o A_w + \mu P_w \tag{6.6}$$

in which V_{lc} and V_{rc} are the shear forces carried by the columns, c_o is the cohesion strength of the mortar joints, A_w is the cross-sectional area of the infill, μ is the friction coefficient which is equal to one for a friction angle of 45^o, P_w is the portion of the externally gravity load which is carried by the infill, and ψ is a reduction factor with $0 \le \psi \le 1$. For a conservative estimate of the strength given the uncertainty of the actual behavior, it is suggested ψ be zero. In this case, the capacity of the frame would be equal to the shear strength of the infill wall. This is not an unreasonable assumption since the failure of the infill in many cases defines the peak strength.

The proposed method utilizes the findings of the parametric study summarized in Table 6.4. According to the results of the study, the strength is affected by the aspect ratio and the vertical load, which are both accounted for in Equations 6.5 and 6.6. Moreover, the analyses of the frames with additional amount of shear reinforcement in the columns indicate that the strength does not change noticeably with the increase of shear reinforcement.

In the calculation of the strength, it has been assumed that the infill is strong enough to resist the compressive loads of the inclined struts and cause the failure of the mortar joints. This is the case for the multi-wythe solid brick infill walls considered here. However, there are cases of weak infill which may fail due to compression. Hence, it is important to check whether the infill would fail due to compressive loads at lateral drifts close to the peak load. This can be done by assuming two diagonal struts carrying the lateral force through the infill. Hence, the force can be distributed in two diagonal struts along 45^{o} angles which initiate near the top of the windward column and the bottom of the leeward column. The compressive stress can be calculated with the assumption that the strut force is resisted by one third of each column as shown in Figure 6.21. In reality, the width of the strut varies along its length but it is narrower close to the columns as shown in Figures 6.3, 6.6, 6.9, 6.12, and 6.15 with the force distributions. The narrower strut close to the columns is also verified by the corner crushing of the masonry in cases of weak infills reported by previous researchers (e.g. Mehrabi 1994).

Step 4: Drift at peak strength, $\delta_{V_{\max}}$

The drift at peak strength cannot be easily calculated with a simplified approach as it depends on a number of parameters, including the interaction between the frame and the infill. This value can be obtained based on Table 7-9 of ASCE 41-06 (2007), which accounts for the aspect ratio of the infill panel and the ratio of its shear strength with respect to the shear strength of the RC columns. As observed in the figures with the force distributions this ratio is lower than 0.7 in all cases examined here at the instant of peak strength. The table accurately predicts the drift at peak strength for the FE model representing Specimen CU1 which is discussed in Chapter 5 and has its peak strength at a drift ratio of 0.32%. However, for models AR-1 and AR-2 the values of the table are not accurate. To further investigate the relation between the value of drift, $\delta_{V_{\max}}$, at peak strength and the aspect ratio, four additional models were created by varying the length of the masonry wall. The lateral force-vs.-lateral drift curves of the models are presented in Figure 6.22. These curves confirm the findings presented earlier for the influence of the aspect ratio of the wall to the structural behavior. Based on these results, the following approximate relation between the aspect ratio, AR_w, and $\delta_{V_{\max}}$ has been derived for a ratio of the shear force carried by the frame to the shear force carried by the infill lower than 0.7.

$$\text{for } AR_w < 2.15: \qquad \delta_{V_{\max}} = 0.75 - \frac{1}{3} AR_w \tag{6.7}$$

for $AR_w \geq 2.15$: $\delta_{V_{\max}} = 0.15$ (6.8)

The relation is compared with the numerical results and the predictions of ASCE 41-06 in Figure 6.23. It should be pointed out that for low aspect ratios the frames exhibit a ductile behavior due to bending with no major load drop. Hence, the relation can be capped for aspect ratios lower than 0.5 with a $\delta_{V_{\max}}$ value of 0.7%. Further investigation may be needed to clarify the performance of frames with lower aspect ratios. However, such cases are not common and do not present practical interest.

Step 5: Residual strength , V_{res}

The residual strength of the structure assuming the opening of dominant shear cracks in the infill and the RC columns can be calculated as the summation of the residual strength of the infill due to friction along the bed joints and the residual shear resistance of the columns after the development of dominant shear cracks in the RC columns. In this case only the shear reinforcement crossed by a diagonal shear crack should be considered.

Single-bay: $V_{res} = 2V_{c,res} + V_{w,res}$ (6.9)

Multi-bay: $V_{res} = \sum V_{c,res} + V_{w,res}$ (6.10)

in which $V_{c,res}$ is the residual shear strength of a column and $V_{w,res}$ is the residual shear strength of the masonry panel(s).

The residual strength of an RC column can be assumed to be equal to the force provided by the transverse reinforcement crossed by a shear crack. For a more conservative approach this strength can be assumed zero since the stirrups sometimes fracture at large drifts after the development of shear cracks. For the infill, only its frictional resistance should be considered. The vertical load applied on the infill assumed to be equal to the externally applied vertical load since the vertical load carrying capacity of a column reduces drastically after the development of a dominant shear crack. In most of the analyses this load is higher than the externally applied load since the leeward column could not carry any load in compression after failing in shear, while the windward column is in tension to resist the overturning moment.

Step 6: Drift at which the residual strength is reached, $\delta_{V_{res}}$

The drift at which the residual strength is reached depends on the convention used to define the residual strength of the structure since in many cases a sudden load drop is followed by mild declining slopes. A conservative approach would be to assume a brittle load drop from the peak load to the residual strength by specifying a drift slightly larger than the drift at peak load. Based on the performance of the frames presented in Figures 6.2, 6.5, 6.8, 6.11, and 6.14, a 40% increase is proposed.

6.11 Validation of Simplified Backbone Curve

The simplified curve proposed in the previous section has been validated with the experimental data from the small-scale and large-scale specimens presented in Chapter 5. Figure 6.24 presents the comparison between the experimentally obtained curves and the curves developed with the proposed approach. In both cases, the simplified curve matches reasonably well the finite element model and the experimental results. The relatively small deviation observed around the peak load on the conservative side as the simplified prediction underestimates the strength. In terms of the residual strength, this has been calculated based on a residual friction coefficient of 0.8 and on the residual strength of the RC columns provided by the transverse reinforcement crossing an assumed shear crack on each column. Although shear cracks in the columns were not observed in the small-scale specimen, the same failure mechanism has been assumed for this frame for consistency. Finally, assuming the strut geometry proposed in the previous section, in both cases the compressive stress along the assumed diagonal struts is around 2.8 MPa (0.4 ksi), which is only a fraction of the compressive strength of masonry prisms presented in Table 5.1.

6.12 Conclusions

A parametric study considering the effect of the geometry, externally applied vertical load, and reinforcement details on the performance of RC frames with solid infill

walls has been conducted with the validated finite element model. The results of the study indicate that the most influential parameter is the aspect ratio of the panel which can change the behavior of the structure drastically. The externally applied vertical load is also influential; however it does not affect the initial stiffness and its effect on the failure mechanism is only evident when its value dropped to zero, which is an extreme case. The longitudinal reinforcement has limited effect on the structural behavior, while the amount of transverse reinforcement can affect the ductility but not the strength of the structure. The study has also considered two-bay infilled frames which exhibit similar failure mechanisms as the single-bay structures. In terms of the lateral load-vs.-drift relations, the results from the single-bay models can be used for the estimation of the resistance of two-bay structures. Finally, the results from the parametric study have been used to develop a simple procedure for the construction of a lateral force-vs.-drift curve. The simplified approach does not capture the failure mechanisms in detail, but provides a quick way to obtain the basic properties of the structural performance of infilled frames. The proposed simplified approach has been validated with the test results from the infilled frames with solid panels discussed in Chapter 5. The comparison indicates that the results of this method are very encouraging as it successfully captures the important features of the lateral force-vs.-drift response.

Tables of Chapter 6

Table 6.1: Overview of the models considered.

	Model	Vertical load kN (kips)	Infill aspect ratio (L_w/h_w) -	Column longitudinal reinforcement ratio (ρ_v) %	Column stirrup spacing cm (in.)	Column stirrup area mm^2 (in^2)
	CU1	338 (76)	0.55	1	29.2 (11.5)	95 (0.15)
Vertical load	Ng-1	0	0.55	1	29.2 (11.5)	95 (0.15)
	Ng-2	178 (40)	0.55	1	29.2 (11.5)	95 (0.15)
	Ng-3	356 (80)	0.55	1	29.2 (11.5)	95 (0.15)
	Ng-4	534 (120)	0.55	1	29.2 (11.5)	95 (0.15)
Aspect ratio	AR-1	338 (76)	1.10	1	29.2 (11.5)	95 (0.15)
	AR-2	338 (76)	0.36	1	29.2 (11.5)	95 (0.15)
ρ_v	Ro-1	338 (76)	0.55	0.5	29.2 (11.5)	95 (0.15)
	Ro-2	338 (76)	0.55	2	29.2 (11.5)	95 (0.15)
	Ro-3	338 (76)	0.55	3	29.2 (11.5)	95 (0.15)
	Ro-4	338 (76)	0.55	4	29.2 (11.5)	95 (0.15)
Stirrup area	St-1	338 (76)	0.55	1	29.2 (11.5)	48 (0.07)
	St-2	338 (76)	0.55	1	29.2 (11.5)	190 (0.29)
	St-3	338 (76)	0.55	1	29.2 (11.5)	285 (0.44)
	St-4	338 (76)	0.55	1	29.2 (11.5)	380 (0.59)
Stirrup spacing	Ds-1	338 (76)	0.55	1	14.6 (5.75)	95 (0.15)
	Ds-2	338 (76)	0.55	1	7.3 (2.875)	95 (0.15)

Table 6.2: Summary of selected tests conducted by Mehrabi et al. (1994) to investigate the effect of the aspect ratio.

Specimen #	*h/L*	Infill	E_c GPa (ksi)	E_m GPa (ksi)	$V_{lc}+V_{rc}$ kN (kips)	V_w kN (kips)	Frame Stiffness kN/mm (kips/in.)	Frame Strength kN (kips)
4	0.67	Weak	17.2 (2500)	4.6 (667)	228 (51.3)	65 (14.7)	75.3 (430)	162 (36.5)
5	0.67	Strong	17.9 (2600)	8.9 (1298)	115 (25.9)	179 (40.1)	224 (1280)	267 (60.0)
10	0.48	Weak	20.1 (2920)	3.9 (572)	228 (51.2)	66 (14.8)	70.1 (400)	189 (42.6)
11	0.48	strong	18.1 (2630)	9.6 (1393)	90 (20.2)	204 (45.8)	257 (1470)	293 (65.8)
12*	0.48	strong	20.1 (2920)	7.3 (1064)	172 (38.6)	269 (60.4)	342 (1950)	363 (81.5)

* the vertical load applied on this specimen was increased from 294 to 440 kN (66 to 99 kips)

Table 6.3: Summary of selected tests conducted by Mehrabi et al. (1994) to investigate the effect of different design considerations for the RC columns.

Specimen #	Infill	Column Dimensions mm x mm (in. x in.)	Longitudinal Reinforcement Ratio %	Area of Stirrups mm^2 ($in.^2$)	Spacing of Stirrups mm (in.)	Frame Stiffness kN/mm (kips/in)	Frame Strength kN (kips)
4	Weak	178x178 (7x7)	3.2%	322 (0.5)	65 (2.5)	75.3 (430)	162 (36.5)
5	Strong					224 (1280)	267 (60.0)
6	Weak	203x203 (8x8)	3.8%	322 (0.5)	38 (1.5)*	84.1 (480)	207 (46.6)
7	Strong					255 (1460)	445 (100)

* at the critical zones near the top and bottom of the columns

Table 6.4: Effect of design parameters on the response of RC frames with solid panels.

Parameter	Initial Stiffness	Strength	Failure Mechanism		
			Infill	Windward Column	Leeward Column
Aspect Ratio	Significant	Significant	No effect	Significant	No effect
Vertical load	No effect	Significant	No effect	Some effect	Minor effect
Ratio of Longitudinal Reinforcement	No effect	No effect	Some effect	Some effect	No effect
Area of Transverse Reinforcement	No effect	No effect	No effect	Significant	No effect
Spacing of Transverse	No effect	No effect	No effect	Significant	Minor effect

Table 6.5: Failing component immediately after the instance of peak lateral capacity.

Cause of load drop after peak load	Model
Crack in Infill	AR-2, Ng-1, Ng-2, Ro-1, **St-1***
Shear Crack in Windward Column	**CU1**, AR-1, **Ng-3**, Ng-4, Ng-5, **Ro-2**, Ro-3, Ro-4,
Shear Crack in Leeward Column	**St-2**, **St-3**, **St4**, **Ds-1**, **Ds-2**

* the bold characters denote the models that have a second peak at a load within 5% of the peak lateral capacity

Figures of Chapter 6

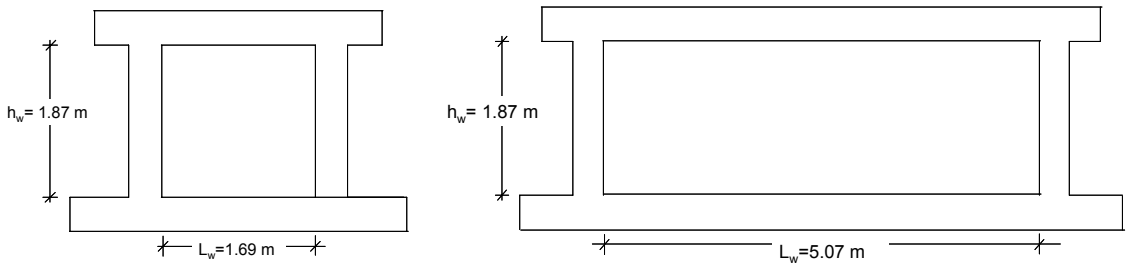

(a) AR-1 ($L_w^{AR-1} = 0.5L_w^{CU1}$) (b) AR-2 ($L_w^{AR-2} = 1.5L_w^{CU1}$)

Figure 6.1: Configurations for panels with different aspect ratios.

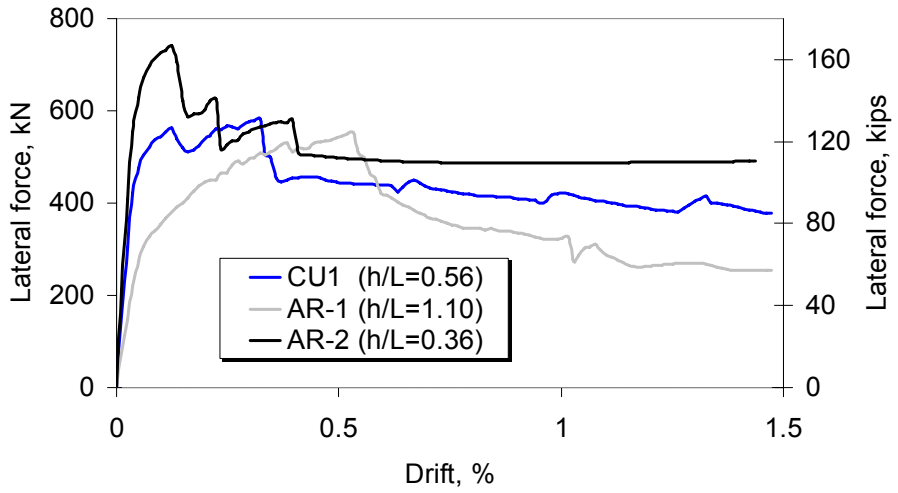

Figure 6.2: Analytical and experimental force-vs.-drift curves for frames with different aspect ratios.

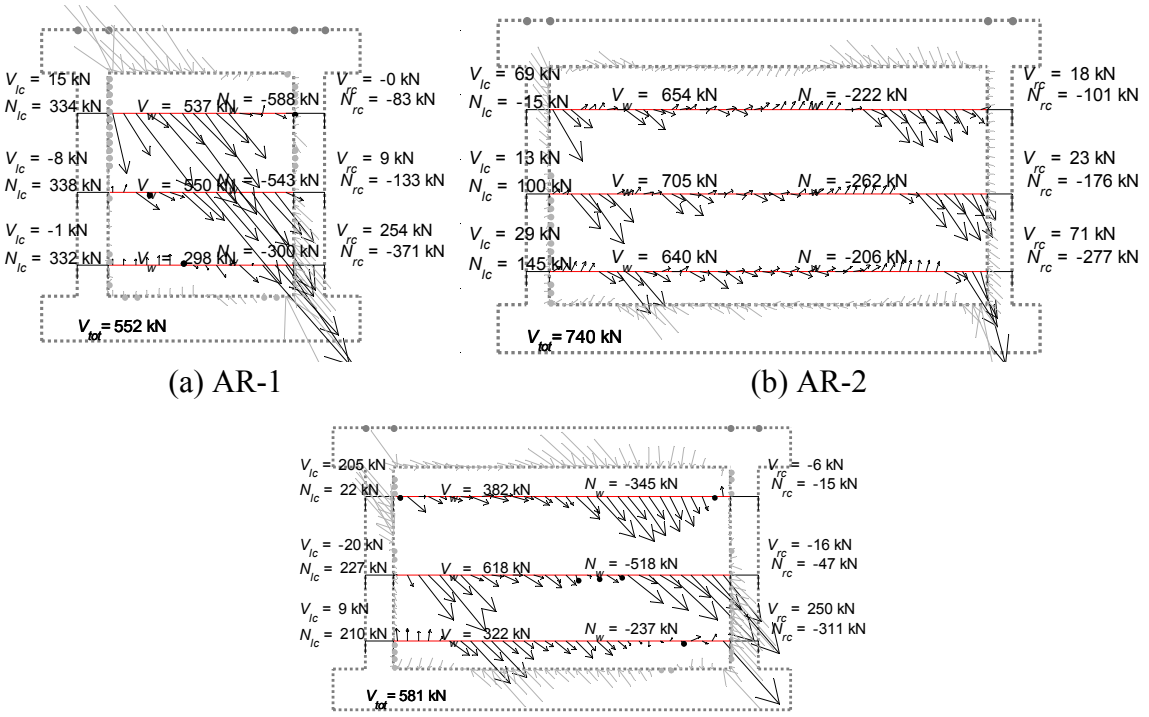

(a) AR-1 (b) AR-2

(c) CU1

Figure 6.3: Force distribution along three cross sections at the instant of peak strength for frames with different aspect ratios.

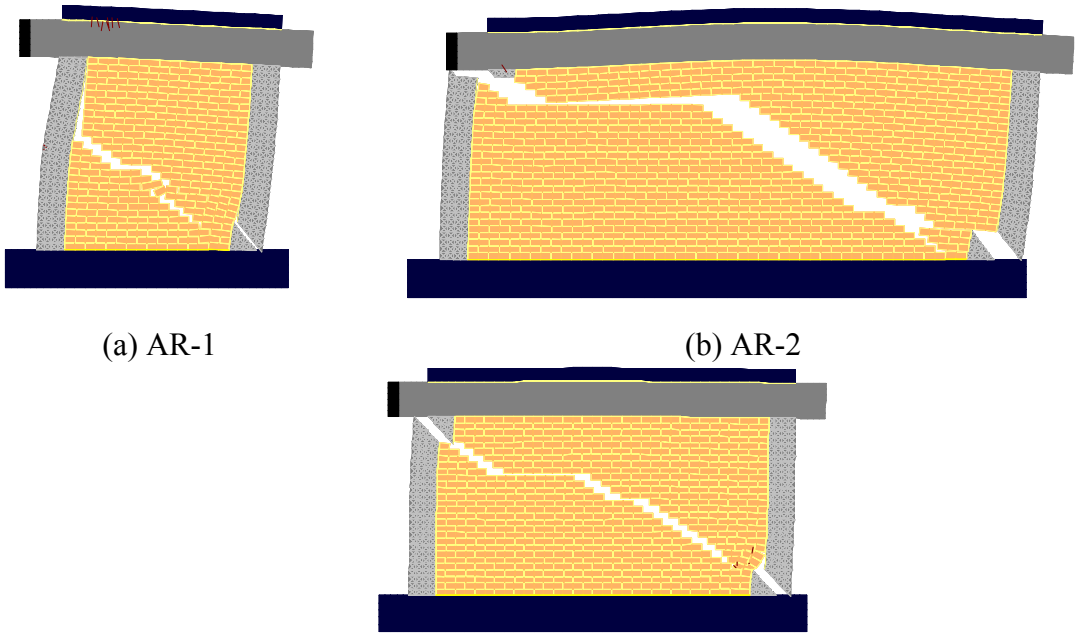

(a) AR-1 (b) AR-2

(c) CU1

Figure 6.4: Cracking patterns at 1.00% drift for frames with different aspect ratios.

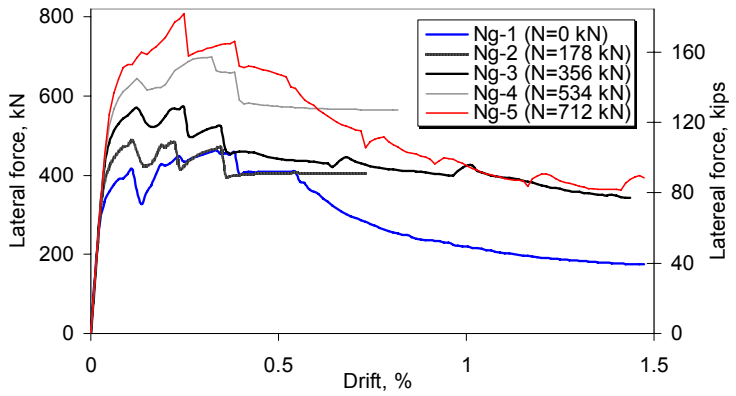

Figure 6.5: Analytical and experimental lateral force-vs.-drift curves for frames with different gravity loads.

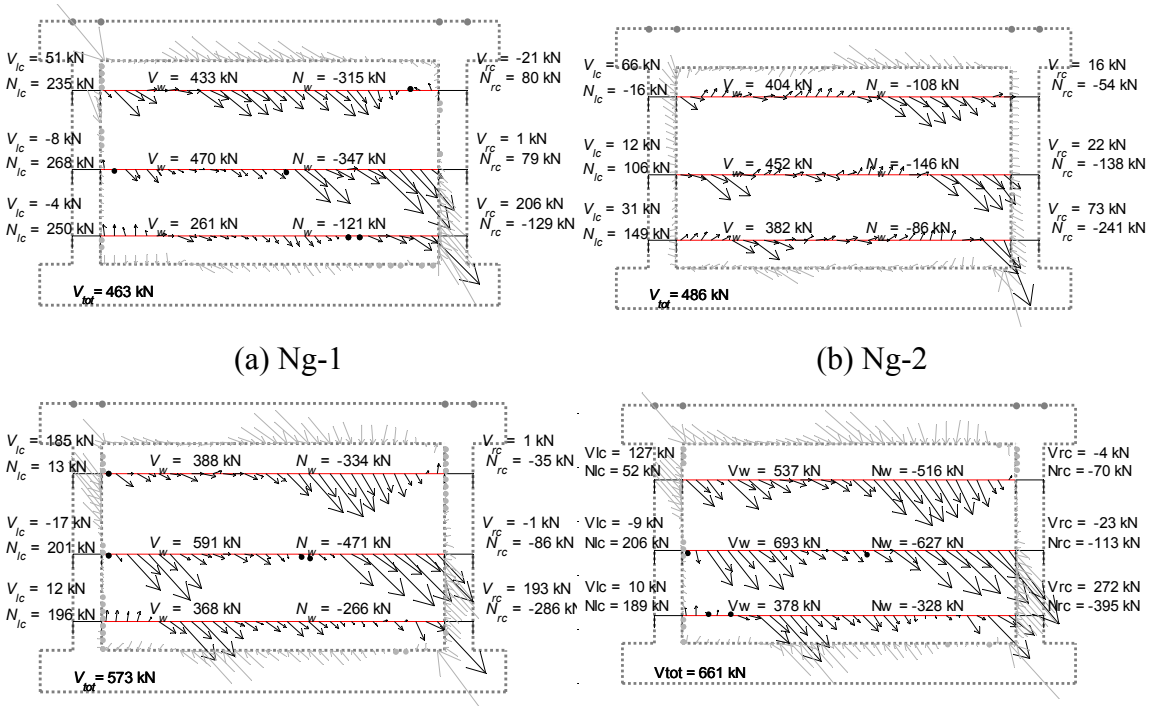

Figure 6.6: Force distribution along three cross sections at the instant of peak strength for frames with different gravity loads.

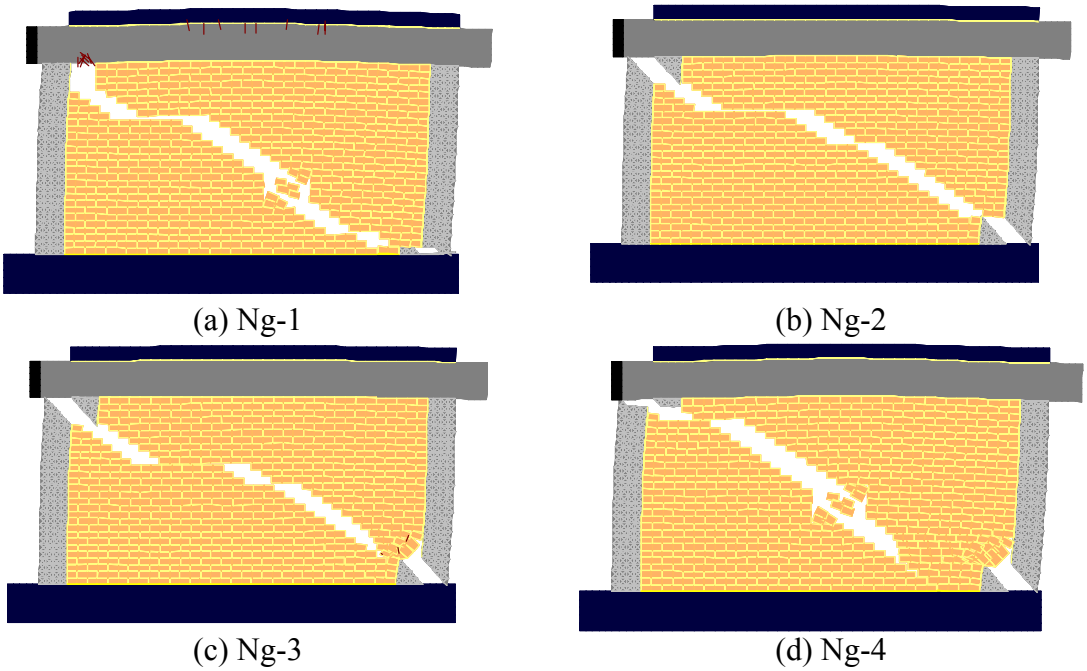

(a) Ng-1 (b) Ng-2

(c) Ng-3 (d) Ng-4

Figure 6.7: Cracking patterns at 1.00% drift for frames with different gravity loads.

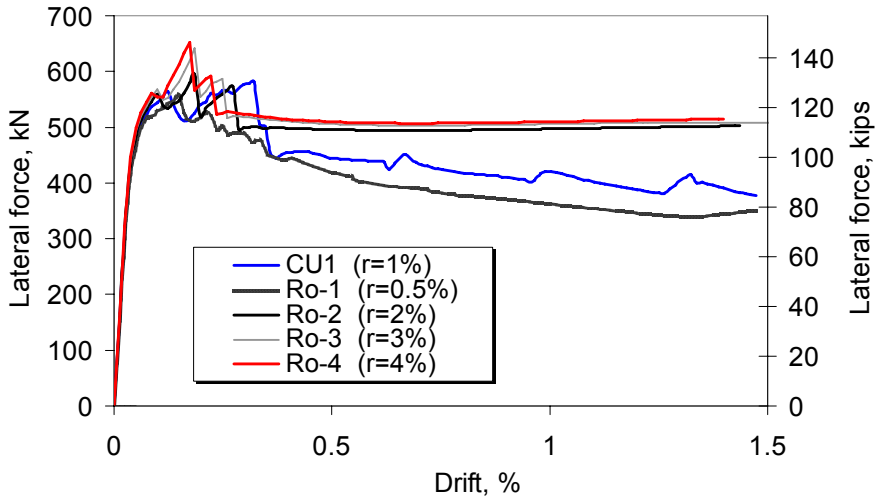

Figure 6.8: Analytical and experimental force-vs.-drift curves for frames with different ratios of longitudinal reinforcement.

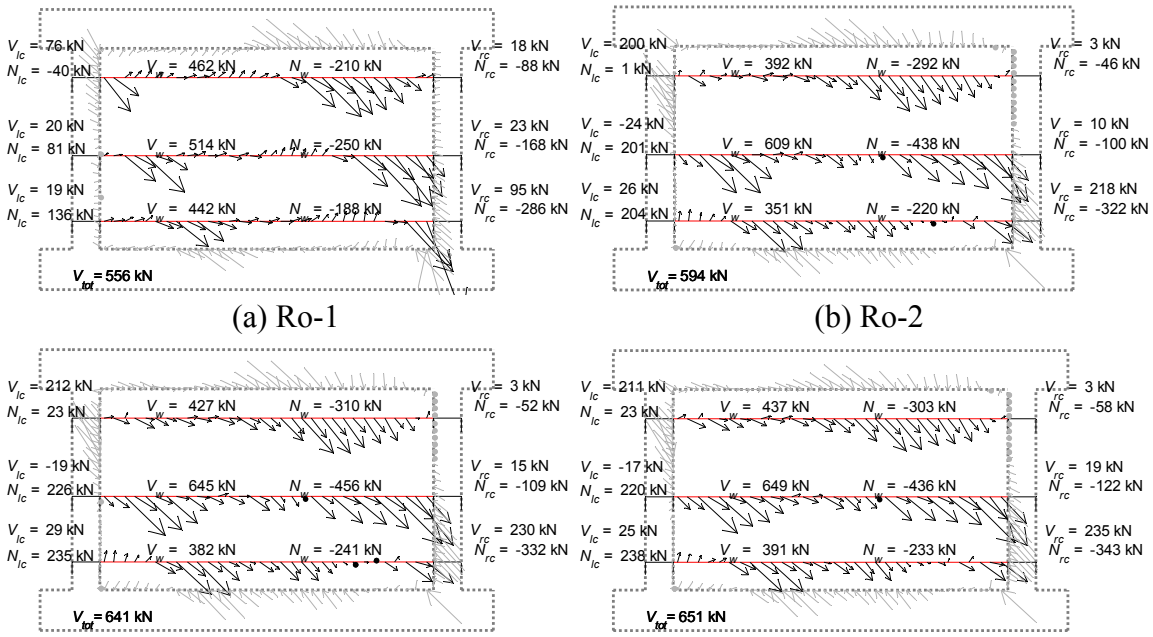

Figure 6.9: Force distribution along three cross sections at the instant of peak strength for frames with different ratios of longitudinal reinforcement.

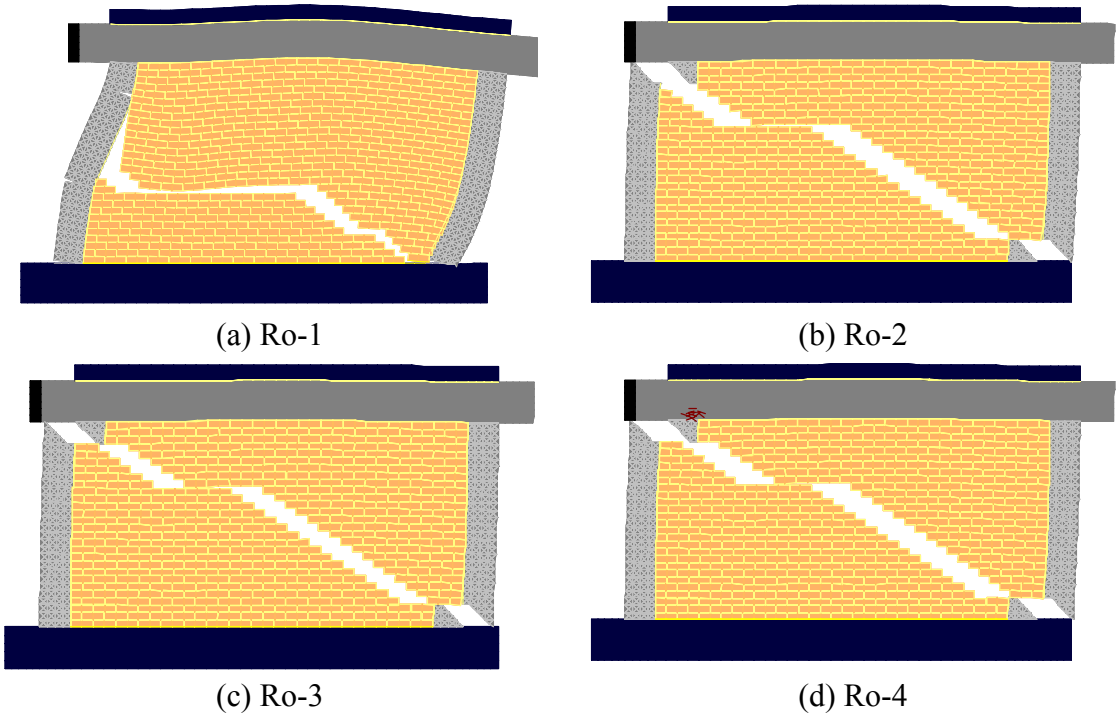

Figure 6.10: Cracking patterns at 1.00% drift for frames with different ratios of longitudinal reinforcement.

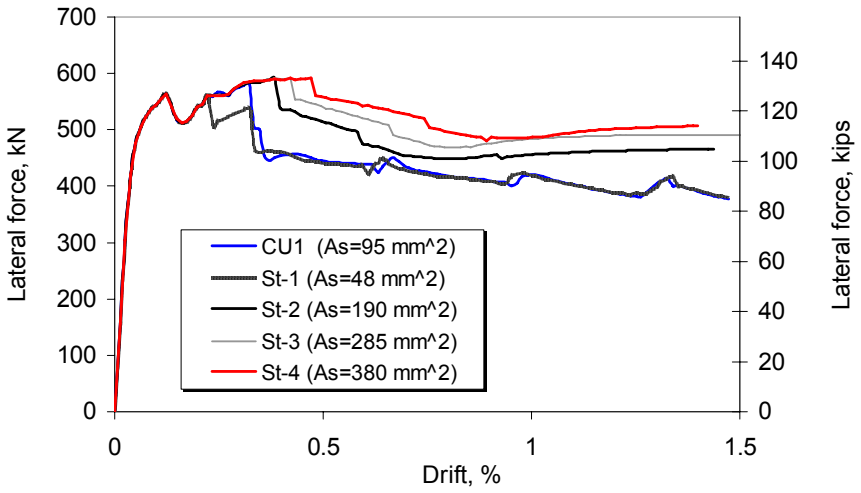

Figure 6.11: Analytical and experimental force-vs.-drift curves for frames with different amounts of transverse reinforcement.

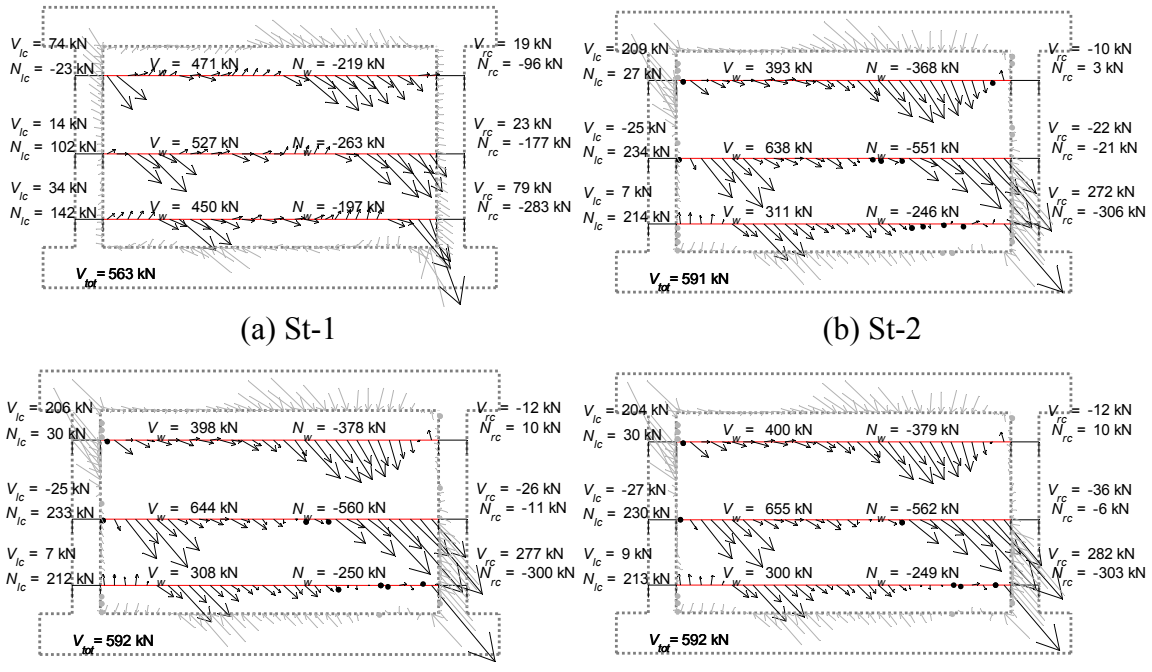

(a) St-1 (b) St-2

(c) St-3 (c) St-4

Figure 6.12: Force distribution along three cross sections at the instant of peak strength for frames with different amounts of transverse reinforcement.

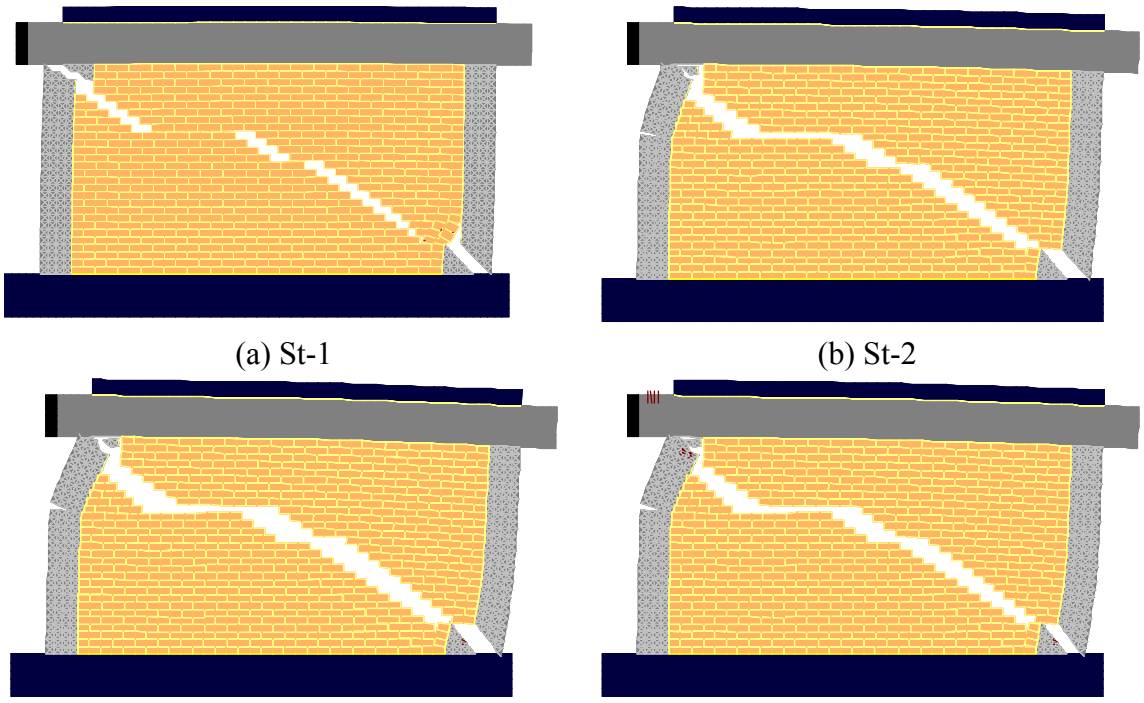

(a) St-1 (b) St-2

(d) St-3 (e) St-4

Figure 6.13: Cracking patterns at 1.00% drift for frames with different amounts of transverse reinforcement.

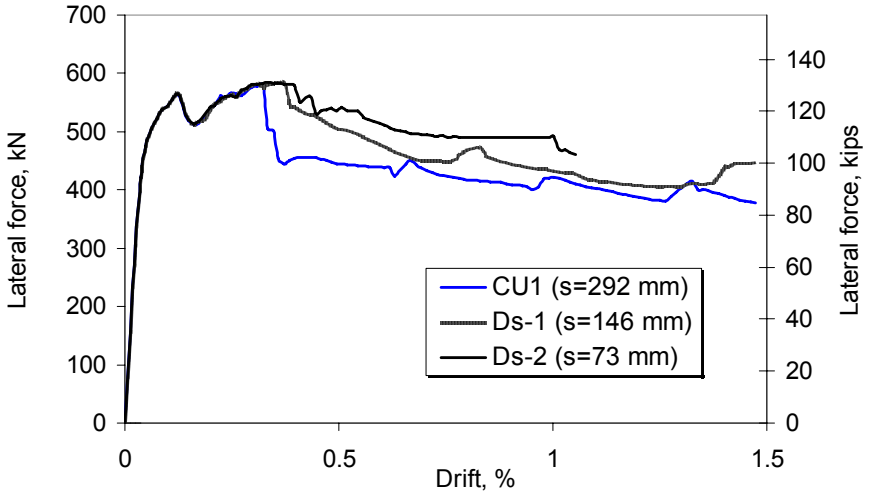

Figure 6.14: Analytical and experimental force-vs.-drift curves for frames with different spacing of transverse reinforcement.

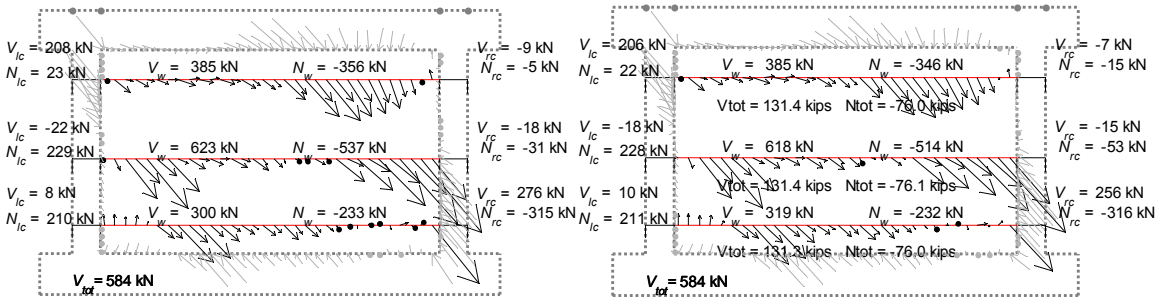

(a) Ds-1 (b) Ds-2

Figure 6.15: Force distribution along three cross sections at the instant of peak strength for frames with different spacing of transverse reinforcement.

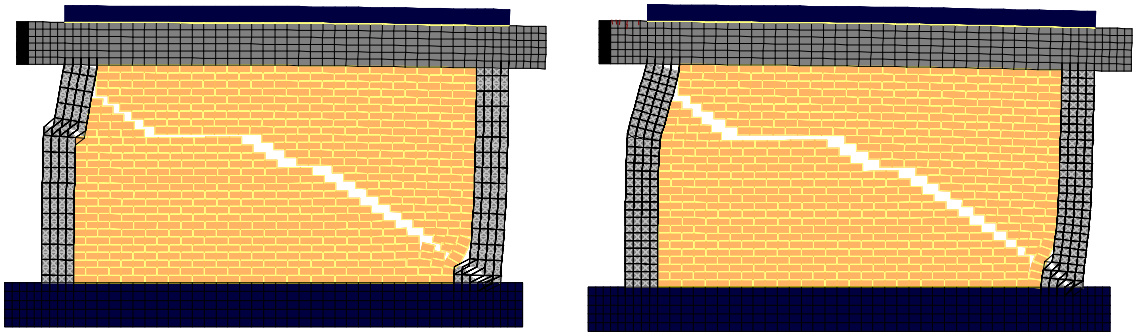

(a) Ds-1 (b) Ds-2

Figure 6.16: Cracking patterns at 1.00% drift for frames with different spacing of transverse reinforcement.

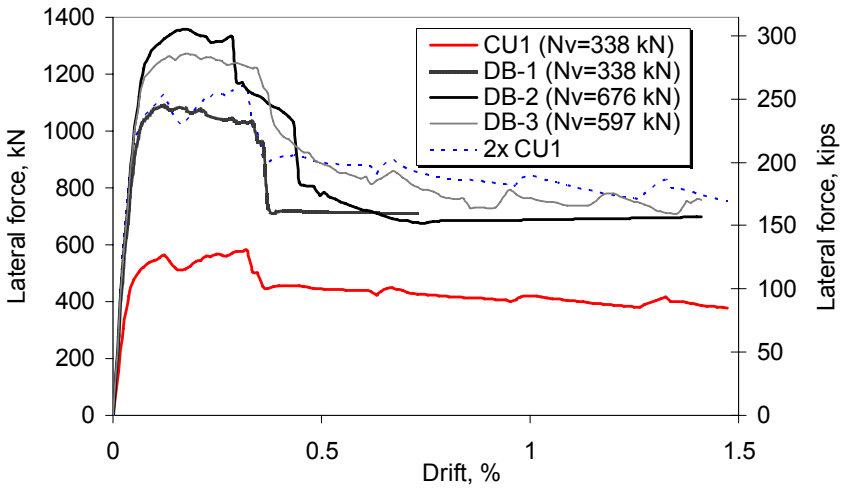

Figure 6.17: Analytical and experimental force-vs.-drift curves for two-bay frames with different vertical load.

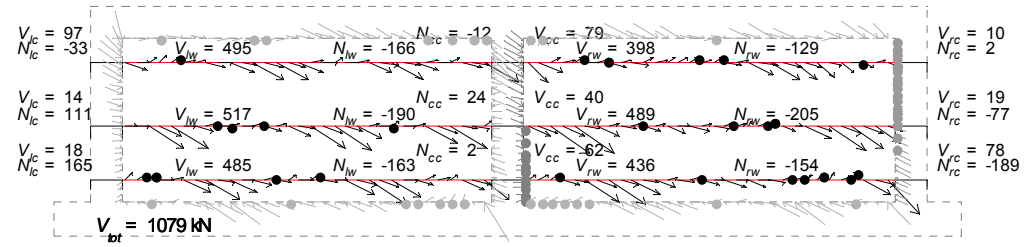

(a) DB-1

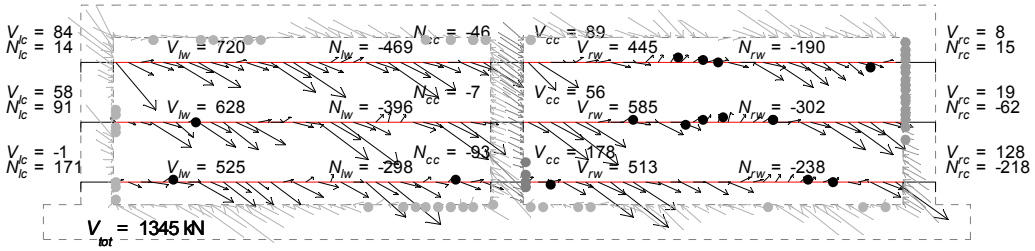

(b) DB-2

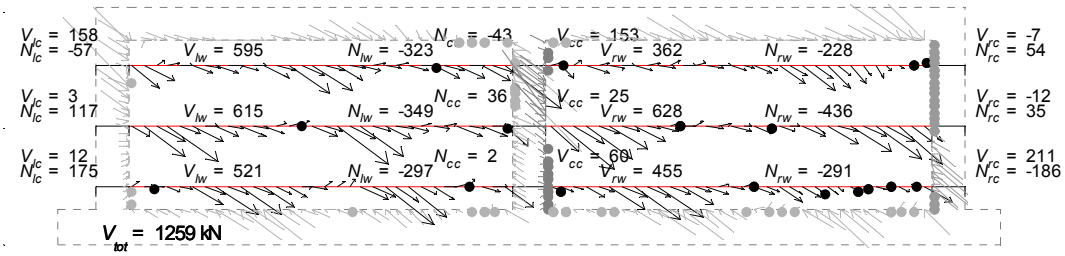

(c) DB-3

Figure 6.18: Force distribution along three cross sections at the instant of the peak strength for two-bay frames with different vertical load.

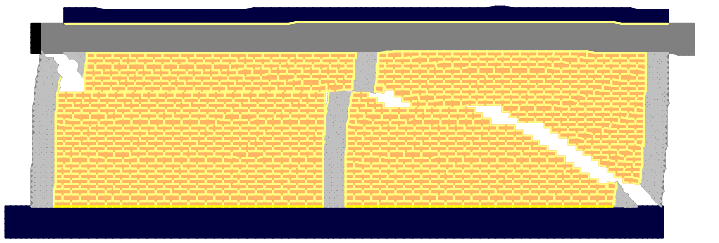

(a) DB-1

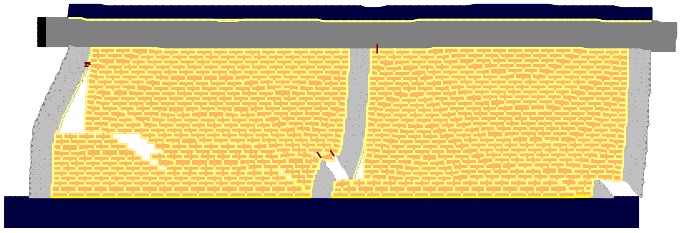

(b) DB-2

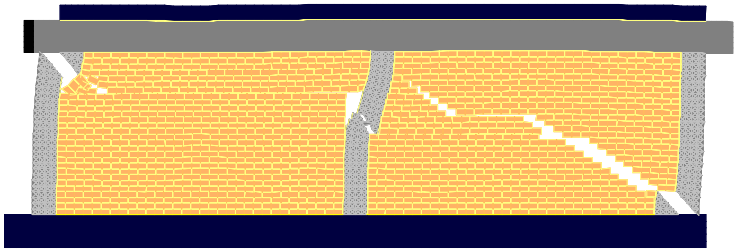

(c) DB-3

Figure 6.19: Cracking patterns at 1.00% drift for two-bay frames with different vertical load.

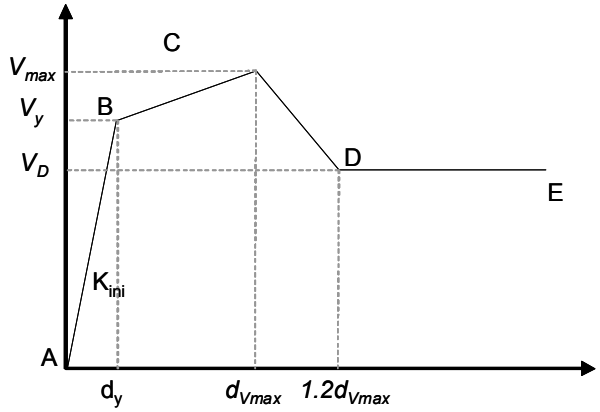

Figure 6.20: Proposed simplified force-vs.-drift curves for RC frames with solid panels.

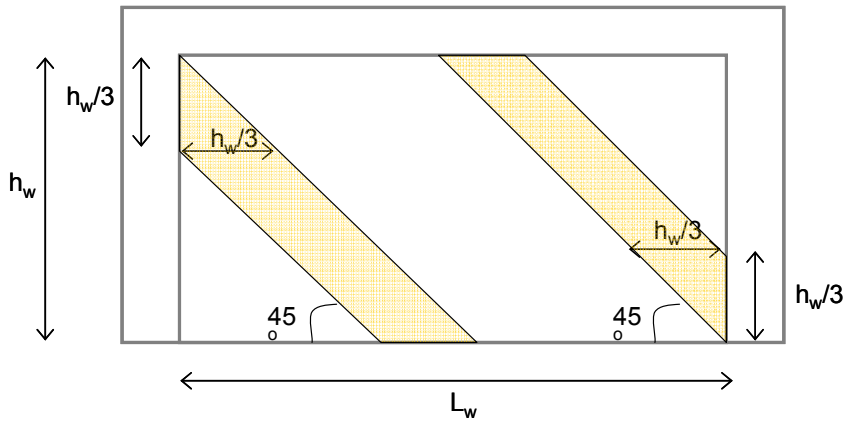

Figure 6.21: Development and geometry of compressive struts in frames with solid infills.

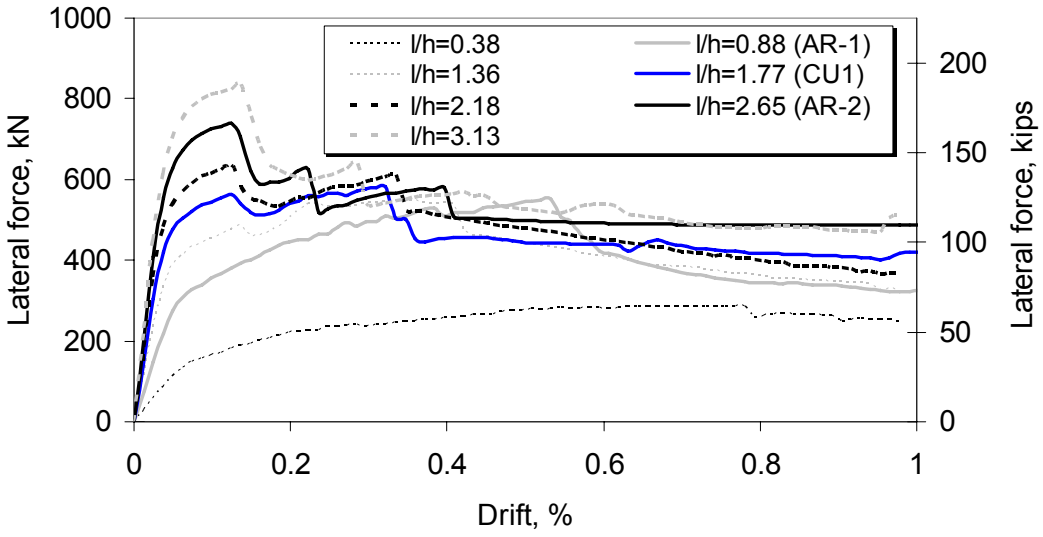

Figure 6.22: Lateral force-vs.-drift response of frames with different aspect ratios.

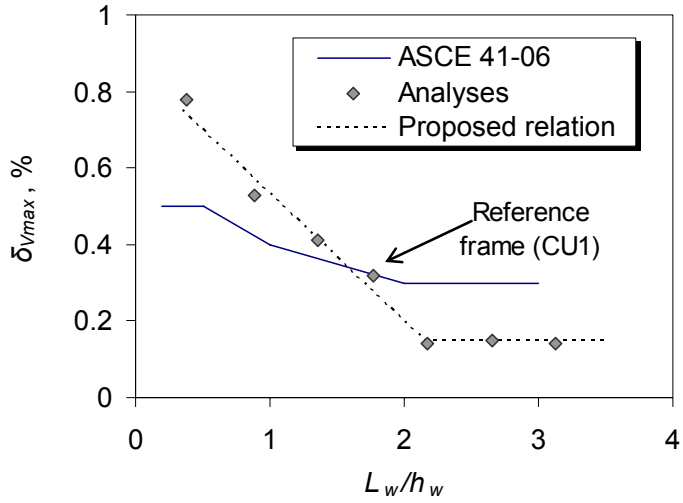

Figure 6.23: Drift at peak load with respect to the aspect ratio of the infill panel.

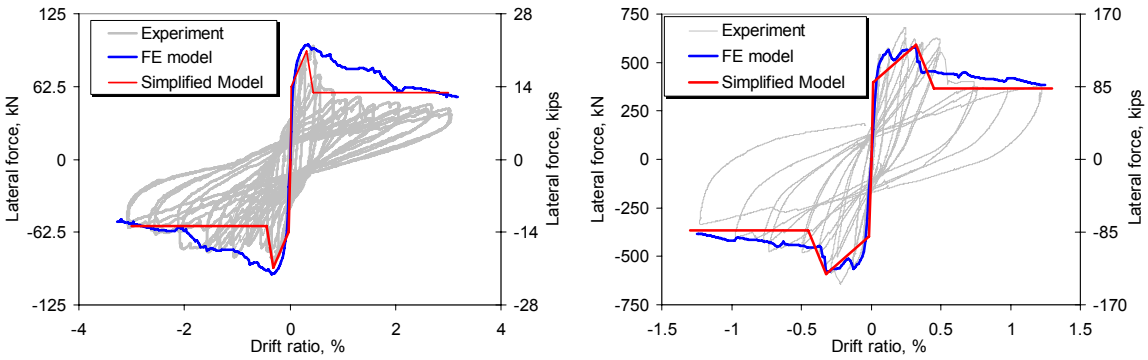

(a) small-scale specimen (b) CU1

Figure 6.24: Comparison of simplified curves with experimental results.

CHAPTER 7

PARAMETRIC STUDY ON THE EFFECT OF OPENINGS

7.1 Introduction

Chapter 5 provided valuable insight on the behavior of infilled RC frames with windows and doors. However, the tests and analyses have not been conclusive as to the exact mechanism of how the openings affect the structural performance. Moreover, the structures considered in Chapter 5 cannot represent the variety of possible opening configurations in terms of size and location. Therefore, further investigation is necessary. A parametric study has been conducted to address this issue. The study considers masonry infilled RC frames with five different opening geometries: four different window sizes and a door. Furthermore, the asymmetric responses of the frames with eccentric openings studied in Chapter 5 indicate that the location of the opening is crucial for the load transfer mechanism that may develop. To address this issue, the study presented in this chapter considers five different locations for each of the opening configurations. The results indicate the size of an opening affects the initial stages of the structural performance. However, when the behavior becomes nonlinear the location of the opening becomes critical for the determination of the failure mechanism. Based on the results of the parametric study, a simplified approach to account for the openings is developed via the construction of a force-vs.-drift curve.

7.2 Background

Although the seismic performance of masonry-infilled RC frames has been investigated in a number of studies, most of these studies (e.g., Mehrabi et al. 1994; Fardis et al. 1999; Al-Chaar et al. 2003; Hashemi and Mosalam 2006, Centeno et al. 2008) have focused on the effect of solid infill panels. One of the few available studies which incorporate openings has been conducted by Kakaletsis and Karayannis (2009). They examined the influence of different opening configurations on the structural performance of eight single-story, one-bay, 1/3-scale RC frames. The infills included a window or a door of three different sizes located concentrically or eccentrically. The frames were designed with current building standards used in Greece, which are similar to Eurocodes 2 and 8. Hence, the reinforcing details were more appropriate for lateral loads compared to the prototype structure considered in this study. Another difference between the two investigations is the fact that they used weak masonry, which consisted of hollow clay tiles. The behavior of a strong frame-weak infill system, can be drastically different than a weak frame-strong infill system (Mehrabi et al. 1994).

The test results indicate that the infill increased the strength and stiffness of the specimens compared to the bare frame. However, for openings of the same shape and location, their size did not considerably affect the behavior of the infilled frames. Although the considerable scaling of the specimens and the reduced number of mortar joints may have altered the failure patterns compared to the full-scale structure, this finding is in agreement with the study presented in Chapter 5. Hence, the study with the

ductile frame design and the weak infills also contradicts the analysis methods (Al-Chaar 2002) which relate the strut area, and therefore the capacity of the masonry wall, to the opening area only.

7.3 Overview of the Parametric Study

To address the issue of how the openings affect the behavior of masonry-infilled frames with openings in a systematic way, a parametric study has been conducted and it is presented in the following sections. The study uses the nonlinear finite element models that have been validated with the experimental results presented in Chapters 3 and 5 to examine the influence of the opening size but also its location within the masonry wall on the structural performance. For consistency, the frame design presented in Figure 5.5 is used in all the analyses presented here. Moreover, to eliminate the differences between the models considered, the material properties from Specimen CU1 have been used in all models. This was the most complete material testing sequence (Citto 2008), and, as indicated in Table 5.1, the properties obtained are closer to the design values specified in Chapter 4 and the material properties obtained from the small-scale specimen.

Five different opening sizes have been considered in this study. They include four different window configurations and a door similar to the one examined in Chapter 5. The different window sizes have been defined by altering the width of the window. The heights of the window and the masonry panels above and below it have been kept constant because they correspond to typical values that are not likely to vary drastically in real structures. The same assumption was made for the door dimensions, since a

significant variation of its height and width is not common. The opening sizes and locations are summarized in Figure 7.1 and Tables 7.1 to 7.5. The first part of the nomenclature of each model indicates the opening size: SW stands for a small window with a full-scale width of 91.4 cm (36 in.), RW stands for a regular window and it has the same dimensions as in Specimen CU2, LW stands for a large window with a width of 182.8 cm (72 in.), and xLW stands for an extra large window with the same dimensions as in Specimen CU6. The models with a door are identified with D and have the same door dimensions as CU5. For every opening size, five different locations in the infill frame have been examined. These include a concentrically placed opening which is symmetric for the two directions of loading, and four eccentric locations which can be grouped in two pairs, which are noted as X and XR, where X is the model number. Since the analysis is monotonic, each pair is essentially the same structure loaded laterally from the two opposite directions with XR representing the loading direction in which the longer masonry pier is on the windward side. To facilitate the comparison of the deformed meshes and the load distributions, all analyses are presented with the load applied on the left side of the specimen.

The different opening locations have been defined according to the distance between the side of the opening and the edge of the closest column. This length is essentially equivalent to the length of the shorter masonry pier. This method of defining the locations was preferred over the distance of the openings centerline from the columns which was adopted in the design of the large-scale specimens tested in CU based on the findings of the finite element analysis of these specimens. The results indicated that the width of the piers between the opening and the column determine the level of the

diagonal compressive forces that can develop in the infill. Therefore, the pier widths influence the load-transfer mechanism and, eventually, affect the maximum resistance and the failure pattern of the structure.

7.4 Infill with Small Windows

The force-vs.-drift curves for the models with a small window are presented in Figure 7.2 together with the analysis for the solid panel. As shown in the figure, all models have similar initial stiffness, up to a force level of 400 kN (90 kips). At this point, the first cracks develop at the interface elements simulating the panel-frame mortar joints. As a result the stiffness of each structure changes beyond this point, which can be considered as a yield point for the infilled frames. The models with a small window have a similar secondary stiffness and reach similar values of strength, in the range of 7 to 13% less than the frame with solid panel. However, the drifts at peak strength and the post-peak behaviors are significantly different for the five models. Figure 7.3 presents the forces applied on the infill from the frame and also the force distributions along three cross sections at the instant of peak lateral load for each frame, while Figure 7.4 shows the deformed meshes at 1.00% drift. These are not the final crack patterns, as in some cases additional shear cracks developed in the columns at larger drifts. However, the cracks developing beyond 1.00% drift can be practically ignored as the structural strength has already dropped to 60% of the peak load at this drift.

Although the peak loads carried by the five frames do not vary considerably, the force distributions are quite different. For models SW-1 and SW-1R, the opening is very

close to one of the columns and it does not allow the development of the diagonal compressive strut from the windward column of model SW-1 and the leeward column of model SW-1. Instead, the force transfer mechanism incorporates a third strut which did not develop in the cases examined in Chapter 5. The development of this strut in the long pier next to the window is facilitated by the small window size and its proximity to the column. As a result, the shear forces in the critical location of the column adjacent to the window remain relatively low, and shear cracks do not develop as shown in Figure 7.4 (a) and (b). It is also interesting to note that the window affects the vertical force distribution as well. In SW-1R, both the axial and shear forces at the bottom cross section of the leeward column are drastically lower than the forces developed at the same cross section when the window is located away from the column. Similar findings can be obtained for the force distribution when the window is located 0.61 m (24 in.) from one of the two columns, as shown in Figure 7.3 (c) and (d) for models SW-2 and SW-2R. The failure patterns shown in Figure 7.4 (c) and (d), indicate that shear cracks develop in the columns, although the columns deform considerably more compared to the frame with a solid panel due to the existence of two parallel cracks in the infill which lead to knee-brace mechanisms in the columns. The additional damage and deformation is induced by the window and causes a more brittle behavior and the reduction of the residual value.

When the window is located in the middle, it does not affect the load transfer mechanism since the inclined struts can develop in a similar fashion as in the solid panel. Consequently, the peak load is reduced only 7% compared to the solid panel and the failure pattern includes shear cracks in the critical column locations: the top of the windward column and the bottom of the leeward column as shown in Figure 7.4 (e).

However, due to the existence of the opening, parallel cracks develop in the masonry piers and accelerate the strength degradation.

7.5 Infill with Regular Windows

The results from the analyses of the models with a regular size window are presented in Figures 7.5, 7.6 and 7.7, in terms of the force-vs.-drift curves, the force distributions at peak load and the deformed meshes at 1.00% lateral drift. Similarly to the frames with small windows, the initial stiffness and yield point of the structures are very close for the five structures with a regular size window. However, the peak load, as well as the corresponding drift and post-peak behavior vary noticeably. The strength values are scattered between 460 and 556 kN (103 and 125 kips). The corresponding drifts also vary with a lower bound being 0.12% and an upper bound at 0.49%. These differences in the behavior can be noted in Figure 7.5 and are caused by the different locations of the window. The window location is the only difference between the models. In the force distribution plots of Figure 7.6, one can see how the different window locations can affect the load transfer mechanism which determines the peak load and failure mechanism. The development of three compressive struts is evident for the models with the regular size window when the latter is close to either column.

In cases RW-1R and RW-2R where the window is close to the leeward column, the direction of the forces in the masonry on the short pier is almost vertical and consequently the shear force carried by the column is low. As a result, these models demonstrate relatively low lateral strength. The failure pattern of these frames is close to

the crack pattern of Specimen CU2 which developed a horizontal crack in the longer (left) pier that led to a shear crack at the mid-height of the left column, as shown in Figure 7.7 (b) and (d). The models RW-1 and RW-2, which have the window close to the windward column developed a knee-braced mechanism due to the resistance provided by the masonry wall below the window. In these cases, the shear forces in the mid-height of the windward (left) column are of the same magnitude as the forces at the top cross section. This indicates the shift of the compression strut downwards due to the small width of the masonry pier between the column and the window.

When the window is located in the center of the frame, the peak force is very close to the strength of the frame with a solid panel and the frame with a concentrically built small window. Actually, the overall behavior including the force-vs.-drift curve, the cracking pattern and the force distribution of this model is closer to the case of a smaller window located in the middle of the wall, than a regular size window located eccentrically. This indicates that the location on an opening can be more important in determining the structural behavior, than its size.

.

7.6 Infill with Large Windows

The force-vs.-drift curves, the force distributions at peak load, and the deformed meshes at 1.00% for the models with a large window are presented in Figures 7.8, 7.9 and 7.10. It is interesting to note that the increase of the window size mainly affects the structural behavior and reduces the peak strength when the opening is close to either column. For the frame with a large window in the middle, the peak load reaches 99% of

the strength of the solid wall. On the contrary, the peak load carried by frames LW-1 and LW-1R is around 80% of the strength of the frame with solid infill.

As in the cases with smaller windows, when the window is close to one of the columns, the strut in the short pier is not as effective. The difference introduced by the large window is that, as shown in Figure 7.9, a third strut cannot develop for this opening size. Models LW-2 and LW-2R reach higher strength compared to LW-1 and LW-1R because two compressive struts develop and distribute the lateral load in the masonry wall. The failure patterns of these frames, as well as the frame with the window in the middle resemble that of the solid panel in that diagonal shear cracks develop in the infill and propagate into the columns causing the shear failure of the columns and a brittle loss of strength. On the contrary, the frames with the window closer to the columns have a lower maximum resistance, since the shear failure of the windward column occurs early due to the reduced compressive load caused by the overturning moment.

7.7 Infill with Extra Large Windows

The dimensions of the extra large window are the same as in Specimen CU6. The results of the analyses for the five different locations of the frame are presented in Figures 7.11, 7.12, and 7.13 in terms of the load displacement curves, the force distributions at the instant of peak strength and the cracking patterns at 1.00% drift. The trends observed in the case of the large window are also observed when the panels incorporate an extra large window. Therefore, all frames appear to ‘yield’ when a lateral load of 350 kN (85.5 kips) is reached. The yield point is followed by a secondary slope

that is similar for the five frames. However, the peak strength reached and the corresponding drift are significantly different for each frame due to the different failure mechanisms that develop.

When the window is located in the middle, the frame reaches a load close to the strength of the solid panel and this load does not drop until 0.7% drift, while the strength reduction exceeds 25% if the window is located close to the columns. In that case, the maximum load is observed early, at a drift of just 0.18%. The force distributions shown in Figure 7.12 indicate that when the shorter masonry pier has a length of 0.30 m (12 in) the lateral forces it can carry are very low. However, for frame xLW-1 a wide compressive strut develops in the longer pier as seen in Figure 7.12(a) due to the resistance of the leeward column which requires a high force required to fail in shear. It is also interesting to point out that the forces developing in the infill and between the infill and the beam are not always inclined as one would expect. This is due to the rotation of parts of the masonry wall after the dominant cracks have developed. Similar behavior was observed in the large-scale specimens tested in CU and is shown in Figure 7.13 for the frames with the large window.

7.8 Infill with Doors

The door dimensions considered here are the same as in Specimen CU5. Figures 7.14, 7.15, and 7.16 present the force-vs.-drift curves, the force distributions along three cross sections when the peak strength is reached, and the deformed meshes at 1.00% drift respectively. The variation in terms of maximum strength is significant for the different

locations since for models D-m and D-2, the peak strength is within 3% of the strength of the frame with the solid panel. However, as the door location shifts closer to the leeward column (right) the reduction in strength exceeds 20%. This is due to the reduced length of the masonry pier next to the column which limits the width and changes the location and orientation of the compressive strut. As the strut shifts towards the upper right corner of the infill panel, it increases the lateral force transferred to the mid-height section of the leeward column, while significantly reducing the shear force at the bottom section of the column. The latter force reduces from 262 and 260 kN (58.9 and 58.5 kips) for models D-1 and D-2 to 60 and 98 kN (13.5 and 22.1 kips) for models D-1R and D-2R. The consequences of the force distribution are depicted in the corresponding failure modes presented in Figure 7.16. When the door is close to the windward column, the high shear forces developing at the bottom section of the leeward column cause it to fail in shear, while significant bending without any shear cracks occurs in this column when the door is close to it, as shown for cases D-1R and D-2R.

It is very interesting to note that in all models with a door, no shear crack develops at the windward column. This is in agreement with the test observations for Specimen CU6 as discussed in Chapter 5. The reason is the reduced confinement of the masonry panel between the windward column and the door. The lack of resistance due to the door allows the slide and bending of the wall. Hence, it provides flexibility which limits the diagonal forces that develop in the wall and prevents the shear failure at the top of the windward column.

7.9 Simplified Force-vs.-drift Curves

The analyses presented in this chapter indicate that the location of an opening inside a masonry panel can considerably affect its structural performance under cyclic loads. To facilitate the comparison of the different models, simplified backbone curves have been created to represent the force-vs.-drift data obtained from each analysis. Although an effort was made to use the backbone adopted in ASCE 41-06 (ASCE 2006) for infilled frames, it was not possible to obtain a reasonable representation for all cases.

Due to the variability of responses, two variations of this curve were also considered. Hence three backbone curves, shown in Figure 7.17, have been considered in this study. Types A and B are penta-linear curves, while Type B-1 occurs when points D and E coincide. The difference between Types A and B is the slope of the third segment which affects the point of maximum lateral strength. In all cases, point B can be considered as the yielding point at which debonding occurs between the RC frame and the masonry panel. Therefore, the structure can be considered to be elastic up to this drift and the slope of segment A-B corresponds to its initial stiffness. The strength increases beyond this point until point C when cracking or sliding occurs in the infill. The behavior beyond point C distinguishes the three curves of Figure 7.17. In Type A, the slope of this segment is positive, thus, the maximum strength develops at point D. This case indicates a more ductile response up to that point, followed by a significant loss of strength, typically caused by the shear failure of the columns. In Type B, the peak load is observed in point C as the strength degradation initiates at that point due to the flexibility and severe bending of one of the columns; more commonly the leeward column. The

degradation is initially not as severe; however, it becomes steep beyond point D, when one of the columns fails in shear. Type B-1 occurs when the third segment is eliminated. This behavior occurs when both columns deform laterally without a shear failure or when one or both columns fail due to shear at the early deformation stages. In the first case the maximum load is noticeably lower than the load of the solid panel, and the post peak slope is very mild. In the second case the peak load is higher and it is followed by a steep decline of the strength with respect to the imposed lateral drift.

The behavior of each frame has been represented with one of the three curves. Table 7.6 summarizes the behavior of the model with solid wall for which a Type A curve is suitable for infilled frames with openings. Table 7.7, identifies which type of curve best fits the performance of each frame. The table also includes information on the decrease of the maximum strength compared to the model with a solid wall. Type B-1 is suitable for more than half of the frames analyzed, while Type A is used for 20% of the frames and the rest are matched with Type B. Tables 7.8 to 7.12 present the information needed to summarize the behavior of each frame based on the simplified representation with the force-vs.-drift relations of Figure 7.17. In the table, K_{ini}, K_2, and K_{res} stand for the initial stiffness along segment AB, the secondary stiffness along segment BC and the stiffness defining the residual strength beyond point E. Parameters V_y, δ_y are the shear force and drift at the yield point B, $V_{\max}$, $\delta_{V_{\max}}$ indicate the shear strength and the corresponding drift, and V_E, δ_E are the force and drift quantities after the major load drop at point E. Finally, $V_{\delta=1\%}$ is the shear force at 1.00% drift and it can provide an indication of the residual strength since at this drift all frames have experienced

significant damage and have lost more than 30% of their peak strength. It should be noted that the maximum drift of a structure in a seismic event would need to consider the out-of-plane component of the motion which has been ignored in this study. The out-of-plane loads are not important initially due to the arching action of the wall within the bounding frame. One cannot rely on the arching action, however, after the in-plane loads have severely cracked the masonry wall (Angel 1994).

The data from the analysis of the frame with the solid infill is summarized in Table 7.5. This information is used to calculate the values in Table 7.13 which presents the average performance of the frames with the same opening size with respect to the model with the solid masonry panel.

7.10 Effect of Size of the Opening

The analysis results presented in the previous section indicate that the openings with the same size can lead to very different failure patterns and peak loads. However, the information presented in Tables 7.8 through 7.12 points out that frames with the same opening size have similar response to the lateral loads initially. The initial part of the response includes the elastic and secondary stiffness, i.e. K_{ini} and K_2, as well as the yield point which is defined by the yield strength, V_y, and the corresponding drift, δ_y. In terms of the simplified curves shown in Figure 7.17, the common behavior includes the first line-segment and the slope of the second segment. Point C and the behavior thereafter are not consistent for the frames with same size openings.

In further detail, one can note in Table 7.13 that the initial stiffness changes significantly for the different opening sizes. However, for a given opening size the deviation is insignificant as the stiffness is in all cases within ±5% of the respective average value. This level of consistency is also demonstrated for the coordinates of the yield point 'B'. The yield strength V_y and the corresponding drift, δ_y, at which the masonry wall separates from the RC frame and, vary for the different opening sizes. However, they are not affected by the different opening locations. In fact, the values of the yield strength are also within 6% of the average value for each opening size. Finally, the secondary stiffness appears to be another characteristic only affected by the opening size and shape. This stiffness value is relatively constant for frames incorporating opening of the same dimensions as it is in most cases within 8% of the corresponding average value. The largest deviation from the respective average values occurs for model SW-2R and it is equal to ±17%.

It is interesting to point out that the ratio between the initial stiffness of each frame with opening and the stiffness of the solid infill is very close to the expression:

$$\frac{K_{ini}}{K_{ini}^{solid}} = 1 - \alpha_i R_A \tag{7.1}$$

in which $R_A = A_{op} / A_{Wtot}$ is the ratio of the opening area, A_{op}, with respect to the area of the solid panel, A_{Wtot}, and α_i is a factor depending on the opening shape. This equation has been verified by the finite element models with $\alpha_w = 2$ for infilled frames with windows of difference sizes and for $\alpha_d = 1.6$ for infilled frames with a door. For the models with a window, the reduction in stiffness is plotted with respect to their size and

location in Figure 7.18. The dotted lines indicate the estimated reduction in stiffness according to Equation 7.1.

Moreover, one can note that the ratio of the secondary to the initial stiffness is close to 10% for all the frames with a window, and 8% for the frames with a door. From these values it appears that the frames with a window have higher initial stiffness, K_{ini}, than frames with a door of equal area. However, the secondary stiffness is lower for the frames with a door than that for frames with a window of similar area. The higher values of K_{ini} for a frame with a door can be explained by the smaller width of a door. This is important when the frame acts as a monolithic structure. After the yield point though, the lack of confinement of the masonry piers due to the door prevents the formation of a diagonal strut between the door and the column. Hence, it reduces the stiffness of the structure. This flexibility becomes more important as the lateral load increases and the infill deforms laterally due to cracking and sliding.

Although the opening dimensions are very influential at the initial loading stages, there seems to be no distinct trend between the opening size and the peak strength and failure mechanism. This is clearly indicated in Figure 7.18(b) which presents the reduction of strength for the frames with windows with respect to the window size and location. Actually, the coordinates of point C and the behavior of the frames beyond that point seem to be influenced more by the location rather than the dimensions of the opening. This influence is studied in the following section.

7.11 Effect of Location of the Opening

The location of a window or door is often overlooked when the strength of such structure is estimated. From the analyses performed in this study, however, it can be concluded that the location considerably affects the failure mechanism and, therefore, the maximum lateral force an infilled frame can withstand. Table 7.7 indicates that Type B curve is suitable to represent the behavior of almost all XX-YR frames, which have an opening close to the leeward column. Moreover, these frames demonstrate the largest loss of lateral strength for every opening size. The reduction in strength is always more than 12% for models XX-1R and 9% for models XX-2R. The difference increases with the size of the opening and reaches 27% for the extra large window. On the contrary, when the opening is located concentrically, the peak strength almost reaches the strength of the solid panel, regardless of the size and shape of the opening. For the five opening scenarios analyzed here, the frames with a concentric door or window have at least 93% of the strength of the frame with a solid panel.

The different strengths exhibited by the models can be explained by considering the failure patterns illustrated in Figures 7.4, 7.7, 7.10, 7.13, and 7.16. It is interesting to note that frames with different sizes of openings but same length of the short pier have similar failure patterns. For instance, Figure 7.19 indicates that all specimens with a 0.61 m (24 in.) leeward masonry pier exhibit similar failure patterns at 1.00% drift. The failure pattern for the five models includes diagonal shear cracks in the windward pier which cause shear failure near the bottom of the leeward column. On the contrary, the windward column deflects in a flexural manner since the short pier between the column and the

opening limits the compressive forces carried by the infill and, therefore, prevents the development of dominant shear cracks in the infill. Figure 7.20 presents the load-vs.-drift curves for the XX-2 models. The curves for the five models, demonstrate different initial and secondary stiffnesses which can be expected since those are only affected by the different opening sizes. The shapes of the curves, however, are very similar reflecting the similar failure patterns. All models have a ductile behavior up to a lateral drift of approximately 0.40%. At this point the peak strength is reached and it is followed by a brittle loss of strength caused by the shear crack in the leeward column.

Another observation is that models with the same opening dimensions and equal but opposite eccentricity, demonstrate similar failure patterns. This can be attributed to the equal areas of the masonry piers on the sides of the opening that allow the development of compressive diagonal forces of similar magnitude. The peak loads, however, are different. The difference in the behavior and the peak load is a result of the lower capacity of the windward column due to the reduced axial load of that column caused by the overturning moment. Although, this is a valuable finding it cannot be quantified due to the complexity of the behavior of the frame-wall system. Hence, it is not yet clear whether a horizontal or diagonal crack will develop in the masonry piers. This is very important as it determines the failure mode of the columns and whether it will include a shear crack or it will lead to the formation of a knee-brace mechanism. This complexity was exhibited by the CU Specimens and in some cases was not fully captured even by the detailed finite element models, between at drift ranges between 0.5 and 1%. Moreover, one should keep in mind that the failure modes are probably affected by the frame design and material properties assumed in this study. Thus, frames with the

same geometry but different reinforcing details and/or different materials may exhibit different behavior in the highly nonlinear region.

7.12 Development of Simplified Force-vs.-Drift Curves for Infilled Frames with Openings

Representing the behavior of an RC infilled frame is a rather difficult task due to the variety of possible responses and the complexity of the frame-infill interaction. This task is even more challenging when the infill panel incorporates openings. The behavior of the frames tested and analyzed in this study provides evidence for the complexity of this effort. Moreover, although this issue has been addressed by a significant number of researchers, there is not a well-validated and widely accepted method available to practicing engineers. The method proposed of superimposing the behavior of a bare frame and the behavior of an unconfined masonry panel cannot be supported by the findings of this study as it ignores the interaction between the frame and the infill that alters the failure modes of both substructures. For example the bare frame tested by Mehrabi et al. (1994) had a ductile behavior as it formed plastic hinges. However, when infilled with a strong infill, the frame failed in a brittle manner due to shear cracks that developed as an extension of the diagonal cracks in the infill, as discussed in Chapter 3.

In this section guidelines are provided for the construction of a simplified force-vs.-drift curve for infilled frames that include openings, based on the findings of this study. This is an extension of the simplified approach proposed in Chapter 6 for infilled frames with solid panels to include the effect of openings. The method proposed

introduces modification to the force-vs.-drift relation of a frame with a solid infill to account for the existence of an opening. Hence, it is assumed that the behavior of a frame with a solid infill has been obtained experimentally or analytically. The analysis of the frame with the solid panel can be conducted with a detailed finite element model similar to the one presented in Chapter 2, or a simplified approach such as the one described in Chapter 6. The Type B-1 curve has been adopted here because it is the most common type among the cases considered. The curve is presented in Figure 7.19 and the behavior it describes is in between the force- and the displacement-controlled behaviors identified in ASCE 41-06 and shown in Figure 7.20. Furthermore, this curve is conservative in terms of the peak strength and ductility of the structure.

Step 1: Initial Stiffness, K_{ini}

The initial stiffness of the frame can be accurately estimated based on the stiffness of the frame with a solid panel K_{ini}^{solid} with the Equation 7.1. Based on the values of Figure 7.18(a) it is proposed $\alpha_w = 2$ for windows and $\alpha_d = 1.6$ for doors.

Step 2: Yield point: V_y , δ_y

Similarly to the frames with a solid panel considered in Chapter 6, the yield point in the force-vs.-drift curve coincides with crack initiation. In infills with openings, the cracks initiate as radiating cracks from the window corners. The drift at which this occurs is slightly larger in the tests presented in Chapter 5 than in the analyses due to the flexibility of the supports that can affect the deformations at such low levels of lateral drift. As for the frames with solid panel, the ratio of the force at 'yield' point to the

maximum force is between 65 and 80%. Hence, the same ratio of 2/3 used in Equation 6.4 can be used for frames with windows and doors.

Step 3: Peak Load: $V_{\max}$

Estimating the peak load depends on a number of factors that cannot be easily accounted for. One could assume a failure mechanism with a limit analysis approach and based on that estimate the peak strength. However, there are many uncertainties associated with such an effort. Even the nonlinear finite element analysis underestimated the actual strength in some cases of the Specimens tested in CU, although the failure mechanisms were well captured. In a conservative approach, one could use the strength of the solid panel with the appropriate reduction factor as follows.

$$V_{\max} = \gamma V_{\max}^{solid} \tag{7.2}$$

in which γ is a strength reduction factor. Based on the results of this study, the value of γ would depend on the size as well as the location of the opening with the latter being equally or more influential than the former. This finding is not in agreement with the approach proposed by Al Chaar 2002 for the estimation of the strength of the frame which only accounts for the size of an opening. In the conservative approach proposed here, a strength reduction factor of $\gamma = 0.80$ is proposed for all openings. As shown in Figure 7.18(b) only two of the cases considered demonstrated larger reduction of strength compared to the frame with a solid panel, with the lower value being 73.5%.

Step 4: Drift at Peak Load: $\delta_{V_{\max}}$

Once the peak load has been defined, the corresponding drift, $\delta_{V_{\max}}$, can be assumed to be equal to that of the frame with a solid masonry panel, which can be

estimated based on Equations 6.7 and 6.8. Table 7.13 indicates that this drift changes with the size of the opening and that for small openings, this is lower than the value of the solid wall. However, the lowest values correspond to frames which reach their peak prematurely at relatively low levels of lateral load. These frames can maintain their lateral resistance without a significant load drop. Hence, assuming a drift value, $\delta_{V_{\max}}$, which is slightly larger than the corresponding value of the finite element analysis allows for a good approximation of the behavior of the frame.

Alternatively, the drift, $\delta_{V_{\max}}$, at peak load can be defined by using the secondary stiffness between the yield point and the point of maximum strength. This can be defined as a function of the initial stiffness according to the formula.

$$K_2 = \beta_i K_{ini} \tag{7.3}$$

in which β_i is the ratio of the secondary to the initial stiffness. Based on the results of the analysis in this study it is proposed $\beta_w = 0.10$ for infills with windows regardless of its size and $\beta_d = 0.08$ for infills with a door. This method is more accurate in terms of estimating the exact stiffness value. However, combined with the assumption of 20% strength reduction compared to the solid infill, it may result in considerably more brittle failure as the backbone curve underestimates the actual energy dissipation capability of the frame. Therefore, although less accurate in terms of the secondary stiffness, the first method of using the values from Equation 6.7 and 6.8 is proposed as it yields a more realistic overall behavior.

Step 5: Point E: $\delta_{V_{res}}, V_{res}$

Point E signifies the point beyond the potential brittle load drop at which the load is close to the residual strength of the structure. If the failure pattern is known or can be safely assumed as in the case of solid infills discussed in Chapter 6, the residual strength can be equal estimated. For instance, if shear failures develop at both columns, the shear resistance of the two columns can be subtracted from the maximum strength. However, the failure mode is not typically known. Consequently, unless a worse case scenario is adopted based on a limit analysis, V_{res} can be related to the maximum load according to the following formula.

$$V_{res} = \gamma_{res} V_{\max} \tag{7.4}$$

in which γ_{res} is a strength reduction factor which can be set equal to 0.50. This is a rather conservative value as the average value obtained from the analysis is 0.79 and the majority of frames exhibit values higher than 0.70. However, there are two cases with values lower than 0.50. Moreover, the tests and analyses presented here do not account for the out-of-plane forces that can be applied during an earthquake. These can rapidly deteriorate the condition and the loading capacity of a cracked wall especially if the latter contains openings.

For the drift $\delta_{V_{res}}$, Equation 6.10 used for the frames with solid panels can be used. This assumption is based on the results of the parametric study and it is over-simplifies the actual behavior which is influenced by the size and the location of the window.

Step 6: Slope of segment E-F: K_{res}

In the case of solid infills, the final segment of the force-vs.-drift relation is modeled with a line of zero slop as constant residual strength is assumed. According to the results of the parametric study presented here, a line with a negative slope of $\theta_{res} = -0.01$ might be more appropriate for infills with openings. However, this is a relatively mild slope and a horizontal line can be a good approximation while providing some simplicity.

With the six-step procedure proposed here, a simplified backbone curve for the behavior of infilled frames with openings can be constructed. The procedure accounts for the affect of the opening size on the structural behavior by adjusting the stiffnesses along three segments of the quad-linear curve proposed. It does not examine the exact location of the opening and adopts a conservative approach by considering the behavior of a weak and brittle structure. According to this approach one curve would be obtained for eccentrically located openings regardless of the direction of loading. This is not necessarily a bad assumption, since the earthquake is a random phenomenon and failure along one loading direction suffices to damage the structure.

7.13 Validation of the Simplified Backbone Curve

The simplified method for the development of the lateral force-vs.-drift curve has been validated with the tests on infilled frames with openings which are presented in Chapter 5. Specimens CU2, CU5, and CU6 have been considered here. Initially, the material values of Table 5.1 were used to obtain the envelop curve of corresponding frame with solid masonry panel according to the procedure proposed in Chapter 6. The

estimated curves were modified according to the methodology developed in this chapter to obtain the envelop curves which are compared to the experimentally obtained curves are in Figure 7.23.

The proposed approach provides reasonably accurate results in the three cases. It should be noted that with the proposed approach the location of the infill is not accounted for. Therefore, the backbone curves are symmetric in the positive and negative directions. It can be observed from Figure 7.23 that in all cases the model can estimate with good accuracy the initial stiffness, yield point and residual strength. However, the strength of the frames is underestimated in the negative direction for Specimen CU2 and the positive direction of CU5. In all other cases the model is sufficiently precise for a quick estimation method, although it slightly overestimates the strength of Specimen CU6 in the positive direction. The main difference between the predicted and the actual behavior is in terms of the ductility as a sudden load drop is built in the development of the model. This may not be accurate in some cases but brittle behavior has been assumed in all cases to ensure conservative estimation of the post peak behavior since the exact behavior cannot be known without conducting a more detailed analysis or a test.

A possible alternative would have been to create a finite element model for the corresponding frame with solid wall for each frame and apply the modifications to that curve. This method would have probably yielded more accurate results but it requires significantly larger amount of time and effort. In case of building with many bays of similar aspect ratios and different opening configurations this would have been a good compromise to obtain a good estimate of its seismic performance without creating a finite element model for every single bay.

7.14 Conclusions

In this chapter a parametric study considering the effect of openings on the structural behavior is presented. The study has been conducted with the nonlinear finite element scheme developed in Chapter 2 and used the frame design and properties of the large-scale specimens tested in CU. The parameters under investigation have been the geometry of the opening, its size, and its location within the infill wall. The location of a window or door is often overlooked when the strength of such structures is estimated. The results, however, indicate that the opening size can determine the initial stiffness of the structure, but for the peak strength, the location of the infill is equally important as it influences the failure pattern of the infill and the bounding frame. To address the lack of predictive tools to assess the performance of infilled frames with openings, guidelines for the development of a simplified quad-linear curve have been developed. The comparison of the envelop curves with the experimental data from the tests discussed in Chapter 5 indicates that the proposed method can provide conservative, but adequately accurate predictions.

Tables of Chapter 7

Table 7.1: Dimensions of models with a small window.

Model	A_{op} m^2 (in^2)	A_{op}/A_{Wtot} %	L_a m (in)	L_b m (in)	L_c m (in)	h_a m (in)	h_b m (in)	h_c m (in)
SW-1	0.45 (702)	7.2	0.30 (12)	0.61 (24)	2.46 (97)	0.51 (20.25)	0.74 (29.25)	0.61 (24)
SW-1R	0.45 (702)	7.2	2.46 (97)	0.61 (24)	0.30 (12)	0.51 (20.25)	0.74 (29.25)	0.61 (24)
SW-2	0.45 (702)	7.2	0.61 (24)	0.61 (24)	2.16 (85)	0.51 (20.25)	0.74 (29.25)	0.61 (24)
SW-2R	0.45 (702)	7.2	2.16 (85)	0.61 (24)	0.61 (24)	0.51 (20.25)	0.74 (29.25)	0.61 (24)
SW-M	0.45 (702)	7.2	54.5 (1.38)	0.61 (24)	54.5 (1.38)	0.51 (20.25)	0.74 (29.25)	0.61 (24)

Table 7.2: Dimensions of models with a regular window.

Model	A_{op} m^2 (in^2)	A_{op}/A_{Wtot} %	L_a m (in)	L_b m (in)	L_c m (in)	h_a m (in)	h_b m (in)	h_c m (in)
RW-1	0.70 (1053)	10.8	0.30 (12)	0.91 (36)	2.16 (85)	0.51 (20.25)	0.74 (29.25)	0.61 (24)
RW-1R	0.70 (1053)	10.8	2.16 (85)	0.91 (36)	0.30 (12)	0.51 (20.25)	0.74 (29.25)	0.61 (24)
RW-2	0.70 (1053)	10.8	0.61 (24)	0.91 (36)	1.85 (73)	0.51 (20.25)	0.74 (29.25)	0.61 (24)
RW-2R	0.70 (1053)	10.8	1.85 (73)	0.91 (36)	0.61 (24)	0.51 (20.25)	0.74 (29.25)	0.61 (24)
RW-M	0.70 (1053)	10.8	1.23 (48.5)	0.91 (36)	1.23 (48.5)	0.51 (20.25)	0.74 (29.25)	0.61 (24)

Table 7.3: Dimensions of models with a large window.

Model	A_{op} m^2 (in^2)	A_{op}/A_{Wtot} %	L_a m (in)	L_b m (in)	L_c m (in)	h_a m (in)	h_b m (in)	h_c m (in)
LW-1	0.90 (1404)	14.4	0.30 (12)	1.22 (48)	1.85 (73)	0.51 (20.25)	0.74 (29.25)	0.61 (24)
LW-1R	0.90 (1404)	14.4	1.85 (73)	1.22 (48)	0.30 (12)	0.51 (20.25)	0.74 (29.25)	0.61 (24)
LW-2	0.90 (1404)	14.4	0.61 (24)	1.22 (48)	1.55 (61)	0.51 (20.25)	0.74 (29.25)	0.61 (24)
LW-2R	0.90 (1404)	14.4	1.55 (61)	1.22 (48)	0.61 (24)	0.51 (20.25)	0.74 (29.25)	0.61 (24)
LW-M	0.90 (1404)	14.4	1.08 (42.5)	1.22 (48)	1.08 (42.5)	0.51 (20.25)	0.74 (29.25)	0.61 (24)

Table 7.4: Dimensions of models with an extra large window.

Model	A_{op} m^2 (in^2)	A_{op}/A_{Wtot} %	L_a m (in)	L_b m (in)	L_c m (in)	h_a m (in)	h_b m (in)	h_c m (in)
xLW-1	1.13 (1755)	17.9	0.30 (12)	1.52 (60)	1.55 (61)	0.51 (20.25)	0.74 (29.25)	0.61 (24)
xLW-1R	1.13 (1755)	17.9	1.55 (61)	1.52 (60)	0.30 (12)	0.51 (20.25)	0.74 (29.25)	0.61 (24)
xLW-2	1.13 (1755)	17.9	0.61 (24)	1.52 (60)	1.24 (49)	0.51 (20.25)	0.74 (29.25)	0.61 (24)
xLW-2R	1.13 (1755)	17.9	1.24 (49)	1.52 (60)	0.61 (24)	0.51 (20.25)	0.74 (29.25)	0.61 (24)
xLW-M	1.13 (1755)	17.9	0.93 (36.5)	1.52 (60)	0.93 (36.5)	0.51 (20.25)	0.74 (29.25)	0.61 (24)

Table 7.5: Dimensions of models with a door.

Model	A_{op} m^2 (in^2)	A_{op}/A_{Wtot} %	L_a m (in)	L_b m (in)	L_c m (in)	h_a m (in)	h_b m (in)
D-1	1.01 (1568)	16.0	0.30 (12)	0.71 (28)	2.36 (93)	0.44 (17.5)	1.42 (56)
D-1R	1.01 (1568)	16.0	2.36 (93)	0.71 (28)	0.30 (12)	0.44 (17.5)	1.42 (56)
D-2	1.01 (1568)	16.0	0.61 (24)	0.71 (28)	2.05 (81)	0.44 (17.5)	1.42 (56)
D-2R	1.01 (1568)	16.0	2.05 (81)	0.71 (28)	0.61 (24)	0.44 (17.5)	1.42 (56)
D-M	1.01 (1568)	16.0	1.33 (52.5)	0.71 (28)	1.33 (52.5)	0.44 (17.5)	1.42 (56)

Table 7.6: Summary of behavior of model with a solid panel.

K_{ini} kN/cm (kips/in)	V_y kN (kips)	δ_y %	K_2/K_{ini} %	V_{max} kN (kips)	$\delta_{V_{max}}$ %	V_E kN (kips)	δ_E %	K_{res}/K_{ini} %	$V_{\delta=1\%}$ kN (kips)
5992 (3422)	457 (103)	0.037	10.1	582 (133)	0.124	454 (102)	0.359	-0.68	400 (90)

Table 7.7: Categorization of load-vs.-drift curve and indication of the reduction of the maximum resistance for each frame.

Curve Type	Solid Panel	Small Window					Regular Window					Large Window					Extra Large Window					Door				
		1	1R	2	2R	M	1	1R	2	2R	M	1	1R	2	2R	M	1	1R	2	2R	M	1	1R	2	2R	M
A	x								x								x		x	x		x				
B		x		x		x	x					x			x						x					
C			x		x			x		x	x		x	x		x		x					x	x	x	x

Legend indicating the reduction in peak resistance compared to the solid infill:
x 0-7.5% x 7.5-15% x 15-22.5% x 22.5-30%

Table 7.8: Summary of behavior of models with a small window.

Model	K_{ini}/K_{ini}^{solid} %	V_y kN (kips)	δ_y %	K_2/K_{ini} %	$V_{\max}$ kN (kips)	$\delta_{V_{\max}}$ %	V_{res} kN (kips)	δ_{res} %	K_{res}/K_{ini} %	$V_{\delta=1\%}$ kN (kips)
SW-1	83.3	381 (86)	0.037	11.2	523 (118)	0.161	412 (93)	0.409	-2.1	282 (63)
SW-1R	87.7	414 (93)	0.038	10.2	508 (114)	0.186	355 (80)	0.471	-0.2	343 (77)
SW-2	81.2	398 (89)	0.040	10.6	527 (118)	0.161	440 (99)	0.384	-1.9	322 (72)
SW-2R	88.4	403 (91)	0.037	7.9	520 (117)	0.235	401 (90)	0.248	-1.4	283 (64)
SW-M	85.3	389 (87)	0.037	9.6	538 (121)	0.211	391 (88)	0.495	-1.0	338 (76)

Table 7.9: Summary of behavior of models with a regular window.

Model	K_{ini}/K_{ini}^{solid} %	V_y kN (kips)	δ_y %	K_2/K_{ini} %	$V_{\max}$ kN (kips)	$\delta_{V_{\max}}$ %	V_{res} kN (kips)	δ_{res} %	K_{res}/K_{ini} %	$V_{\delta=1\%}$ kN (kips)
RW-1	75.6	368 (83)	0.040	11.0	480 (108)	0.149	391 (88)	0.384	-1.8	287 (64)
RW-1R	80.1	381 (86)	0.038	9.4	497 (112)	0.161	289 (65)	0.632	-0.1	286 (64)
RW-2	75.1	366 (82)	0.040	10.6	515 (116)	0.458	379 (85)	0.570	-1.2	330 (74)
RW-2R	81.1	383 (86)	0.038	9.2	461 (104)	0.124	340 (76)	0.793	-0.9	321 (72)
RW-M	78.4	370 (83)	0.038	9.5	574 (129)	0.260	402 (90)	0.570	-1.3	348 (78)

Table 7.10: Summary of behavior of models with a large window.

Model	K_{ini}/K_{ini}^{solid} %	V_y kN (kips)	δ_y %	K_2/K_{ini} %	$V_{\max}$ kN (kips)	$\delta_{V_{\max}}$ %	V_{res} kN (kips)	δ_{res} %	K_{res}/K_{ini} %	$V_{\delta=1\%}$ kN (kips)
LW-1	68.5	344 (77)	0.041	9.3	477 (107)	0.211	338 (76)	0.471	-0.0	337 (76)
LW-1R	68.2	363 (82)	0.043	10.1	442 (99)	0.136	398 (89)	0.805	-0.2	394 (89)
LW-2	69.3	338 (76)	0.040	9.4	544 (122)	0.297	544 (122)	0.297	-0.4	316 (71)
LW-2R	72.8	355 (80)	0.040	9.5	532 (120)	0.248	516 (116)	0.533	-1.1	339 (76)
LW-M	72.0	351 (79)	0.040	8.9	575 (129)	0.322	575 (129)	0.322	-0.2	312 (70)

Table 7.11: Summary of behavior of models with an extra large window.

Model	K_{ini}/K_{ini}^{solid} %	V_y kN (kips)	δ_y %	K_2/K_{ini} %	$V_{\max}$ kN (kips)	$\delta_{V_{\max}}$ %	V_{res} kN (kips)	δ_{res} %	K_{res}/K_{ini} %	$V_{\delta=1\%}$ kN (kips)
xLW-1	61.2	335 (75.4)	0.045	9.3	528 (119)	0.471	402 (90)	0.533	-2.1	328 (74)
xLW-1R	60.7	346 (77.8)	0.046	9.4	427 (96)	0.161	390 (88)	0.594	-0.3	380 (85)
xLW-2	61.9	337 (75.8)	0.044	10.3	501 (113)	0.359	251 (56)	0.768	-0.2	248 (56)
xLW-2R	64.6	330 (74.3)	0.042	9.3	461 (104)	0.693	347 (78)	0.904	-0.1	347 (78)
xLW-M	63.7	330 (74.1)	0.048	10.3	556 (125)	0.347	333 (75)	0.830	-1.7	308 (69)

Table 7.12: Summary of behavior of models with a door.

Model	K_{ini}/K_{ini}^{solid} %	V_y kN (kips)	δ_y %	K_2/K_{ini} %	$V_{\max}$ kN (kips)	$\delta_{V_{\max}}$ %	V_{res} kN (kips)	δ_{res} %	K_{res}/K_{ini} %	$V_{\delta=1\%}$ kN (kips)
D-1	72.4	353 (79.3)	0.040	9.7	501 (113)	0.372	424 (95.4)	0.384	-2.6	284 (63.7)
D-1R	77.4	377 (84.8)	0.040	8.1	442 (99)	0.124	382 (85.8)	0.198	-0.9	314 (70.6)
D-2	70.6	366 (82.2)	0.042	8.4	569 (128)	0.359	486 (109.4)	0.409	-2.8	342 (76.8)
D-2R	77.4	377 (84.7)	0.040	7.2	448 (101)	0.161	363 (81.5)	0.632	-1.2	318 (71.5)
D-M	73.6	370 (83.1)	0.041	7.0	564 (127)	0.372	231 (52)	1.003	-0.1	231 (52)

Table 7.13: Summary of behavior of all models with respect to the model with solid infill panel.

Model	A_{open}/A_{total} %	K_{ini}/K_{ini}^{solid} %	V_y/V_y^{solid} %	δ_y %	K_2/K_2^{solid} %	$V_{\max}/V_{\max}^{solid}$ %	$\delta_{V_{\max}}$ %	V_{res}/V_{res}^{solid} %	δ_{res} %	K_{res}/K_{res}^{solid} %
SW	7.2	85.3	86.9	0.038	83.7	90.0	0.19	88.0	0.40	166.4
RW	10.8	78.2	81.8	0.039	77.2	86.9	0.23	79.3	0.59	120.7
LW	14.4	70.2	76.7	0.041	65.9	88.3	0.24	104.4	0.49	41.0
xLW	17.9	62.4	73.5	0.044	60.3	85.0	0.41	75.9	0.73	80.7
D	16.0	74.3	80.7	0.040	59.5	86.8	0.28	83.1	0.53	164.4

Figures of Chapter 7

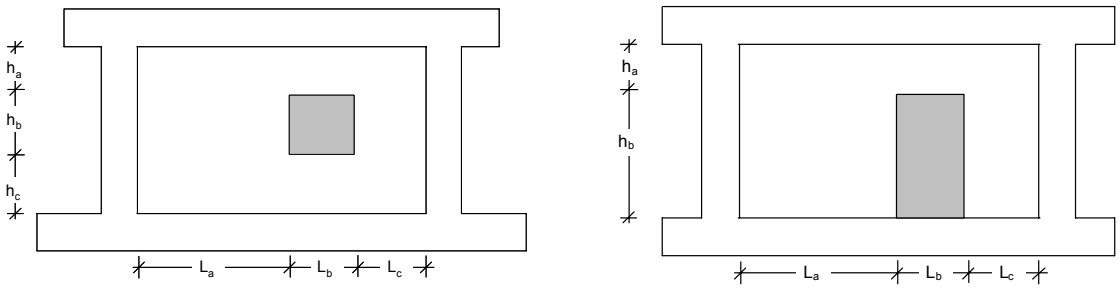

(a) with window (b) with door

Figure 7.1: Opening configurations.

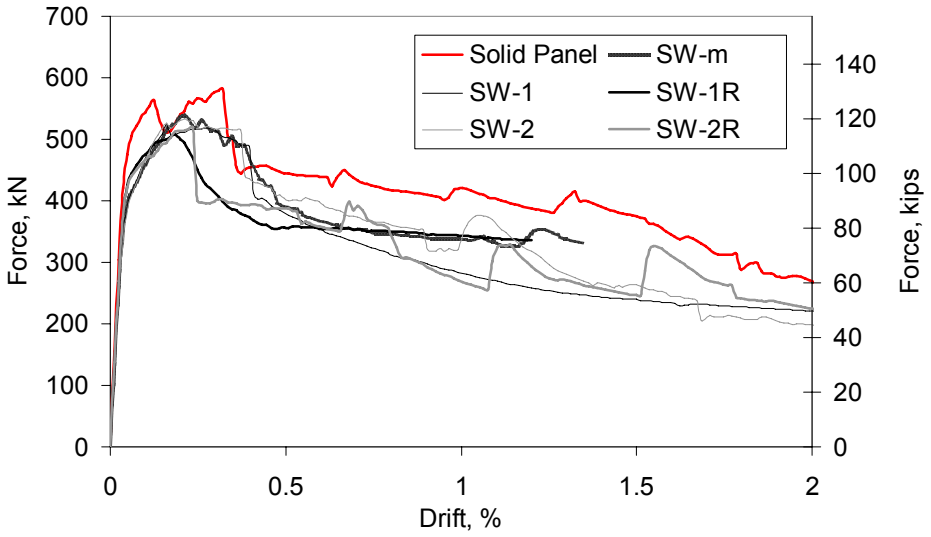

Figure 7.2: Lateral force-vs.-drift relations for models with a small window.

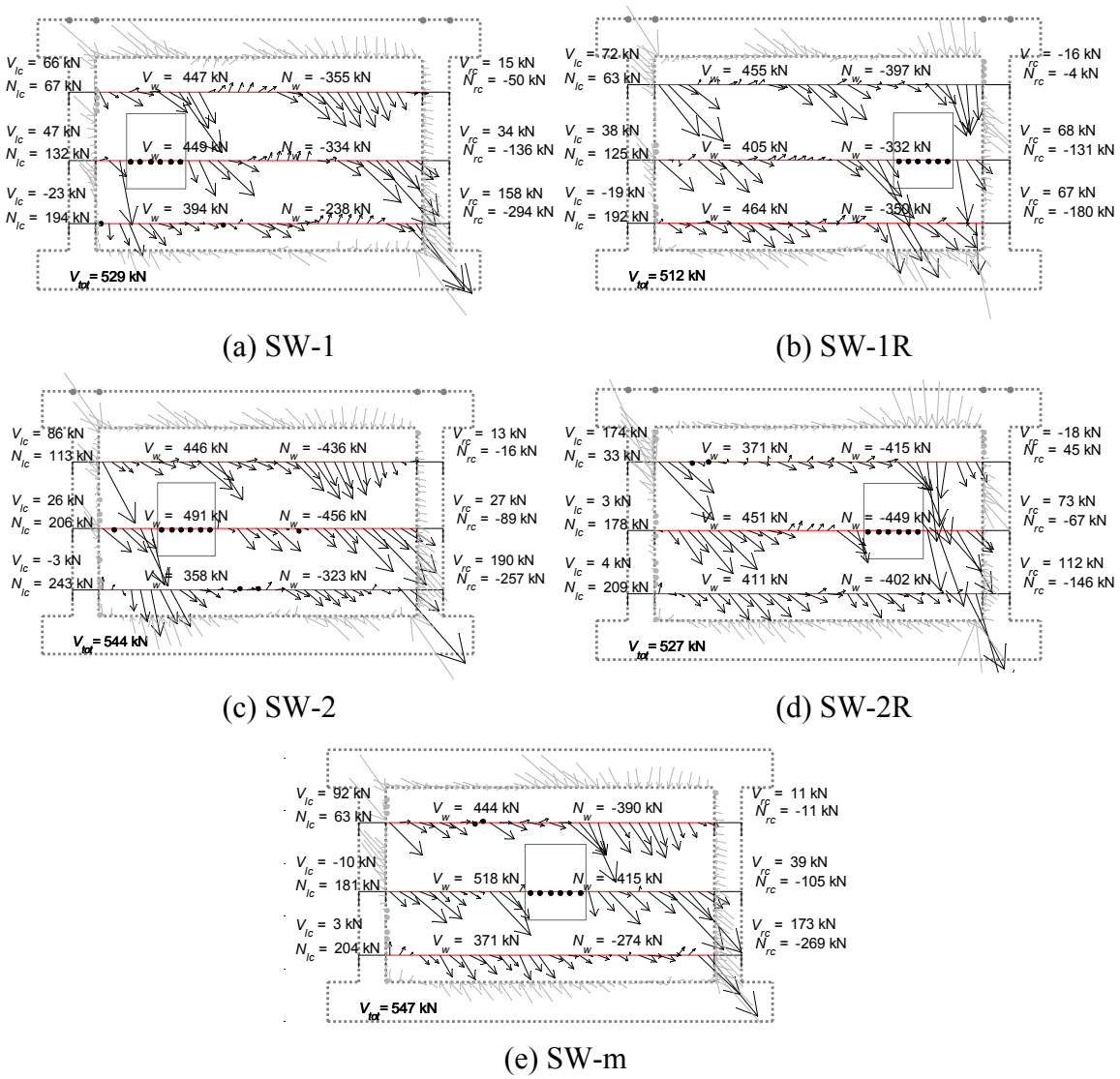

Figure 7.3: Force distribution along three cross sections at the instant of peak strength for frames with a small window.

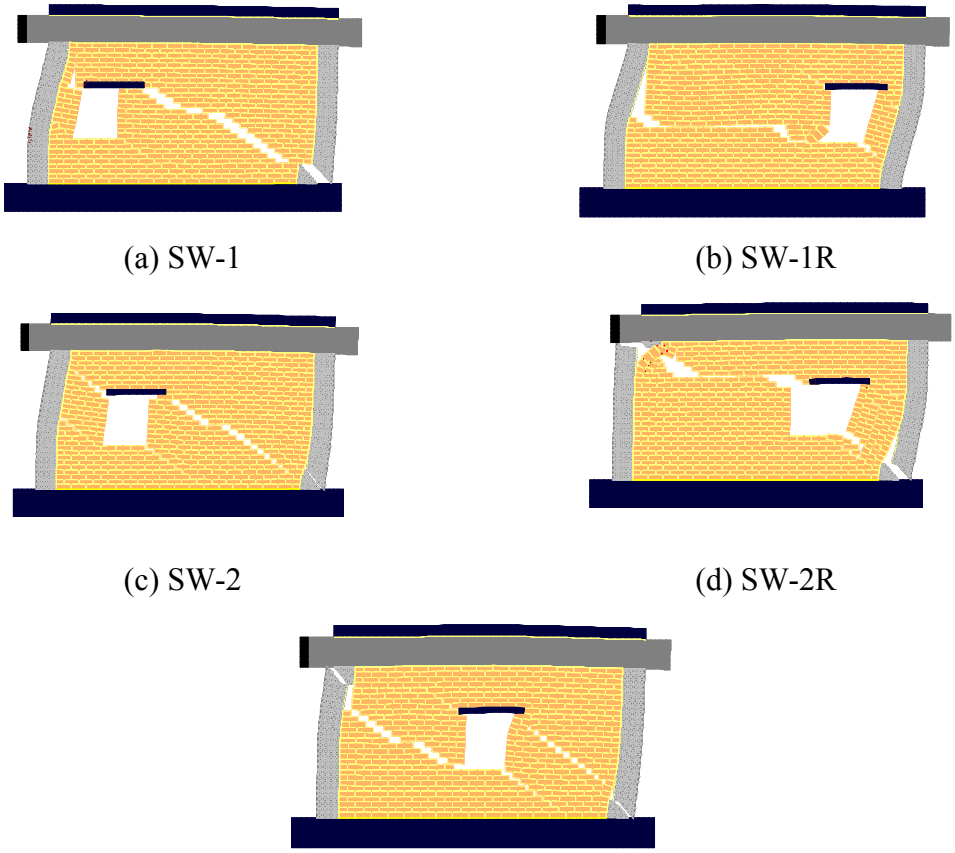

(a) SW-1 (b) SW-1R

(c) SW-2 (d) SW-2R

(e) SW-m

Figure 7.4: Crack patterns at 1.00% drift for frames with a small window.

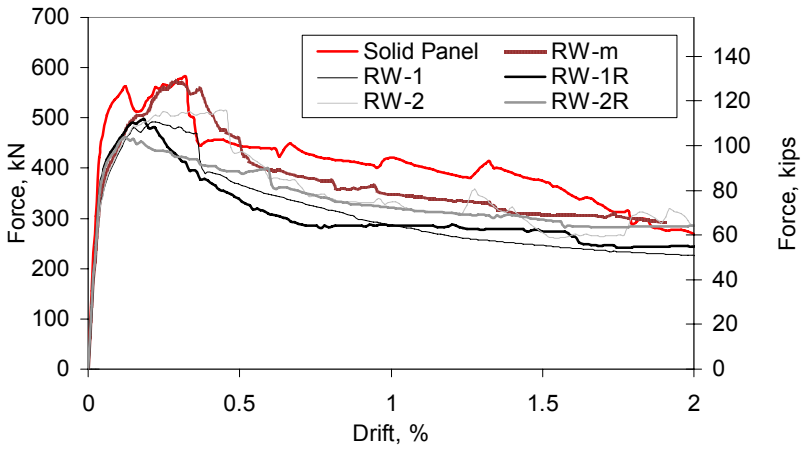

Figure 7.5: Lateral force-vs.-drift relations for the models with a regular window.

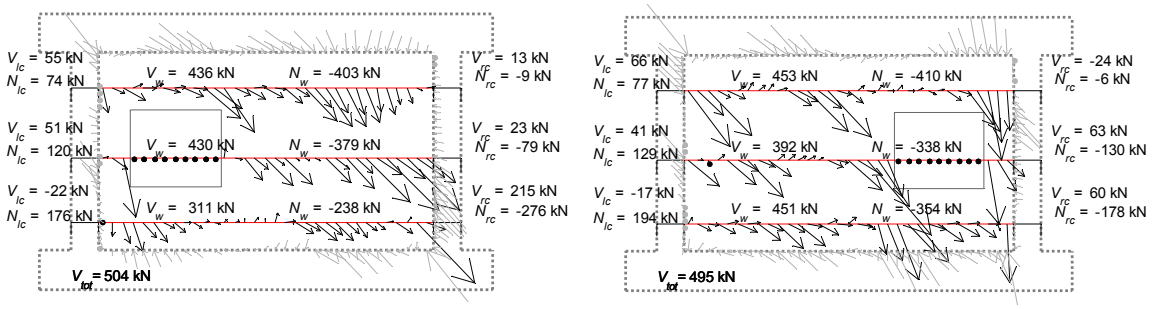

(a) RW-1 (b) RW-1R

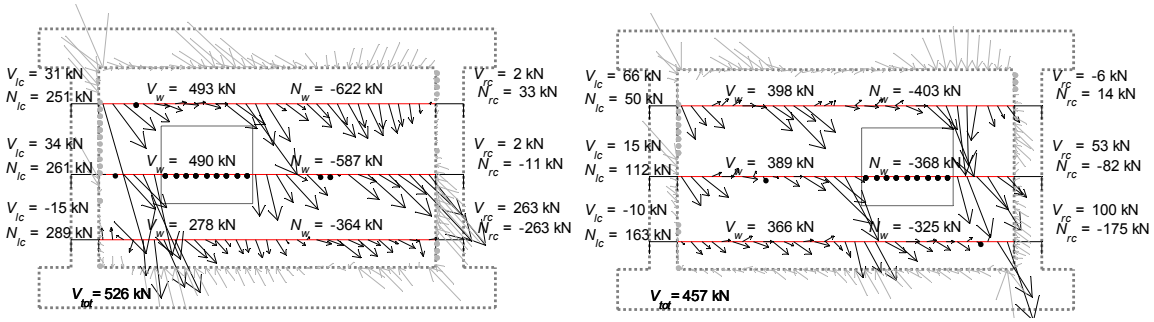

(c) RW-2 (d) RW-2R

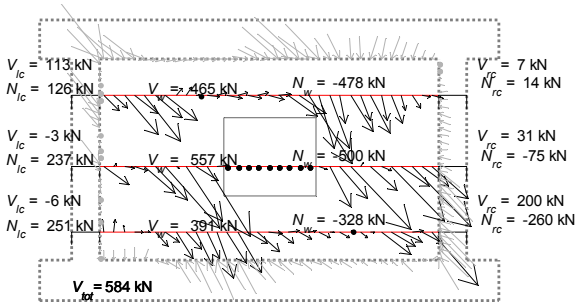

(e) RW-m

Figure 7.6: Force distribution along three cross sections at the instant of peak strength for frames with a regular window.

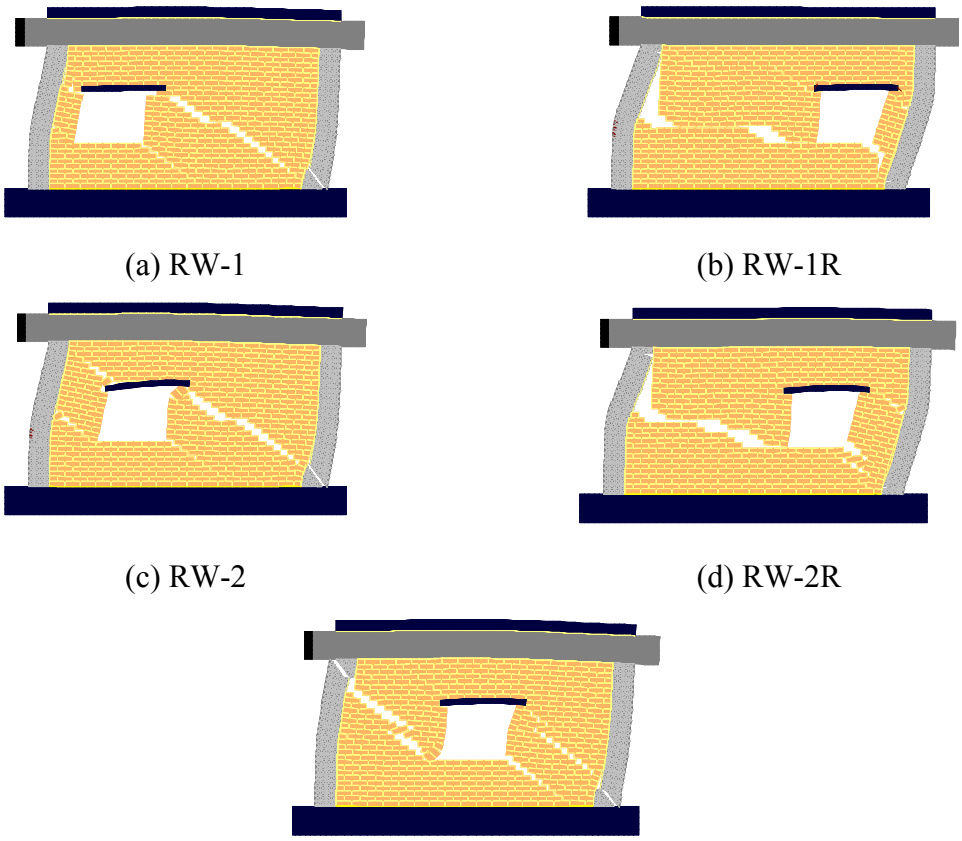

(a) RW-1 (b) RW-1R

(c) RW-2 (d) RW-2R

(c) RW-m

Figure 7.7: Crack patterns at 1.00% drift for frames with a regular window.

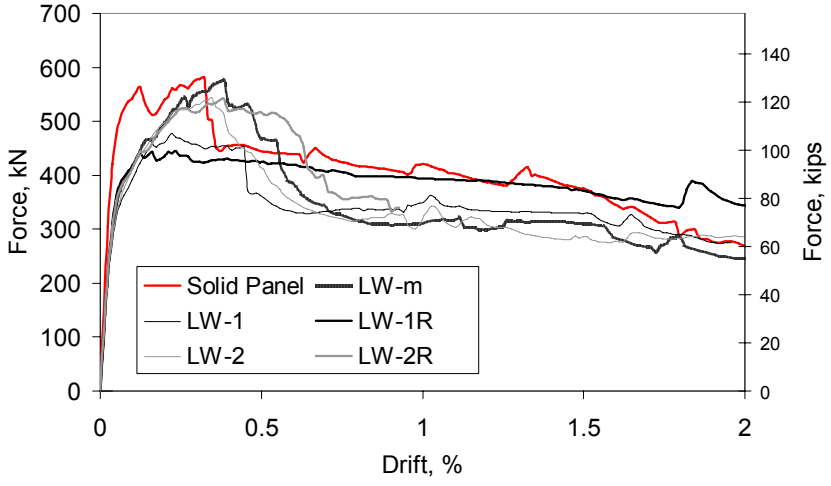

Figure 7.8: Lateral force-vs.-drift relations for models with a large window.

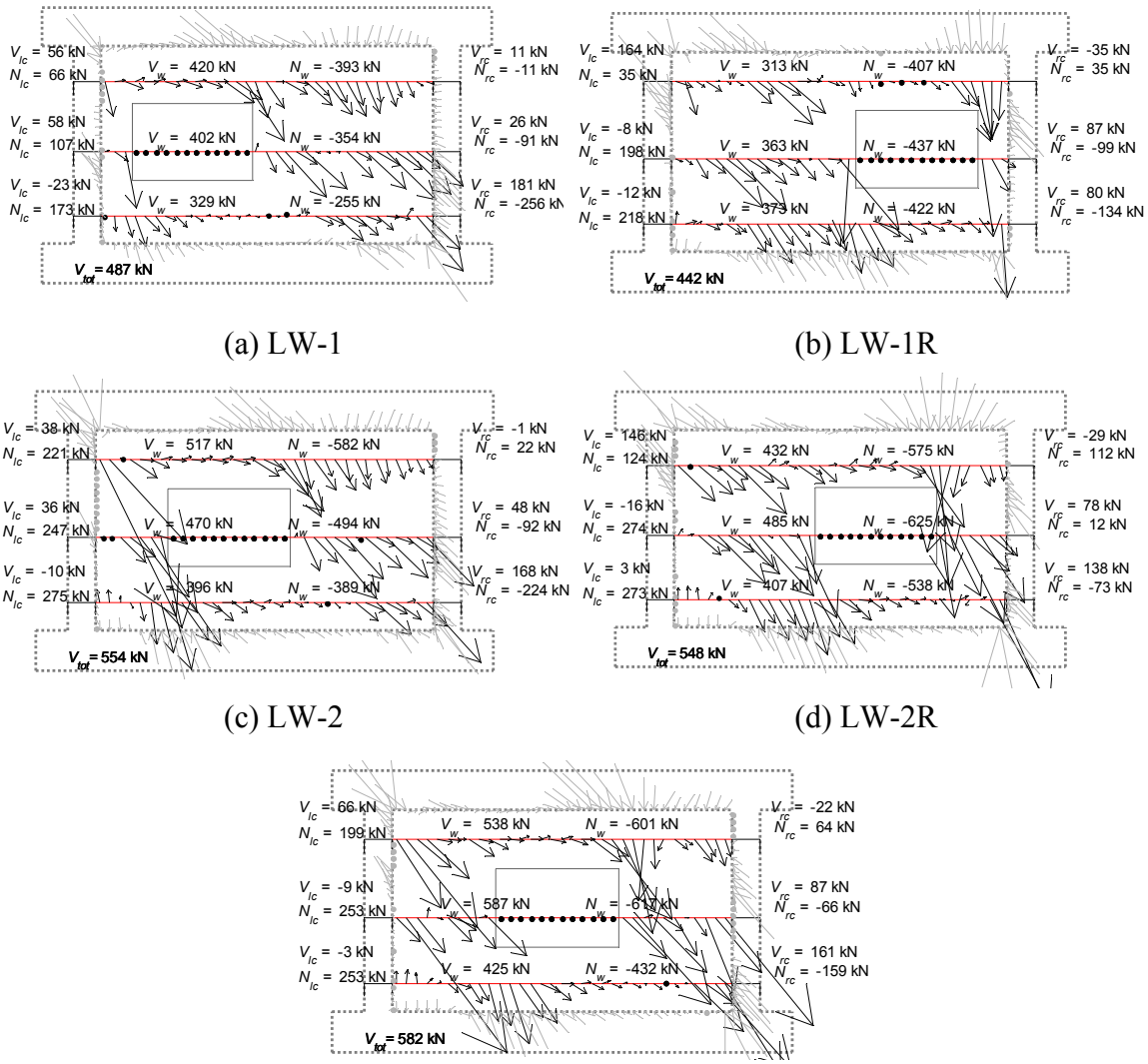

Figure 7.9: Force distribution along three cross sections at the instant of peak strength for frames with a large window.

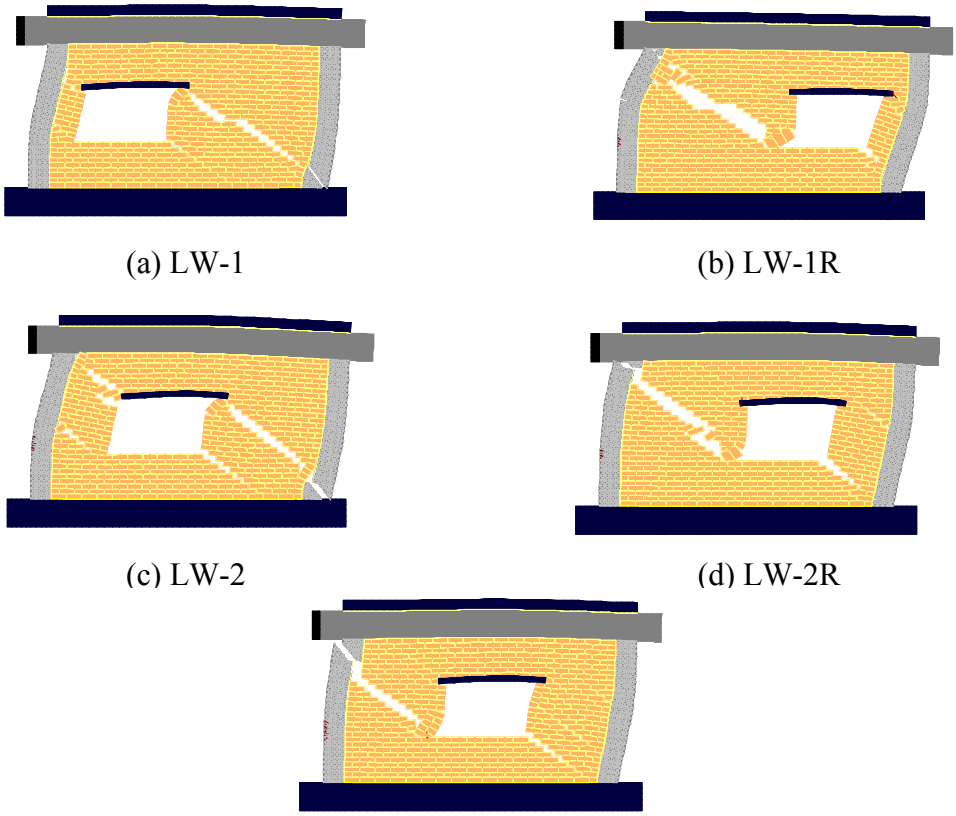

(a) LW-1 (b) LW-1R

(c) LW-2 (d) LW-2R

(e) LW-m

Figure 7.10: Cracking patterns at 1.00% drift for frames with a large window.

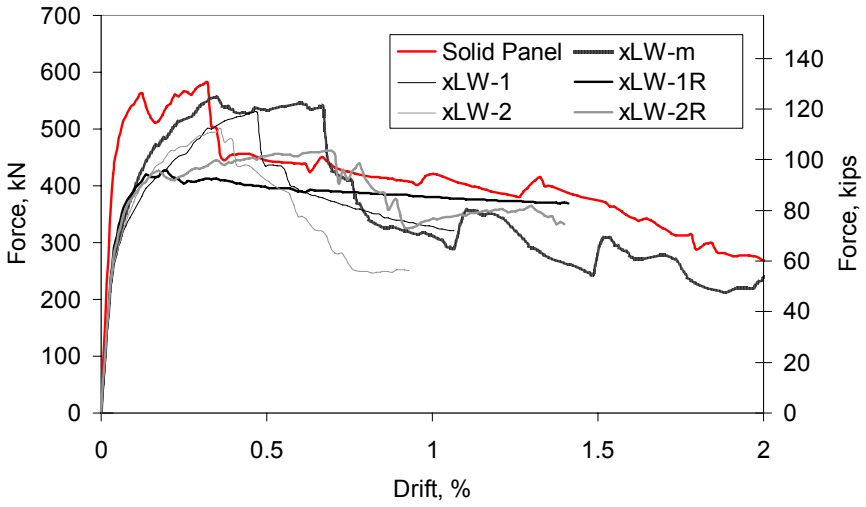

Figure 7.11: Lateral force-vs.-drift relations for models with an extra large window.

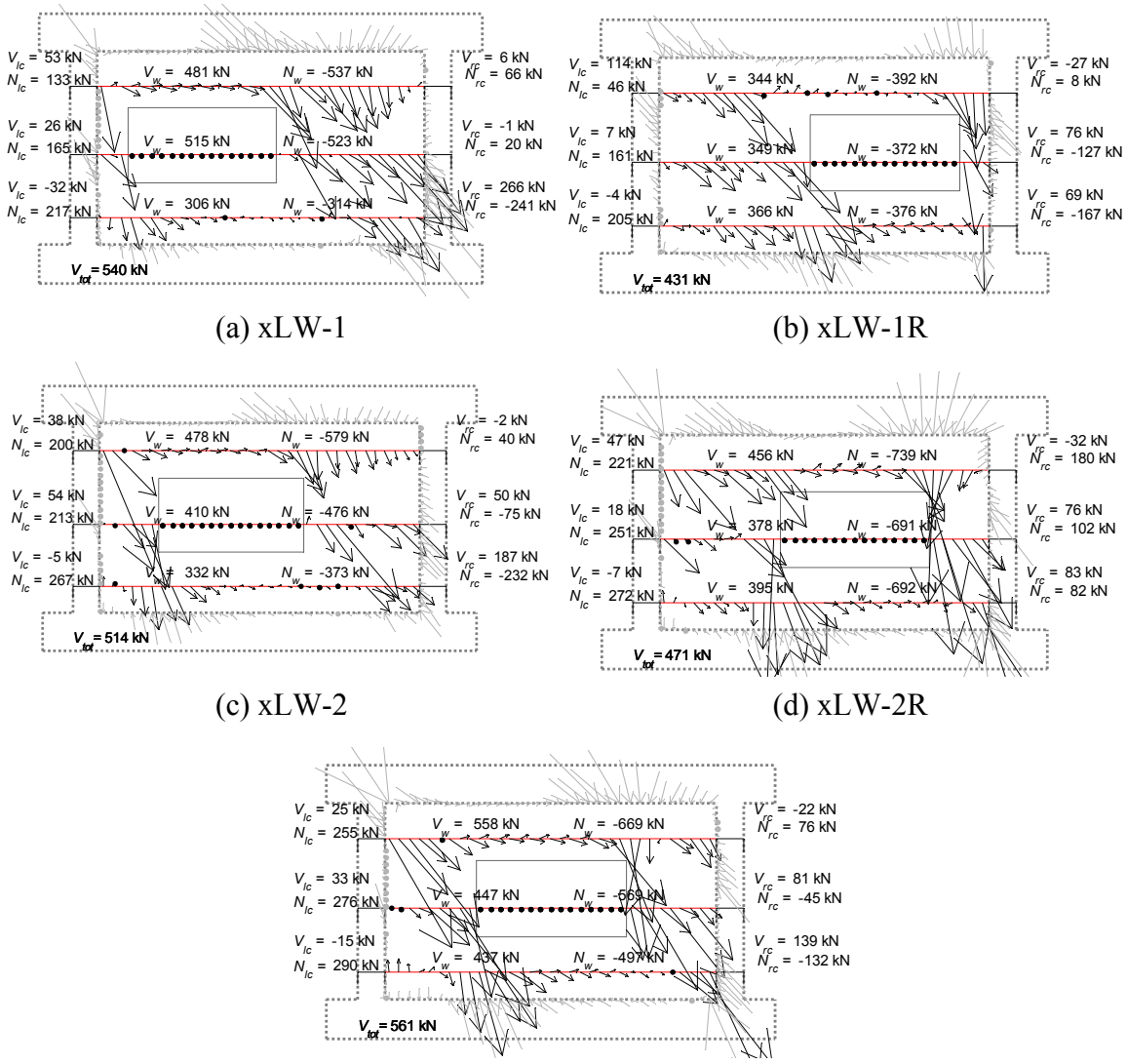

Figure 7.12: Force distribution along three cross sections at the instant of peak strength for frames with an extra large window.

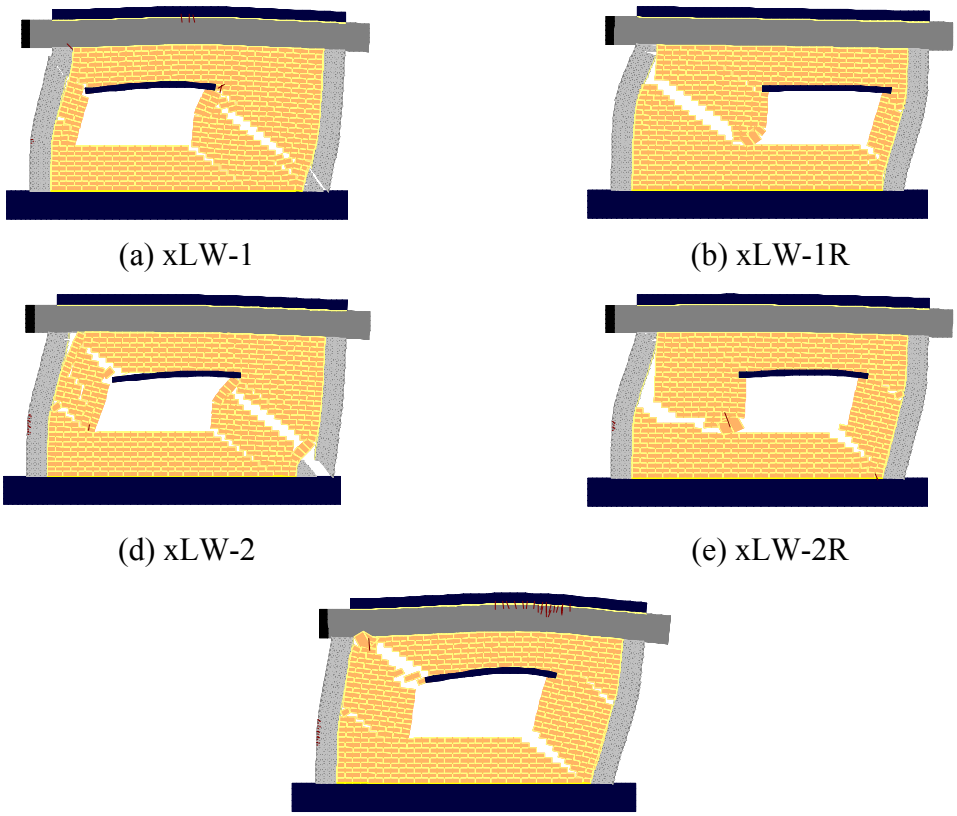

(a) xLW-1 (b) xLW-1R

(d) xLW-2 (e) xLW-2R

(e) xLW-m

Figure 7.13: Cracking patterns at 1.00% drift for frames with an extra large window.

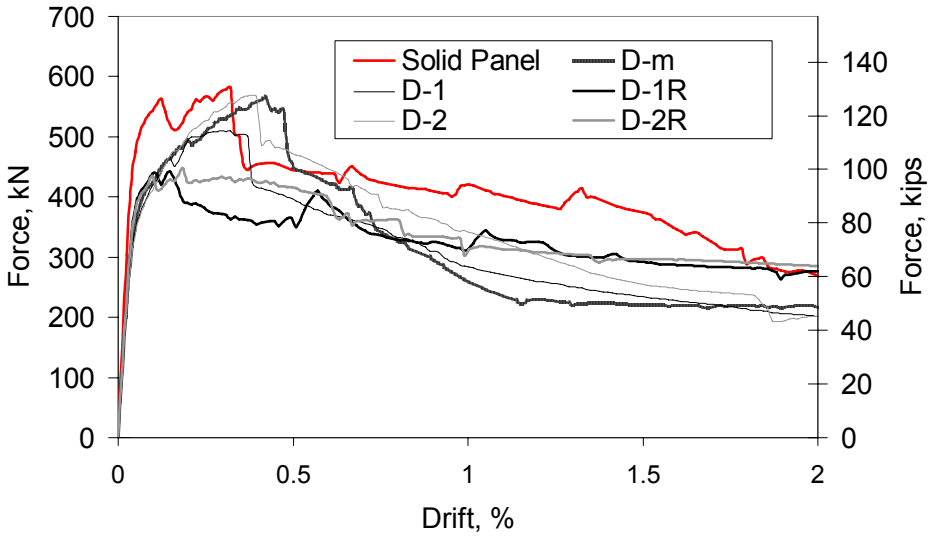

Figure 7.14: Lateral force-vs.-drift relations for models with a door.

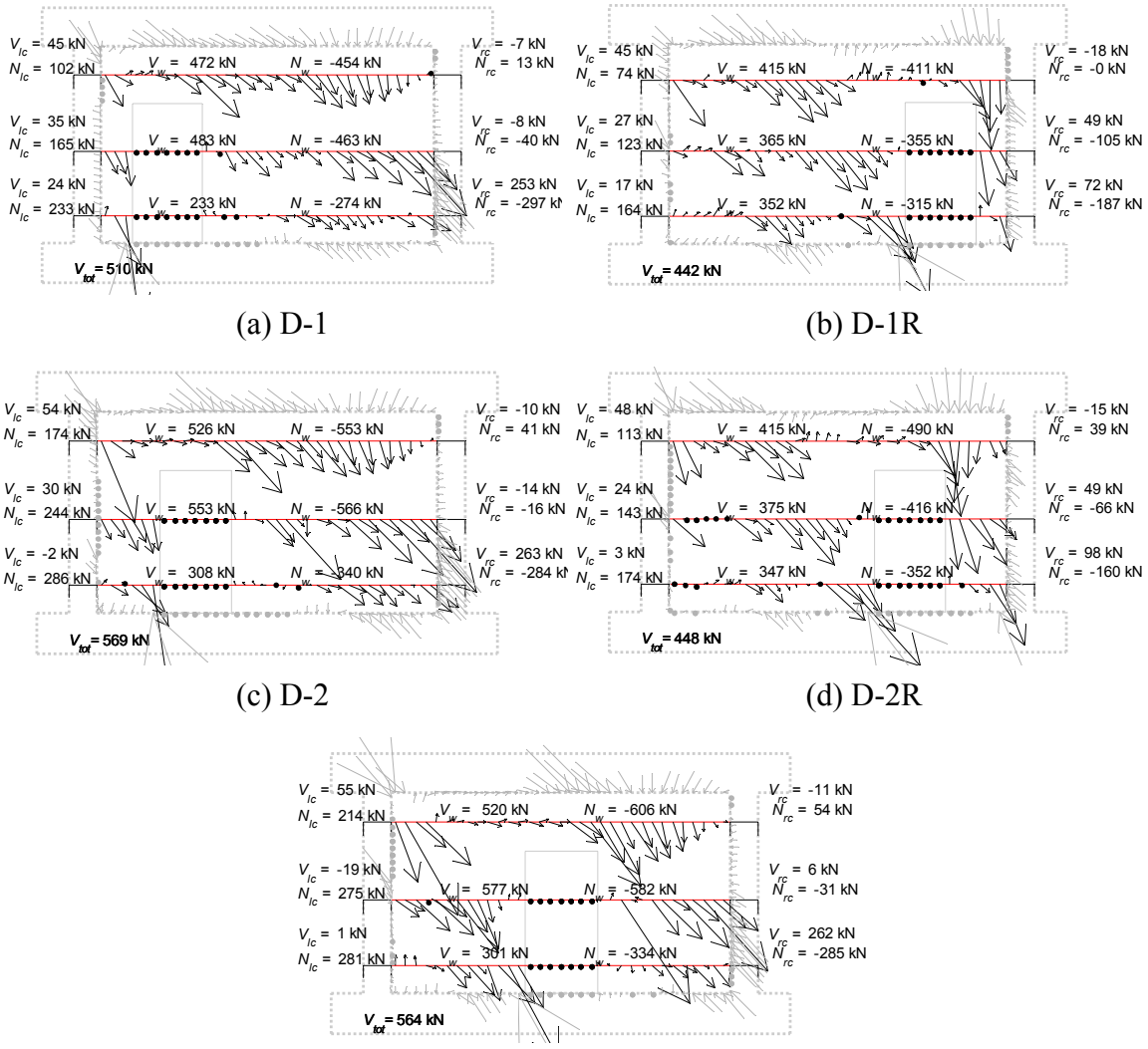

Figure 7.15: Force distribution along three cross sections at the instant of peak strength for frames with a door.

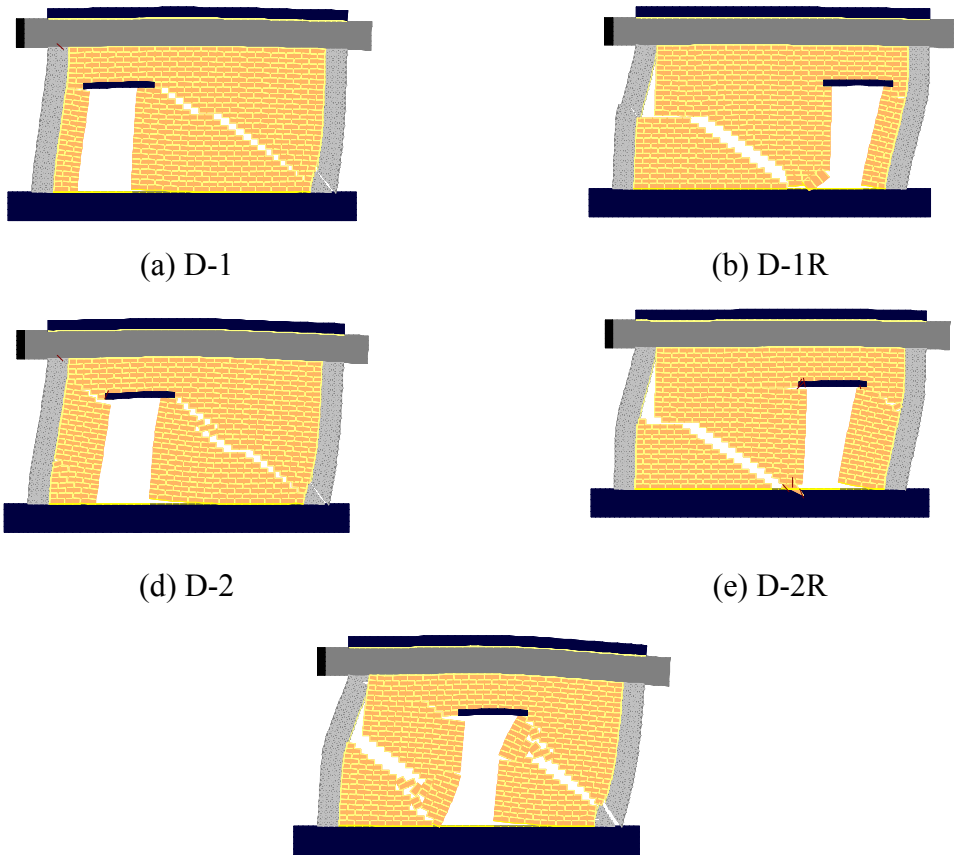

(a) D-1 (b) D-1R

(d) D-2 (e) D-2R

(c) D-m

Figure 7.16: Cracking patterns at 1.00% drift for frames with a door.

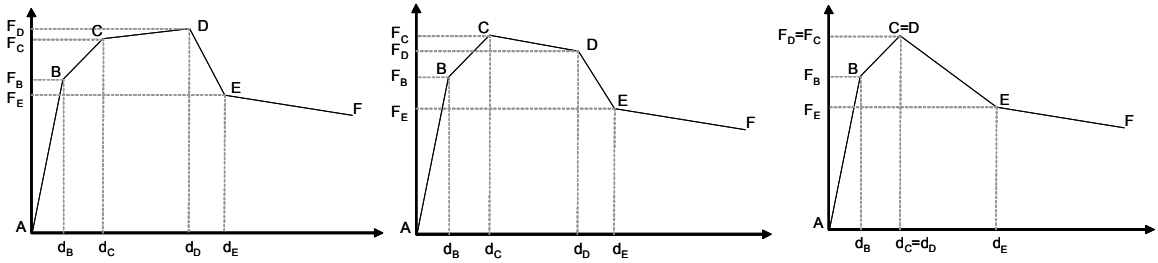

(a) Curve A (b) Curve B (c) Curve B-1

Figure 7.17: Possible force-vs.-displacement backbone curves.

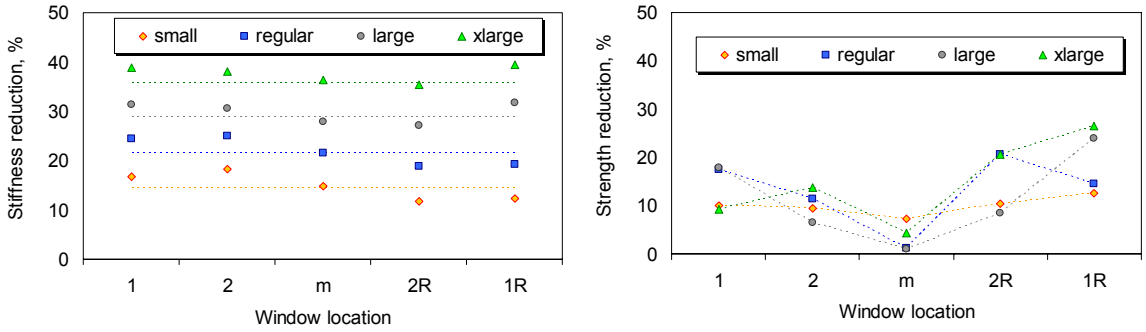

(a) reduction in stiffness (b) reduction in strength

Figure 7.18: Reduction in stiffness and strength of the infilled frames with windows compared to the frame with a solid panel.

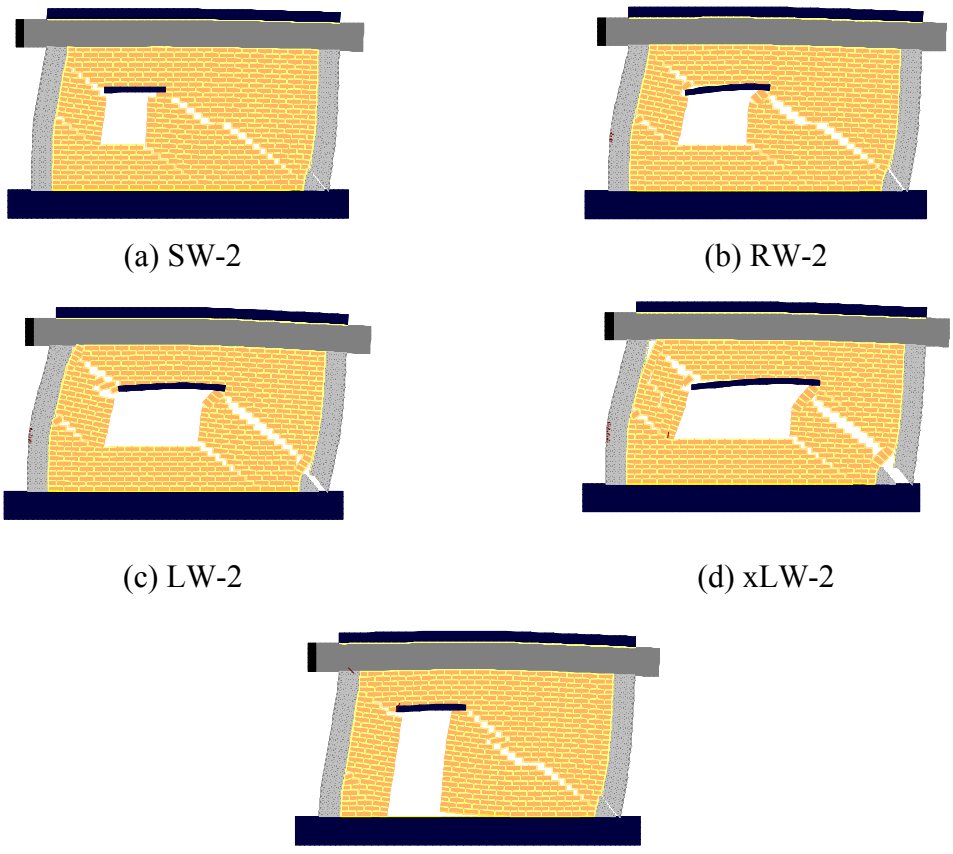

(a) SW-2 (b) RW-2

(c) LW-2 (d) xLW-2

(e) D-2

Figure 7.19: Cracking patterns at 1.00% drift for the XW-2 models.

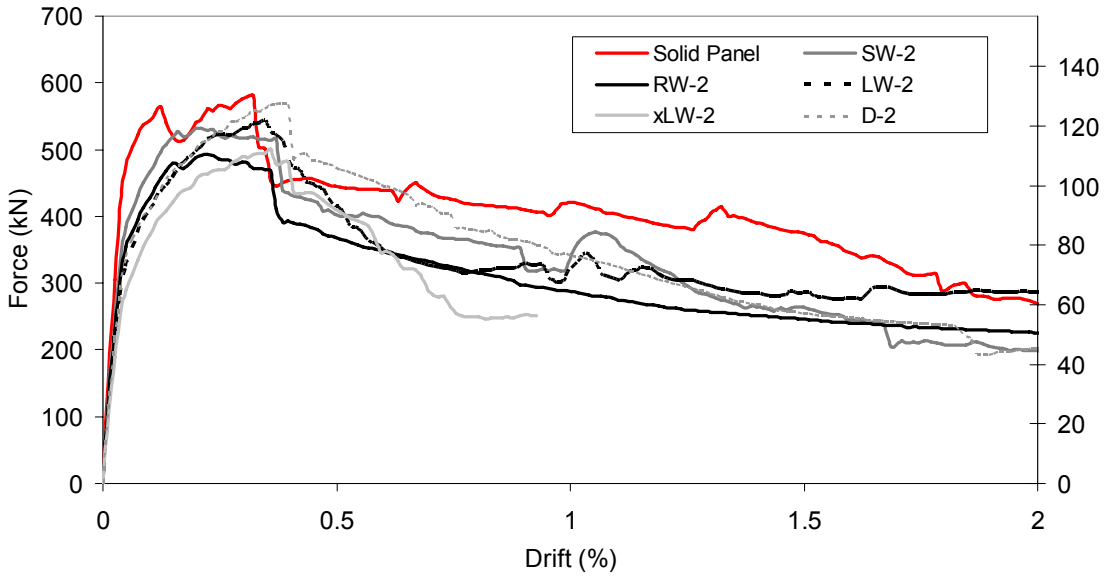

Figure 7.20: Force-vs.-drift curves for XX-2 models.

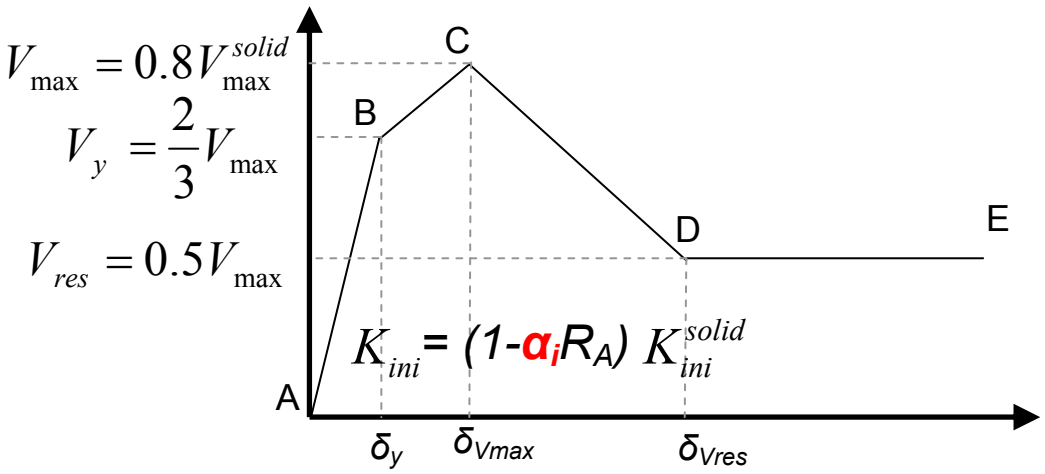

Figure 7.21: Proposed force-vs.-displacement backbone curve for infilled frames with openings.

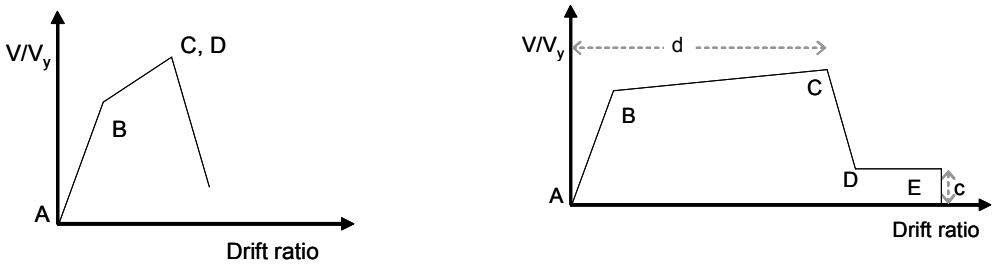

(a) Force-controlled behavior (b) Displacement-controlled behavior

Figure 7.22: Backbone curve for infilled frames used in ASCE 41-06.

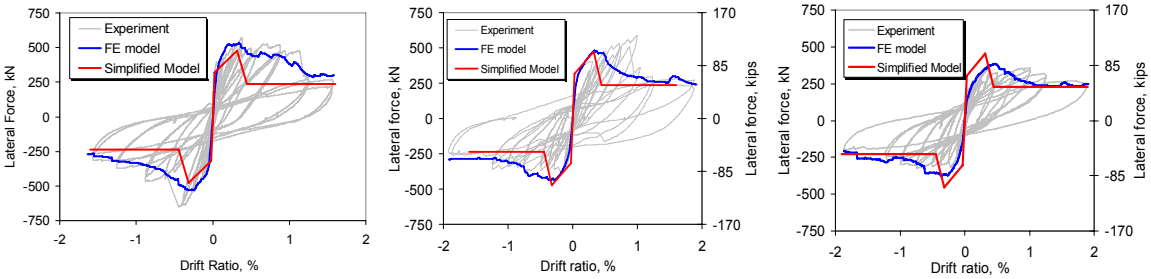

(a) Specimen CU2 (b) Specimen CU5 (c) Specimen CU6

Figure 7.23: Comparison of experimentally and analytically obtained curves for the single-story, single-bay frames with openings tested in CU.

CHAPTER 8

SHAKE-TABLE TESTS OF A THREE-STORY TWO-BAY INFILLED RC FRAME: SPECIMEN DESIGN, TEST SETUP, INSTRUMENTATION, AND MATERIAL PROPERTIES

8.1 Introduction

This chapter discusses the specimen design, test setup, material properties, and instrumentation for the shake-table tests of a three-story, two-bay infilled RC frame. The specimen was a 2/3-scale model of the external frame of the prototype structure presented in Chapter 2 and was the largest structure of this type ever tested on a shake table. The challenges associated with the design of the test specimen involved the incorporation of different gravity and inertia masses, appropriate scaling of the prototype, and the prevention of unrealistic failure modes such as rocking, twisting, and out-of-plane collapse of the frame. During the construction of the specimen, a large number of material samples and small masonry assemblies were obtained and an extensive set of material tests was conducted to obtain the properties of the reinforcing bars, concrete, and masonry materials and assemblies. Special setups were built to measure the tensile and shear properties of the brick-mortar interface due to its influence on the structural behavior according to the sensitivity analysis presented in Chapter 3. The specimen was instrumented with an array of 285 sensors and was subjected to a sequence of 44 dynamic

tests, which are discussed in detail in Chapter 9. Issues associated with the design, scaling, and construction of the test structure are discussed in this chapter. Key results from the material tests are also presented.

8.2 Frame Design

The three-story specimen corresponds to the exterior frame along lines A and D of the prototype structure shown in Figure 4.1, scaled with a length scaling factor of 2/3. The dimensions and reinforcing details of the specimen are presented in Figure 8.1, while the details of the cross sections of the RC members are shown in Figure 8.2.

The design of the column members was modified as compared to the prototype structure to increase the tensile capacity of the columns. This modification was introduced in view of a second specimen, which would be tested to investigate the effectiveness of a retrofit scheme consisting of overlays of Engineered Cementitious Composite (ECC) (Kyriakides 2010) and Fiber Reinforced Polymeric (FRP) materials (Shing et al. 2009). The strengthening of the infill panels of the second frame was expected to increase its lateral strength. To ensure that the RC columns had sufficient capacity to resist the overturning moment, a higher ratio of flexural reinforcement was used in the columns of the specimen as compared to the prototype. The longitudinal reinforcement ratio was increased from 1% to 2% at the first story and 1.5% at the second story since the overturning moment and, therefore, the tensile axial forces in the columns reduce with height. These values of reinforcement ratio are common for existing

structures (Caughey 1936) built in the 1920s, which typically have longitudinal reinforcement ratios within 1% and 4% as discussed in Chapter 4. The amount of flexural reinforcement was not expected to significantly affect the performance of the RC columns, which, according to the quasi-static tests, were anticipated to have a shear dominated failure mode. Moreover, lap splices were not included at the base of the first-story columns to avoid premature lap splice failure, since this is not a characteristic failure mechanism for a structure of this type. The modification of the prototype design was introduced in the unretrofitted specimen considered here to eliminate the differences and facilitate the comparison of the behavior of the two test specimens. Finally, the beam at the roof was modified to be identical to the beams at the two lower stories. This change was introduced to facilitate the construction and has practically no effect on the structural performance.

The infill walls had two wythes of brick units built with Type N mortar consisting of 1 part Portland cement, 1 part lime, and 5 parts sand. Type N was selected due to its workability and resemblance of the mortar found in existing structures built in the 1920s. At each story, the specimen had a solid infill wall in the west bay and an infill wall with an eccentrically located window opening in the east bay as shown in Figure 8.3. The dimensions and location of the window are similar to those of the Specimen CU2 presented in Chapter 5.

8.3 Scaling Considerations

As mentioned in the previous section, the specimen tested on the outdoor shake-table at UCSD corresponds to the external frame along lines A and D of the prototype structure. Since the prototype building has infill walls only on the exterior, the internal frames along lines B, C, and 2 are significantly less stiff and weaker than the external frames. Therefore, their contribution to the lateral resistance of the structure is practically negligible. Although the frames in the interior do not contribute in the lateral resistance, they carry a significant portion of the gravity loads from the floor slabs and joists. As a result, the inertia/seismic mass associated with the external frames is larger than the gravity mass as illustrated in Figure 8.4 by the different tributary areas for the frame along line A.

As discussed in Chapter 6, the vertical loads can affect the performance of an infilled RC frame; therefore it is important to simulate the appropriate loads in the shake-table tests. For a dynamic test, it is also important to maintain the properly scaled inertia forces. Hence, an accurate simulation of the prototype would require the inclusion in the test setup of the scaled mass of half of the prototype together with an auxiliary structure that could carry the gravity load representing the load carried by the internal frames. In such a configuration the auxiliary structure should not add to the lateral strength to the system. However, this was not a feasible solution for the tests discussed here. To address the disparity between the gravitational and seismic masses, concrete blocks were built as floor slabs at each level to simulate the required gravity mass. Furthermore, the

acceleration time-histories were increased in amplitude and compressed in time to generate the inertia forces that satisfy the similitude requirement.

In terms of the scaling factors, this procedure can be summarized as follows. Considering that the gravity acceleration can only have a scaling factor of one, the mass of the specimen, M_{spec}, needed to simulate the gravity mass carried by the external frame of the prototype can be calculated according to the similitude law (Harris and Sabnis 1999).

$$M_{spec} = M_{prot}^{grav} S_L^{\,2} \tag{8.1}$$

in which M_{prot}^{grav} is the gravity mass carried by the external frame of the prototype structure and S_L is the length scaling factor of 2/3. The scaling factor for the seismic mass can be calculated as the ratio of the mass of the specimen, M_{spec}, to the seismic, M_{prot}^{seis}, carried by the exterior frame of the prototype structure.

$$S_m^{seis} = M_{spec} \Big/ M_{prot}^{seis} \tag{8.2}$$

The seismic acceleration scaling factor can be then calculated from the following formula.

$$S_a^{seis} = S_F \Big/ S_m^{seis} \tag{8.3}$$

in which S_F is the scaling factor for the force and can be calculated based on the scaling factors for length, S_L, and stress, S_σ.

$$S_F = S_L^{\ 2} S_\sigma \tag{8.4}$$

The time scaling factor can be then calculated with the following formula.

$$S_t = \sqrt{\frac{S_L}{S_a^{seis}}} \tag{8.5}$$

The scaling factors for all other quantities can be determined according to the similitude requirement from S_L^s, S_m^{seis}, and S_σ, which is the scaling factor for the stress and is equal to one. The scaling factors are summarized in Table 1. A detailed derivation of the scaling factors with two approaches can be found in Appendix B. From this point on, the ground motion levels mentioned in this dissertation are with respect to the full-scale prototype structure. When applied on the specimen, the base motions are modified by the acceleration and time scaling factors.

8.4 Shake Table

The shake-table tests were performed on the Large High Performance Outdoor Shake Table (LHPOST) housed at the Englekirk Structural Engineering Center of the University of California, San Diego (UCSD). This shake table has a 12.20 by 7.62 m (40 by 25 ft) platen and has a vertical payload of 4 MN (900 kips) for 1.28 g peak acceleration and 20 MN (4500 kips) for 0.3g (Restrepo et al. 2005). The table is unidirectional and can generate base excitations along the East-West direction of up to ±0.75 m (±30 in.) of peak displacement, ±1.80 m/sec (±70.8 in./sec) velocity, and ±4.2 g

of acceleration for bare table conditions (Ozcelik et al. 2008). The design, controller, and performance of the LHPOST are described in detail by Van den Einde et al. (2004), Restrepo et al. (2005) and Ozcelik (2008).

8.5 Test Set-Up

The mass required to simulate the gravity loads was attached to the frame shown in Figure 8.1, through the addition of thick slabs at levels 1, 2, and 3. Although the external frame of the prototype is connected to the floor slabs only on one side, the slabs of the specimen extended to both sides of the frame. This configuration was selected to provide symmetry to the test structure and prevent undesired behavior that an eccentric center of mass would cause under dynamic excitation. This adjustment was necessary to represent the behavior of the three-dimensional prototype, in which the centers of mass and rigidity coincide. Therefore, the external frame would not deform out-of-plane under uniaxial base excitation within its plane.

The slabs simulating the gravity mass were designed to be relatively narrow and thick, with an out-of-plane width of 0.97 m (38 in.) and a height of 0.48 m (19 in.). This compact geometry was selected to eliminate issues related to the structural stability introduced by long cantilever slabs. In the roof, the slab dimensions were smaller due to the smaller amount of gravity load which needed to be simulated. If directly connected to the beams of the frame, the thick slabs would act as a single, unrealistically rigid, beam which would prevent any deformation of the beams and joints of the frame. To avoid this

undesired kinematic constraint, a gap of 51 mm (2 in.) was introduced between the slabs and the beams of the frame. Thus, the slabs were only connected to the frame through three transverse beams at each floor. This gap resulted in the creation of four slabs per floor with the configuration illustrated in Figures 8.5 and 8.6. Moreover, at the connection of the slabs with the transverse beams the thickness of the slab was reduced by slots on top and bottom. The slots were 51 mm (2 in.) wide and were arranged in the way shown in Figure 8.7, to form a concrete joint of 102 mm (4 in.) height which would connect the slabs to the transverse beam. The reinforcement connecting the slabs to the transverse beams was bended to form an 'X' inside the joint, as shown in Figure 8.7. This design configuration provided pin supports to the slabs with minimal moment capacity since the joints would crack to allow the relative rotation between the transverse beams and the slabs. The gap between the frame and the slabs in combination with the pin connections between the slabs and the transverse beams enabled the transfer of gravity and inertia forces generated by the mass of the slabs, but minimized the rotational constraints imposed by the slabs to the joints and longitudinal beams of the main frame.

The RC frame and the masonry infills were constructed by professional contractors. The frame was constructed first in four stages that lasted one week each. In the first week, the foundation slab beam was casted. In each of the following weeks, the RC columns of a story together with the concrete slabs of the floor above were casted in a single concrete pour. After the construction of the frame the masonry walls were built in two weeks, with techniques similar to those followed in the 1920s. After the RC frame was constructed, two steel towers were secured on the shake table on the north and south

side of the structure to prevent a potential out-of-plane collapse of the frame during severe shaking. The steel towers did not interact with the structure during the tests due to a 13 mm (0.50 in.) gap between the towers and the specimen. The final test set-up is illustrated in Figure 8.8. Important aspects of the construction are presented in Appendix C together with detailed drawings of the RC structure and details o the reinforcement scheme.

8.6 Instrumentation

An extensive array of sensors was deployed on the specimen and the two steel towers. The instrumentation array included 144 strain gages, 71 displacement transducers, and 59 uniaxial accelerometers. Eleven cameras were used to monitor and record the structural behavior during shaking. Eight of these cameras were mounted on the structure focusing on critical locations of the specimen to record the relative deformations mainly in the first but also the second story. All sensors were sampled at 240 Hz, while the cameras captured 40 frames per second.

Since each accelerometer could measure the acceleration along one direction of motion, metal cubes were attached on the structure to mount the accelerometers on their sides to obtain measurements along X, Y and Z directions, with X being the direction of motion, Y the out-of-plane direction, and Z the vertical direction. Six additional accelerometers were mounted at the middle and at the west end of the foundation slab of the specimen and seven accelerometers were attached on each of the two steel towers to

monitor their response. The locations of all the accelerometers mounted on the structure are illustrated in Figure 8.9, together with the coordinate system. The positive directions of X, Y, and Z do not follow the right-handed Cartesian coordinate system, but are in agreement with the notation used by the controller of the shake table.

The strain gauges were attached on the longitudinal and transverse reinforcing steel bars at the bottom half of the specimen where the damage was anticipated. A total of 52 strain gauges were installed on the longitudinal reinforcement of the second-story columns to monitor the axial force and also the development of strains in the lap-splice region. Another 92 strain gauges were installed along two cross sections near the ends of the beams and columns of the first story. Eight of these strain gauges were damaged during the construction of the concrete frame and the removal of the formwork. This did not present a problem due to the redundancy of the instrumentation scheme, which is demonstrated in Figure 8.10. To achieve more reliable measurements and have a degree of redundancy in the instrumentation, four longitudinal bars, two at each member side of the RC member, were instrumented at each specified location. In the locations where three or more bars existed on the same side, the two corner bars were instrumented. On each bar, two gauges were attached on its north and south sides to measure the deformation of the neutral axis. In the results presented in the following sections, the readings of the two gauges on each bar have been averaged.

The displacement transducers included String Pots (SP) and Linear Variable Differential Transformers (LVDT) which were installed at the locations illustrated in Figure 8.11. They were used to measure support movements, deformations of the frame,

relative deformations of the structural members, and monitor the separation between the frame and the infill.

The most critical of the displacement quantities measured were the displacements of the frame at the floor levels. According to the initial instrumentation plan, these would have been measured with respect to the steel towers with two SPs per floor attached on the slabs and the north and south towers. The initial tests, however, indicated that the motion of the towers was comparable in magnitude to that of the frame and, therefore, contaminated the displacement measurements as shown in Figure 8.12(a). Metal shims and a higher post tensioning force were used to improve the attachment of the towers on the shake table. Furthermore, an alternative solution was provided through the use of LVDTs mounted on cantilever poles of high stiffness and low mass, as shown in Figure 8.13. One pole was installed at each level with an LVDT attached at its top to measure the relative deformation between two consecutive slabs. The interstory displacements were also calculated using the measurements of the SPs installed on the structure. As shown in Figure 8.11, the SPs were attached on the beam-column joints to measure the deformation along the beams and columns and the diagonal deformation of the infill walls. The relative lateral displacement between two floors was obtained using the trigonometric properties of the triangles formed by the string pots. The comparison of the floor displacement values obtained with the two methods indicates an excellent agreement, as shown in Figures 8.12 (a) and (b). Figure 8.12 (b) indicates that the displacements measured by the string pots with respect to the tower show good agreement with the other methods for a test at 100% level of Gilroy. The improvement is

due to the better attachment of the steel towers on the platen which reduced their motion, but more importantly due to the increased structural displacements which reduce the relative importance of the tower motion. Although these factors reduced the error of the measurements of the story displacements with respect to the steel towers for intense base motions, the story displacements presented in this thesis are obtained through the LVDTs and SP. Key components of the instrumentation plan and details of the supports used to mount the sensors on the test specimen are presented in Appendix D.

8.7 Material Properties

An extensive testing program was conducted to obtain the material properties for the RC frame and the masonry walls. The reinforcing steel bars were tested in tension, while typical compressive tests of concrete cylinders, brick units, masonry prisms, as well as mortar cylinders and cubes were conducted using specimens obtained during the construction of the specimen. The prisms included four bricks and three mortar joints, the concrete cylinders were 15 cm (6 in.) in diameter and 30 cm (12 in.) in height while the dimensions for the mortar cylinders were 5 cm (2 in.) in diameter and 10 cm (4 in.) in height and the cubes had dimensions 10x10x20 cm (4x4x8 in). The cylinders were casted in plastic molds, whereas for the cubes, for lack of a standard method, the molds were created by stacking bricks in a way similar to the one described in C1019 (ASTM 2005) for grout. Moreover, tensile splitting tests were conducted for the concrete and mortar cylinders. For every batch of concrete and mortar used in the specimen construction, these tests were conducted at both the 28-day mark after the construction of the respective structural element and also on November 10th, 2008. That day the specimen

was subjected to a Design Basis Earthquake which can be considered to be the first major shake-table test. The average material properties measured on the day of test are summarized in Tables 8.2 for steel, 8.3 for concrete and 8.4 for masonry. Representative stress-vs.-strain relations are included in Appendix E.

The sensitivity study presented in Chapter 3 indicates that the most critical material properties influencing the seismic performance of infilled frames are the properties of the brick-mortar joints. While a number of test methods can be found in literature involving laboratory and in-situ tests (Lourenco 1996, da Porto 2005), two sets of tests were conducted to obtain the properties of the mortar joints. One was the bond wrench test which was used to obtain information on the tensile strength of the brick-mortar interface and the second test was the triplet shear test which involves the shearing of masonry triplets under different but constant normal stresses. The test setup for the bond wrench test was designed according to the testing standard C1072 (ASTM 2000). This testing procedure was selected over the direct tension tests due to the simplicity and stability of the test set up which is illustrated in Figure 8.14. The bond wrench test determines the flexural strength of the mortar-brick interface in masonry prisms by testing one bed joint at a time, as shown in Figure 8.15. Due to the flexural component of the tests, the results can overestimate the actual tensile strength.

Another important test for the characterization of the mortar joints and the brick-mortar interface test is the shear test of masonry triplets. The triplets are assemblies of three bricks connected with mortar joints, with the middle brick being offset 2.5 to 5 cm (1 to 2 in.) with respect to the top and bottom bricks. In a triplet test, the middle brick is

forced to slide against the other two bricks while constant normal pressure is applied on the brick mortar interface. The test setup designed for the triplet tests is presented in Figure 8.16 and consists of four metal rigid plates, held together by four rods. The triplet is placed in between the two middle metal plates which are allowed to slide along the rods. The two external plates are fixed and in one of the two compartments on the left and right of the triplet, a screw and a load cell are located to apply and measure the normal load. In the third compartment springs are installed. The benefit of having the spring force as the reaction to the normal load applied by the screw is that the springs can provide some flexibility to accommodate the dilatation of the mortar joint failing in shear (Mehrabi et al 1994), while maintaining the normal load more or less constant. Therefore, the spring constant should not compress significantly when the normal load is applied, while it can accommodate the dilatation of the mortar joints without imposing significant additional loads. These two conditions impose an upper and a lower bound for the spring constant. In the tests conducted here, for the four different levels of normal stress, 345 kPa (50 psi), 689 kPa (100 psi), 1035 kPa (150 psi), 1380 kPa (200 psi), four different spring constants were used, since the goal was to limit the increase of the normal force due to the dilatation of the mortar joint to less than 5% in all cases. As indicated by the figures in Appendix E, this goal was successfully met.

The most important test results are summarized in Tables 8.5, 8.6, and 8.7 and Figure 8.17, while detailed stress-vs.-strain relations are included in Appendix E. It should be noted that due to the complexity of the test setups for the triplet and bond wrench tests, these tests were conducted 280 days after the construction of the specimens.

Therefore the test results reflect strength values higher than those of the infill walls in the three-story specimen. The strength increase is indicated by the compressive strengths of mortar cylinders, masonry prisms, and the tensile strength of mortar calculated from split cylinder tests are also provided. The specimens for these tests were built and stored together with the prisms and triplets used in the bond wrench and shear tests, and yielded increased strength values compared to similar tests conducted the day of the first major shake-table test. The increase for the compressive strength of masonry prisms was 25% while the mortar cylinders were found to be 15% stronger in compression and 34% stronger in tension. Although it is not straight forward to deduce the exact strengths in tension and shear of the brick-mortar interfaces during the shake-table tests, the values obtained 280 days after the construction can be used with an assumed reduction of 15-20%.

8.8 Conclusions

This chapter discusses the preparations of the shake table tests of a two-third scale external frame of the prototype structure presented in Chapter 5. The test setup included the infilled three-story, two-bay RC frame under investigation and a set of concrete slabs used to simulate the gravity loads. The slabs were attached to the frame through transverse beams and hinges so that they did not impose any kinematic restrictions on the main frame. The mismatch between the inertia and the gravity masses was accounted for through the modification of the scaling factors for the time and horizontal acceleration.

The specimen was heavily instrumented with an extensive array of sensors used to monitor the strains on reinforcing rebars, the accelerations of the specimen at the floor levels and the displacements and deformations of the structural members. Finally, during the construction of the three-story specimen a large number of concrete, mortar, and masonry specimens were constructed so that a set of tests could be conducted to obtain the material properties. Among others, these tests included methods to test the tensile and shear strengths of the mortar joints and the brick-mortar interface. The test results from the dynamic tests of the shake table and the evaluation of the test setups discussed in this chapter are presented in the following chapter.

Tables of Chapter 8

Table 8.1: Scaling factors.

Quantity	Symbol	Scale Factor
Length	S_L	2/3
Elastic modulus	S_E	1.00
Stress	S_σ	1.00
Strain	S_ε	1.00
Curvature	S_κ	3/2
Area	S_A	4/9
Moment of inertia	S_I	16/81
Force	S_F	4/9
Moment	S_M	8/27
Gravity mass	S_m^{grav}	4/9
Gravitational acceleration	S_a^{grav}	1.00
Seismic mass	S_m^{seis}	0.20
Seismic acceleration	S_a^{seis}	2.27
Time	S_T	0.542
Frequency	S_f	1.85

Table 8.2: Average properties of reinforcing steel bars.

Bar #	Type	Nominal Diameter mm (in.)	Yield Stress MPa (ksi)	Tensile Strength MPa (ksi)	Strain at Fracture
2	plain	6.4 (0.250)	431 (62.5)	472 (68.5)	0.091
3	deformed	9.5 (0.375)	521 (75.6)	737 (107)	0.056
4	deformed	12.7 (0.500)	490 (71.0)	772 (112)	0.147
5	deformed	15.9 (0.625)	472 (68.5)	752 (109)	0.130
8	deformed	25.4 (1.000)	424 (61.5)	719 (104)	0.143

Table 8.3: Average concrete properties measured on the day of the first major test (11-10-2008).

Story	Elastic Modulus	Compressive Strength	Strain at Peak Stress	Tensile Strength*
	GPa (ksi)	MPa (ksi)	-	MPa (ksi)
Foundation	15.58 (2259)	35.96 (5.22)	0.0028	3.20 (0.46)
1st Story	15.14 (2195)	37.99 (5.51)	0.0032	3.47 (0.50)
2nd Story	17.44 (2528)	41.95 (6.08)	0.0033	3.96 (0.57)
3rd Story	16.98 (2463)	39.17 (5.68)	0.0032	4.04 (0.568)

* obtained from split-cylinder tests

Table 8.4: Average masonry properties measured on the day of the first major test (11-10-2008).

	Masonry Prism			Brick Unit	Mortar Cylinders		Mortar Cubes
Story	Elastic Modulus	Comp. Strength	Strain at Peak Stress	Comp. Strength	Comp. Strength	Tensile Strength*	Comp. Strength
	GPa (ksi)	MPa (ksi)	-	MPa (ksi)	MPa (ksi)	MPa (ksi)	MPa (ksi)
1st Story	5.41 (0.79)	19.80 (2.87)	0.0045	48.95 (7.10)	4.00 (0.58)	1.06 (0.15)	10.05 (1.46)
2nd Story	6.82 (0.99)	23.61 (3.43)	0.0041	48.95 (7.10)	4.10 (0.59)	1.24 (0.18)	6.41 (0.93)
3rd Story	6.52 (0.95)	22.81 (3.31)	0.0049	48.95 (7.10)	4.33 (0.62)	1.24 (0.18)	10.43 (1.51)

* obtained from split-cylinder tests.

Table 8.5: Shear properties of first-story mortar joints measured 280 days after casting.

Compressive Normal Stress	Peak Shear Strength	Residual Shear Strength	Mortar Joint Tensile Strength	Mortar Cylinder Comp. Strength*	Mortar Cylinder Tensile Strength*	Prism Comp. Strength*
kPa (psi)	kPa (psi)	kPa (psi)	kPa (psi)	MPa (ksi)	MPa (ksi)	MPa (ksi)
344 (50)	637 (93)	462 (67)	448 (65)	4.39 (0.64)	1.68 (0.24)	25.00 (3.63)
689 (100)	841 (122)	724 (105)				
1034 (150)	1193 (173)	1000 (145)				
1379 (200)	1400 (203)	1303 (189)				

*All specimens were casted during the construction of the three-story specimen and were kept in a storage room until the shear tests would be conducted.

Table 8.6: Shear properties of second-story mortar joints measured 280 days after casting**.

Compressive Normal Stress	Peak Shear Strength	Residual Shear Strength	Mortar Joint Tensile Strength	Mortar Cylinder Comp. Strength*	Mortar Cylinder Tensile Strength*	Prism Comp. Strength*
kPa (psi)	kPa (psi)	kPa (psi)	kPa (psi)	MPa (ksi)	MPa (ksi)	MPa (ksi)
344 (50)	938 (136)	359 (52)	554 (80)	4.87 (0.70)	1.69 (0.24)	28.32 (4.11)
689 (100)	841 (122)	710 (103)				
1379 (200)	1475 (214)	-				

*All specimens were casted during the construction of the three-story specimen and were kept in a storage room until the shear tests would be conducted.

** The test sequence is not complete due to the fracture of specimens during transportation.

Table 8.7: Shear properties of third-story mortar joints measured 280 days after casting**.

Compressive Normal Stress	Peak Shear Strength	Residual Shear Strength	Mortar Joint Tensile Strength	Mortar Cylinder Comp. Strength*	Mortar Cylinder Tensile Strength*	Prism Comp. Strength*
kPa (psi)	kPa (psi)	kPa (psi)	kPa (psi)	MPa (ksi)	MPa (ksi)	MPa (ksi)
344 (50)	1000 (145)	476 (69)	495 (72)	5.09 (0.74)	1.40 (0.20)	30.48 (4.42)
1034 (150)	1496 (217)	1027 (149)				

*All specimens were casted during the construction of the three-story specimen and were kept in a storage room until the shear tests would be conducted.

** The test sequence is not complete due to the damage of specimens during transportation.

Figures of Chapter 8

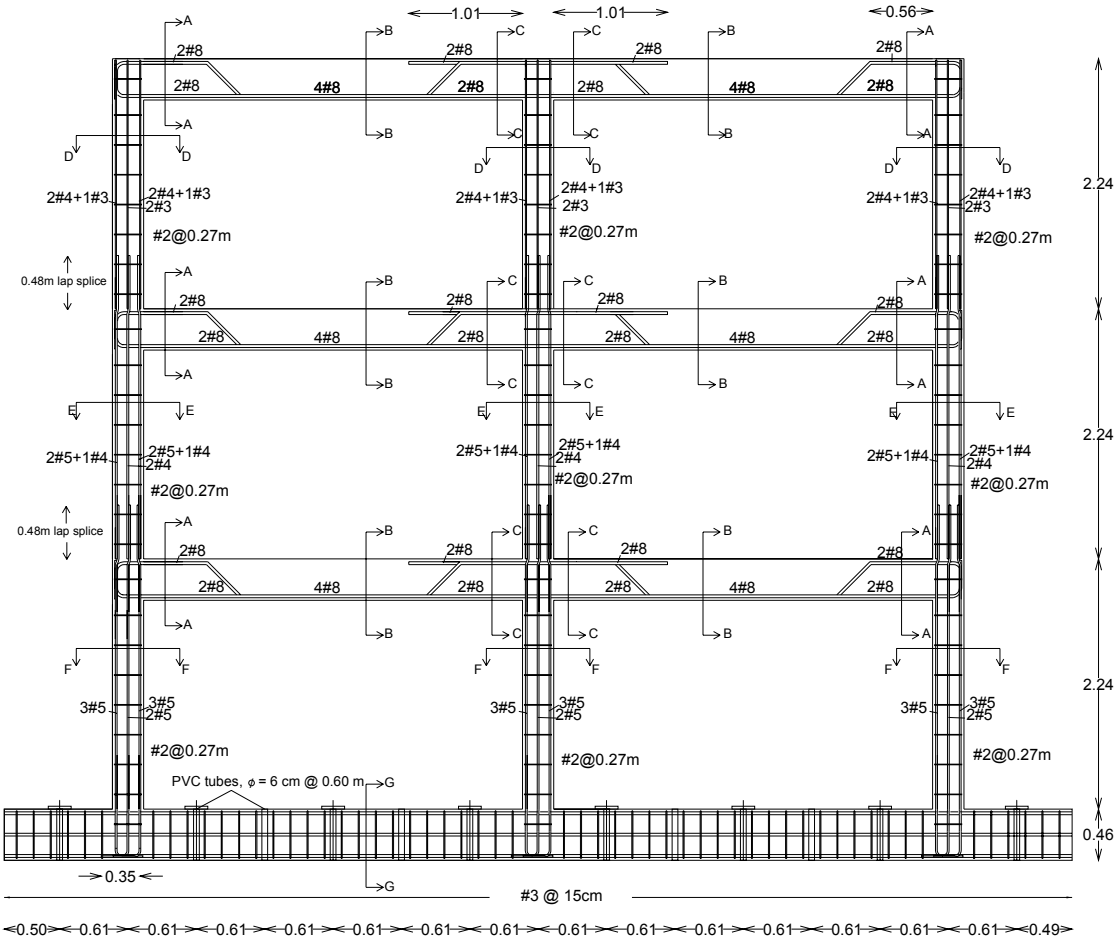

Figure 8.1: Design of three-story specimen tested at UCSD (dimensions in m; for nominal bar diameters, see Appendix A).

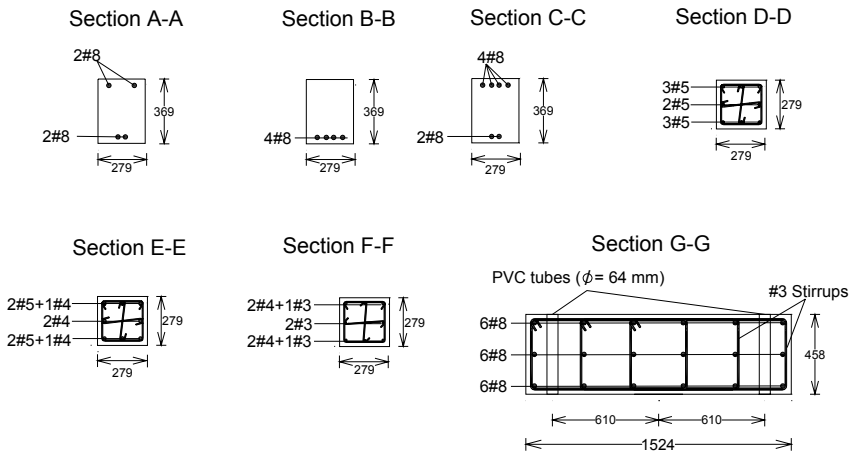

Figure 8.2: Cross sections of RC members (dimensions in mm; for nominal bar diameters see Appendix A).

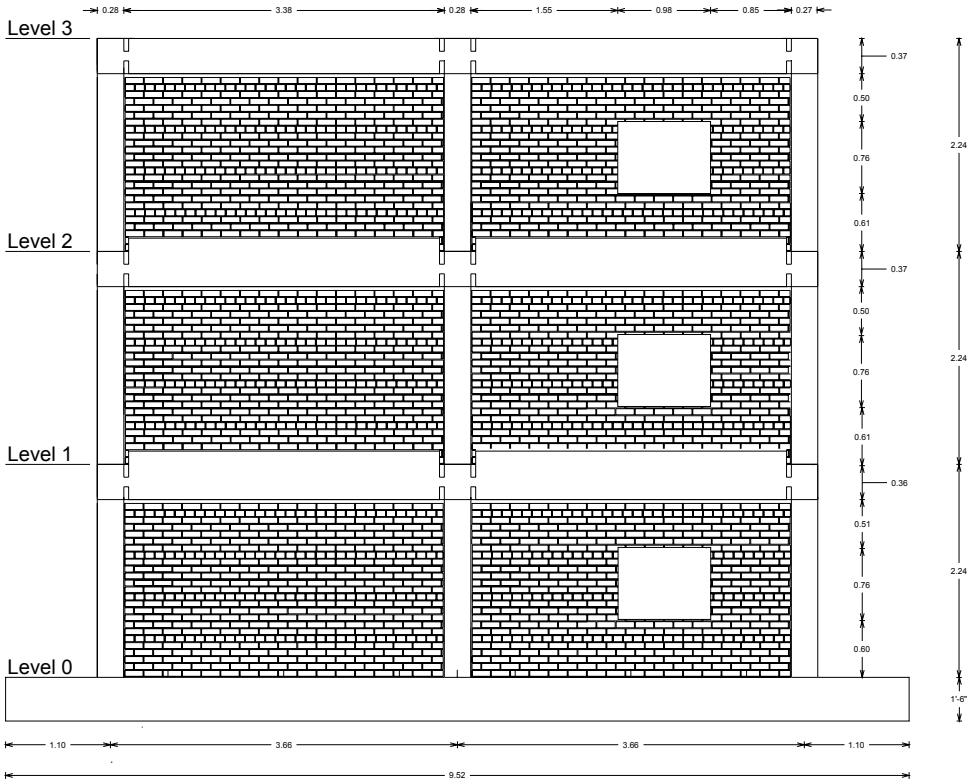

Figure 8.3: Elevation of test specimen (dimensions in m).

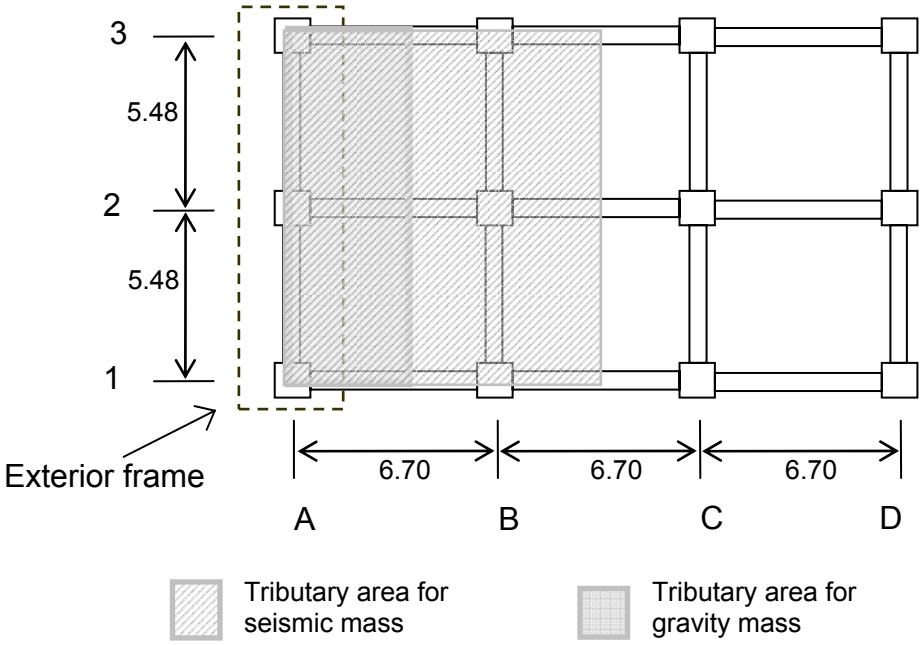

Figure 8.4: Plan view of the prototype structure (dimensions in m).

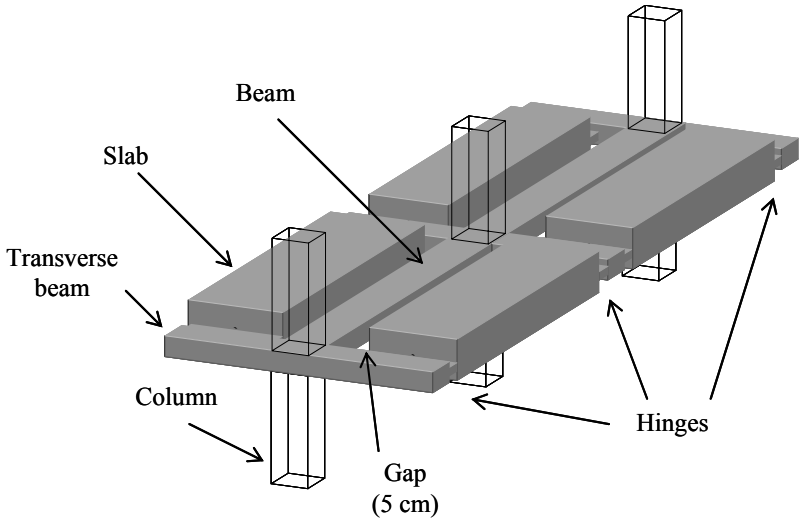

Figure 8.5: Isometric view of the beam-slab configuration.

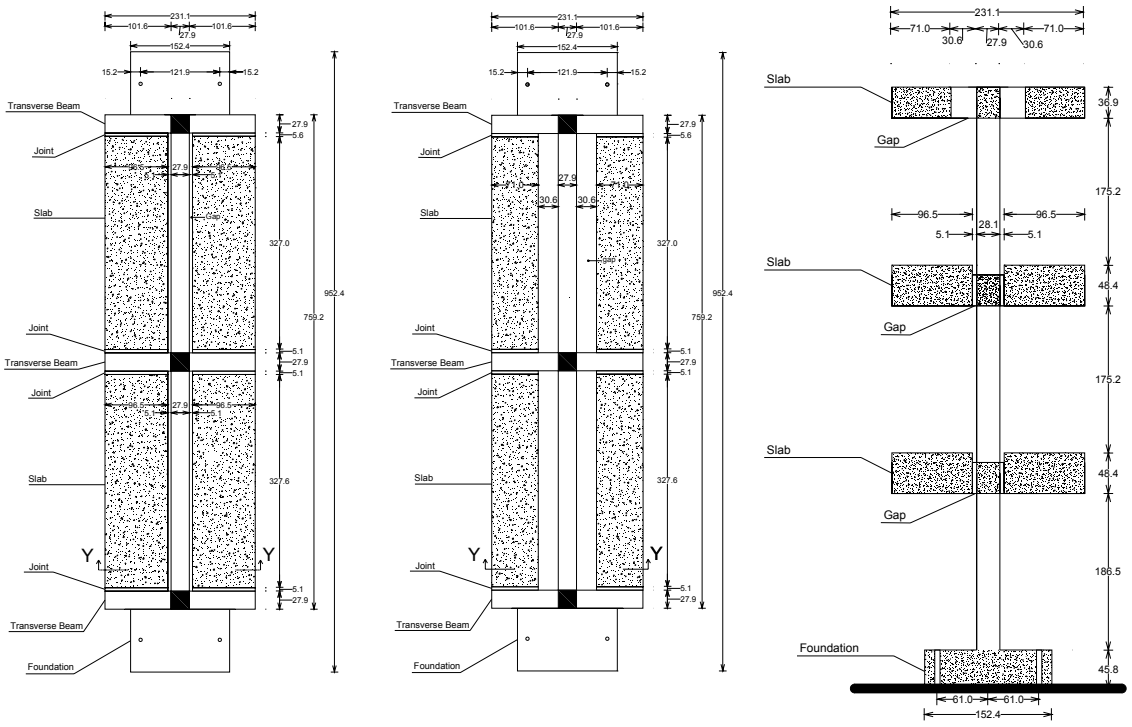

(a) first and second story slabs (b) roof slabs (c) section Y-Y

Figure 8.6: Slabs simulating the gravity load (dimensions in mm).

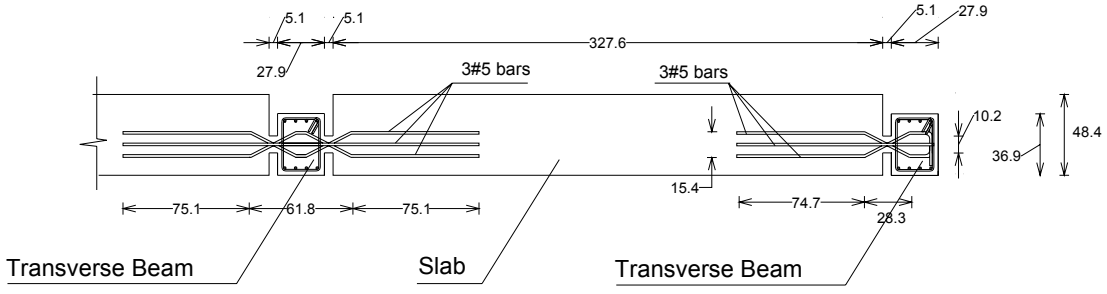

(a) second and third floor

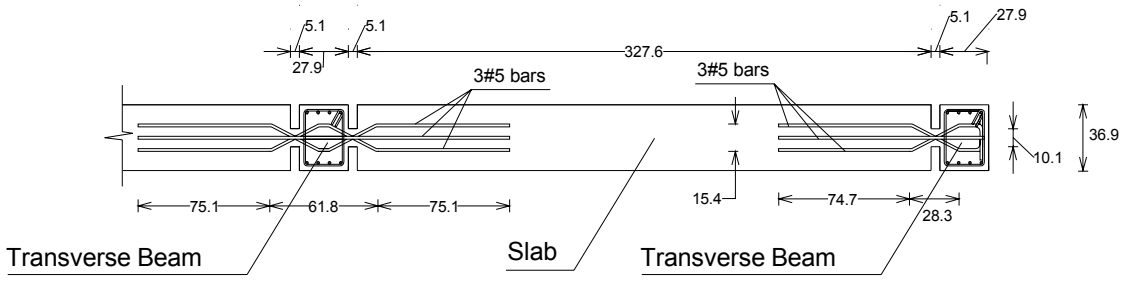

(b) roof

Figure 8.7: Reinforcing detail of slab-to-transverse beam connections (dimensions in mm; for nominal bar diameters see Appendix A).

(a) front view (b) side view

Figure 8.8: Test specimen and set-up.

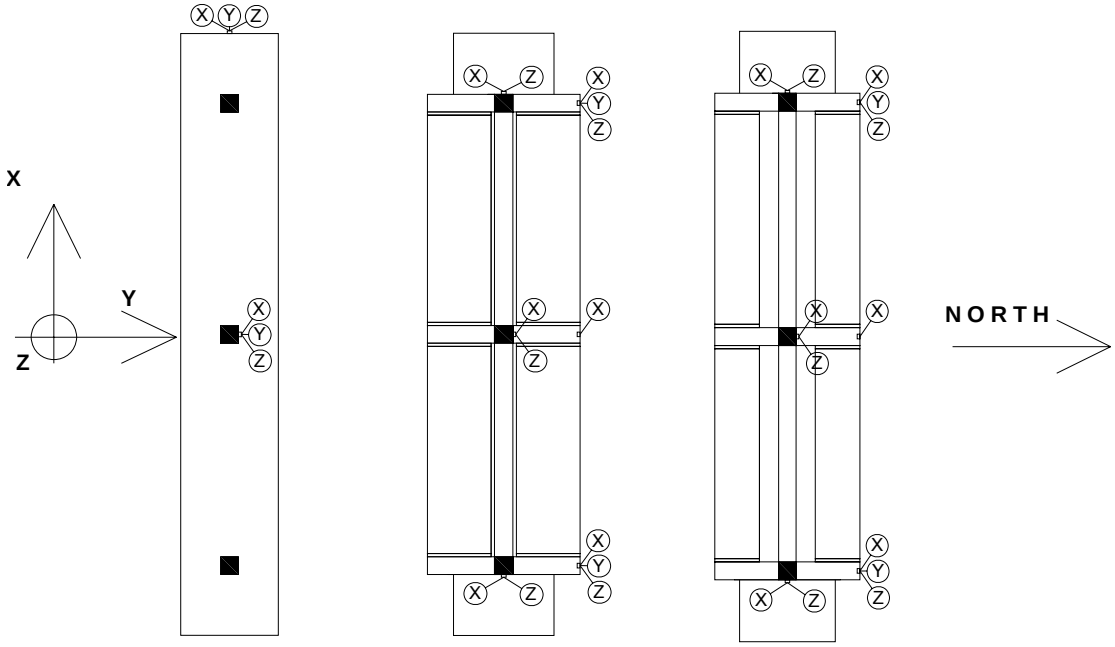

(a) foundation (b) first and second story (c) roof

Figure 8.9: Locations of accelerometers.

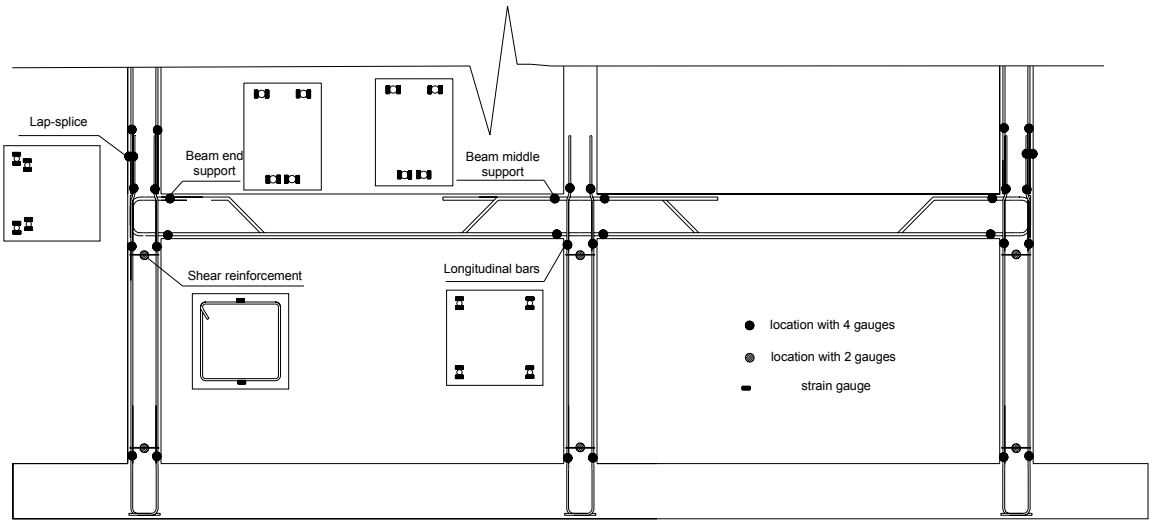

Figure 8.10: Locations of strain-gauges (only the instrumented bars are shown for clarity).

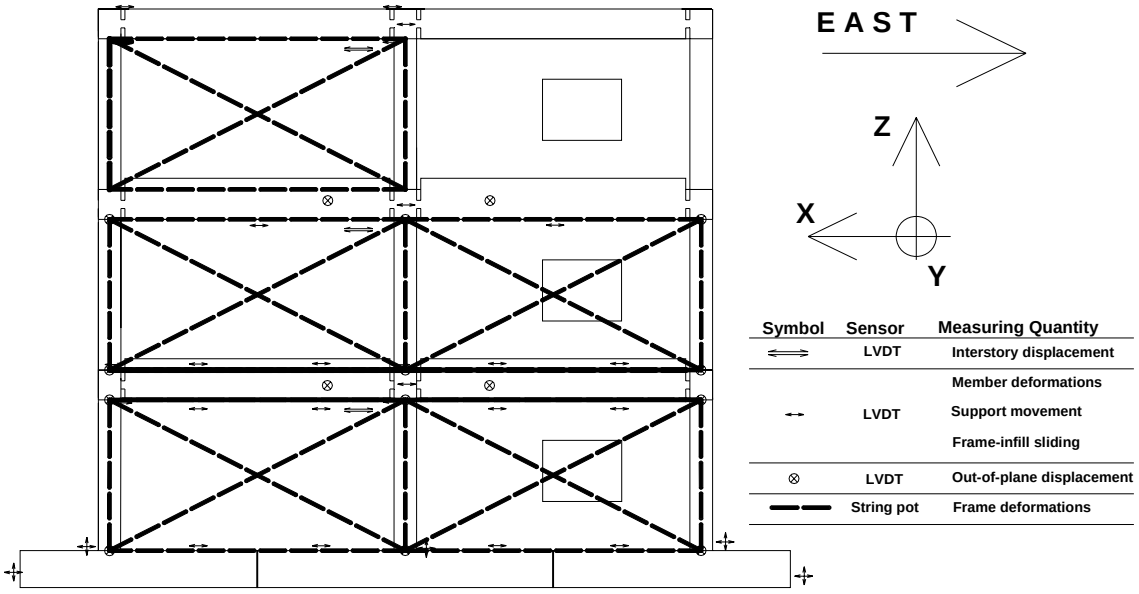

Figure 8.11: Locations of displacement transducers.

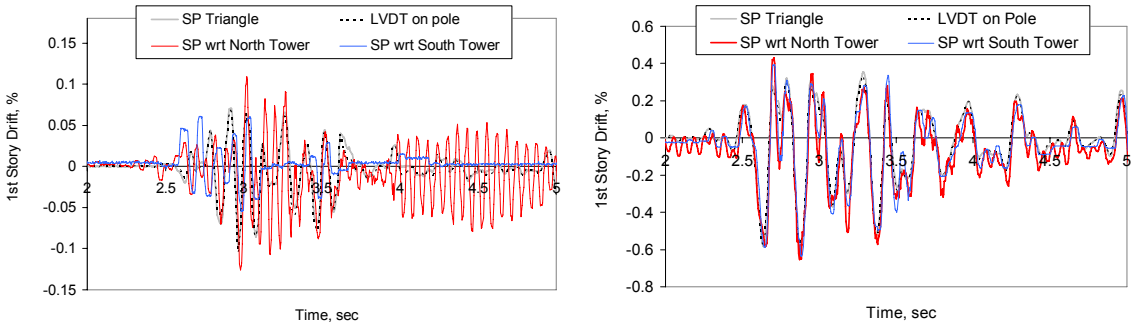

(a) 67% of Gilroy (test 21) (b) 100% of Gilroy (test 35)

Figure 8.12: Comparison of the interstory displacement obtained with different measuring methods.

(a) first and second story poles (b) pole support (c) mounted LVDT

Figure 8.13: Sensors measuring the interstory drift.

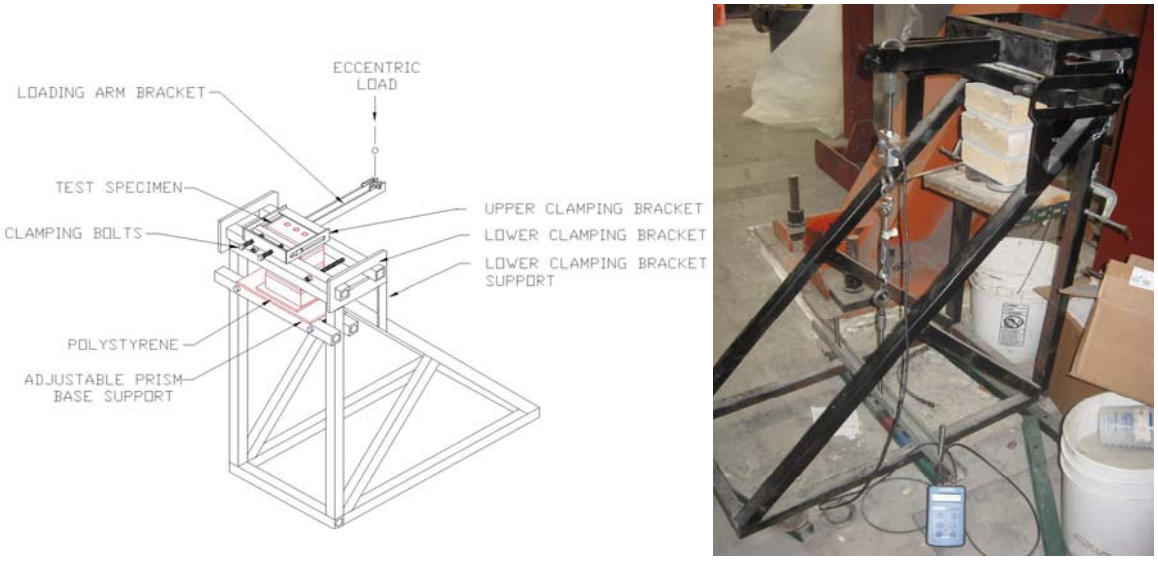

(a) test setup (b) implementation in UCSD

Figure 8.14: Bond wrench test setup.

(a) failed mortar-brick (b) failure surface

Figure 8.15: Bond wrench test specimens.

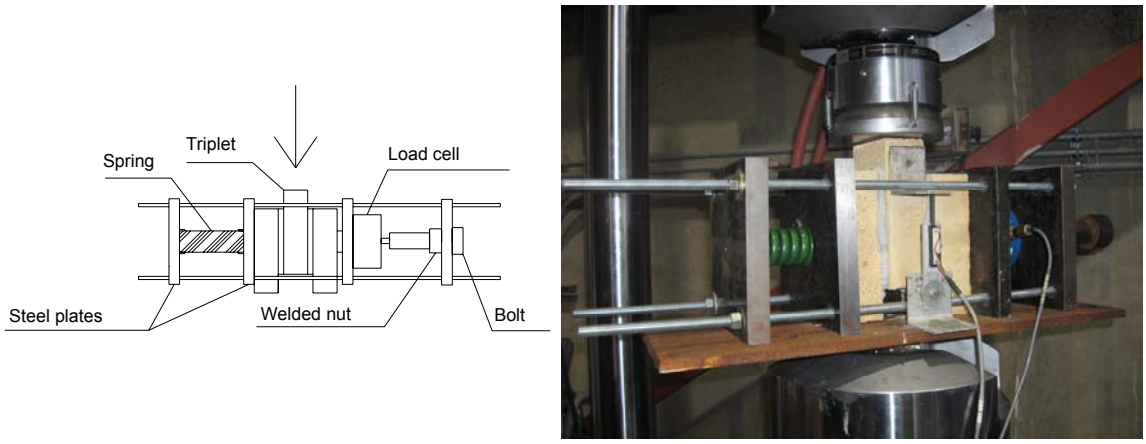

(a) test schematic (b) picture of test setup

Figure 8.16: Shear tests of masonry triplets.

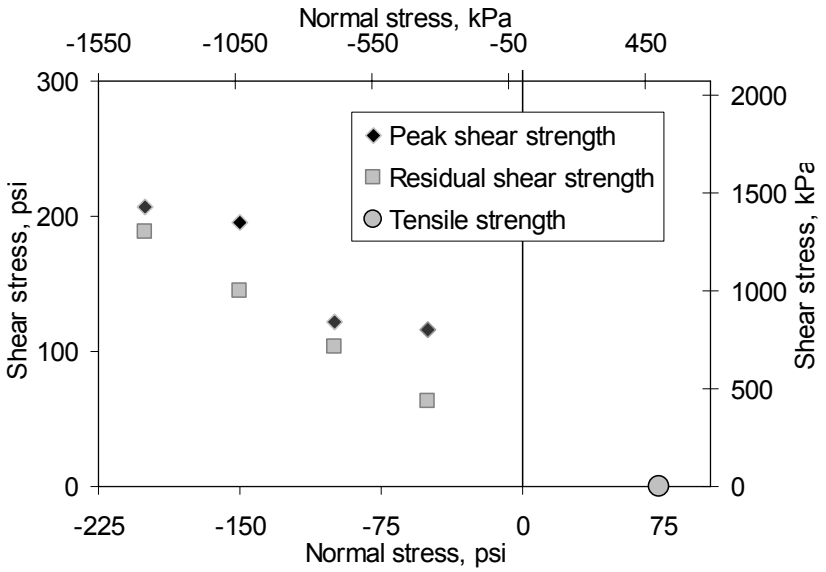

Figure 8.17: Shear and tensile strengths of mortar joints (tested 280 days after the test).

CHAPTER 9

SHAKE-TABLE TESTS OF A THREE-STORY TWO-BAY INFILLED RC FRAME: TEST RESULTS

9.1 Introduction

This chapter discusses the dynamic tests conducted on a three-story, two-bay RC frame infilled with masonry walls. The frame was tested on the unidirectional outdoor shake table located at the Englekirk Structural Engineering Center at UCSD in the fall of 2008. The specimen was a 2/3-scale version of the external frame of the prototype structure presented in Chapter 4. The specimen design, test setup, instrumentation and the properties of the materials used in the construction are discussed in detail Chapter 8. The specimen was subjected to a sequence of 44 dynamic tests with the focus being on 14 scaled earthquake records. The goal of the testing protocol was to gradually induce damage to the structure by subjecting it to ground motions of increasing intensity. The structure was able to sustain a Design Basis Earthquake (DBE) representative of a Seismic Design Category (SDC) D site with minor damage. The damage was more significant when the specimen was subjected to a Maximum Considered Earthquake (MCE). However, it did not collapse despite the damage in the infill panels and the RC columns of the first story. The seismic performance of the structure and the earthquake-induced damage are discussed in detail in this chapter.

9.2 Testing Protocol

The test structure was subjected to a sequence of 44 dynamic tests including ambient-vibration recordings and shake-table tests with input accelerations of white-noise signals and scaled earthquake records. The main goal of the testing sequence was to gradually damage the structure by subjecting it to seismic ground motions of increasing intensity. The ambient vibration of the structure was recorded at the beginning and at the end of each testing day, while the shake table was fixed on six static vertical bearings with the hydraulic system inactive to prevent any motion of the table. Moreover, between the earthquake records, white-noise signals with Root Mean Square (RMS) acceleration amplitudes of 0.03 and 0.04g were used as base excitations. The ambient vibration recordings and the low-amplitude white-noise tests were conducted so that the modal parameters of the structure can be identified, since changes of the identified dynamic properties can be a good indication of the induced damage (Doebling et al. 1996 and 1998, and Moaveni et al. 2009).

The core of the testing sequence involved 14 scaled earthquake motions which were obtained by scaling the acceleration time-histories recorded at the Gilroy 3 station during the 1989 Loma Prieta and at El Centro during the 1940 Imperial Valley earthquake. The two acceleration records are shown in Figure 9.1. It can be noted that the Gilroy 3 record has a Peak Ground Acceleration (PGA) of 0.56 g and the strong motion only lasts for a few seconds. On the other hand, the El Centro record has a lower PGA of

0.31 g with duration of more than 20 seconds. For Seismic Design Category (SDC) D the mapped spectral accelerations (S_S and S_1) for the short and 1-sec periods are 1.50 and 0.60g, respectively (FEMA P695 and ASCE 7-05). Hence, for structures with a natural frequency of 0.1 sec, which is the estimated frequency of the prototype infilled frame considered here, 67% of the Gilroy 3 motion corresponds to a Design Basis Earthquake (DBE). Moreover, for this structure the 100% level of the Gilroy 3 motion corresponds to a maximum considered earthquake (MCE). This correspondence is based on the spectral accelerations for the fundamental period of the undamaged structure and is illustrated in Figure 9.2. For periods slightly larger than the fundamental period of the structure, however, the Gilroy 3 record exceeds the MCE by up to 33%.

Considering the correspondence between the MCE and the Gilroy record and the goal of gradually inducing damage to the structure without over-testing it though, the loading protocol presented in Table 9.1 was assembled. The recording from Gilroy 3 was selected because its original amplitude matches the spectral acceleration of the MCE for this structure. When applied to the test specimen, the accelerograms were compressed in time and scaled in amplitude based on the scaling factors shown in Table 8.1. However, the ground motion levels mentioned in this dissertation are with respect to the prototype.

9.3 White-Noise Tests and Ambient-Vibration Recordings

At the beginning and at the end of every test day, the ambient vibration of the specimen was recorded while the table was locked to prevent any movement. The

purpose for these recordings was to obtain the modal properties of the specimen at the different stages of the testing sequence. However, when processed, the ambient-vibration recordings did not provide useful information due to the level of noise in the recorded signals and the insufficient resolution of the accelerometers.

Between the scaled earthquake records, dynamic tests were conducted with the input to the shake table being white-noise acceleration signals with RMS amplitudes of 0.03 and 0.04 g. The white-noise tests were conducted to provide acceleration recordings for the estimation of the modal parameters of the specimen without inducing any damage to the structure. The estimation of the modal characteristics is important since the changes in the natural periods, damping ratios, and mode shapes are excellent indicators of the damage induced by the earthquake records. The estimation of the modal properties is based on the assumption that at low levels of ground excitation, a damaged structure can be considered as a quasi-linear system. This assumption is only valid for very small deformations since for a damaged structure, the stiffness is not constant and different deformation levels would yield different tangent and secant stiffnesses and different damping values.

Figure 9.3(a) presents the Fourier Amplitude Spectra (FAS) of the accelerograms recorded at the foundation of the structure during white-noise tests 5, 34, and 41 (see Table 9.1), which correspond to the undamaged structure, and to a damaged specimen with minimal and significant damage, respectively. The three spectra significantly deviate from the notion of a white-noise signal due to distinct peaks and troughs. The first major peak in all cases coincides with the oil-column resonant frequency, which is measured at

10.66 Hz for bare table condition (Ozcelik 2008) but decreases when the mass on the platen increases. This peak is followed by a trough caused by the notch filter applied to the command signal sent to the servovalves by the shake-table controller. The second peak indicates an amplification of the motion triggered by the interaction between the shake table and the specimen. The frequency of the second peak is initially at 20 Hz coinciding with the estimated fundamental period of the structure. However, it shifts to lower frequencies for Tests 34 and 41 due to earthquake induced damage which changed the dynamic properties of the structure. Thus, the FAS of the three recordings indicate differences in the frequency content of the base motions. This difference could only be caused by the table-specimen interaction.

The interaction between the shake table and the specimen is also demonstrated in Figure 9.4, which presents the FAS for the longitudinal and vertical acceleration components measured at the foundation of the structure. One can observe that the FAS of the vertical acceleration do not show a distinct peak around the resonance frequency of the shake-table system, but has a second peak at the same frequency range as the second peak of the longitudinal component. The frequency of the second peak changes for the different tests closely following the trend of the longitudinal acceleration. Its amplitude, however, decreases as the damage of the structure increases since the cracks in the specimen tend to isolate the mass of the superstructure from the shake table reducing the interaction between the two in the vertical direction. Another interesting observation on the response of the shake table is the fact that for a uniaxial input motion along X, transverse acceleration along Y was also recorded on the table. As indicated in Figure

9.3b, the amplitude of the unintentional transverse excitation is approximately 10% of the excitation along X.

As demonstrated in Figures 9.3 and 9.4, the dynamic characteristics of the shake table and its interaction with the structure resulted in an input to the structure which deviated from the concept of a white-noise signal. Therefore, an output-only system identification method which considers only the acceleration recordings on the structure would not yield reliable results. Instead, a system identification method that considers both the input motion as well as the structural response was used. The deterministic-stochastic subspace identification (DSI) method which is an input-output method was selected to analyze the white-noise tests. Furthermore, the three components of acceleration along the X, Y, and Z directions were considered to accurately identify the translational but also the torsional natural modes of vibration at ten stages of the loading protocol (Moaveni et al. 2010). Table 9.2 presents the modal properties for the first two longitudinal and torsional modes of the undamaged structure and the evolution of their characteristics due to the accumulating structural damage.

While the behavior of the specimen and the detailed results of each test are discussed in the following sections, a number of observations can be made based on the results from the system identification performed using the recordings from ten white-noise tests. First, the identified natural frequencies decreased consistently as structural damage accumulated due to the earthquake excitations. At the same time the damping ratios increased, reflecting the increased levels of energy dissipated by the damaged specimen. The reduction of the natural frequencies and the increase of damping ratios is

more significant for the translational modes of vibration than for the modes dominated by torsion. The results in Table 9.2 also indicate that the specimen practically remained elastic during the initial low-level earthquakes as the first noticeable deterioration of the structural properties occurred after Test 21 at 67% level of Gilroy, which corresponds to the DBE. Significant change in the structural properties occurred after the structure was subjected to the 100% of Gilroy. The reduction of the first-mode natural frequency by more than 50% can be translated to a reduction of the stiffness to approximately one fourth of its initial value. Finally, the increase of the damping ratio from 2.0% to 15.7% signifies the increase of the energy dissipated by the sliding along the fractured mortar joints.

9.4 Tests with earthquake records

The performance of the three-story specimen during 14 shake-table tests simulating seismic excitation is discussed here. The goal of the testing sequence was to progressively damage the structure through base motions of increasing intensity. Any analysis of the test results after the cracking of the structure should account for the effect of the load history and the pre-existing damage due to earlier tests.

Prior to the tests, the shake table was calibrated to closely reproduce the desired accelerograms. This was achieved by reproducing the time-histories with a bare shake table prior to the construction of the test specimen. Based on the acceleration recorded on the table, the input time-histories were modified with On-Line Iterations (OLIs)

(Filiatrault et al. 2000). OLI is a control technique that repeatedly modifies the command input to the shake table based on the feedback acceleration measured on the bare table. The goal is to fine-tune the table by repeatedly modifying the input acceleration time-history so that the output time-history would provide a close representation of the desired motion (Thoen 2004; Ozcelik 2008). However, due to control issues and the interaction between the table and the specimen discussed in the previous section, the time-histories that the specimen was subjected to were slightly distorted compared to the desired motion.

The difference between the desired ground motion and the base motion measured during the test introduces the need to re-evaluate the scaling coefficients for the recorded motions as percentages of the historical records of Gilroy 3 and El Centro. For an elastic structure this can be achieved by considering the spectral acceleration values of the recorded and desired motions at the fundamental period of the structure. However, the damage induced to the specimen by the test sequence changed the natural periods as presented in Table 9.2. Consequently, the natural period of the undamaged structure cannot be used for the determination of the actual scaling coefficients for the recorded motions applied to damaged structure with a different fundamental period. To address this issue, the fundamental periods estimated from the white-noise tests before and after each seismic test were used to define the lower and upper bounds for the first-mode period during each test. Then, the scaling factor that minimized the difference between spectral values of the original ground motion and of the actual table motion over that period range could be calculated. As shown in Table 9.3, the re-evaluation of the scaling

coefficients indicates that for ground motions up to 91% of Gilroy, the table provided in most cases spectral accelerations slightly lower than the desired ones for the period intervals of interest. For higher excitation levels though, the table amplified the input motions with the 100 and 120% of Gilroy actually reaching 113% and 133% of the original motion.

The re-evaluated scaling coefficients account for the difference between the desired and the obtained base motion and also for the change of the fundamental period of the structure due to the induced damage. They do not account, however, for the disparity between the original Gilroy record and the code spectrum for periods different than the initial period of the structure. As illustrated in Figure 9.2, the Gilroy 3 spectrum precisely matches the MCE acceleration spectrum considered here for the initial period of the structure. Nonetheless, for other structural periods the difference between the two spectra can be significant. For instance, between 0.11 and 0.26 sec, the original Gilroy time-history is considerably more intense than the MCE. According to the results of the system identification presented in Table 9.3, the dominant period of the structure changes drastically during the testing sequence due to the induced damage. Therefore, another coefficient was needed to directly compare the recorded base motion with the MCE spectrum defined by FEMA P695 (2009). The coefficient selected here is the average value of the ratio of the spectral acceleration of the recorded motion to the corresponding values of the MCE for the period range defined by the values of the first modal period before and after each test.

The scaling coefficients obtained with this method are included in Table 9.3 to provide a more accurate picture of the excitation levels. For the tests beyond the elastic range, gil91 was as intense as the MCE while gil100 and gil120 are considerably higher for the relevant range of periods. Hence, the base motion in gil100 was 13% higher than the intended record, but if the difference between the original Gilroy record and the MCE is considered for periods between 0.14 and 0.26 sec, the structure was subjected to a motion 43% more intense than the MCE. Similarly, gil120 was 55% more demanding than the MCE, while the test with the El Centro motion was practically as demanding as the MCE. From this point on, the initially assigned scaling factors are used in this dissertation to identify the tests, although these values are only the nominal values reflecting the intended level.

9.4.1 Low amplitude tests

The initial phase of testing involved low amplitude tests conducted to study the structural behavior in the elastic range. The initial part of the testing sequence included one test at 10% of Gilroy 3, three tests at 20%, and two tests at 40%. The 20% and 40% level tests were repeated to resolve issues related to the supports of the steel towers, the instrumentation, and the control of the shake table. The elastic response spectra for the six recorded base motions are presented in Figure 9.5. The small differences between the response spectra of the records obtained from the same excitation levels were caused by

the different OLIs which were used to generate these motions while issues related to the control algorithm of the shake table were being addressed.

Thorough inspections of the test specimen after each test indicated that the structure did not sustain any visible damage during the first six tests. The experimental observation is in agreement with the results of the system identification, which are presented in Table 9.2 and indicate insignificant changes of the modal characteristics of the structure until the gil67a test. The differences in the modal periods and damping ratios observed in white-noise Tests 5, 9, and 13 are minimal and within the margin of error of the system identification method. Therefore, they are of no practical interest as the structure can be considered elastic during the first six earthquake tests.

Table 9.4 summarizes the maximum values of selected response quantities measured during the tests. The peak values of roof acceleration, base shear, and overturning moment, closely follow the increase or decrease of the re-evaluated scaling coefficients which have been based on the spectral acceleration value of the recorded ground motion for a period equal to the fundamental period of the specimen and 5% damping. The peak deformation and strain values are extremely low and are indicative of the minimal structural deformations during the initial tests.

Some general remarks on the structural behavior can be made considering the information presented in Figures 9.6 to 9.12. Figure 9.6(a) illustrates the maximum relative story displacements normalized with respect to the frame height. In all cases, most of the deformation occurs in the first story. The profile of peak floor accelerations

normalized with the Peak Ground Acceleration (PGA) for each motion is presented in Figure 9.6(b). In all cases the PGA is recorded in the negative direction and the peak acceleration value is 1 to 15% lower, while in the original record the difference is 3%. The peak floor accelerations appear to vary linearly with height with the only exception being the values recorded during the gil10. This is the only case that a hyperbolic curve would be more appropriate to describe the acceleration profile.

In Figure 9.7(a) the effective height is presented. This is defined as the height at which the equivalent force that could result in the same peak shear force and the peak overturning moment as the ground motion. The test data indicates that the effective height is 4.28 m (168 in.), which corresponds to a height equal to 1.92 times the story height. Accounting for the reduced roof mass of the test specimen, the commonly assumed uniform and inverse triangular distributions would yield effective heights of 1.83 and 2.15 times the story height. Thus, the actual force distribution is closer to the uniform distribution, although a trapezoidal distribution of lateral forces would be a more accurate representation. Figure 9.7(b) presents the ratio of the peak base shear to the product of the mass of the structure and the first-mode spectral acceleration. This ratio is more-or-less constant with a value of 0.88. Finally, the base shear-vs.-the first story inter-story drift is shown in Figure 9.8 for the last two tests, gil20c and gil40b, of the initial part of the testing sequence. The story shear forces are calculated as the products of the average readings of the six accelerometers measuring the story accelerations along the X-direction and the corresponding story masses. The first story shear force is the summation of the three forces.

Among the six initial earthquake tests, only test gil40b is discussed here in detail for brevity. This test is selected since it was the most intense of the initial set of tests. The time-histories of the inter-story drifts and shear forces are illustrated Figure 9.9. Although the shear forces were fairly well distributed in the three stories throughout the seismic event, the structural deformations concentrated in the first story. The peak drift value in the first story is ten times the peak value in either of the other two stories signifying a soft-story dominated response. Figure 9.10 presents the time-histories of the strains measured on the longitudinal and transverse column reinforcement measured at the locations indicated in Figure 8.10. From the strain distribution it is evident that the east and west columns sustained larger axial deformations than the middle. In all cases, the highest strains were recorded at the bottom cross sections of the first story. The readings from the gauges on the stirrups indicate that strains in the middle column are about 40% of those in the external columns, but in all cases the strains at the top and bottom sections of each column are of similar magnitude.

Figure 9.11 presents the measurements of the displacement transducers used to monitor the sliding between the infill walls and the first story and foundation beams. The recorded values are within the level of noise of the instrument and practically indicate that no sliding occurred until this point in the testing sequence. Therefore, it can be assumed that the structure deformed monolithically during this set of tests. However, it is interesting to observe the rotation of the hinges supporting the east slabs at the first and third levels, which are illustrated in Figure 9.12. Although the angles are small, it can be

observed that the hinges on the first story were activated, even for small deformations of the structure in the elastic range.

9.4.2 67% of Gilroy

The 67% of the Gilroy 3 record corresponds to a design level earthquake for SDC D, as demonstrated in Figure 9.2. A second test was conducted at this excitation level to study the effect of the loading history on the structural performance after the specimen sustained mild inelastic deformations under the first test at this excitation level. In between the two tests, a low level test was performed at 20% of the Gilroy record. The purpose for this test was to compare the response with tests gil20a, gil20c, and gil20d and examine if the minimal damage induced by a design basis earthquake would alter the response of the structure to a low intensity seismic event. The response spectra of the two 67% ground motions are shown in Figure 9.13.

The fundamental period of the structure increased from 0.056 to 0.063 sec after these two tests were performed. Although not significant, the increase of the period and the damping ratio indicate the first noticeable change of the structural properties. At the same time, the characteristics of the other three identified modes practically did not change as shown in Table 9.2. The slight damage which caused the change in the dynamic characteristics was verified by the inspection of the specimen after the gil67a test. This test caused the development of the first observable cracks in the first story of the structure. In the west bay, which had a solid panel, the cracks developed at the

interface between the infill wall and the bounding frame, as shown in Figure 9.14. In the panel with the opening in the east bay, the crack initiation resembled the quasi-static test of specimen CU2 discussed in Chapter 5. In this panel, the cracks radiated from the window corners, as shown in Figure 9.15. Despite the cracks in the infill and the separation between the infill and the frame, the structure could be considered structurally safe. A real building with this extent of damage would only require minor cosmetic repairs. After the gil67b, a quick inspection indicated that no new cracks developed while the existing cracks propagated further around the frame-infill interface in the west bay and in the infill around the window of the east bay.

A summary of the tests and the peak values of selected response quantities are provided in Table 9.5. It is interesting to note that although the PGA was higher during gil67a, gil67b had a higher spectral acceleration for the period of the structure measured before and after the test. Consequently, the re-evaluated scaling factor was higher for the gil67b test. This is illustrated in the acceleration response spectra of Figure 9.13. The test results indicate that the test gil67b caused larger displacements and shear forces. The higher demand during the second test is also depicted in the values of peak roof acceleration and overturning moment, while the strains also appear to be considerably larger for the second test. These findings justify the re-evaluation of the scaling factors based on the spectral accelerations.

The significant difference in the structural response cannot be justified only by the difference in the earthquake loads. The increase in all deformation quantities included in Table 9.6 also reflects the effect of the loading history since the structure was not in the

same state prior to the two tests due to the cracks which developed during gil67a. The damage sustained during gil67a altered its stiffness and affected the structural behavior during gil67b.

More insight into the behavior of the structure is provided by Figures 9.16, 9.17, and 9.18. Figure 9.16 presents the profiles of peak story displacements and shear forces. It is interesting to note that although the peak shear forces did not change significantly for the two tests, the deformation of the structure was considerably increased in the case of gil67b. This nonlinear behavior is evident in Figure 9.17, where a yielding point appears in both directions of loading during the tests at 67% of Gilroy. In the positive direction, the shear force at the base increased in the second test and actually reached the highest value exhibited by the structure in this direction during the entire testing sequence. On the other hand, in the negative direction, the structural behavior resembles an elastic-perfectly plastic behavior. The difference in the two loading directions and between the two tests can be observed in the frame-infill sliding presented in Figure 9.18. In both cases, sliding occurs at the top of the west bay (solid panel) and is larger when the structure deforms towards the east which is the negative direction for the inter-story drift.

9.4.3 83% and 91% of Gilroy

Two tests were conducted at 83% and 91% levels of Gilroy. The response spectra for the recorded base motions are shown in Figure 9.19. These levels were intermediate levels between the 67% and 100% of Gilroy which were considered to represent a DBE

and an MCE respectively. This correspondence is only valid for the undamaged structure though. Considering the fundamental period of the damaged structure and the recorded base motion, although the re-evaluated scaling coefficient for gil91 is 83%, it could be considered the MCE level test according to the information provided in Table 9.3.

The peak base shear reached in the negative direction during gil83 was the highest shear force recorded during all tests and, hence, it corresponds to the strength of the structure. This test also caused the first noticeable damage in the RC frame. As shown in Figures 9.20 and 9.21, a set of horizontal and diagonal cracks developed in both infill panels in the first story of the specimen and minor cracks appeared near the top of the west and middle of the first story columns. Moreover, cracks in the interface between the RC frame and the masonry panel were observed in the second story for the first time. The crack pattern in the east bay of the first story was similar to the pattern observed in the quasistatic test of the CU2 specimen discussed in Chapter 5, as the cracks opened around the window and propagated towards the columns. In the west bay of the first story, two major horizontal sliding cracks developed. Close to the columns, the cracks had a 30^{o} inclination near the top of the west column and the mid-height of the middle column. This crack pattern was created by the seismic forces acting towards the east end of the specimen, which correspond to negative shear forces according to the sign convention used in analysis of the test results.

The cracking pattern after the gil83 test, shown in Figures 9.20 and 9.21 caused noticeable damage, but would not threaten the structural safety of an actual building. It is important to note, though, that it drastically changed the structural behavior, as indicated

in Table 9.7, which presents the peak values of selected response quantities for the tests at 83 and 91% levels of Gilroy. The values in the table are indicative of the nonlinear behavior since gil91, which is a more intense seismic even in terms of PGA and spectral acceleration, caused lower peak shear force, moment, and roof acceleration than the 83% test. During gil91, the first-story drift increased by 43% despite the lower peak value of the base shear. Moreover, the peak axial strain in the columns was reduced by 15% while the peak strain recorded on the stirrups increased 55%.

The peak strain values indicate that the specimen did not move as a monolithic wall as in the previous tests when the infill resisted the lateral forces and the RC columns resisted the overturning moment. Instead, the damage in the infill decreased its resistance and the RC frame was exposed to a larger portion of the lateral load which caused an increase of the frame deformations. The frame action is indicated by the increase of the peak strain on the beam reinforcement by more than 120%, while the peak rotation of the slab hinges was three times larger than during the 83% test. The change in the loading conditions of the frame is depicted in Figure 9.22 which presents the axial strains, curvature, and strain on stirrups for the middle columns for the two tests. The strain of the stirrups was close to the yield value and was the highest value of strain noted in any column as indicated in Table 9.8. This signifies a substantial difference as compared to the strain distribution shown in Figure 9.10 for the elastic structure under the gil40b excitation. During that test, the middle column registered the lowest strains among the three columns in the first story considering both the longitudinal and the transverse reinforcement. The other difference between the tests is the ratio of strains recorded on

stirrups to strains recorded on longitudinal bars increased from 0.4 to 1.5 for the middle column in test gil91%. The trend of increased transverse strains and reduced axial strains is common for the east and west columns. In Table 9.8 the residual values are also presented; however, up to this excitation level, the residual strains and deformations are small and are probably caused by cracks in the concrete frame as the yielding strain of the reinforcement has not been reached.

The profiles of peak story displacements and shear forces are shown in Figure 9.23. As mentioned earlier, the behavior in the negative direction of loading in test gil91 is indicative of the nonlinear behavior, as it registers the largest first story displacement despite the lowest peak shear force value noted in any direction for the two tests. The same conclusion can be derived from Figure 9.24 which presents the lateral load-vs.-drift relation for the first story. The reduction of the stiffness of the specimen in the negative direction during the gil91 as a result of the sustained damage can be also observed in the figure.

9.4.4 100% and 120% of Gilroy

The elastic response spectra of the base motions recorded during the gil100 and gil120 tests are presented in Figure 9.25. The 100% level of the Gilroy 3 record corresponds to an MCE event for the structure under consideration at its initial state, while the 120% level represents an even more intense and rare seismic event. However, these excitations were applied to a damaged structure. Considering the period of the

damaged structure and the amplification of the input motion due to the shake table dynamics the motion recorded at the base of the structure during the gil100 was 13% higher than the original Gilroy record in terms of the spectral acceleration for the fundamental period of the structure during the test. Moreover, considering the disparity between the Gilroy record and the code-defined spectrum (FEMA P695), this test was 43% higher than the MCE for the range of periods estimated with the white-noise excitation before and after the seismic test. Similarly, the gil120 test corresponds to 133% of Gilroy 3 but in terms of the MCE considered here, it is 55% higher. The updated scaling factors together with the existing damage induced by the previous tests should be considered in the analysis of the test results.

The crack pattern developed in first and second stories of the specimen after the gil100 is presented in Figures 9.26, 9.27, and 9.28. The cracks at the east and west ends of the first story after the 100% level tests strongly resemble the cracking pattern of the single-bay, single-story CU1 and CU2 specimens tested in CU. However, a different pattern developed around the middle column. As shown in Figure 9.27(b), in this middle section of the first story cracks only developed in the upper half of the infill frame, contrary to the cracks developing near the bottom of the leeward column in the single-bay, quasi-static tests. Figure 9.28 presents the cracking pattern in the second story which only involves horizontal tensile cracks on the west column and separation between the frame and the infill. Overall, the structure sustained significant damage which concentrated in the first story. A real building with similar damage after a seismic event

would be safely occupied provided that extensive repairs were carried out in the infill and columns.

The structure was heavily damaged after the 120% level test as illustrated in Figures 9.29 through 9.31, with the more important damage noted in the middle column. As shown in Figure 9.30(b), severe diagonal cracks developed at 2/3 of the column height and were a result of the pre-existing crack pattern in the infill. As depicted in Figure 9.27(b), after the gil100 test two major sliding cracks developed in the panel in the east bay, while one crack at a height in-between these cracks developed in the solid panel of the west bay. During the 120% test, the cracks of the east panel propagated through as diagonal shear cracks in the middle column to form continuous cracks spanning the infills in the two bays and the column in-between. Hence it provided a continuous sliding surface where damage would concentrate. Dominant cracks also developed in the top of the west column and bottom of the east column as shown in Figure 9.30(a) and (c). On the second story of the specimen a minor horizontal crack developed at the bottom of the west panel, which was probably a result of tensile failure of the joint. This crack combined with the horizontal cracks of the west and middle columns may be indicative of the bending stresses developing in the second story. The infill wall in the east bay developed minor cracks radiating from the window corners. The damage in the second story is shown in Figure 9.31, while the inspection of the third story did not reveal the development of any visible cracks. In view of the accumulation of damage by the tests up to this point, a real structure with similar extent of damage would probably be beyond repair if conventional repair techniques were considered.

The extensive damage sustained by the structure under the gil100 and gil120 tests is depicted in the peak values of major response quantities presented in Table 9.9. Despite the larger PGAs and spectral accelerations compared to the gil91 test, the roof acceleration, base shear, and overturning moment did not increase in these tests due to the nonlinearity in the response and the energy dissipation. Indicative of the specimen's ability to dissipate energy at these damage states are the damping values above 10%, which the system identification estimated for the structure after the gil91 test. The deformation-related quantities, however, increased drastically during the gil100 and gil120 tests as the peak first-story drift was 0.55 and 1.06% respectively.

Table 9.10 summarizes the peak and residual strain values in the beams and columns. These indicate that the longitudinal and transverse column reinforcement yielded in all three columns, with the exception of the stirrups in the east column. The table also indicates significant residual strains after the 120% test in the three columns, while Figure 9.32 shows the strains in the east column for the two tests. The large values of strain recorded at the bottom of the first story columns justify the decision made prior the construction of the specimen to eliminate the lap-splices and use continuous rebars in the first story. According to the values in these tables, the beams were not loaded axially but rotated, as the rotation of the slabs hinges points out. Finally, during these tests, the out-of-plane displacement increased compared to the previous tests and in the gil120, it covered half of the gap provided between the structure and the steel towers.

The normalized story lateral force and displacement along the height of the structure are presented in Figure 9.33 while the first-story shear-vs.-drift relation is

illustrated in Figure 9.34. During the gil120 test, the peak value of first-story drift was doubled as compared to that during the gil100 test. However, the structural damage capped the shear force which did not exceed the peak values registered in previous tests. It is also interesting to note that the structural behavior was not symmetric in the two directions of loading. The non-symmetrical behavior was more pronounced in the gil120 test during which the same level of lateral force resulted in a 100% larger displacement in the negative direction compared to the positive direction. Approximately one quarter of the displacement in this direction was residual displacement at the end of the test as the specimen did not return to its initial position. The residual deformations on the structure can be observed through the displacement time histories recorded by the displacement transducers located at the interface between the RC horizontal members and the infill walls in the first two stories which are presented in Figure 9.35.

9.4.5 250% of El Centro

After gil120, the fundamental period of the structure had shifted due to the induced damage to 0.18 sec, which is beyond the spectral peak of the scaled Gilroy record. Therefore, it was decided to use the acceleration record obtained in El Centro during the 1940 Imperial Valley Earthquake. The record was appropriately scaled in amplitude and compressed in time to satisfy the similitude requirement. As shown in Figure 9.36, this record has the advantage that it closely follows the shape of the response spectra used in the building codes. Based on the estimated structural period before the

test, a scaling factor of 250% was assigned to the scaled record to match the MCE spectrum.

The ec250 was a rather destructive test for the specimen. During the test, a significant portion of the east bay masonry panel collapsed on the table and wide shear cracks dismantled the three columns of the first story, as shown in Figure 9.37 and 9.38. At the end of the test, the structure could not carry its own weight and was leaning against the support towers. If it had not been for the steel towers, the structure would have collapsed on the shake table. The analysis of the recordings indicated that the specimen failed early during the ec250 test by moving out-of-plane. A shown in Figure 9.39, by the constant out-of-plane displacement the towers prevented the collapse by continuously supporting the structure until the end of the test. As indicated by Figure 9.39(b), the specimen failed out-of-plane at the very early stages of the ground motion. In a real structure, the RC members in the planes transverse to the tested frame would have supported the structure and prevented this collapse mechanism. Therefore, a real structure would have probably behaved in-plane in a manner similar to the test structure. However, there is no method available to estimate the forces developed between the towers and the specimen and this hinders the extraction of meaningful conclusions for the larger part of the recorded test data.

Despite the undesired out-of-plane failure, it is interesting to observe the failure mechanism shown in Figures 9.37 and 9.38 since it represents a possible mechanism for real structures. The most impressive failure was the shear crack that developed near the bottom of the east column which was the leeward column for loading along the negative

direction. This failure occurred early in the test and was followed by the gradual collapse of the infill wall in the east bay of the specimen as it was not confined against moving eastwards. This was the wall that included a window. The latter played an important role not only in the development of the cracks which initiated at its corners, but also in reducing the out-of-plane stability of the infill panel, when two triangular pieces of the masonry wall detached from the rest of the wall. The same triangles had formed around the windows in the CU2 and CU6 tests which included windows as discussed in Chapter 5. However, as shown in Figures 5.11 and 5.20, in the static tests the triangles remained within the wall, and supported the lintel beam and the masonry above the window. In the dynamic tests, these triangular pieces fell outside of the plane of the frame and as a result the unsupported lintel beam collapsed in the following cycles of motion. This dramatic post-peak behavior cannot be simulated in the quasi-static tests; nonetheless it could occur in a real earthquake as illustrated in Figure 1.1. This difference demonstrates the need for dynamic tests.

9.5 Observations Regarding the Structural Behavior

The sequence of tests conducted on the outdoor shake table has provided a remarkable amount of data and insight on the seismic behavior of RC frame with a non-ductile design which are infilled with masonry walls. The most important results are presented in the previous section, while a more detailed set of figures is included in Appendices F and G.

In this section, an overview of the structural behavior and the range of values of some critical quantities are presented for the ensemble of the seismic tests. Table 9.11 summarizes the state of the structure after each test and associates the first-story drift with the damage observed and the repair needed if the structure is repairable. From this table, it can be observed that the first-story drift reached 0.55% for major cracks to develop. This value is significantly higher than the 0.3% drift that is specified in ASCE 41-06 as the drift beyond which drastic loss of shear resistance is observed. Moreover, it is important to mention that the structure having sustained that level of damage was able to maintain its integrity when subjected to a base motion with spectral accelerations 55% higher than the spectral accelerations corresponding to an MCE as specified by FEMA P695 (2009). Moreover, based on the testing protocol, it can be claimed that the structure behaved in a satisfactory manner as it survived a sequence of six base motions exceeding the DBE, without being repaired between the tests.

9.5.1 Story Shear and Drift

The first-story lateral force-vs.-drift relation for the six more intense tests under the Gilroy excitation is illustrated in Figure 9.40. The most significant features of the load-vs.-displacement curve are the yield point at drift of 0.05% and the insignificant loss of strength as the specimen maintained 95% of the peak lateral strength until a drift of 1.06% despite the damage it sustained. Moreover, one can note the reduction of stiffness and the increased area of the hysteresis loops as the intensity of the base motion

increased. It is also evident that due to the loss of strength the displacement of the first story increased drastically during the last set of tests. This increase of the inter-story drift was limited to the first story as the peak values for the second and third story were in all cases a fraction of the first-story drift and did not exceed 0.10%. This is indicated in Figure 9.41 but it was also directly observed after the tests through the minimal cracking of the second story and the lack of cracks in the third story of the specimen. In terms of the peak shear forces, it is interesting to note that in the last six tests, the shear force distribution did not change by the accumulation of damage as shown in Figure 9.44. The peak shear force in the positive direction was reached during the gil67b test and in the negative direction during the gil83 test at drifts of 0.166% and 0.28% respectively, as shown in Figure 9.42.

The nonlinear relation between the lateral force and the lateral drift is a result of the damage sustained by the structure. The drop of the base shear with respect to a reference value calculated from the elastic response spectra considering the initial period of the structure but also the period before each test is presented in Figure 9.43. The reference value is used here as a scaling quantity of the experimentally measured base shear. During the elastic range the ratio between the peak base shear and the equivalent elastically calculated force is close to 0.9 and it is the same for the two normalization methods as essentially the same period is used in the calculation. After the gil67a test, the induced damage differentiates the two periods and therefore the corresponding spectral acceleration values. However, for both normalization methods the same trend is followed as the ratio of the measured base shear with respect to the equivalent elastic force shifts to

lower values. Eventually, if the initial period is used the ratio drops to 0.46 for the gil120 test. If the period before the test is considered, the ratio drops even further to 0.27.

Another interesting observation can be made with regards to the distribution of lateral forces along the height of the structure. As shown in Figure 9.44, the ratios remained practically constant throughout the tests. The shear force in the third story was around 28% of the base shear while in the second story the shear force was around 67% of the total force. The consistency in the distribution of the story shear forces is interesting considering the peak acceleration profiles shown in Figure 9.45(a). The peak story accelerations did not increase linearly with height as illustrated in Figure 9.6(b) for the undamaged specimen. Instead, the normalized values indicate that the amplification of the base acceleration was smaller for the damaged structure and the peak floor accelerations tend to be equal to the PGA for gil100 and gil120. Considering the values of peak roof acceleration presented in Tables 9.5, 9.7, and 9.9 for the six tests, it can be observed that the damage of the specimen limited the story acceleration and as the PGA value increased for the strong tests, the peak story accelerations tended to be uniform. The same observation can be made if Figure 9.45(b) is considered. This figure shows that the peak story accelerations, normalized by the spectral acceleration decreased as the damage accumulated and the ground motion intensity increased.

9.5.2 Out-of-plane displacements and hinge rotations

The out-of-plane behavior of the specimen and the rotation of the slab hinges were monitored throughout the testing sequence to evaluate the effectiveness of the design of the test setup. Figure 9.46 presents the peak values of these quantities during each test. It can be observed that both hinges in the first story rotated, allowing the relative rotations of the concrete joints. The rotations appear to be initially negligible, although as Figure 9.11 indicates the hinges were activated even during the low level tests. Up to this point the structure moved as a rigid block, sustaining minor deformations and strains. However, this changed when the structure sustained some damage and the rotations increased after the DBE level tests. It is interesting to point out that the rotation in the middle support was larger than the rotation in the east end. This is expected if the deformed mesh of the laterally loaded structure is considered since the middle joint of the frame would rotate due to the deformation of both beams, while the end joint rotates due to the deformation of the east beam only.

In terms of the out-of-plane displacement, the value is relatively small, especially if the out-of-plane excitation induced due to eccentricities of the shake table is considered. The X and Y components of the base acceleration recorded during the ec250 are shown in Figure 9.47. The peak amplitude of the out-of-plane component was 0.15 g and corresponds to 8% of the peak longitudinal acceleration. Despite the input transverse acceleration and the unavoidable eccentricities of the structure, the out-of-plane motion of the structure is minimal. In all the tests beyond the elastic range of the structure the

displacement perpendicular to the plane of the structure on the third floor was less than 1% of the first story in-plane displacement.

9.5.3 Lap Splice

As stated earlier, in a previous section, eliminating the lap-splice of the longitudinal rebars was a wise decision due to the large strains that developed in these bars in the last three seismic tests. In the second story, however, the lap splice was maintained and the two external corner rebars in the east and west columns were instrumented to monitor the transfer of strains. However, no satisfactory results were obtained. As shown in Figure 9.48 for the east column under the gil67a excitation, the highest strains were recorded on the first story bar ending in this region, and at the cross-section in the middle of the lap splice region. This behavior was not expected and a possible explanation would be the development of micro-cracks in the concrete that locally increased the strains on these bars.

9.6 Conclusions

The shake table tests of a two-third scale external frame of the prototype structure presented in Chapter 5 were discussed in this chapter. The specimen was subjected to 44 dynamic tests including ambient vibration recordings, white-noise tests, and 14 tests of

appropriately scaled historic ground motions. The goal of the testing protocol was to gradually damage the specimen with the seismic tests of increasing intensity while the recordings from the white-noise tests were used to identify the modal properties at every damage state, and also re-evaluate the scaling factors based on the actual recordings and the spectral accelerations for the dominant mode of the structure.

The frame behaved elastically until it was subjected to a design level earthquake. Under this excitation, the first minor cracks developed in the first-story panels initiating along the frame-infill interface and around the window corners. As the intensity of the base motions increased, the structure sustained damage which concentrated in the first-story masonry walls. The horizontal and diagonal shear-sliding cracks in the infill panels eventually propagated through the columns. As the damage accumulated, the first dominant shear cracks in the columns developed during the gil100 test; however, they were not wide enough to threaten the structural integrity of the specimen until the structure was subjected to a seismic event exceeding the demand of an MCE by 50%. Up to this point, the structure was able to maintain its shear capacity despite being subjected to six base motions exceeding the DBE demand. Although the structure practically collapsed in a spectacular manner during the initial cycles of a seventh high-intensity motion, the sequence of tests provided a remarkable amount of data and useful information on the behavior and failure mode of infilled RC frames.

Tables of Chapter 9

Table 9.1: Testing Protocol.

Date	Test
Friday, 31 October 2008	1. Free vibration after a longitudinal instant excitation 2. Free vibration after a torsional instant excitation 3. 10 min ambient vibration
Monday, 3 November 2008	4. 10 min ambient vibration 5. 5 minutes "white" noise 0.3-25Hz RMS=0.03g 6. 10% of GIL3C 7. 5 minutes "white" noise 0.3-25Hz RMS=0.03g 8. 20% of GIL3C 9. 5 minutes "white" noise 0.3-25Hz RMS=0.03g 10. 10 min ambient vibration
Thursday, 6 November 2008	11. 10 min ambient vibration 12. 40% of GIL3C 13. 5 minutes "white" noise 0.3-25Hz RMS=0.03g 14. 10 min ambient vibration
Monday, 10 November 2008	15. 10 min ambient vibration 16. 20% of GIL3C 17. 5 minutes "white" noise 0.3-25Hz RMS=0.04g 18. 20% of GIL3C 19. 40% of GIL3C 20. 5 minutes "white" noise 0.3-25Hz RMS=0.04g 21. 67% of GIL3C 22. 5 minutes "white" noise 0.3-25Hz RMS=0.04g 23. 20% of GIL3C
Wednesday, 12 November 2008	24. 10 min ambient vibration 25. 5 minutes "white" noise 0.3-25Hz RMS=0.04g 26. 67% of GIL3C 27. 5 minutes "white" noise 0.3-25Hz RMS=0.04g 28. 83% of GIL3C 29. 5 minutes "white" noise 0.3-25Hz RMS=0.04g 30. 10 min ambient vibration
Thursday, 13 November 2008	31. 10 min ambient vibration 32. 5 minutes "white" noise 0.3-25Hz RMS=0.04g 33. 91 % of GIL3C 34. 5 minutes "white" noise 0.3-25Hz RMS=0.04g 35. 100% of GIL3C 36. 5 minutes "white" noise 0.3-25Hz RMS=0.04g 37. 10 min ambient vibration
Tuesday, 18 November 2008	38. 10 min ambient vibration 39. 5 minutes "white" noise 0.3-25Hz RMS=0.04g 40. 120% of GIL3C 41. 5 minutes "white" noise 0.3-25Hz RMS=0.04g 42. 10 min ambient vibration 43. 250% of ELC 1940 44. 10 min ambient vibration

Table 9.2: Identified modal parameters.

White-noise test	Preceding earthquake test(s)	1st-L Mode		1st-T Mode		2nd-L Mode		2nd-T Mode	
		f (Hz)	ξ (%)	f (Hz)	ξ (%)	f (Hz)	ξ (%)	f (Hz)	ξ (%)
5	none	18.1	2.0	21.2	1.5	41.2	1.1	57.8	1.1
9	10% of Gilroy 3 20% of Gilroy 3	18.1	2.4	21.0	1.5	41.1	1.0	57.4	1.3
13	40% of Gilroy 3	18.0	1.9	21.3	1.3	41.6	1.0	58.0	1.0
22	20% of Gilroy 3 20% of Gilroy 3 40% of Gilroy 3 67% of Gilroy 3	16.7	3.3	20.8	1.5	40.2	1.4	56.3	0.7
25	20% of Gilroy 3	16.5	3.37	-	-	39.6	1.3	54.9	1.1
27	67% of Gilroy 3	15.9	3.8	20.2	1.8	38.6	3.0	54.6	1.2
29	83% of Gilroy 3	14.8	6.1	19.7	1.5	35.5	4.4	52.7	2.1
34	91% of Gilroy 3	13.5	12.2	18.1	-	32.1	5.0	48.7	2.3
36	100% of Gilroy 3	8.5	15.7	18.2	1.5	27.3	4.8	46.0	2.1
1141	120% of Gilroy 3	5.3	15.6	17.4	1.6	22.6	4.2	43.3	2.7

Table 9.3: Re-evaluated scaling coefficients.

Test ID	Test Name	Nominal Scale Factor	Re-evaluated scale coefficient	$S_a^{i\,recorded} / S_a^{MCE}$ *
6	gil10	10% of Gilroy 3	8%	0.08
8	gil20a	20% of Gilroy 3	16%	0.16
12	gil40a	40% of Gilroy 3	40%	0.39
16	gil20b	20% of Gilroy 3	17%	0.16
18	gil20c	20% of Gilroy 3	17%	0.16
19	gil40b	40% of Gilroy 3	44%	0.42
21	gil67a	67% of Gilroy 3	65%	0.64
23	gil20d	20% of Gilroy 3	14%	0.14
26	gil67b	67% of Gilroy 3	69%	0.69
28	gil83	83% of Gilroy 3	73%	0.77
33	gil91	91% of Gilroy 3	83%	0.96
35	gil100	100% of Gilroy 3	113%	1.43
40	gil120	120% of Gilroy 3	133%	1.55
43	ec250	250% of El Centro**	256%	1.03

*The average ratio of spectral acceleration of the recorded base motion to that of an MCE in the period range defined by the fundamental period before and after each test.
**the re-evaluated scale factor for this motion is based on the structural period before the test since no white-noise test could be conducted afterwards due to severe damage.

Table 9.4: Peak values of selected structural response quantities obtained during the initial low excitation level tests.

Quantity		gil10	gil20a	gil40a	gil20b	gil20c	gil40b
Actual scale factor	[%]	8	16	40	17	17	44
PGA	[g]	0.14	0.27	0.69	0.32	0.34	0.79
S_a (T_1=0.056)	[g]	0.23	0.46	1.17	0.49	0.50	1.29
Roof Acceleration	[g]	0.26	0.51	1.14	0.53	0.53	1.27
Base shear	[kN] (kips)	127 (28.5)	254 (57.2)	606 (136.3)	275 (61.8)	286 (64.2)	623 (140.1)
Overturning moment	[kN-m] (Kips-ft)	555 (4916)	1096 (9703)	2575 (22790)	1173 (10381)	1202 (10643)	2663 (23569)
First story drift	[%]	-	-	-	0.0019	0.0023	0.0113
Column axial strain	[x10^{-6}]	29	66	499	68	71	337
Beam axial strain	[x10^{-6}]	18	21	21	8	7	11
Strain of column stirrups	[x10^{-6}]	46	11	21	10	10	19
Out-of-plane displacement	[mm] (in)	0.15 (0.006)	0.16 (0.006)	0.49 (0.019)	0.25 (0.010)	0.29 (0.011)	0.55 (0.021)

Table 9.5: Peak values of selected response quantities recorded during tests gil67a, gil20d, and gil67b.

Quantity		gil67a	gil20d	gil67b
Actual scale factor	[%]	65	14	69
PGA	[g]	1.14	0.28	1.03
S_a $(T_1)^*$	[g]	1.98	0.47	2.34
Roof Acceleration	[g]	1.90	0.47	2.25
Base shear	[kN] (kips)	907 (204)	246 (36.1)	1131 (254)
Overturning moment	[kN-m] (Kips-ft)	35434 (4003)	9189 (1038)	39528 (4466)
First story drift	[%]	0.097	0.015	0.166
Column axial strain	[x10^{-6}]	908	68	1384
Beam axial strain	[x10^{-6}]	96	25	206
Strain of column stirrups	[x10^{-6}]	195	72	653
Hinge rotation	[deg]	0.0085	0.0036	0.0120
Out-of-plane displacement	[mm] (in)	1.8 (0.07)	0.5 (0.02)	2.54 (0.10)

*The first mode period identified before each test is used.

Table 9.6: Peak and residual values of deformation quantities recorded during tests gil67a and gil67b.

		gil67a		gil67b	
	Quantity	peak	residual	peak	residual
Inter-story drift [%]	1st story	0.097	-0.004	0.166	-0.004
	2nd story	0.001	0.000	0.031	0.000
	3rd story	0.001	0.000	0.035	0.001
Axial strain [x10^{-6}]	West column	806	39	1149	10
	Middle column	736	31	1029	42
	East column	908	16	1384	25
	West beam	96	15	206	32
	East beam	55	16	93	22
Transverse strain [x10^{-6}]	West column	195	66	653	71
	Middle column	64	29	233	81
	East column	100	30	156	35

Table 9.7: Peak values of selected response quantities recorded during tests gil83 and gil91.

Quantity		gil83	gil91
Actual scale factor	[%]	73%	83%
PGA	[g]	1.16	1.29
$S_a (T_1)^*$	[g]	2.70	3.34
Roof Acceleration	[g]	2.38	2.36
Base shear	[kN] (kips)	1143 (257)	1133 (254)
Overturning moment	[kN-m] (Kips-ft)	4627 (40953)	4390 (38858)
First story drift	[%]	0.28	0.40
Column axial strain	[x10^{-6}]	1683	1427
Beam axial strain	[x10^{-6}]	206	456
Strain of column stirrups	[x10^{-6}]	1053	1637
Hinge rotation	[deg]	0.02	0.06
Out-of-plane displacement	[mm] (in)	2.9 (0.12)	4.6 (0.18)

*The first mode period identified before each test is used.

Table 9.8: Peak and residual values of deformation quantities recorded during tests gil83 and gil91.

		gil83		gil91	
	Quantity	peak	residual	peak	residual
Inter-story drift [%]	1st story	0.28	-0.014	0.40	-0.023
	2nd story	0.04	0.001	0.07	0.002
	3rd story	0.07	0.001	0.08	0.002
Axial strain [x10^{-6}]	West column	1682	47	1427	-205
	Middle column	1285	70	1076	59
	East column	1556	-122	1380	-223
	West beam	456	50	360	58
	East beam	117	30	179	57
Transverse strain [x10^{-6}]	West column	1053	282	1292	282
	Middle column	708	124	1636	150
	East column	149	53	397	127

Table 9.9: Peak values of selected response quantities recorded during tests gil100 and gil120.

Quantity		gil100	gil120
Actual scale factor	[%]	113%	133%
PGA	[g]	1.59	1.90
$S_a\ (T_1)^*$	[g]	3.9	6.5
Roof Acceleration	[g]	2.38	2.43
Base shear	[kN] (kips)	1081 (243)	1082 (243)
Overturning moment	[kN-m] (Kips-ft)	4631 (40993)	4799 (42474)
First story drift	[%]	0.55	1.06
Column axial strain	[$x10^{-6}$]	3464	6435
Beam axial strain	[$x10^{-6}$]	380	509
Strain of column stirrups	[$x10^{-6}$]	2470	7847
Hinge rotation	[deg]	0.09	0.12
Out-of-plane displacement	[mm] (in)	6.1 (0.24)	9.5 (0.37)

*The first mode period identified before each test is used.

Table 9.10: Peak and residual values of deformation quantities recorded during tests gil100 and gil120.

		gil100		gil120	
	Quantity	peak	residual	Peak	residual
Inter-story drift [%]	1st story	0.55	-0.03	1.06	-0.24
	2nd story	0.07	0.00	0.10	0.00
	3rd story	0.10	0.00	0.03	0.00
Axial strain [x10^{-6}]	West column	2322	327	2426	1125
	Middle column	1586	266	4360	1447
	East column	3463	1595	6435	3391
	West beam	248	85	343	85
	East beam	380	73	510	81
Transverse strain [x10^{-6}]	West column	2470	210	-7847	-911
	Middle column	1673	125	2065	899
	East column	760	149	380	143

Table 9.11: Association of peak first-story drift and structural damage.

Test	No damage (no repair)	Minor damage (no repair)	Some damage (some repair)	Major damage (extensive repair)	Major damage (beyond repair)	Collapse
gil10 through gil40b	0.011%					
gil67a		0.097%				
gil20d		0.015%				
gil67b		0.116%				
gil83			0.28%			
gil91			0.40%			
gil100				0.55%		
gil120					1.06%	
ec250						x

Figures of Chapter 9

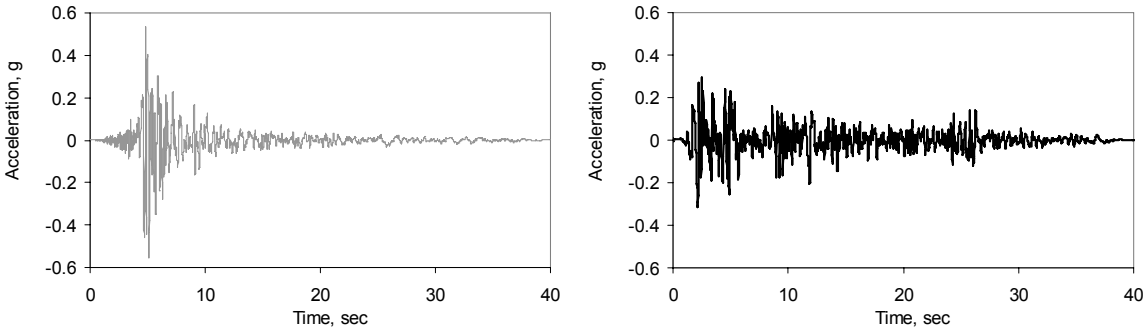

(a) Gilroy 3 (1989) (b) El Centro (1940)

Figure 9.1: Acceleration time-histories.

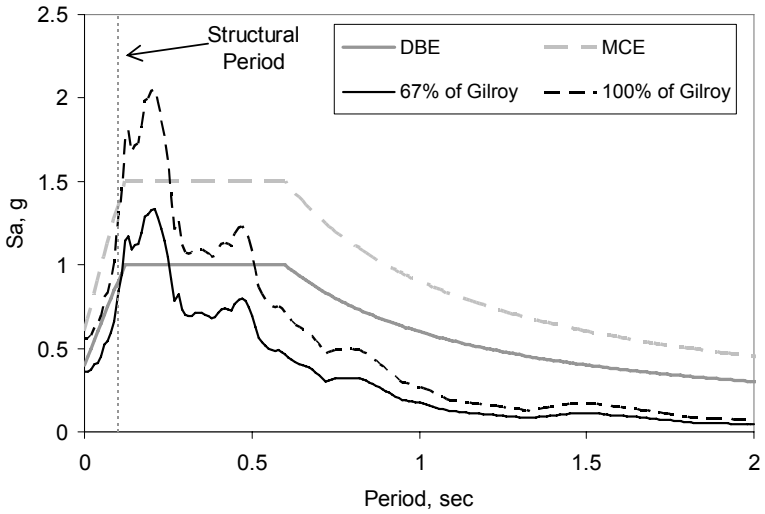

Figure 9.2: Acceleration response spectra (ξ=5%).

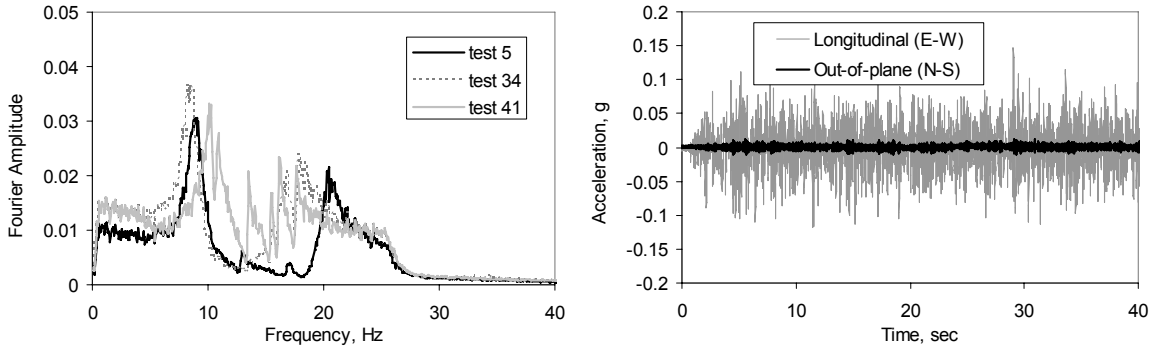

(a) FAS from white noise tests of the undamaged and damaged structure

(b) base excitation recorded during white noise test 5

Figure 9.3: Acceleration recordings at the center of the foundation of the specimen during white-noise excitations.

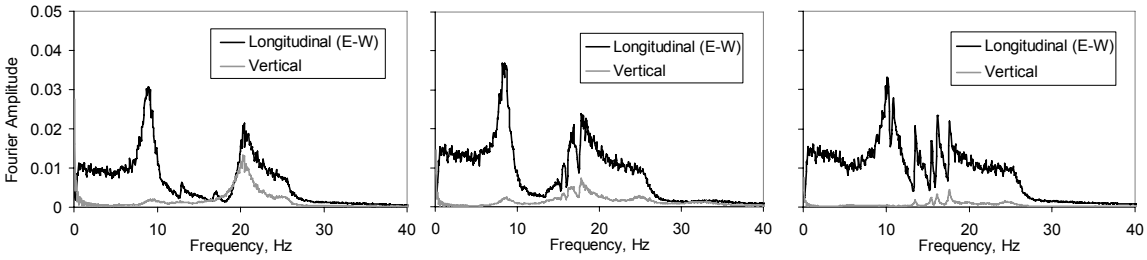

(a) test 5

(b) test 34

(c) test 41

Figure 9.4: FAS of longitudinal and vertical acceleration components recorded at the foundation during three white-noise tests.

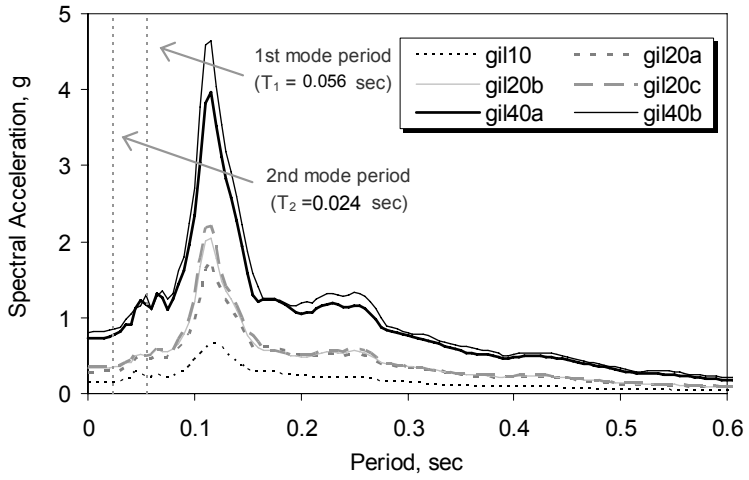

Figure 9.5: Response spectra of recorded base excitation during low level tests (ξ=5%).

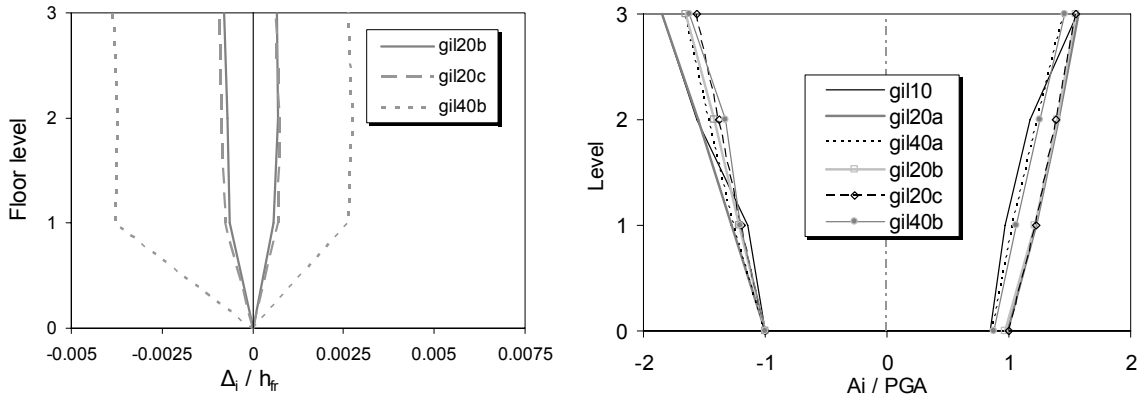

(a) displacements (b) accelerations

Figure 9.6: Profiles of maximum story displacements and accelerations for low level tests.

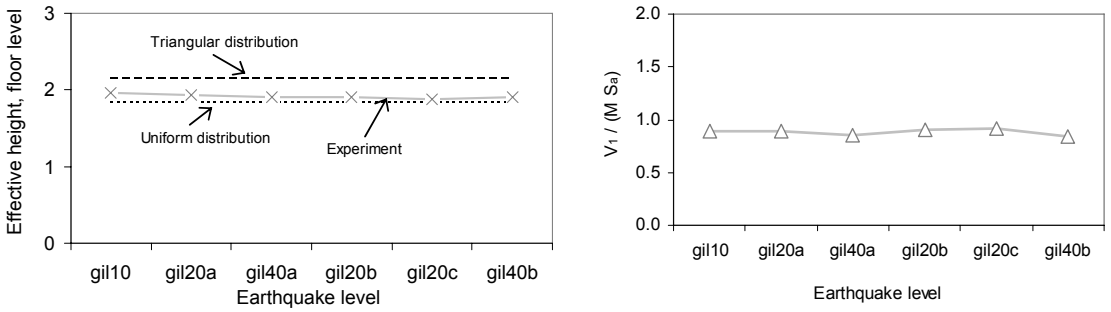

(a) effective height (b) normalized base shear

Figure 9.7: Effective height and normalized base shear for low-level tests.

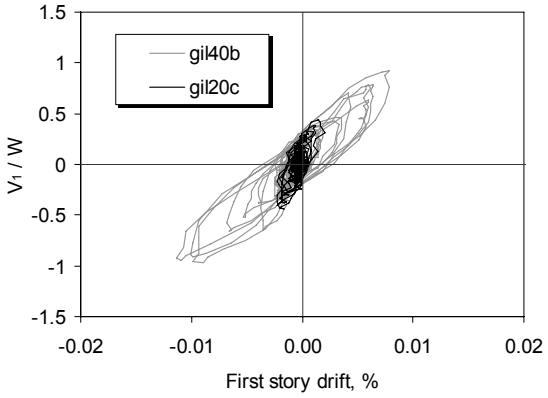

Figure 9.8: Base shear-vs.-first story inter-story drift for 20% and 40% levels of Gilroy.

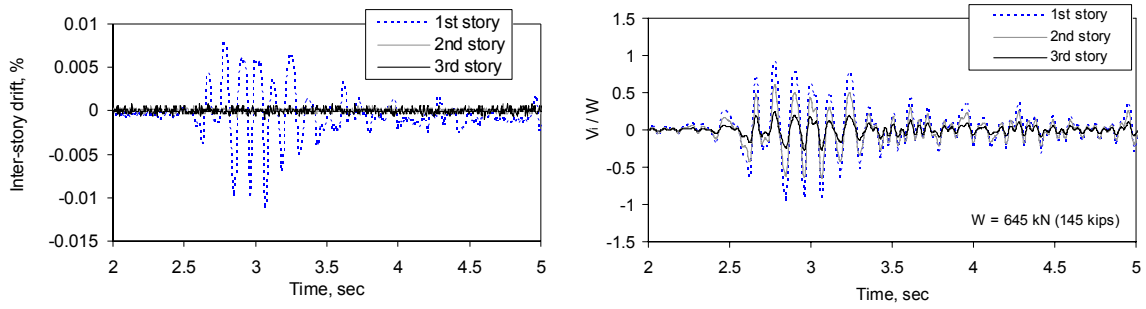

(a) Inter-story drifts (b) story shear forces

Figure 9.9: Time-histories of inter-story drifts and shear forces during gil40b.

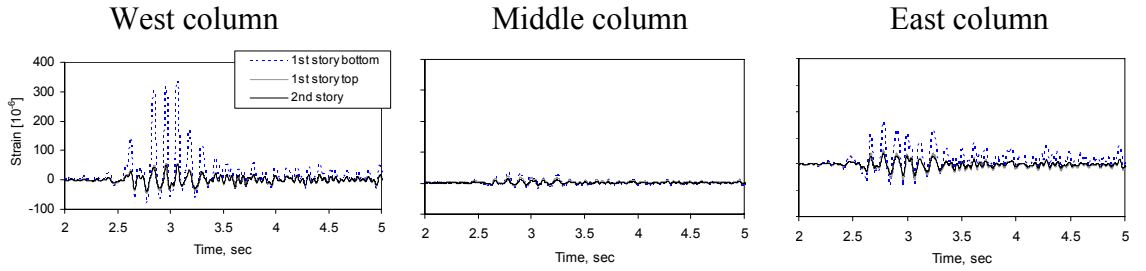

(a) average strain recorded on longitudinal bars (first and second story)

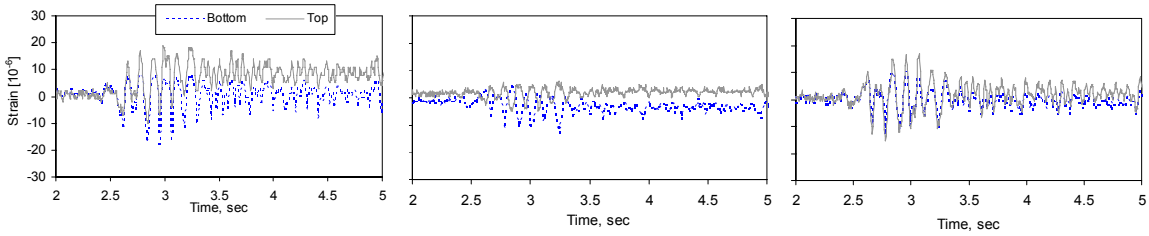

(b) average strain recorded on stirrups (first story)

Figure 9.10: Average axial strain and strain on stirrups in west, middle, and east column during gil40b (see Figure 8.10 for gauge locations).

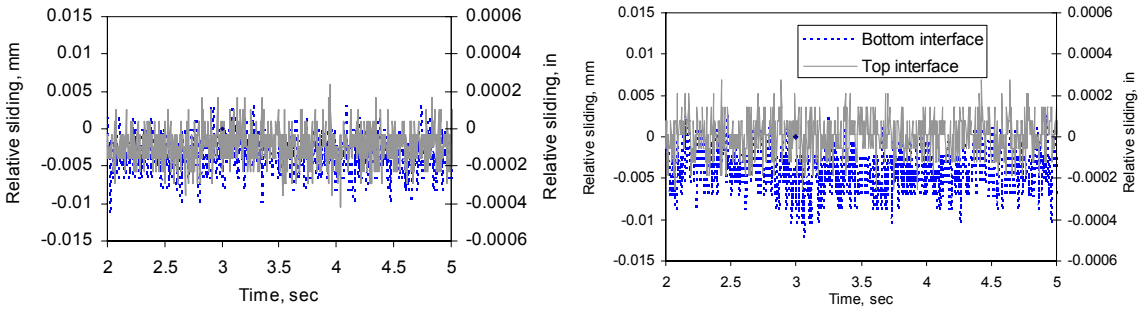

(a) West Bay (b) East Bay

Figure 9.11: Frame-infill sliding in the first story during gil40b.

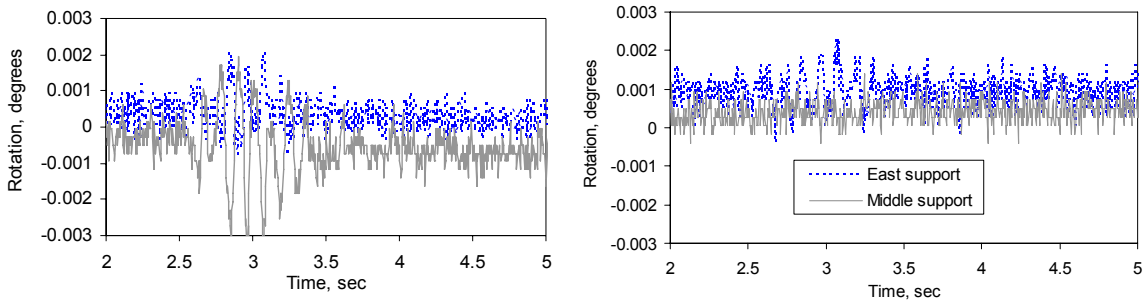

(a) 1st story (b) 3rd story

Figure 9.12: Hinge rotation at the ends of the slabs in the first and third story.

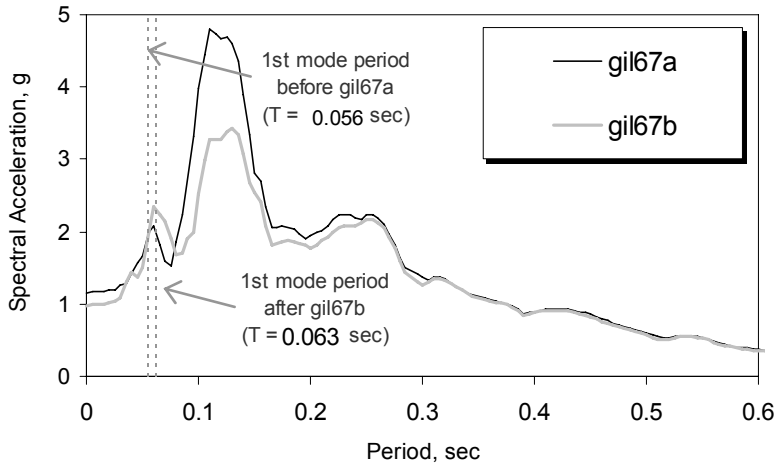

Figure 9.13: Response spectra of the two base motions recorded during gil67a and gil67b.

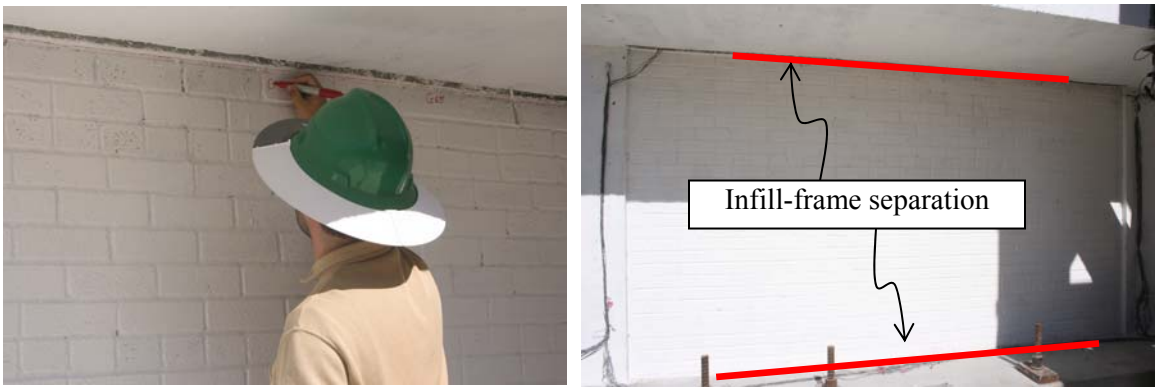

(a) frame-infill separation (b) overall view

Figure 9.14: Cracks marked after gil67a in the west bay of the first store.

(a) stair-crack at window corner (b) overall view

Figure 9.15: Cracks marked after gil67a in the east bay of the first store.

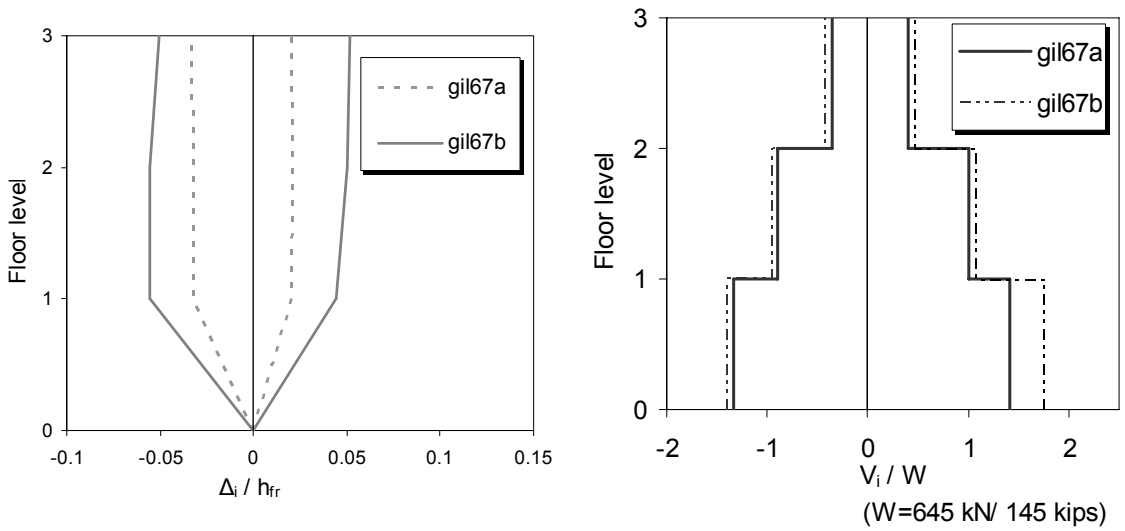

(a) story displacement (b) shear force

Figure 9.16: Profiles of normalized peak story displacements and shear forces during tests gil67a and gil67b.

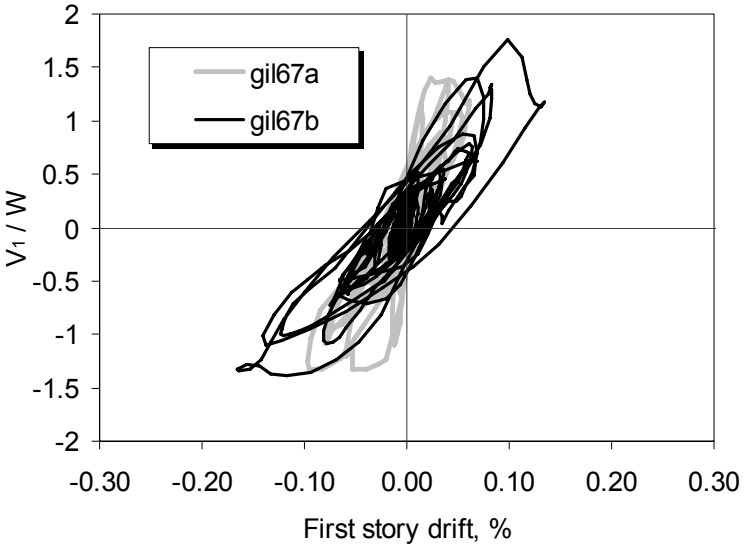

Figure 9.17: First story shear-vs.-drift relation developed under gil67a and gil67b.

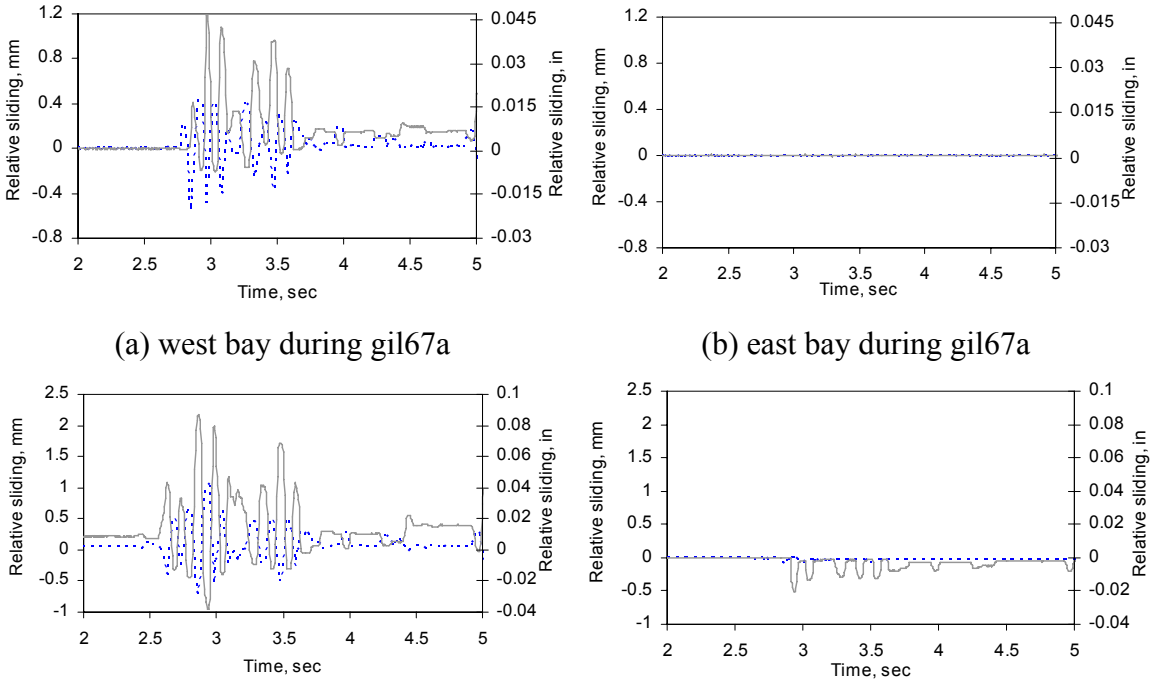

(a) west bay during gil67a

(b) east bay during gil67a

(c) west bay during gil67b

(d) east bay during gil67b

Figure 9.18: Frame-infill sliding in the first story during test gil67a and gil67b.

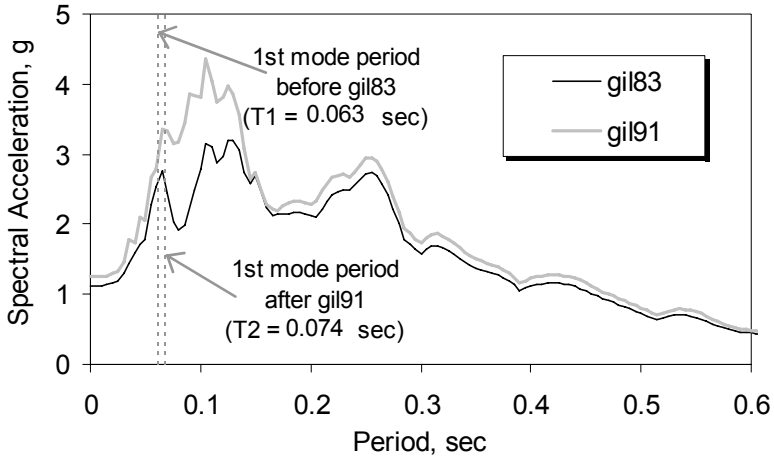

Figure 9.19: Response spectra of the base motions recorded during gil83 and gil91.

(a) west panel (b) east panel

Figure 9.20: Cracks in first story panels after gil83.

(a) west column (b) middle column

Figure 9.21: Cracks in first story columns after gil83.

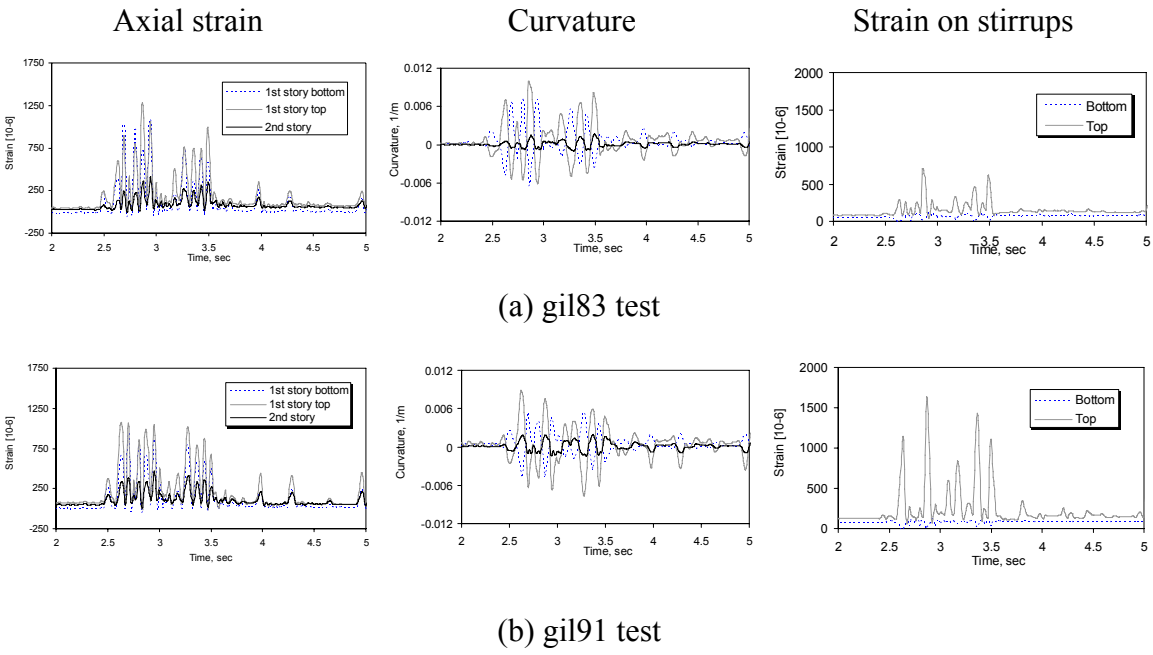

(a) gil83 test

(b) gil91 test

Figure 9.22: Average axial strain, curvature and strain recorded on stirrups in the middle column during gil83 and gil91 (see Figure 8.10 for gauge locations).

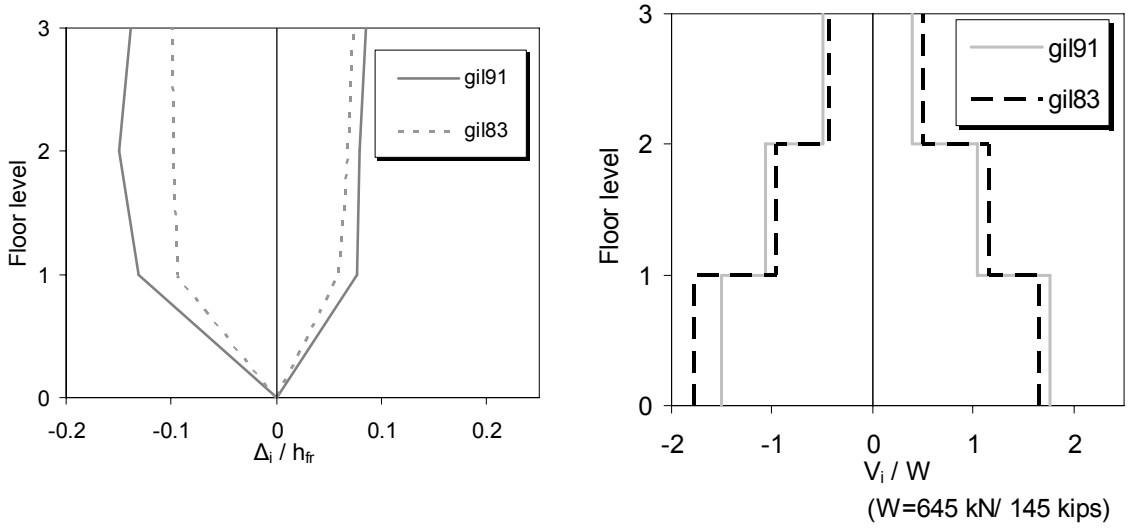

(a) story displacement (b) shear force

Figure 9.23: Profiles of normalized peak story displacements and shear forces during gil83 and gil91.

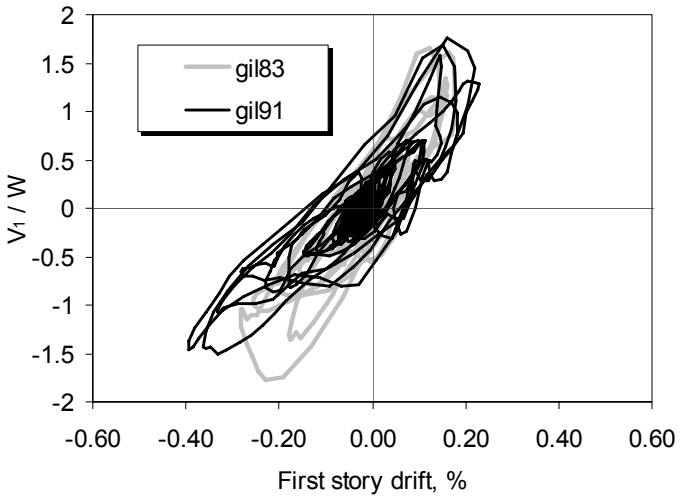

Figure 9.24: First story shear-vs-drift relation under the gil83 and gil91.

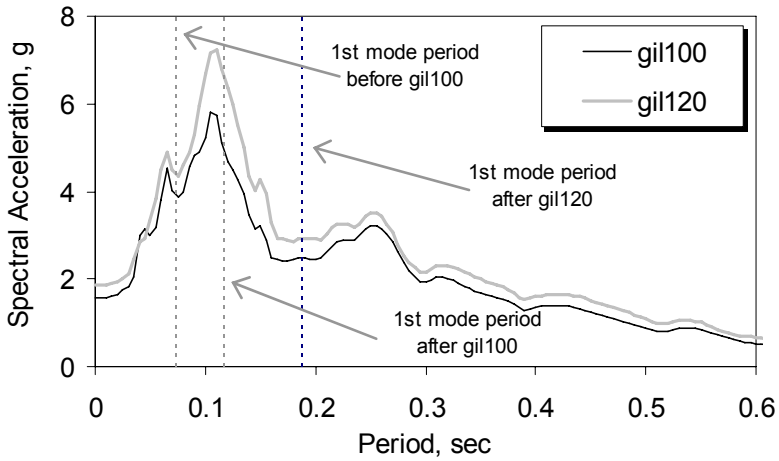

Figure 9.25: Response spectra of the base motions recorded during gil83 and gil91.

(a) west bay (b) east bay

Figure 9.26: Damage in first story after gil100.

(a) west column (b) middle column

Figure 9.27: Cracks in the infill and column in the first story after gil100.

(a) west column (b) east column

Figure 9.28: Crack pattern in second story after gil100.

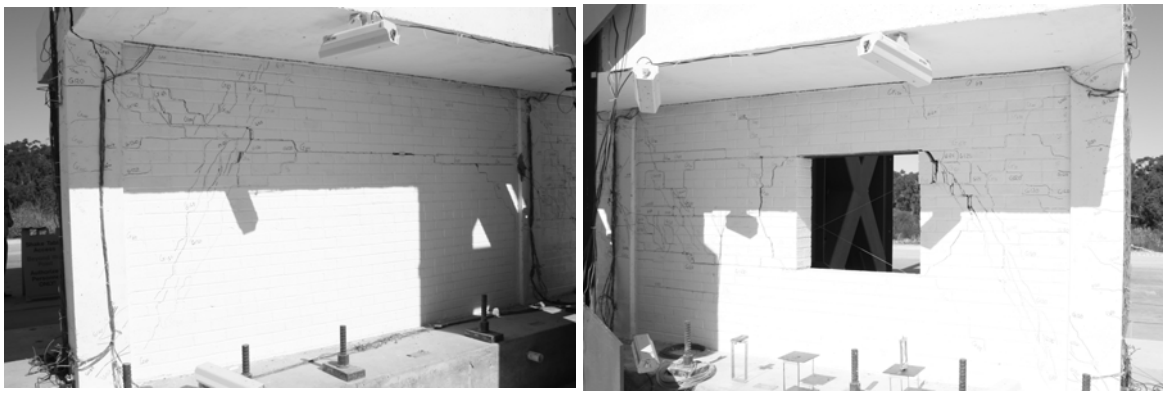

(a) west bay (b) east bay

Figure 9.29: Damage in the first story after gil120.

(a) west column (b) middle column (c)east column

Figure 9.30: Damage of first-story columns after gil120.

(a) west column (b) middle column (c) east panel

Figure 9.31: Damage in the second story after gil120.

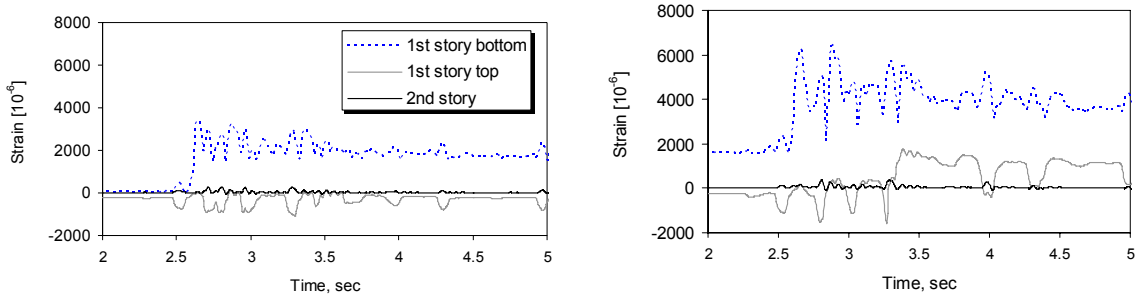

(a) gil100 (b) gil120

Figure 9.32: Time histories of average strain along three cross section on the east column in the first and second story.

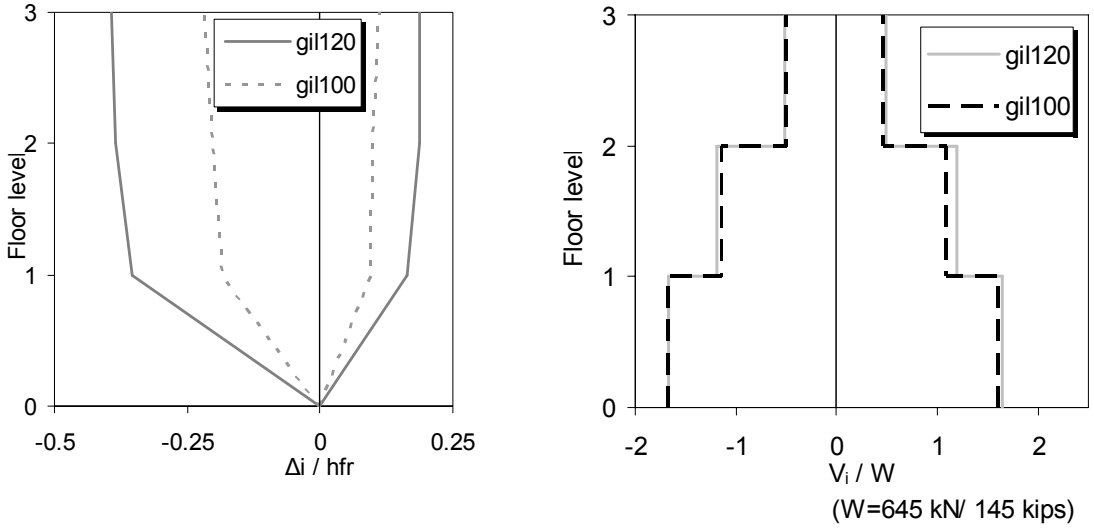

(a) story displacements (b) story shear-forces

Figure 9.33: Profiles of normalized peak story displacements and shear forces during gil100 and gi120.

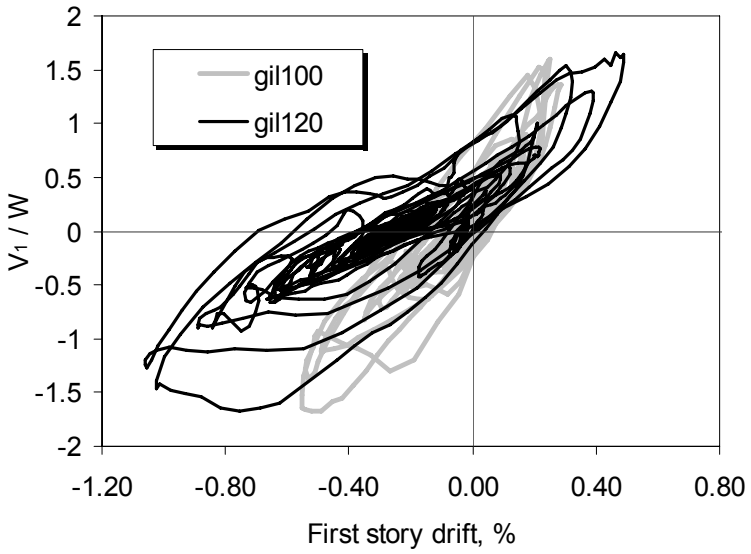

Figure 9.34: First story shear-vs-drift relation under the gil100 and gil120.

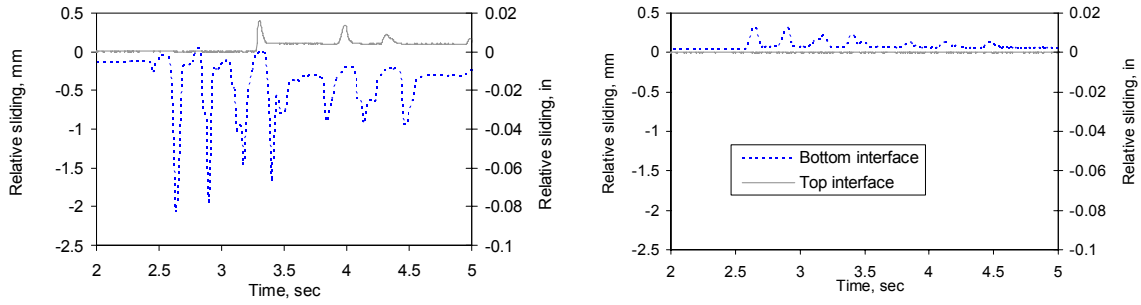

(a) second story west bay

(b) second story east bay

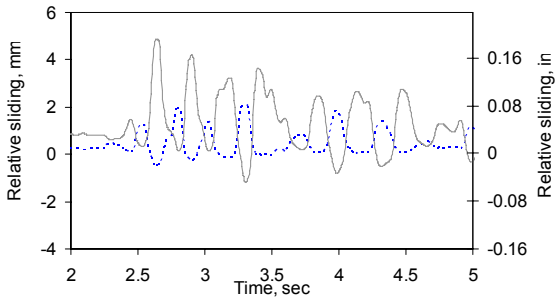

(c) first story west bay

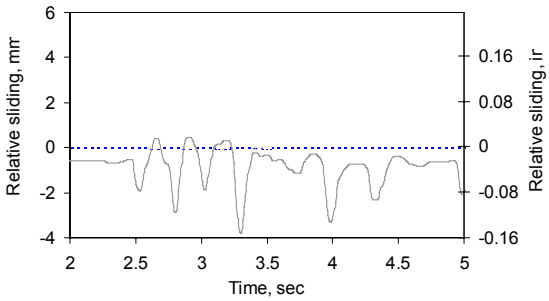

(d) first story east bay

Figure 9.35: Frame-infill sliding in the first story during gil120.

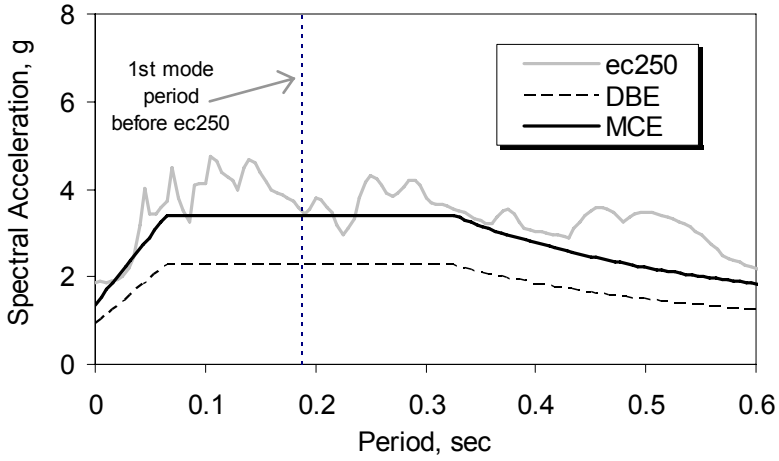

Figure 9.36: Response spectra of the base motion recorded during ec250.

(a) west column-top

(b) west column-bottom

(c) overview

(d) middle column-mid-height

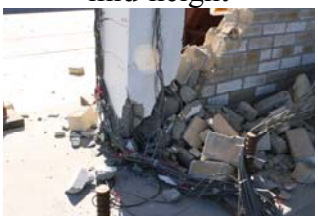

(e) east column-bottom

Figure 9.37: Overview of damaged specimen and details of column failure in the first story after ec250.

(a) west bay

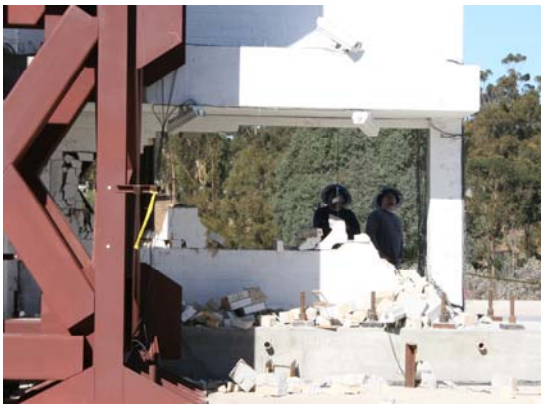

(b) east bay

Figure 9.38: First story panels after ec250.

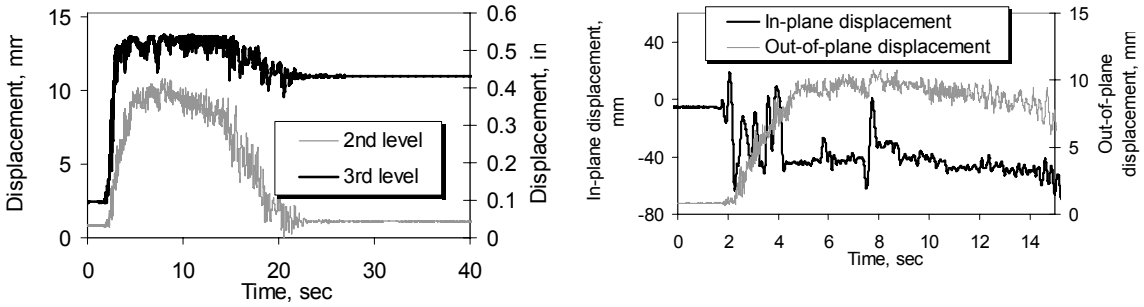

(a) Out-of-plane displacements

(b) in- and out-of-plane displacements of second level

Figure 9.39: In-plane and out-of-plane displacement during ec250.

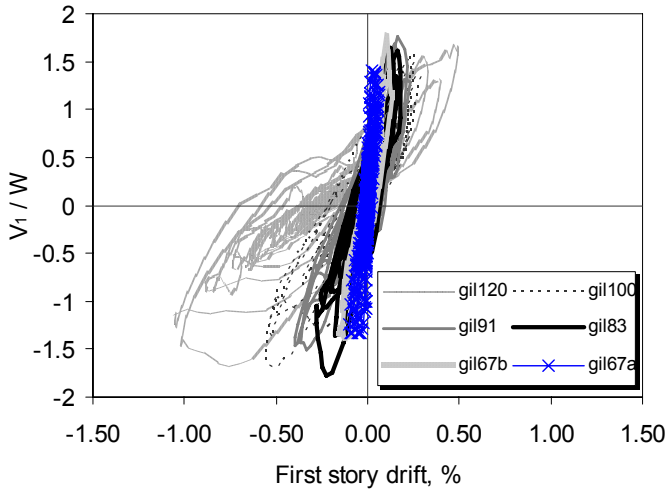

Figure 9.40: First story shear-vs-drift relation developed for the six last tests under the Gilroy excitation.

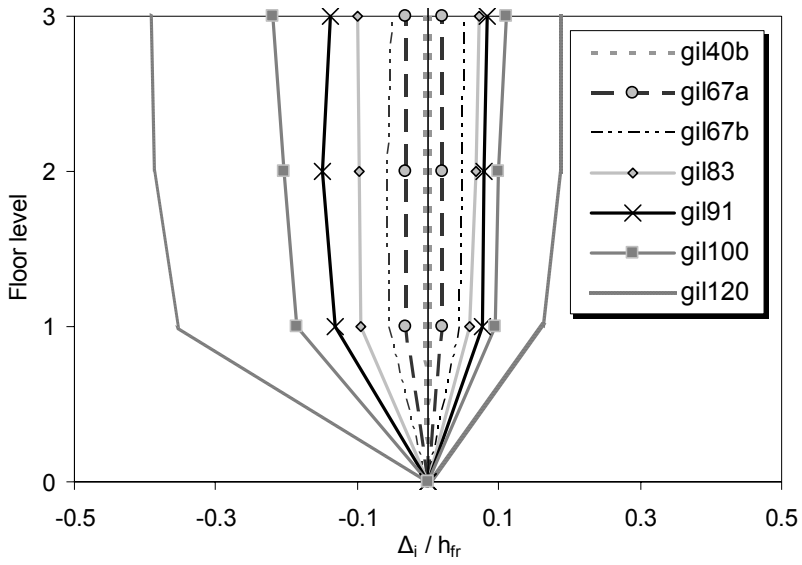

Figure 9.41: Profiles of normalized peak story displacements for all tests.

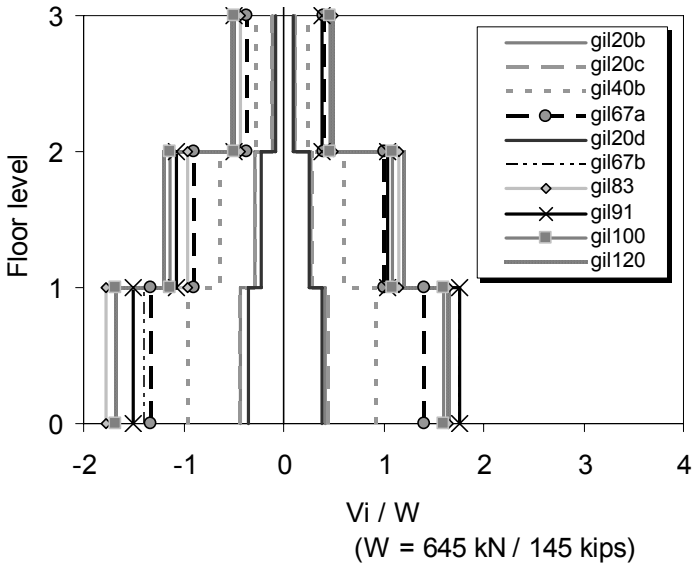

Figure 9.42: Profiles of normalized peak shear forces for all tests.

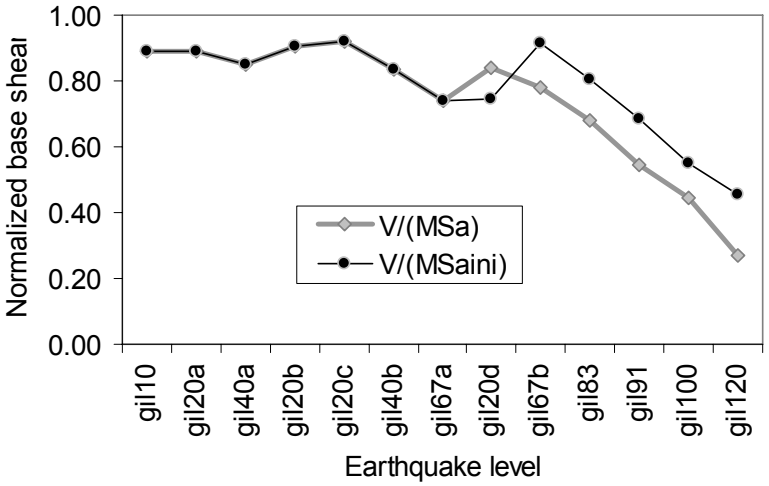

Figure 9.43: Ratio of peak shear force to elastic demand for all tests.

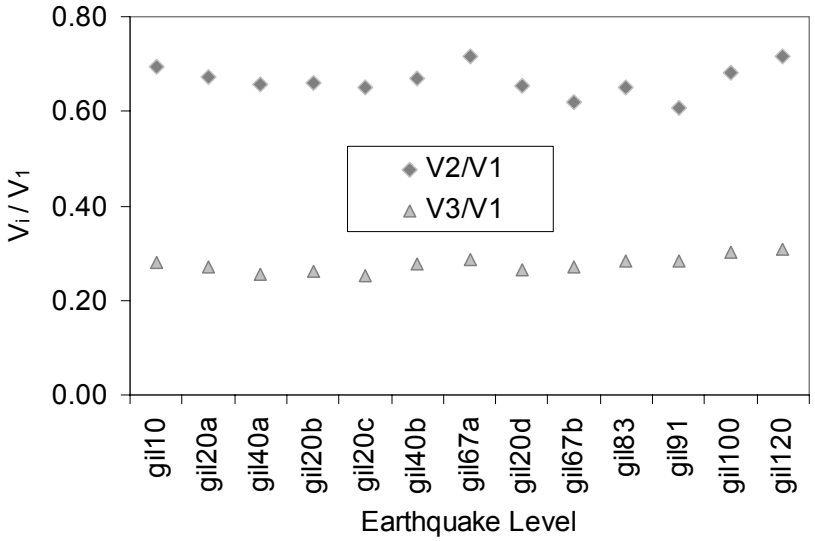

Figure 9.44: Story shear forces for all tests.

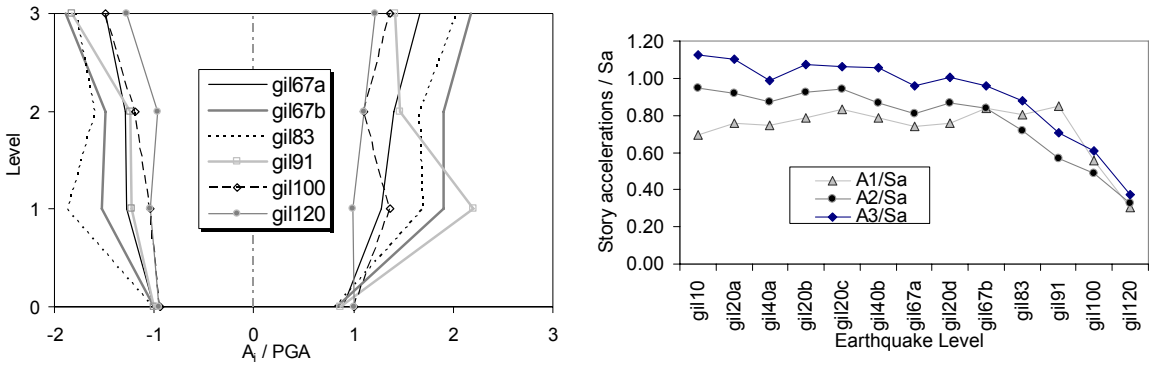

(a) profiles of peak story accelerations normalized by the PGA

(b) peak story accelerations for each test normalized by the spectral acceleration

Figure 9.45: Normalized peak story accelerations.

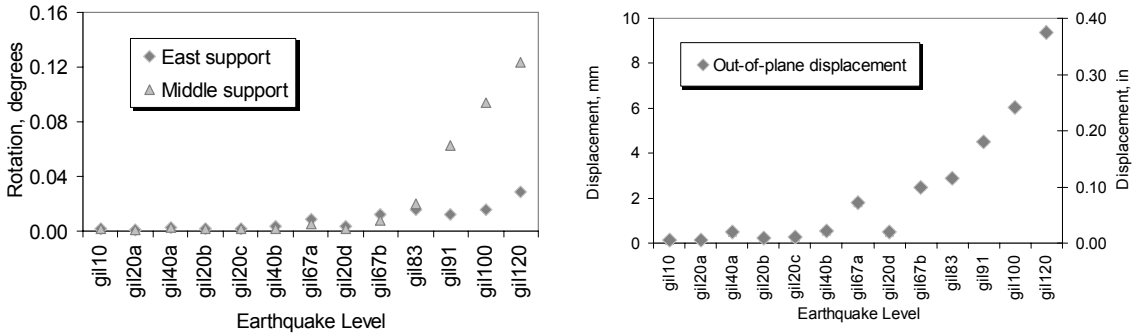

(a) hinge rotations

(a) out-of-plane displacement

Figure 9.46: First story hinge rotations and third story out-of plane displacement.

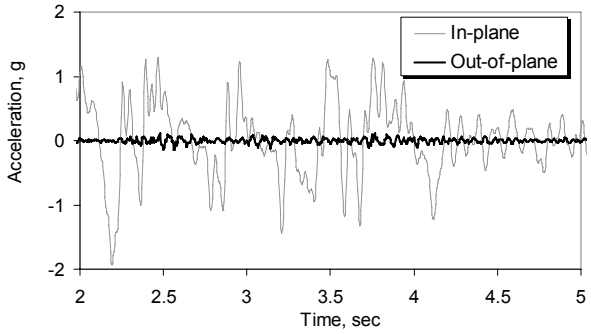

Figure 9.47: In- and out-of-plane acceleration components of the base motion during the ec250 test.

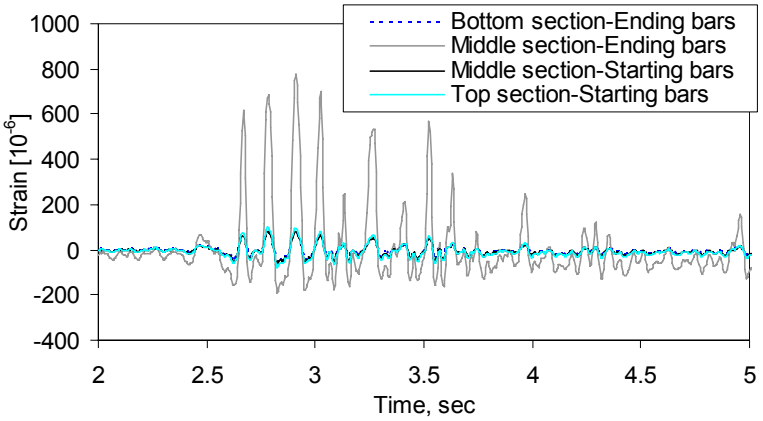

Figure 9.48: Strains in the lap-splice region in the second story column during the 67% level test.

CHAPTER 10

SIMPLIFIED AND FINITE ELEMENT MODELING OF MULTI-STORY MULTI-BAY INFILLED FRAMES

10.1 Introduction

This chapter discusses methods to model the response of multi-story, multi-bay infilled frames under in-plane lateral loads. This is an important step to span the gap between the analyses and tests of single-story, single-bay frames and the simulation of the behavior of real structures with multiple bays and stories. The methods discussed in this chapter range from detailed finite element models developed with the methodology presented in Chapter 2, to simplified analytical tools based on the lateral force-vs.-drift curves developed in Chapters 6 and 7 for frames with solid infills and infills with openings. The lateral force-vs.-drift relations obtained with either of these methods can be used as envelop curves to develop a model consisting of frame elements for the RC frame and diagonal struts representing the infill walls. These models can be subjected to cyclic loads and, therefore, can be used for dynamic analysis. A method to calibrate such models is developed in this chapter. The three analytical methods have been validated with the data from the three-story, two-bay structure tested on the shake table, which is presented in Chapters 8 and 9.

10.2 Simplified Estimation of Force-vs.-Drift Relation

The simplest approach proposed here aims at developing a lateral force-vs.-lateral drift curve for multi-story, multi-bay structures based on the methods developed in Chapter 6 for the frames with solid infills and Chapter 7 for frames with openings in the infill panels. This approach is intended to provide a quick and conservative estimate of the performance of the structure without modeling the actual failure mechanism.

Since the vertical load and the material properties are different at each story of the structure, the simplified curves are expected to be different. The material properties used for the calibration of the curves are presented in Tables 8.3 through 8.7. Initially, the performance of a single-bay, single-story panel with solid infill was estimated for every story, assuming that it carries half of the total vertical load at that story. Another curve was then created according to the methodology discussed in Chapter 7 to represent the performance of the infill with the window. To obtain the estimation of the story shear force-vs.-the story drift, the two curves were added for each story.

Figure 10.1(a) presents the two curves developed for the two bays used to simulate the first story of the specimen, while Figure 10.1(b) presents the shear force-vs.-drift relations obtained for every story. In Figure 10.2 the relation obtained for the first story is compared with the experimentally measured force-vs.-drift curve. The simplified model captures accurately the initial stiffness and provides a good estimate for the lateral strength of the frame. However, it largely underestimates the ability of the structure to maintain its lateral strength as a considerable load drop is assumed after the peak load is

reached. This is to be expected though, as explained in Chapters 6 and 7 since the simplified method is intended to provide conservative estimates of the actual behavior.

Finally, the peak values of the shear forces obtained from the shake table tests at the second and third story were 769 and 330 kN (172.8 and 74.2 kips) respectively as presented in Chapter 9. For the second story, this value slightly exceeds the yield point of the force-vs.-drift relation shown in Figure 10.1(b). Exceeding the yield point signifies minor cracks along the frame-wall interface for the west bay with the solid infill and minor cracks radiating from the window corners for the east bay. Moreover, the peak shear force at the third story is lower than the yield point; therefore no cracks are expected. As discussed in Chapter 9, this was exactly the performance observed in the second and third story during the shake-table tests.

10.3 Push-Over analysis with Finite Element Method

The nonlinear finite element modeling methodology developed in Chapter 2 can be used to model the performance of infilled frames under monotonic lateral loads. The model created to simulate the performance of the three-story structure included 37895 nodes and 35960 elements. For simplicity, the material properties have been assumed to be uniform along the height of the building and the material test data obtained for the first story have been used to calibrate all the material models. This is an acceptable assumption which is not expected to influence the accuracy of the analytical solution considering that the material properties along the height of the specimen did not vary

significantly, and the fact that the damage is anticipated to concentrate in the first story. The calibrated material models for the compressive behavior of the concrete and masonry are presented in Figure 10.3, while the calibrated initial yield surface and final failure surface for the mortar interface elements is presented in Figure 10.4. In the figure it can be observed that the two prisms from the first story tested on the day of the first major test have 27% difference in their peak strengths. In the calibration, the data from Prism A was used since all prisms tested on that date from the second and third story had similar strengths as Prism A. As in the cases of the single-story, single-bay specimens tested in Colorado, two monotonic analyses were conducted.

Figure 10.5 presents the lateral force-vs.-first story drift of relation obtained from the finite element model. The obtained curve follows the experimentally measured curve with adequate accuracy although it slightly overestimates the strength in both directions. Moreover, in the positive direction the model indicates that the nonlinear behavior initiates earlier than in the tests. Overall, however, the analytical model can capture the behavior of the structure. This is also evident considering the failure pattern shown in Figure 10.6, which includes dominant shear cracks in the top of the west column, at 2/3 of the height for the middle column and at the bottom of the east column. Moreover, the cracking pattern in the infill resembles the cracking pattern of the actual structure shown in Figures 9.37 and 9.38. The only aspect of the failure mechanism not captured by the model is the out-of-plane failure of the masonry wall around the window, however this cannot be possible captured with the proposed model of a planar structure subjected to in plane lateral loads.

10.4 Development of a Strut Model for Cyclic Analyses

Simplified models for the simulation of the performance of masonry infilled frames have been proposed by a number of researchers (e.g. Zarni and Tomazevic 1985, Syrmakezis and Vratsanou 1986, Chrisaflli 1997, Al Chaar 2002, and Crisafulli and Carr 2007) and typically consist of diagonal struts or panel elements used to simulate the masonry infills. The different methods proposed may include a range of configurations with one, through five struts. However, regardless of the number of struts and the calibration method, this approach is not general enough to reliably capture the response of these structures and the complex failure mechanisms that may develop. The lack of a reliable simplified method is even more pronounced when the infill walls include openings.

To address this issue and propose a simplified analytical method for the development one should be aware of the possible shortcomings of such methods. Hence, the method proposed here aims at developing a simplified analytical tool to simulate the lateral force-vs.-lateral drift relation of infilled frames without capturing the actual failure mechanism. The proposed method consists of five steps which are described in this section.

Step 1: Development of the force-vs.-drift relation for a single-bay, single-story frame with solid infill.

The method proposed here requires the estimation of the performance of a single-story, single-bay frame with a solid masonry panel in terms of an envelop curve. Such

curves are required for all bays with different aspect ratios that may exist in a real structure. The envelop curves can be obtained though testing, finite element analysis, or the simplified method developed in Chapter 6. It is evident that the first and second methods can provide more accurate results; however, they require more resources, time, and effort. Hence, the simplified method proposed here can be a practical alternative.

Step 2: Development of the force-vs.-drift relation for single-bay, single-story frames with openings.

Once the force-vs.-drift relation is obtained for the solid panel, the procedure outlined in Chapter 7 can be used to develop the corresponding curves for all panels of the structure that have similar aspect ratios and include doors and windows. This step is concluded when an envelop curve for every single-bay subassemblage of the structure is developed.

Step 3: Development of the force-vs.-drift relation for single-bay, single-story bare RC frames.

This step involves the development of a model which can simulate the behavior of a bare RC for every single-bay, single-story structure considered in step 1. This model is relatively simple to construct with commercially available software for structural analysis. The models do not need to account for the shear effects. Such capabilities have been developed recently (Marini and Spacone 2006); however they are not available in commercial software. Moreover, the shear behavior of the RC members in the case of infilled frames depends on the interaction with the masonry infill. Capturing this

interaction with strut models is rather difficult and would require complicated models combining a number of struts simulating the masonry wall.

Step 4: Calibration of the strut constitutive law.

In every infilled bay of the structure the masonry panel can be replaced with two diagonal struts. These can be connected through rotational hinges to the opposite joints of the RC frame so they are only subjected to axial loads. The cross-sectional area of the struts should be selected so that in combination with the calibrated constitutive law the addition of a pair of diagonal struts to each frame model developed in step 3 would result in the force-vs.-displacement curve of the corresponding infilled frame developed in step 2. Since a monotonic model is considered in the calibration, only one strut connecting the top of the windward column to the bottom of the leeward column is required, assuming that the struts would have practically no tensile resistance.

Step 5: Development of a model for the entire structure.

After the calibration of the struts for each bay of the structure, the model of an entire frame of the structure can be assembled. A three dimensional model of the structure can provide information on its torsional response which may be important for structures with significant irregularities.

10.5 Validation of the Strut Model

The proposed modeling approach with struts has been used to develop a model of the shake-table specimen in OpenSEES (McKenna and Fenves 2000). A simple model consisting of 27 frame elements was created as shown Figure 10.7. Flexibility-based inelastic beam-column elements (Spacone et al. 1996) have been used to model the RC columns and the masonry struts. The former have been divided into fibers so that the steel reinforcement can be modeled. The uniaxial behavior of the steel fibers was represented with the Menegotto-Pinto (1973) steel model, while for the concrete and masonry the Concrete02 material model from the available library was used. The concrete and steel models have been validated with the material tests summarized in Chapter 8.

The model for the strut was calibrated with the goal of matching the simplified curve developed for each bay of the structure. Hence, the models for the RC frames were the same for the entire structure, but different properties for the struts were developed for the bays with solid infill and the bays with openings. For simplicity, the models were the same for the three stories. Figure 10.8 presents the response of the single-story, single-bay bare frame and the frames infilled with a solid panel and a panel with a window. The responses of the infilled frames have been calibrated to simulate the envelop curves developed with the simplified method proposed in section 10.2. The small deviation between the simplified curves and the responses of the OpenSEES models with the diagonal struts is caused by the constitutive law which was used to for the diagonal struts. Hence the model is less stiff that the target curve and has a less steel strength degradation

following the peak load. Overall, however, it provides a reasonably good match of the desired envelop curves for the two infilled frames considered here.

The Rayleigh formulation was adopted to model the damping in the structure damping, due to its mathematical convenience. A term proportional to the initial stiffness of the structure was used and the value of damping assumed in the model was 5% which is the most commonly use. However, according to recent studies, initial stiffness proportional damping could lead to significantly increased damping forces when the structural stiffness decreases due to damage. Although not quantified, such trend would be in accordance with the increase of the identified damping values summarized in Table 9.2.

The model was subjected to a loading sequence which included the accelerograms recorded at the base of the specimen during the tests gil67a, gil67b, gil83, gil91, gil100, and gil120. The lateral force-vs.-drift response of the numerical model is compared with the experimental response in Figure 10.9. The comparison indicates that the model underestimates the initial stiffness of the structure, which is expected considering the material law used to simulate the axial behavior of the struts. Nonetheless, the model predicts with good accuracy the peak strength. It also captures the non-symmetrical displacements that the experimental structure sustained. Finally, although the most peak behavior of the model is considerably more brittle, similarly to the simplified curve presented in Figure 10.2.

The peak values of inter-story drift ratios for the three stories in due to each base excitation are summarized in Table 10.1. The table also presents the corresponding values obtained during the testing sequence from the test specimen. From the comparison, it can be observed that the model initially considerably overestimates the interstory drift ratios, especially in the first story. However, for the gil120, the drift predicted by the numerical model is only 12% higher than the actual value. Moreover, the model simulates the soft story mechanism as the inter-story drift ratios for the second and third stories are very small in and do not change due to the accumulation of damage.

The comparison of the model with the shake-table test results indicates that the model can capture main features of the response. This is very encouraging considering the simplified approach followed to obtain this model. An improved match between the two curves can obtained if the initial backbone curve is based on less conservative assumptions. Furthermore, a material model which can simulate the higher initial stiffness of the simplified curve can lead also improve the numerical results.

10.6 Conclusions

This chapter discusses detailed and simplified analytical methods which can be used for the assessment of the seismic performance of infilled RC frames. The proposed methods include three approaches. Initially the simplified method developed in Chapters 6 and 7 is used to obtain a conservative estimate of the structural response. The results of the simplified method are satisfying considering the simplicity of the method used but are

inferior to those of the finite element method which is also used to simulate the structural behavior. The finite element model captures successfully the failure mode of the frame and provides an envelope curve very close to the structural response. Finally, a simple method to develop models for cyclic analysis has been developed and validates. The method uses the simplified curves to calibrate the struts used to represent the effect of the masonry panels. This method cannot capture the failure mechanism and the interaction between the frame and the panel. With the appropriate calibration though, it can provide useful information on the structural response.

Tables of Chapter 10

Table 10.1: Comparison of analytically predicted and experimentally obtained peak inter-story drift ratios (values in %).

Excitation	Experiment			Strut model		
	1st story	2nd story	3rd story	1st story	2nd story	3rd story
gil67a	0.10	0.00	0.00	0.43	0.18	0.08
gil67b	0.17	0.03	0.04	0.44	0.12	0.05
gil83	0.28	0.04	0.07	0.67	0.14	0.07
gil91	0.39	0.07	0.08	0.97	0.16	0.07
gil100	0.55	0.07	0.01	1.08	0.16	0.08
gil120	1.06	0.10	0.03	1.19	0.15	0.08

Figures of Chapter 10

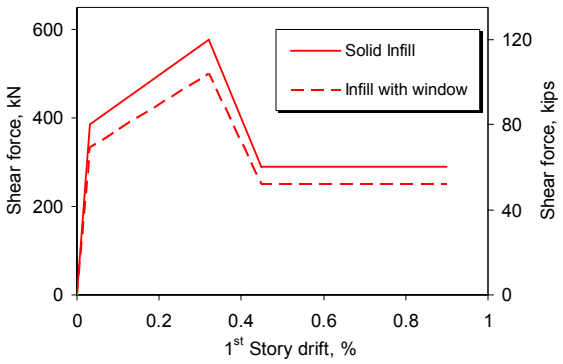

(a) hypothetical single-bay frames in the first story

(b) combined relations for the three stories

Figure 10.1: Lateral force-vs.-drift curves for the three-story shake-table specimen derived with the proposed simplified method.

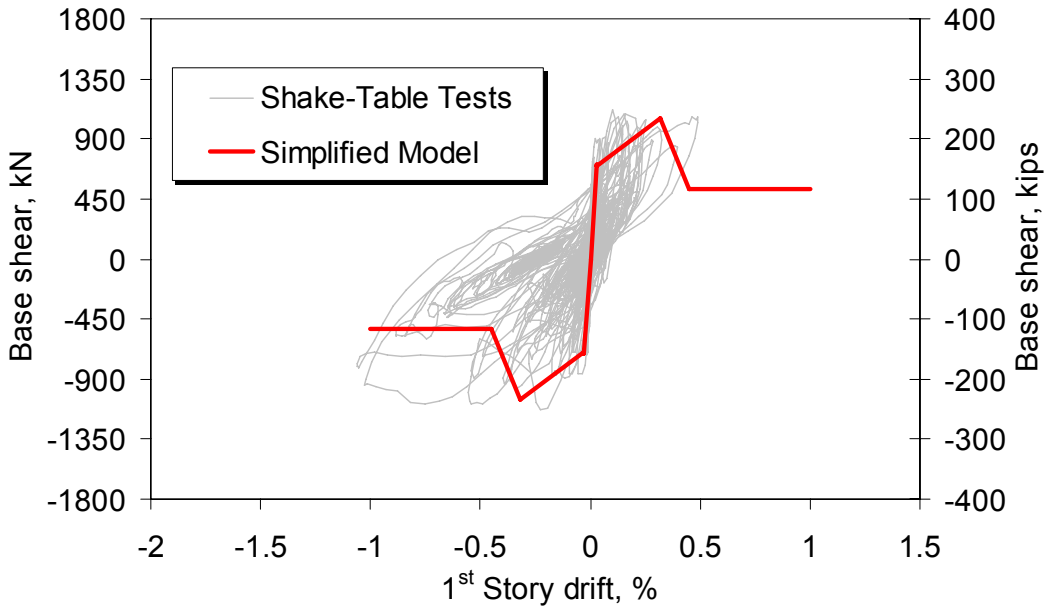

Figure 10.2: Comparison of the simplified analytical model with the experimental lateral force-vs.-drift curves for the three-story shake-table specimen.

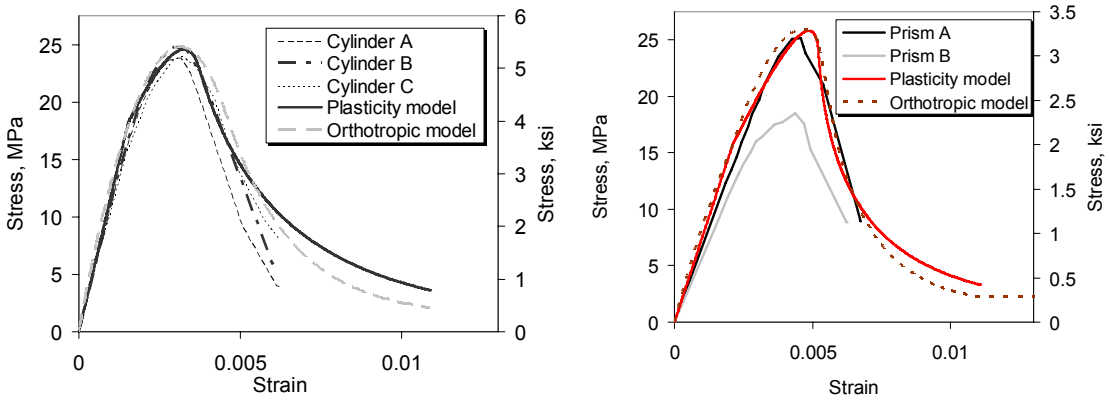

(a) compressive behavior of concrete (b) compressive behavior of brick

Figure 10.3: Calibrated material models for concrete and brick in compression.

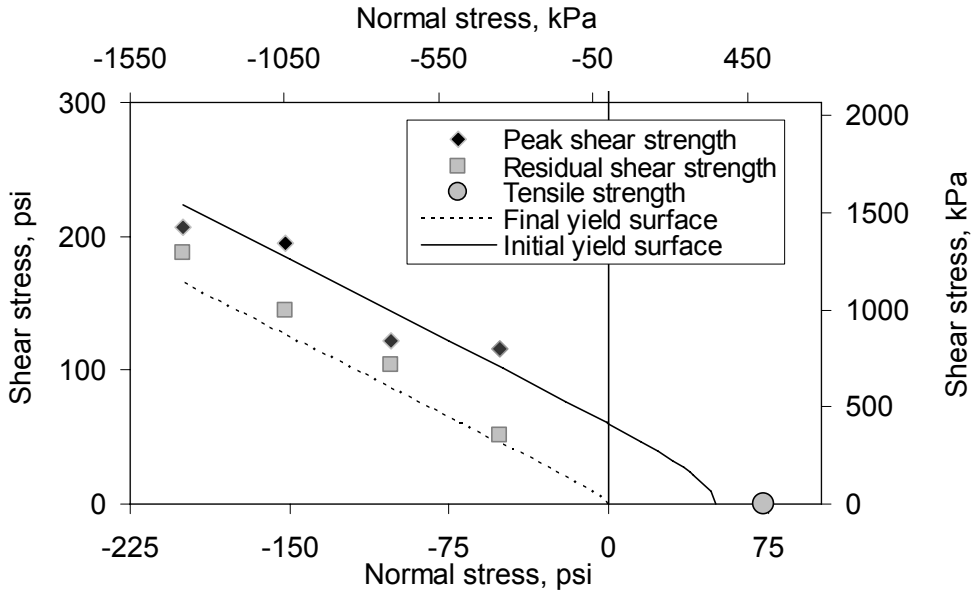

Figure 10.4: Calibrated yield surfaces for interface elements representing mortar.

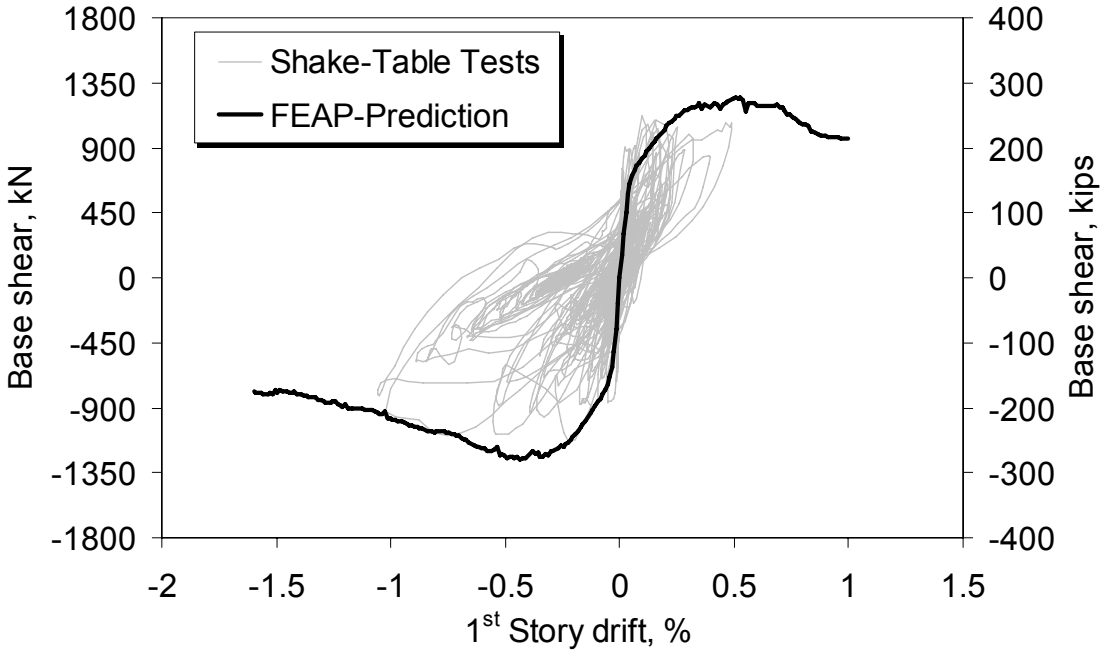

Figure 10.5: Comparison of the lateral force-vs.-drift curves for the three-story shake-table specimen obtained from the tests and the finite element model.

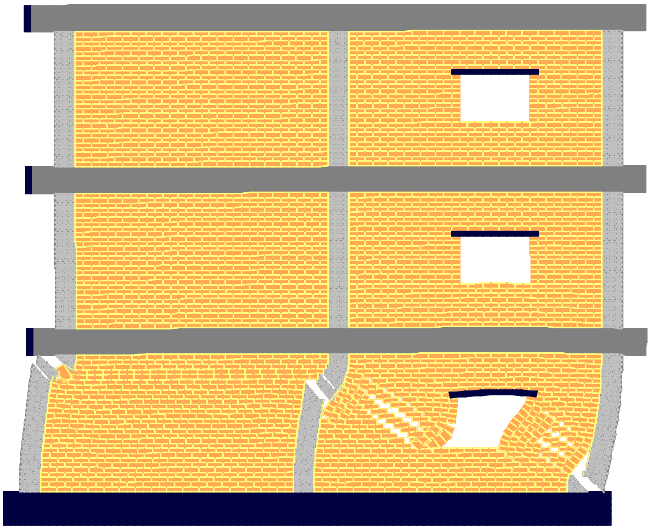

Figure 10.6: Deformed mesh at 1% lateral drift ratio.

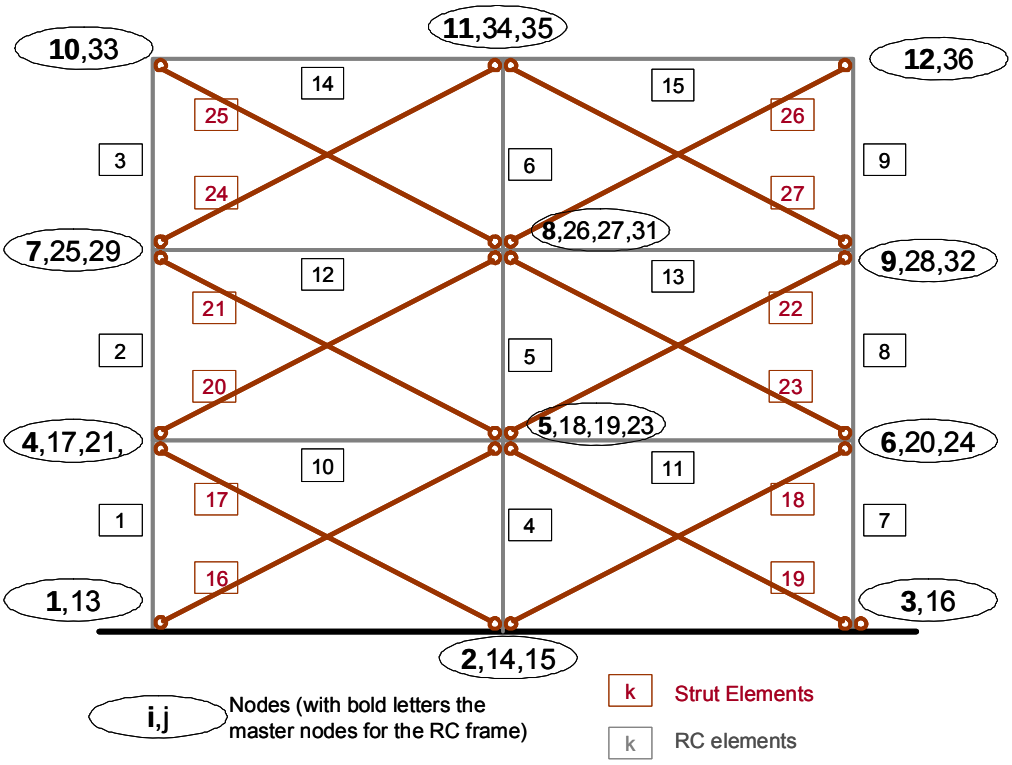

Figure 10.7: Strut model of the three-story shake table specimen.

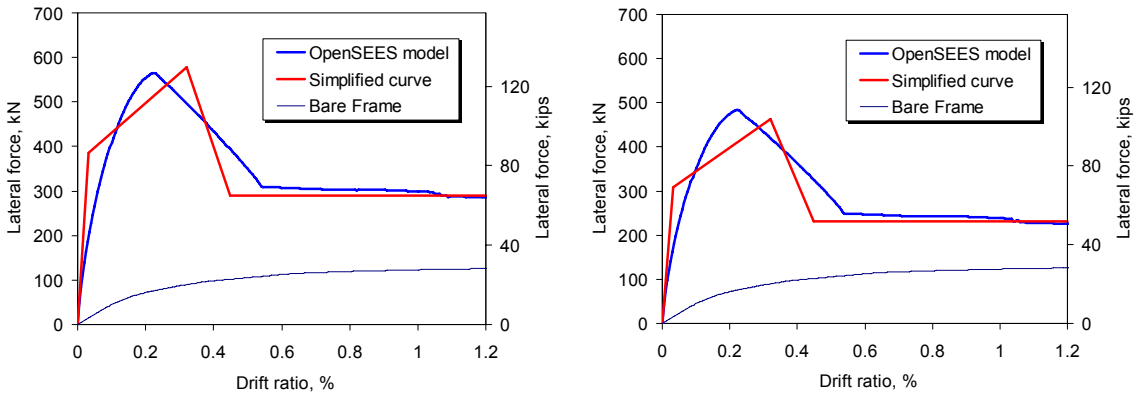

(a) solid infill (b) infill with window

Figure 10.8: Calibrated response of single-story, single-bay frames.

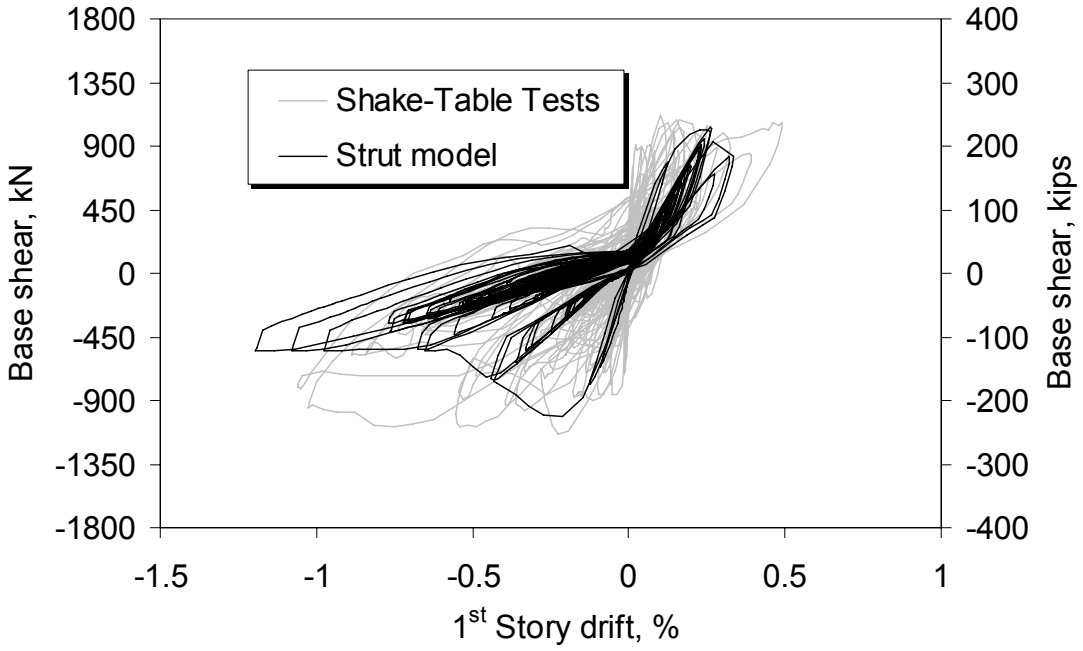

Figure 10.9: Base shear force-vs.-first-story drift for the strut model and the shake-table specimen for tests gil67a, gil67b, gil83, gil91, gil100, and gil120.

CHAPTER 11

SUMMARY AND CONCLUSIONS

11.1 Summary

The scope of this dissertation is to advance, through analytical and experimental research, the state of knowledge on the behavior of masonry infilled RC frames under seismic loads and provide analytical tools to assess this behavior. To achieve this goal, the study has considered planar structures subjected to in-plane loads through experimental testing, detailed finite element models, and simplified analytical tools.

The focal point of the experimental study was a three-story RC frame with infill panels on its perimeter, which represented the construction practice in California in the 1920s. The structure was designed for gravity loads based on the allowable stress approach. Modern materials were considered in the design so that models of the structure could be constructed for the experimental investigation.

The first phase of the experimental investigation consisted of cyclic quasistatic tests of five single-story, single-bay infilled RC frames which were substructures of the prototype structure. The tests included a small-scale specimen and four large-scale specimens. The small-scale and one of the large-scale frames had solid masonry walls, while three frames had infill panels with an eccentrically located window or a door.

In the second phase of testing, a large-scale, three-story, two-bay infilled frame was tested on the outdoor shake table at UCSD. The specimen, which was the largest of its type ever tested on a shake table, included a solid infill panel and a panel with an eccentric window at each story. The gravity load corresponding to the prototype structure was simulated with thick slabs connected with hinges to transverse beams, while the disparity between gravity and inertia masses was accounted for with the appropriate scaling of the acceleration records in time and amplitude based on the similitude law. The specimen was instrumented with 285 sensors and was subjected to 44 dynamic tests including ambient vibration recordings, white-noise tests used to identify the modal properties at every damage state, and 14 tests of appropriately scaled historic ground motions which gradually damaged the specimen.

The testing sequence was used to validate the developed analytical tools. These include a finite element modeling methodology and simplified analytical method. The proposed finite element modeling methodology combines the discrete and smeared-crack approaches. With this modeling scheme the RC members are modeled with a combination of triangular smeared-crack and zero-thickness interface elements to circumvent the inherent inadequacy of the former to simulate the brittle shear behavior of RC members. A consistent scheme is proposed for the reinforcement to ensure that any potential crack would cross the same amount of longitudinal and transverse reinforcement as in reality. The modeling scheme for the masonry wall involves two smeared-crack elements for the masonry units which are interconnected with a zero-thickness interface element allowing splitting of the masonry unit and the relative rotation

or sliding motion within a fractured unit. Zero-thickness cohesive interface elements simulate the mortar joints to capture the mixed-mode fracture of mortar joints.

A rigorous mechanics-based framework was developed for the calibration of the material models for the smeared- and discrete-crack elements representing concrete, brick and mortar elements. The framework was validated with experimental data obtained from this, as well as previous research efforts. For two infilled frames with distinct failure mechanisms, a sensitivity analysis was conducted to evaluate the sensitivity of the model to all the material parameters. Furthermore, parametric studies were conducted to assess the influence of a number of parameters to the structural performance, including design parameters, such as the amount of longitudinal and transverse reinforcement, the geometry of the frame, as well as the vertical load, the number of bays, and the location and the size of openings in the infill panel. The results from these parametric studies were used to assess the influence of each parameter and develop a simplified method to estimate the lateral force-vs.-drift performance of infilled frames.

11.2 Conclusions

A number of interesting conclusions can be drawn from the experimental study. The comparison of the tests on frames with solid infills and different scaling factors showed that small-scale specimen had limitations in representing the full-scale structure. The inability to scale the size of brick units and mortar joints led to a distinct failure mechanisms of the small-scale specimen despite having the same frame design and

masonry specifications. Hence, results from small-scale specimens can be used for the validation of analytical models, but should be interpreted with caution.

The quasistatic tests indicated that the existence of openings in masonry walls can affect their response to lateral loads in terms of the stiffness, strength, failure mechanism and post peak behavior. At the early loading stages, minor diagonal cracks radiated from the window corners and prevented the separation along the wall-frame interface developed in the case of frames with solid infills. These cracks did not influence the peak load, but at large drifts they caused the separation of triangular pieces of the masonry wall from the frame. This was not hazardous under in-plane loads during a quasistatic test, but could create problems under more realistic loading scenarios.

The analysis of the frames with the finite element method indicated that inclined compressive struts develop in the infill, but not along the diagonal of the panel as commonly perceived. Instead, two struts tend to develop in each direction of loading at angles close to 45^{o} and they act against the top of the windward column and the bottom of the leeward column in single-bay configurations. The struts, if fully developed, can cause the shear failure of the columns at the locations they act against. In case of openings in the infill panel, these affect the structural performance only if they reduced the width of the masonry piers and hinder the development of the two diagonal struts at the locations and orientations those develop in a solid infill. A change of the location or orientation of a strut reduces the load carried by the strut and therefore the lateral capacity of the frame. However, it also alters the failure mechanism of the column, as the shear failure of the latter can be avoided due to reduced diagonal force leading to bending

deformations. This was the outcome of the parametric study on openings which indicated that the opening size can determine the initial stiffness of the structure, but for the peak strength and failure mechanism the width of the masonry piers is equally important.

In many aspects the behavior of the single-bay, single-story frames was similar to that of the three-story, two-bay frame tested on the shake table, as indicated by the similar cracking patterns and lateral strength. The latter could be calculated as a summation of the strength of two single-bay frames resembling those in the first story of the specimen. The post peak behavior of the shake-table specimen did not include a significant load drop as it was able to maintain its lateral capacity until a lateral drift close to 1%. However, after this point the frame practically collapsed due to the shear failure of the columns and the detachment of triangular pieces of the masonry wall around the first story window. The cracks were initially identical to those developed in the quasistatic tests, but led to a different crack pattern as the sliding cracks at different heights in the two panels induced shear cracks in the mid-height of the middle column. After this crack was developed, the triangular pieces were detached from the masonry wall leading to a considerably more destructive failure in the dynamic tests. This behavior is closer to that of actual structures and indicates the usefulness of the large-scale shake-table tests, which provided a remarkable amount of data and information on the behavior of infilled frames.

The test which caused the collapse of the structure was the seventh test exceeding the intensity of the design basis earthquake for Seismic Design Category D. Among these tests, three had spectral accelerations equal or higher than those of the maximum considered earthquake. Considering the severity of the testing protocol, the frame

behaved remarkably well despite the sustained damage which concentrated in the first story eventually leading to a soft-story mechanism. Hence, it can be concluded that in this case the infill panels improved the performance of the structure which developed its peak strength but only minor cracks under excitation levels similar to that of the design basis earthquake. However, it should be pointed out that the frame tested on the shake table was built with extreme caution and did not incorporate vertical irregularities and discontinuities, or torsional effects often associated with the failure of real structures.

The behavior of the shake-table specimen, as well as that of the quasistatically tested specimens has been well captured by the developed finite element methodology. The comparison between the test results and the analytical predictions showed that the numerical models could successfully capture the highly nonlinear load-displacement relation of their physical counterparts, but most importantly they successfully reproduced the failure mechanisms and simulate interaction between the infill walls and the RC frames. The analysis conducted to investigate the sensitivity of the finite element models to the material parameters indicated that the initial stiffness and peak strength of infilled frames can be estimated quite accurately as they are governed by material parameters that can be calibrated with relatively simple tests. Moreover, reasonable variations in the values of these parameters do not change considerably the results of the analyses. This is an important finding because of the expected uncertainty and variability associated with the material properties of hand-made material like mortar.

The validated models have been used to assess the influence of all material properties, design details, geometry of the RC frame, and the size and location of

openings in the masonry wall. The influence of the material parameters was investigated with the validated models of two frames infilled with solid (strong infill) and hollow (weak infill) brick units which fail in different ways and induce different failure mechanisms in the bounding frames. The investigation considered 51 parameters for mortar and masonry units for the infill and concrete reinforced with steel bars for the frame and concluded that the properties of the mortar joints appear to be the most influential for both types of infill. More specifically, the values governing the initial shear strength of the mortar joints are the most important. However, the shear behavior can be accurately estimated *in-situ* with the shove tests or other similar tests which are relatively simple to conduct on existing structures.

The parametric study on the design of the RC frame focused on the reinforcement details of the concrete columns and investigated the influence of the amount of longitudinal and transverse reinforcement. For the non-ductile frame considered here, the study indicated that for values or reinforcement ratio between 1 and 4%, the overall performance of the structure and its failure mechanism were not affected significantly. On the contrary, the amount of shear reinforcement influenced the structural behavior since reducing the spacing or increasing the cross-sectional area of the stirrups prevented the loss of strength caused by shear cracks.

The parametric study on the geometric configuration indicated that the most influential parameter is the aspect ratio of the infill. The aspect ratio affected the axial forces and the shear capacity of the columns, and the cross-sectional area of the infill which determined the cohesive force resisting the crack of the infill. In cases of short

bays, the development of a single strut in the infill changed the failure mechanism as a flexural behavior dominated, even in the case of the non-ductile frames examined in this study. The externally applied vertical load is also influential as it affects the shear capacity of the columns, and the frictional resistance along the mortar joints. The study also considered two-bay infilled frames which exhibited similar failure mechanisms as the single-bay structures, although the location of the shear cracks in the columns changed for columns with infills on both sides. This is an important finding with implications on the design of such structures since the entire height of the structure should be considered as a critical region where potential shear cracks may develop. In terms of the lateral load-vs.-drift relations, the results from the single-bay models can be used for the estimation of the resistance of two-bay structures. The results of this study were verified by the performance of the shake-table tests.

The tests and finite element analyses presented in this study have indicated that the interaction between the masonry walls and the bounding frame can lead to a variety of rather dissimilar failure mechanisms. The actual failure mechanism depends on a number of parameters including the material properties of the RC frame and the masonry panel, the geometry and design of the frame, and the existence, geometry, and locations of openings. Capturing this complex behavior and the exact failure pattern with simplified analytical methods is not possible. However, based on the results of this study, it has been possible to develop simplified force-vs.-drift relations for infilled frames. The proposed approach is intended to provide a quick and conservative estimation of basic information of the structural behavior of each single-bay infilled frame, including its

stiffness and strength. By considering the performance of all bays, a model for a complete frame can be assembled. This model can be used to conduct dynamic analyses of multi-story, multi-bay frames. Nonetheless, the results should be interpreted with caution due to the simplification assumptions made to allow the development of the curves.

11.3 Recommendations Future Research

The research presented in this doctoral dissertation is a step towards the full understanding and accurate assessment of the actual behavior of infilled RC structures during earthquakes. This section includes a number of recommendations for the directions of future research, which may involve:

- further validation of the analytical methods presented here to increase the level of confidence in these methods as prediction tools. The validation is especially recommended for the simplified approach which was developed based on observations, statistical analyses, and conservative assumptions.

- the development of cyclic material laws which can be incorporated in the proposed finite element methodology to allow the simulation of the structural performance under cyclic loads. These models should be calibrated in accordance with the calibration framework developed in this study.

- the consideration of three-dimensional structures subjected to three-dimensional loads in both experimental and analytical models.

- the expansion of the experimental database through tests of different structural configurations built according to different design philosophies and construction practices.

- the development of retrofitting strategies to improve the seismic performance of these structures and prevent brittle failures. The retrofit schemes can include overlays of shotcrete, engineered cementitious composite materials and fiber reinforced polymers for the infill, or the strengthening of the columns with concrete, FRP or steel jackets.

APPENDIX A

GEOMETRY OF STEEL BARS

Table A.1: Geometry of steel reinforcement bars.

Bar ID	Diameter		Area	
	[mm]	(in)	[mm^2]	(in^2)
#2	6.35	(0.25)	31.7	(0.05)
#3	9.53	(0.375)	71.3	(0.11)
#4	12.70	(0.5)	126.7	(0.20)
#5	15.88	(0.625)	197.9	(0.31)
#6	19.05	(0.75)	285.0	(0.44)
#7	22.23	(0.875)	387.9	(0.60)
#8	25.4	(1.00)	506.7	(0.79)

APPENDIX B

DERIVATION OF SCALING FACTORS

B.1 Introduction

This appendix presents the derivation of the scaling factors for the shake-table tests. The scaling factors for three independent quantities need to be defined initially so that the scaling factors for all other quantities can be defined according to the similitude law. For the three-story specimen the scaling factors need to account for the mismatch between the inertia and the gravity mass which is described in Chapter 7. As a consequence, the scaling factors can be derived with two approaches which are described below.

B.2 First Approach

The length scaling factor was defined according to the specimen design to be 2/3. Since commonly available materials were used in the tests, their strength and elastic stiffness could not be scaled and a scaling factor of one is required for the stress. Similarly the acceleration of gravity cannot be scaled and its scaling factor is by default equal to one. Therefore, the three independent scaling factors would be

- Length: $S_L = 2/3$
- Stress: $S_\sigma = 1$

- Acceleration: $S_a = 1$

Based on these three scaling factors and the similitude law, the scaling factors for the other quantities can be defined as follows.

- Strain: $S_\varepsilon = 1$
- Curvature: $S_\kappa = 1/S_L = 3/2$
- Area: $S_A = S_L S_L = 4/9$
- Volume: $S_V = S_L S_L S_L = 8/27$
- Moment of inertia: $S_I = S_L S_L S_L S_L = 16/81$
- Force: $S_F = S_A S_\sigma = 4/9$
- Moment: $S_M = S_F S_L = 8/27$
- Mass: $S_m = S_F / S_a = 4/9$
- Time: $S_t = \sqrt{S_L / S_a} = \sqrt{2/3} = 0.816$
- Frequency: $S_f = 1/S_t = 1.224$

In the case of the three-story specimen the mass causing the inertia forces during a seismic test would need to be larger than the gravity mass attached to the frame due to the difference in the tributary areas illustrated in Figure 8.4. The ratio of seismic to gravity mass is the same for the prototype and the specimen and is defined as $\lambda_M = M_{prot}^{seis} / M_{prot}^{grav} = M_{spec}^{seis} / M_{spec}^{grav}$. The value of the mass ratio is equal to 2.27, which

indicates that the mass of the specimen is 2.27 smaller than the mass required to generate the appropriate seismic forces. Consequently, the actual scaling factor for the seismic mass can be calculated from the following equation.

- Inertial Mass $S_m^{seis} = S_m^{grav} \Big/ \lambda_M = 0.20$

However, the seismic forces need to satisfy the force scaling factor. Therefore, the seismic acceleration, and, therefore, the time and frequency scaling factors would need to be adjusted accordingly to generate the appropriate seismic forces.

- Seismic acceleration: $S_a^{seis} = \lambda_M S_a^{grav} = 2.273$
- Time $S_t^{seis} = \sqrt{S_L^{seis} \Big/ \lambda_M S_a^{grav}} = \sqrt{1 \Big/ \lambda_M} S_t^{grav} = 0.542$
- Frequency: $S_f^{seis} = \sqrt{\lambda_M} \ 1 \Big/ S_t^{grav} = 1.846$

B.3 Alternative Approach

The scaling factors for the dynamic quantities of mass, seismic acceleration, time, and frequency can be also calculated by if the actual scaling factor for the mass is directly calculated by considering the actual mass of the specimen and the seismic mass of the prototype.

- Seismic mass: $S_m^{seis} = M_{spec}^{grav} \Big/ M_{prot}^{seis}$
- Seismic acceleration: $S_a^{seis} = S_F^{seis} \Big/ S_m^{seis} = S_F \Big/ S_M^{seis}$
- Time: $S_t^{seis} = \sqrt{S_L^{seis} \Big/ S_a^{seis}} = \sqrt{S_L \Big/ S_a^{seis}}$

- Frequency: $S_f^{seis} = 1 \Big/ S_t^{seis}$

It can be shown that the two approaches reach the same scaling factors with the second approach being more direct and simpler to apply.

$$S_m^{seis} = \frac{M_{spec}^{grav}}{M_{prot}^{seis}} = \frac{M_{spec}^{grav}}{M_{prot}^{grav}} \frac{M_{prot}^{grav}}{M_{prot}^{seis}} = \frac{M_{spec}^{grav}}{M_{prot}^{grav}} S_m^{grav}$$

Similarly, for the acceleration, it is:

$$S_a^{seis} = S_F^s \Big/ S_M^{seis} = \frac{S_F M_{prot}^{seis}}{M_{spec}^{grav}} = \frac{S_F M_{prot}^{seis}}{M_{spec}^{grav}} \frac{M_{prot}^{grav}}{M_{prot}^{grav}} = \frac{M_{prot}^{seis}}{M_{prot}^{grav}} \frac{S_F}{S_M^{grav}} = \frac{M_{prot}^{seis}}{M_{prot}^{grav}} S_a^{grav}$$

Finally, the time scaling factor can be estimated as:

$$S_t^{seis} = \sqrt{\frac{S_L}{S_a^{seis}}} = \sqrt{\frac{M_{prot}^{grav} S_L}{M_{prot}^{seis} S_a^{grav}}} = \sqrt{\frac{M_{prot}^{grav}}{M_{prot}^{seis}}} \sqrt{\frac{S_L^{grav}}{S_a^{grav}}} = \sqrt{\frac{M_{prot}^{grav}}{M_{prot}^{seis}}} S_t^{grav}$$

The last three equations can be also written with the consideration of the seismic to gravity mass ratio, $\lambda_M = M_{spec}^{seis} \Big/ M_{spec}^{grav}$.

- Mass: $S_m^{seis} = 1 \Big/ \lambda_M \, S_m^{grav}$
- Acceleration: $S_a^{seis} = \lambda_M S_a^{grav}$
- Time: $S_t^{seis} = \sqrt{\frac{1}{\lambda_M^s}} S_t^g$

It is evident that the scaling factors derived with the two approaches are identical.

APPENDIX C

DRAWINGS AND CONSTRUCTION STAGES OF THE THREE-STORY SPECIMEN

C.1 Introduction

This appendix presents a complete set of drawings and the pictures from the construction of the specimen tested at the LHPOST at UCSD.

C.2 Drawings

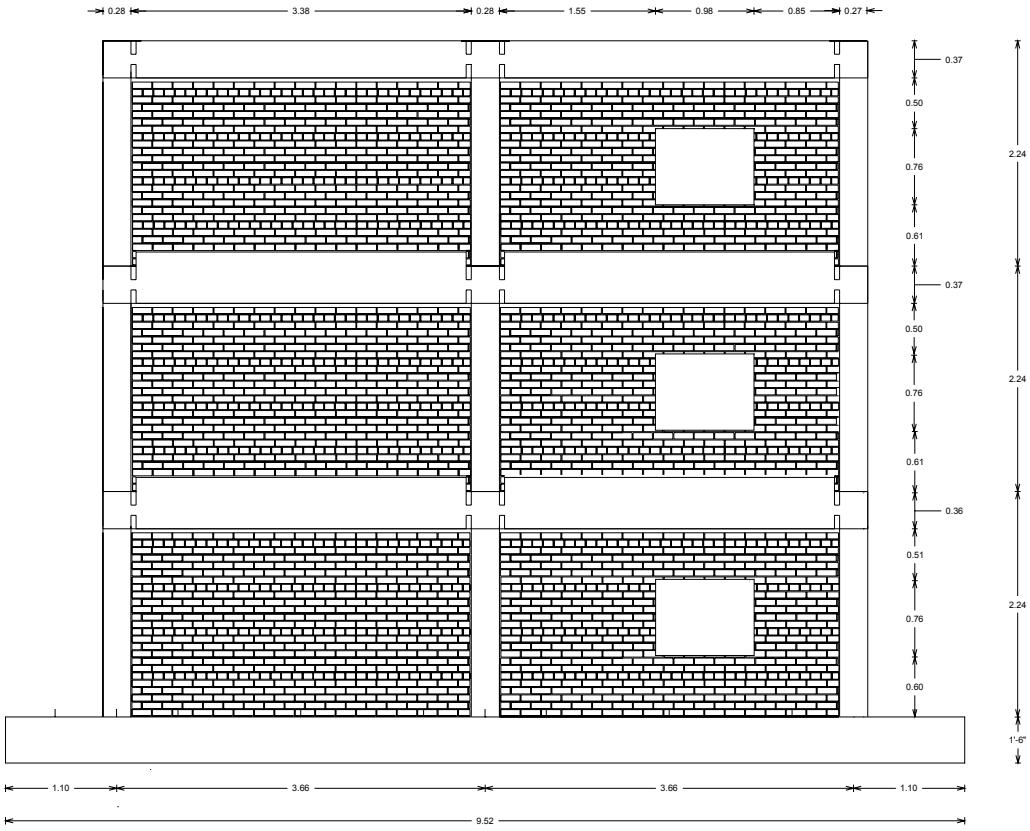

Figure C.1:Elevation of the shake table specimen.

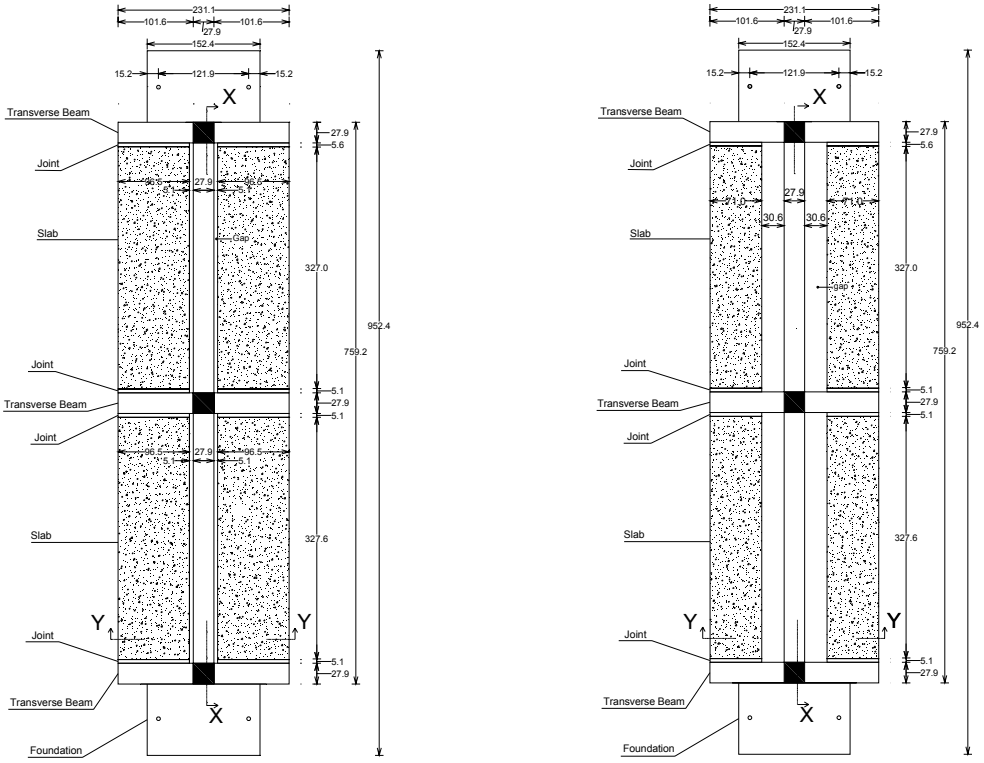

(a) first and second story (b) roof

Figure C.2: Plan view.

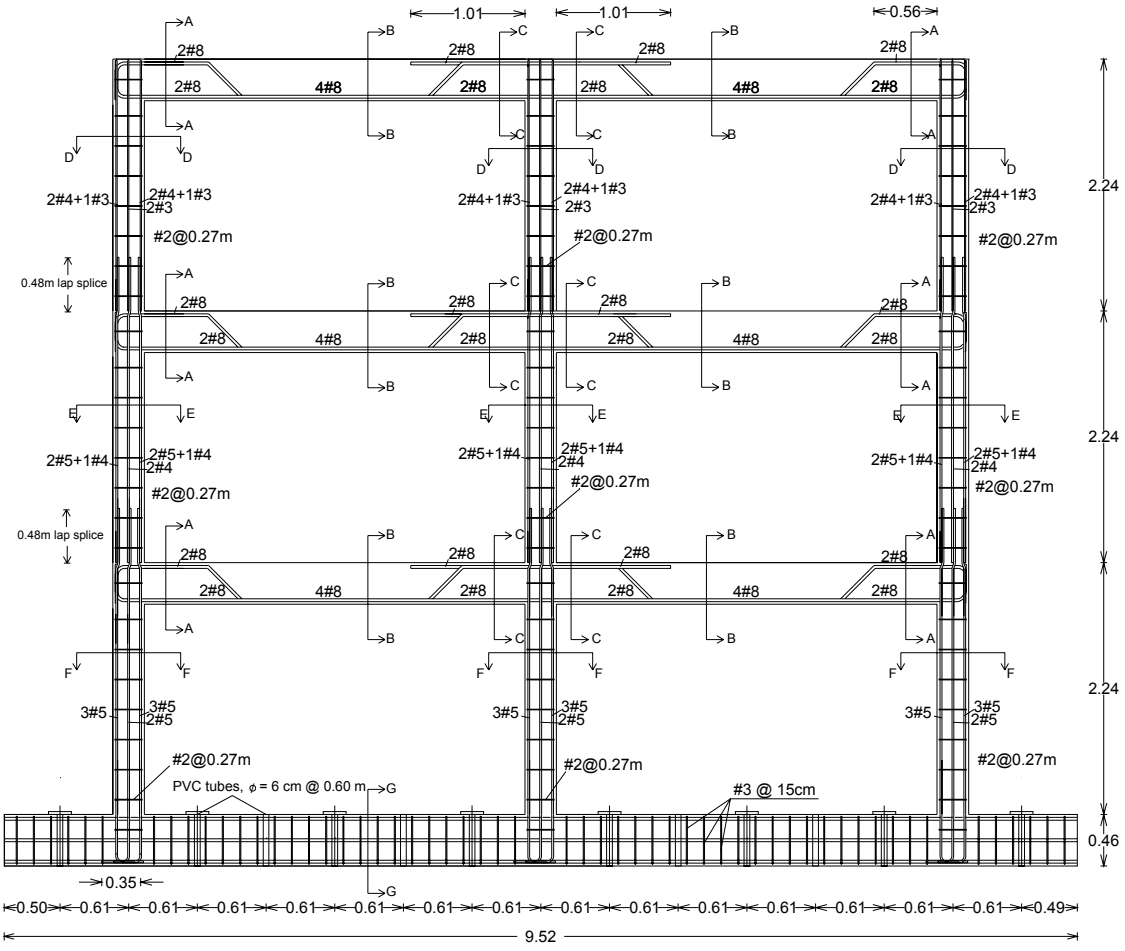

Figure C.3: Design of RC frame.

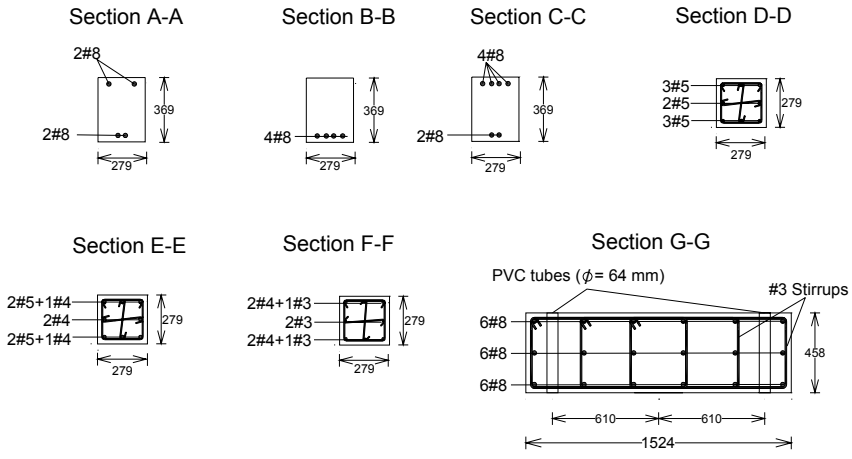

Figure C.4: Reinforcement details of RC members.

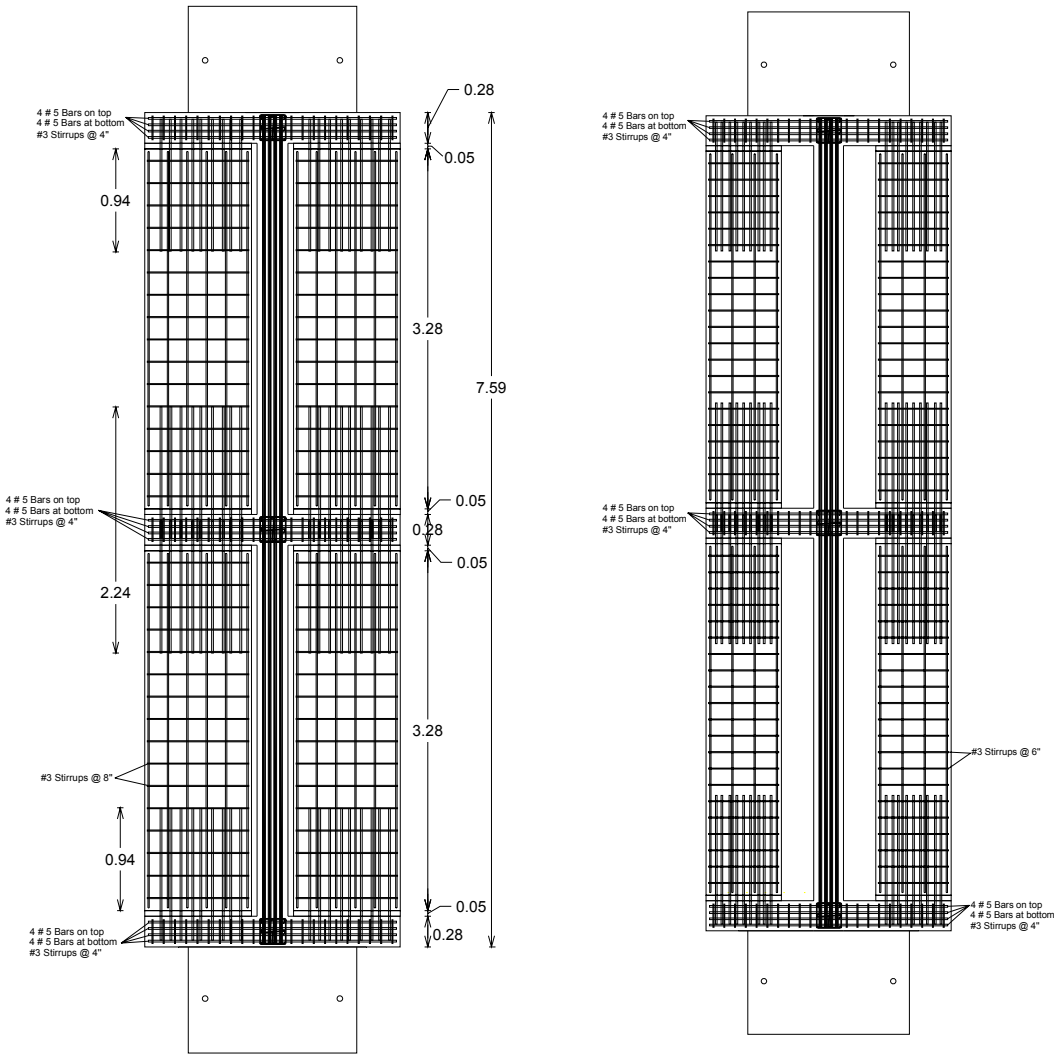

(a) first and second story (b) roof

Figure C.5: Design of concrete slabs.

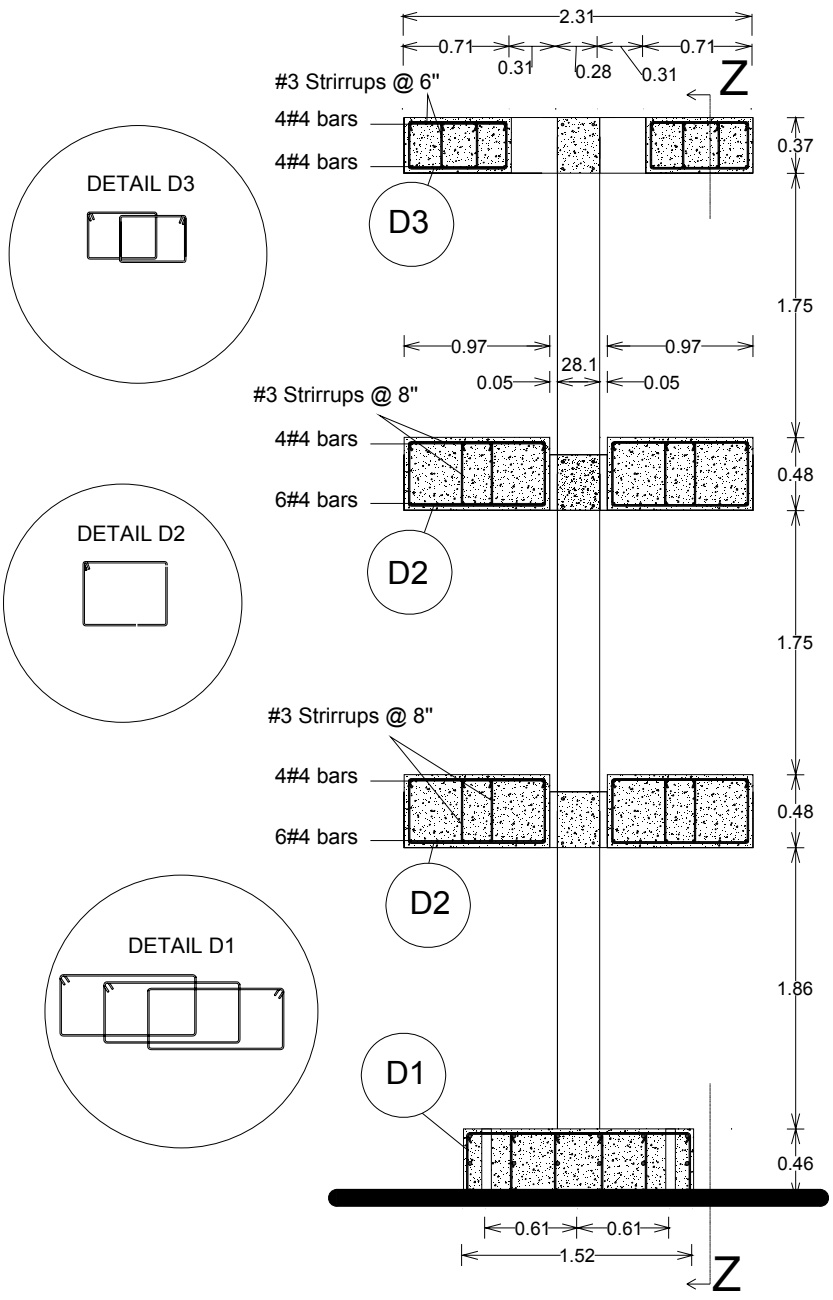

Figure C.6: Reinforcement of concrete slabs.

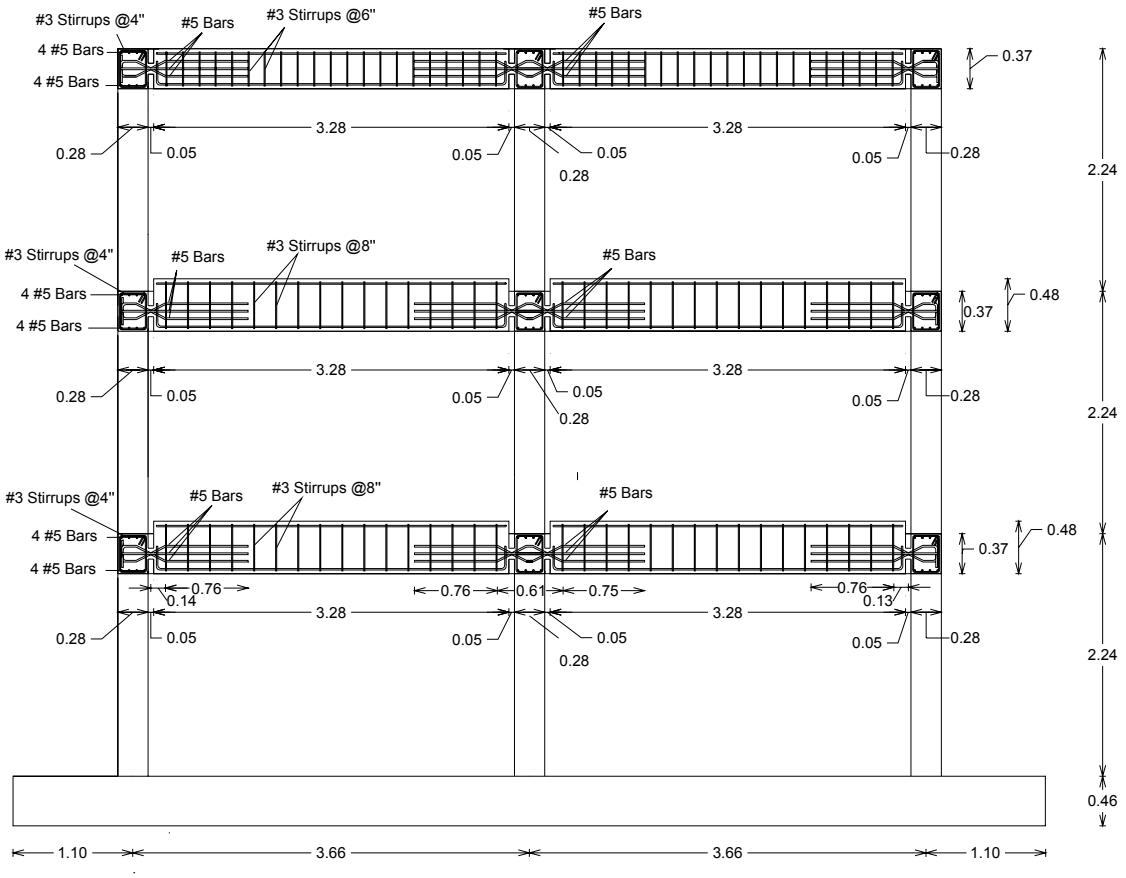

Figure C.7: Reinforcement of concrete slabs (Section Z-Z).

C.3 Construction Stages

This appendix presents a complete set of drawings and the pictures from the construction of the specimen tested at the LHPOST at UCSD.

Figure C.8: Reinforcement and formwork for the foundation.

Figure C.9: Concrete pour for the foundation..

Figure C.10: Detail of first story column.

Figure C.11: Detail of first story beam-slab connection reinforcement.

Figure C.12: Detail of joint reinforcement.

Figure C.13: First story beam and column reinforcement.

Figure C.14: Concrete pour for the first story columns, beams, and slabs.

Figure C.15: Detail of middle column-beam reinforcement..

Figure C.16: Slab reinforcement and foam used to form concrete hinge.

Figure C.17: Detail of column lap-splice.

Figure C.18: Transverse beam and slab reinforcement.

Figure C.19: Steel reinforcement and foam used for slab-to-beam connection.

Figure C.20: Detail of column reinforcement.

Figure C.21: Completed RC frame with form work.

Figure C.22: Completed RC frame.

(a) installation of a steel tower

(b) gap between the specimen the steel tower

Figure C.23: Installation of the steel towers.

Figure C.24: Laying the head course.

Figure C.25: First bay almost infilled.

Figure C.26: Dry-packing of beam-to-infill wall.

Figure C.27: Last brick.

Figure C.28: Completed infilled frame.

Figure C.29: Laying bricks with running bond.

Figure C.30: Building triplet specimens.

APPENDIX D

INSTRUMENTATION DETAILS

This appendix presents a set of pictures of the supports used to mount the array of sensors discussed in Chapter 7 on the three-story specimen tested at LHPOST at UCSD.

Figure D.1: LVDTs used to measure the rotation of slab-to-beam hinge connection at the first story.

(a) LVDT on the top surface

(b) LVDT on the bottom surface

Figure D.2: LVDTs used to measure the rotation of slab-to-beam hinge connection at the roof level.

(a) at the roof

(b) at the second story

Figure D.3: Accelerometers near the middle column.

Figure D.4: Accelerometers near the west end of the foundation.

Figure D.5: Accelerometers at east end of the structure at the roof level.

Figure D.6: LVDTs measuring the sliding of the infill wall with respect to the beam.

Figure D.7: LVDT measuring the sliding of the infill wall with respect to the beam.

(a) at the first story

(b) at the second story

Figure D.8: String pots measuring the displacement of the structure with respect to the steel towers.

(a) poles used to measure the interstory displacements

(b) pole installed at the first story

Figure D.9: Elevation.

Figure D.10: LVDT measuring the first story displacement.

Figure D.11: LVDT measuring the displacement between first and second story levels.

Figure D.12: String pots measuring the frame deformations (top of West column).

Figure D.13: String pots measuring the frame deformations (bottom of middle column).

Figure D.14: Attachment of strings measuring the frame deformations (top of East column).

APPENDIX E

MATERIAL PROPERTIES

The stress-vs.-strain of the materials used in the construction of the shake-table specimen is presented in this chapter.

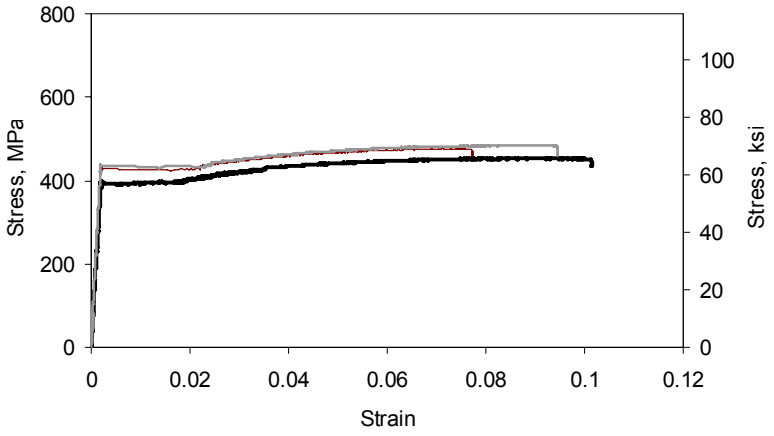

Figure E.1: Tensile stress-vs.-strain behavior for #2 bars.

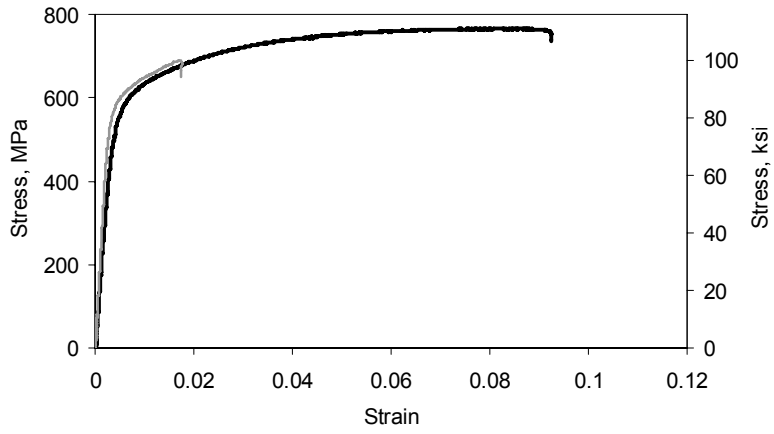

Figure E.2: Tensile stress-vs.-strain behavior for #3 bars.

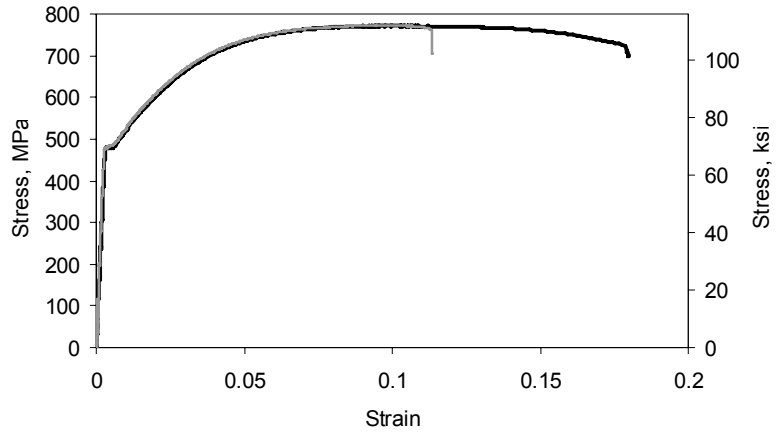

Figure E.3: Tensile stress-vs.-strain behavior for #4 bars.

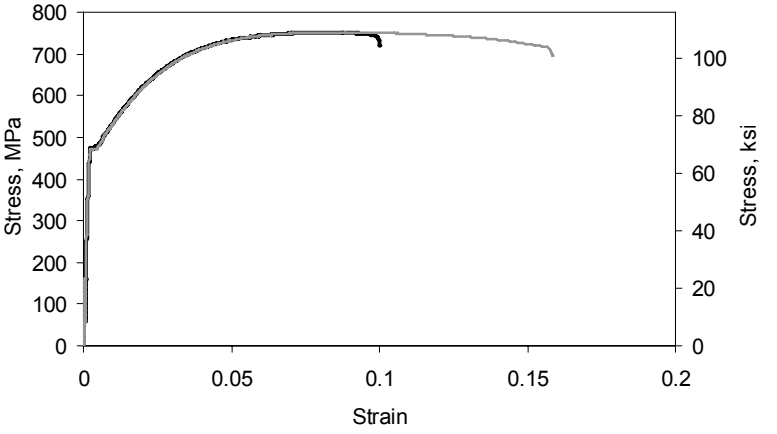

Figure E.4: Tensile stress-vs.-strain behavior for #5 bars.

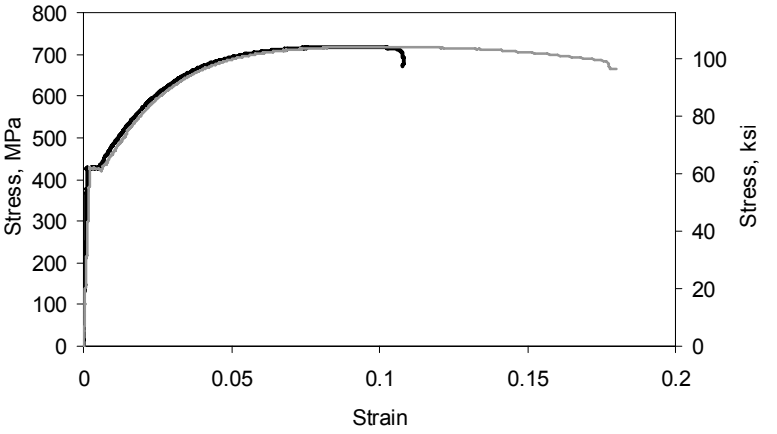

Figure E.5: Tensile stress-vs.-strain behavior for #8 bars.

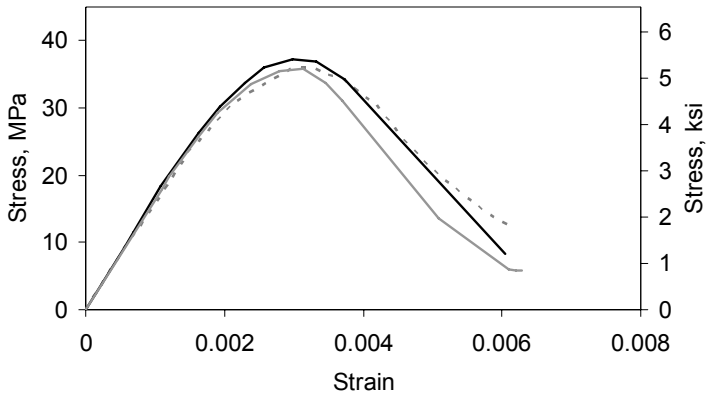

Figure E.6: Compressive stress-vs.-strain behavior for first story concrete obtained the day of the first major test (11-10-2009).

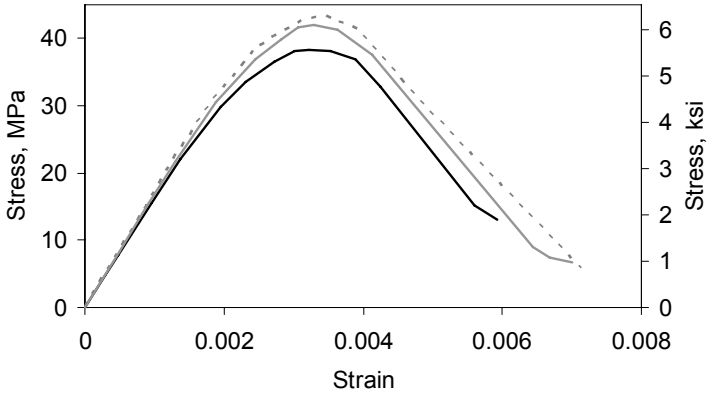

Figure E.7: Compressive stress-vs.-strain behavior for second story concrete obtained the day of the first major test (11-10-2009).

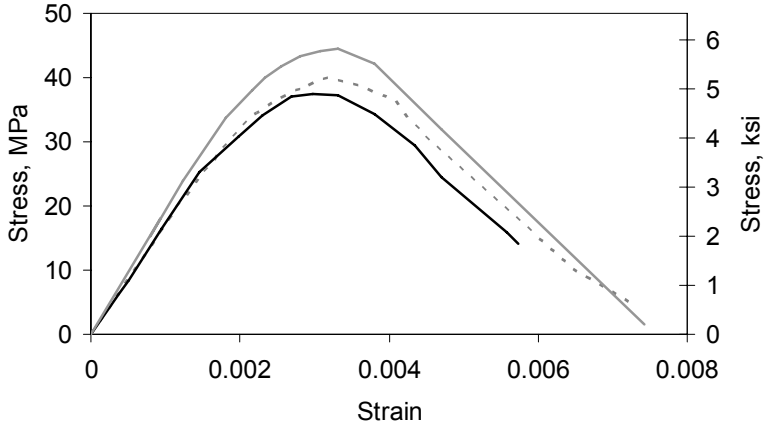

Figure E.8: Compressive stress-vs.-strain behavior for third story concrete obtained the day of the first major test (11-10-2009).

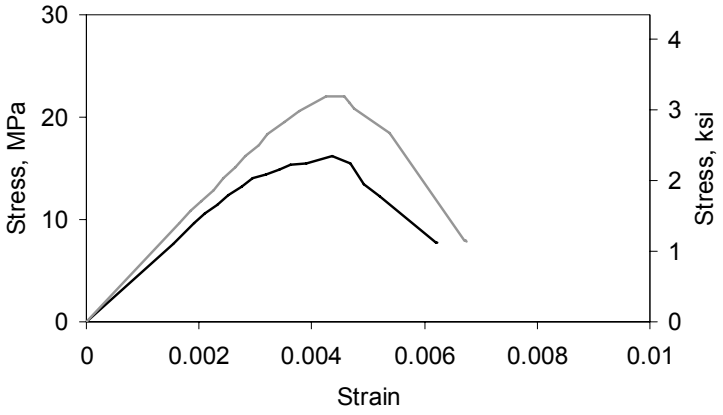

Figure E.9: Compressive stress-vs.-strain behavior for first story masonry prisms obtained the day of the first major test (11-10-2009).

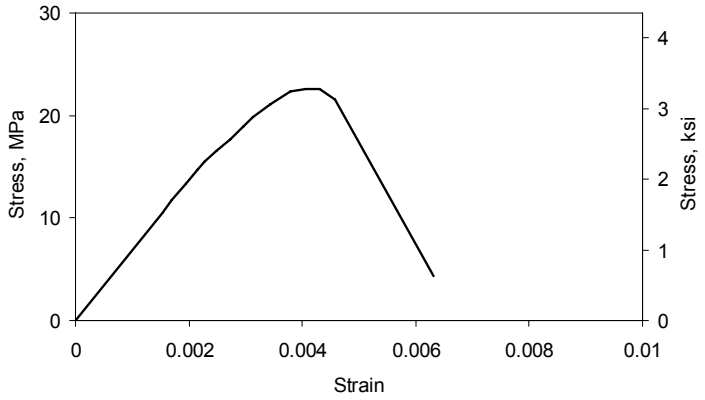

Figure E.10: Compressive stress-vs.-strain behavior for second story masonry prisms obtained the day of the first major test (11-10-2009).

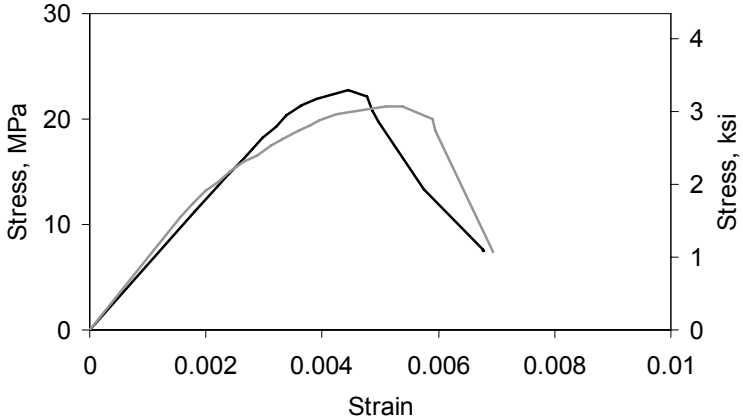

Figure E.11: Compressive stress-vs.-strain behavior for third story masonry prisms obtained the day of the third major test (11-10-2009).

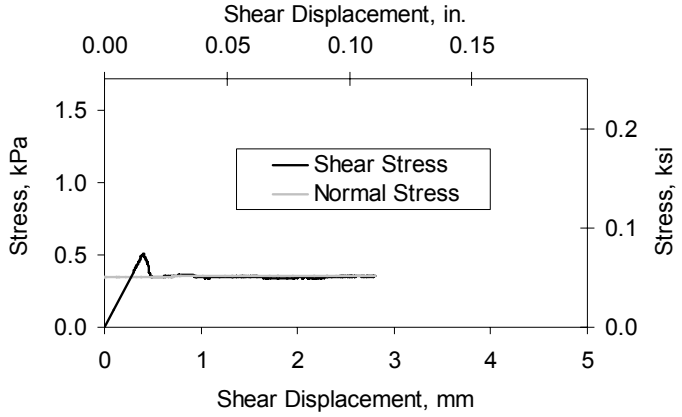

Figure E.12: First story triplet test under normal stress of 0.35 MPa (0.05 ksi).

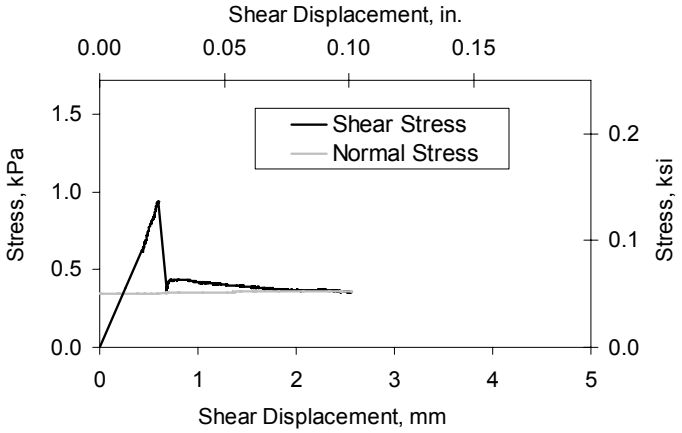

Figure E.13: Second story triplet test under normal stress of 0.35 MPa (0.05 ksi).

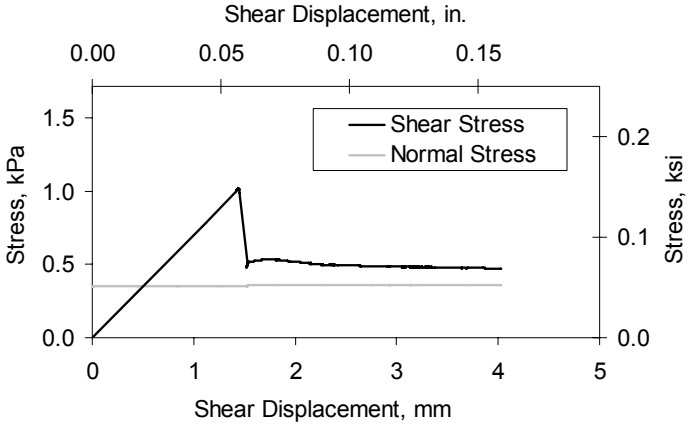

Figure E.14: Third story triplet test under normal stress of 0.35 MPa (0.05 ksi).

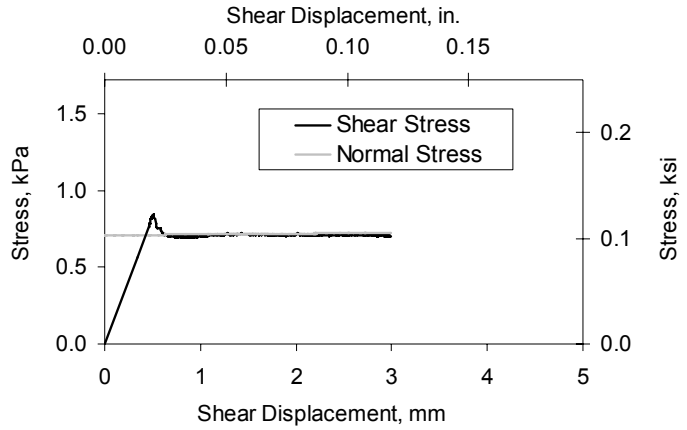

Figure E.15: First story triplet test under normal stress of 0.69 MPa (0.1 ksi).

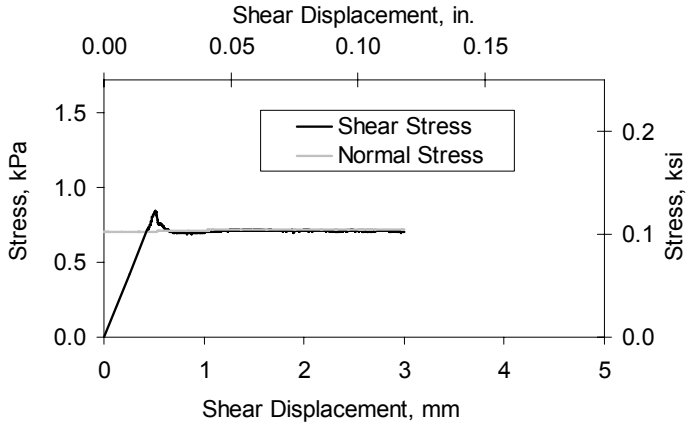

Figure E.16: Second story triplet test under normal stress of 0.69 MPa (0.1 ksi).

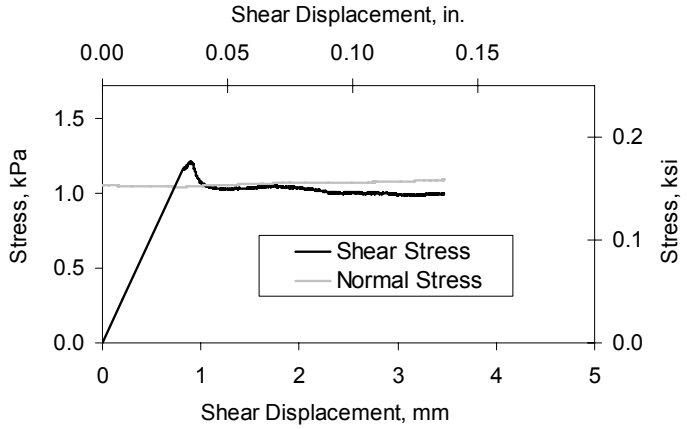

Figure E.17: First story triplet test under normal stress of 1.03 MPa (0.15 ksi).

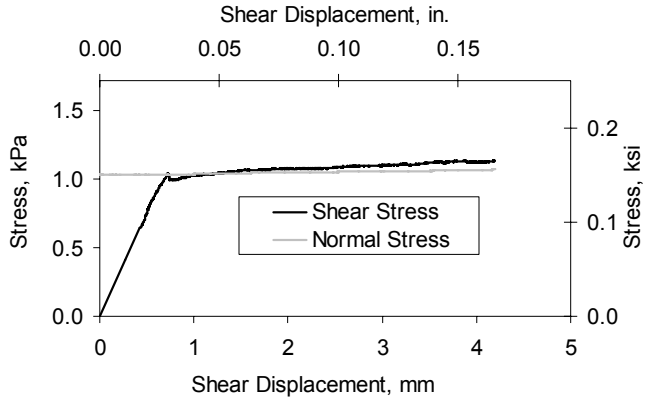

Figure E.18: Second story triplet test under normal stress of 1.03 MPa (0.15 ksi).

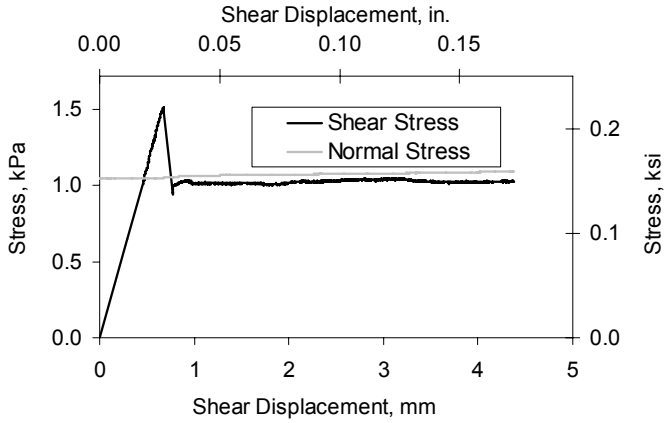

Figure E.19: Third story triplet test under normal stress of 1.03 MPa (0.15 ksi).

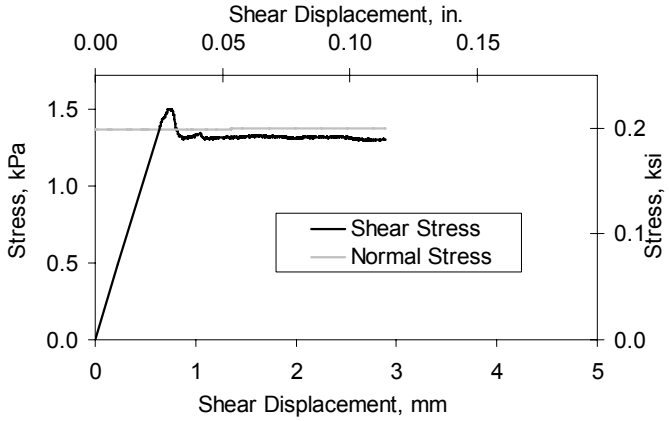

Figure E.20: First story triplet test under normal stress of 1.38 MPa (0.2 ksi).

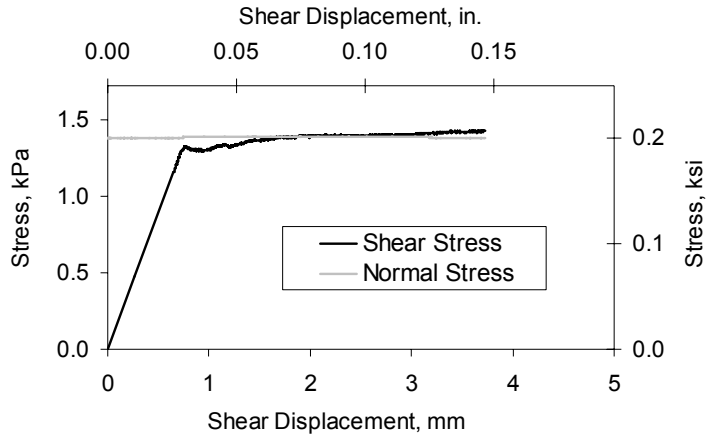

Figure E.21: First story triplet test under normal stress of 1.38 MPa (0.2 ksi).

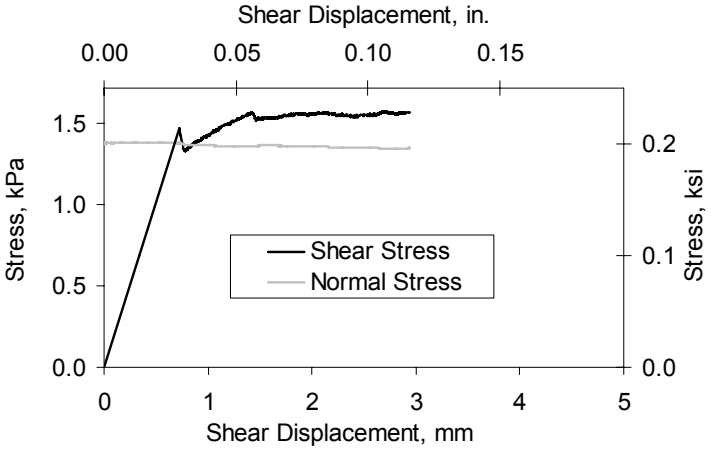

Figure E.22: Second story triplet test under normal stress of 1.38 MPa (0.2 ksi).

REFERENCES

ACI 501-36T, 1936. "Building Regulations for Reinforced Concrete." Farmington Hills, Mi.

ACI 530.1-99 (1999). "Building Code Requirements & Specifications for Masonry Structures and Related Commentaries." Farmington Hills, Mi.

ACI 318-89 (1989). "Building Code Requirements for Structural Concrete (ACI 318-89) and Commentary." Farmington Hills, Mi.

ACI 318-05 (2005). "Building Code Requirements for Structural Concrete (ACI 318-05) and Commentary." Farmington Hills, Mi.

ACI 318-08 (2008). "Building Code Requirements for Structural Concrete (ACI 318-08) and Commentary." Farmington Hills, Mi.

Al-Chaar, G. (2002), "Evaluating Strength and Stiffness of Unreinforced Masonry Infill Structures." *Report No. ERDC/CERL TR-02-1*, US Army Corps of Engineers.

Al-Chaar, G.K., J.B. Berman, and S.C. Sweeney (2003). "Investigation of FRP for seimic rehabilitation of RC structural frames with URM infill." *Report No. ERDC/CERL TR-03-10*, US Army Corps of Engineers.

Al-Chaar, G., A.B. Mehrabi, and T. Manzouri (2008). "Finite element interface modeling and experimental verification of masonry-infilled R/C frames." *The Masonry Society Journal*, Vo. 26(1), 47-65.

Amadei, B., S. Sture, and S. Saeb (1989). "An evaluation of masonry joint shear strength in existing buildings." Report to N.S.F., Vol 1, Civil Eng. Dept. University of Colorado at Boulder.

American Society for Testing and Materials (ASTM) (1997). "Chemical-Resistant Nonmetallic Materials; Vitrified Clay Pipe; Concrete Pipe; Fiber-Reinforced Cement Products; Mortars and Grouts; Masonry; Precast Concrete". *ASTM Volume 04.05*, West Conshohocken, PA.

Anagnos, T. (2009). *Personal Communication.*

Anagnos, T., M.C. Comerio, C. Goulet, J. Steele, and J.P. Stewart (2010). "Development of a Concrete Building Inventory: Los Angeles Case Study for the Analysis of Collapse Risk.' *Proc. 9th National & 10th Canadian Conf. on Earthquake Eng.*, Toronto, Canada.

Angel, R., D. Abrams, D. Shapiro, J. Uzarski, M. Webster(1994). "Behavior of reinforced concrete frames with masonry infill walls." *Report No. UIUC-ENG-94-2005.* University of Illinois at Urbana-Champaign. IL.

ASCE/SEI 7-05 (2006). "Minimum Design Loads for Buildings and Other Structures." ASCE, Reston, Va.

ASCE/SEI 41-06. (2006). "Seismic Rehabilitation of existing buildings." ASCE, New York.

Attard, M. M., A. Nappi, and F. Tin-Loi (2007). "Modeling fracture in Masonry." *J. Struct. Eng.*, ASCE, Vol. 133(10), 1385-1392.

Bazant Z. P. and E. Becq-Giraudon (2002). "Statistical prediction of fracture parameters of concrete and implications for choice of testing standard." *Cement and Concrete Research*, Elsevier, Vol. 32, 529-556.

Bazant, Z.P. and B.H. Oh (1983). "Crack Band theory for fracture of concrete". *Materials and Structures*, 31, RILEM, 16(93), 155-177.

Billington, S.L., M.A. Kyriakides, B. Blackard, K. Willam, A. Stavridis, and P.B. Shing (2009). "Evaluation of a sprayable, ductile cement-based composite for the seismic retrofit of unreinforced masonry infills." *Proceedings of ATC* & SEI *Conference* on Improving the Seismic Performance of Existing Buildings and Other Structures, Applied Technology Council and Structural Engineering Institute, San Francisco, CA.

Blackard, B., K. Willam, and S. Mettupulayam (2009). "Experimental observations of masonry infilled RC frames with openings." *ACI Special Publication SP-265*, American Concrete Institute, Farmington Hills, MI.

Calvi, G.M., D. Bolognini, and A. Penna (2004). "Seismic performance of masonry-infilled RC frames: benefits of slight reinforcement." *Proceedings of 6th Nat. Conf. on Seismology and Earthquake Engineering*, Guimaraes, Portugal, 253-276.

Carol, I., P.C. Prat, and C.M. Lopez (1997). "Normal/shear cracking model: application to discrete crack analysis." *ASCE Journal of Engineering Mechanics,* 123 (8), 765-773.

Caughey R.A., 1933. Reinforced Concrete. Edwards Brothers Inc. Michigan.

Centeno J., C.E. Ventura, S. Foo (2008). "Shake Table Testing of Gravity Load Designed Reinforced Concrete Frames with Masonry Infill Walls." *Proceedings of the 14th World Conference on Earthquake Engineering*, Beijing, China.

Charney F.A. (2008). "Unintended consequences of modeling damping in structures " *ASCE Journal of Structural Engineering* .134:4.

Chiou Y.J., J.C. Tzeng, and Y.W. Liou (1999). "Experimental and analytical study of masonry infilled frames." *J. Struct. Eng.*, ASCE, Vol. 125(10), 1109-1117.

Citto C. (2008). "Two-Dimensional Interface Model Applied to masonry structures." *Master's Thesis*. University of Colorado at Boulder.

Crisafulli, F.J. (1997). "Seismic behavior of reinforced concrete structures with masonry infills." *Doctoral Dissertation*, University of Canterbury, Christchurch, New Zealand.

Crisafulli, F.J. and A.J. Carr (2007). "Proposed macro-model for the analysis of infilled frame structures." *Bulletin of the New Zealand Society for Earthquake Engineering,* 40 (2), 69-77.

Colangelo, F. (2005). "Pseudo-dynamic seismic response of reinforced concrete frames infilled with non-structural brick masonry." *Earthquake Engineering and Structural Dynamics*, Vol. 34, pp. 1219-1241.

da Porto F. (2005). "In plane cyclic behavior of thin layer joint masonry." *Doctoral Diessrtation*. University of Trento, Trento, Italy.

da Porto F., E. Garbin, C. Modena, M.R. Valluzi (2005). "Filure modes for in plane loaded masonry walls made with thin layer mortar." *Proceedings of the 10th Canadian Masonry Symposium,* Banff, Canada.

Doebling, S.W., C.R. Farrar, M.B. Prime, and D.W. Shevitz (1996). *Damage identification in structures and mechanical systems based on changes in their vibration characteristics: a detailed literature survey.* Los Alamos National Laboratory Report, LA-13070-MS, Los Alamos, NM.

Doebling, S.W., C.R. Farrar, and M.B. Prime (1998). "A summary review of vibration-based damage identification methods." *The Shock and Vibration Digest,* 30(2), 99-105.

Drysdale, R.G., A.A. Hamid, and L.R. Baker (1999). "Masonry Structures-Behavior and Design." *The Masonry Society*, Boulder, CO.

EERI (1996). "1994 Northridge Earthquake Reconnaissance Report." *Earthquake Spectra*, Vol. 12, Issues S1 and S2.

EERI (2000). "1999 Kocaeli, Turkey earthquake reconnaissance report." *Earthquake Spectra*, Vol. 16, Issue S1.

European Committee for Standardization. EN 1992-1-1:2004 (2004). "Eurocode 2-Design of Concrete Structures. Part 1-1: General rules, and rules for buildings." European Committee for Standardization.

European Committee for Standardization. EN 1998-1:2004 (2005). "Eurocode 8-Design of for Earthquake Resistance. Part 1: General rules seismic actions, and rules for buildings." European Committee for Standardization.

Fardis, M.N., S.N. Bousias, G. Franchioni, and T.B. Panagiotakos (1999). "Seismic response and design of RC structures with plan-eccentric masonry infills." *Journal of Earthquake Engineering and Structural Dynamics*, Vol. 28, 173-191.

FEMA 306 (1998). "Evaluation of earthquake damaged concrete and masonry wall buildings: basic procedures manual." Federal Emergency Management Agency, Washington, D.C.

FEMA 356 (2000). *Prestandard and Commentary for the Seismic Rehabilitation of Buildings*, prepared by the American Society of Civil Engineers, Reston, VI.

FEMA P440A (2008). *Effects of Strength and Stiffness Degradation on Seismic Response*, prepared by Applied Technology Council, Redwood City, CA.

FEMA P695 (2009). *NEHRP Quantification of Building Seismic Performance Factors*. Federal Emergency Agency, Washington, DC.

Filiatrault, A., S. Kremmidas, F. Seible, A.J. Clark, R. Nowak, A.B.K Thoen (2000). "Upgrade of First Generation Uniaxial Seismic Simulation System with Second Generation Real-Time Three-Variable Digital Control System." *Proceedings of 12th World Conference in Earthquake Engineering*, Auckland, New Zealnad.

Fiorato, A.E., M.A. Sozen, and W.L. Gamble (1970). "An investigation of the interaction of reinforced concrete frames with masonry filler walls." *Report No. UILU-ENG 70-100*, Dept. of Civ. Eng., University of Illinois at Urbana-Champaign.

Hall J.F., (2006). Problems encountered from the use (or misuse) of Rayleigh damping. Jounral or Earthquake Engineering and Structural Dynamics. Vol. 35, pp 525-535.

Harris H.G. and G.M. Sabnis (1999). "Structural modeling and experimental techniques." *CRC Press*, Boca Raton, FL.

Hashemi, A. and K.M. Mosalam (2006). "Shake-table experiment on reinforced concrete structure containing masonry infill wall." *Journal of Earthquake Engineering and Structural Dynamics*, Vol. 9(1), 73-83.

Hassanzadeh M. (1990). "Determination of fracture zone properties in mixed mode I and II." *Journal of Engineering Fracture Mechanics*. Col 35. No 4/5, 845-853.

Hilsdorf, H. K. (1966). "Investigation into the failure mechanism of brick masonry under axial compression." *Designing, Engineering and Construction with Masonry Products*, F. B. Johnson, Ed., Gulf Publishing, Houston, TX, 34-41

International Conference of Building Officials (ICBO) (2001). *Guidelines for Seismic Retrofit of Existing Buildings.* ICBO, Whittier, Ca.

Kakaletsis, J. and G. Karayannis (2009). "Experimental investigation of infilled reinforced concrete frames with openings." *ACI Structural Journal*, March-April Issue, pp. 132-141.

Kyriakides, M.A. (2010), "Seismic Retrofit of Unreinforced Masonry Infills in Non-Ductile Reinforced Concrete Frames using Engineered Cementitious Composites," Doctoral Dissertation, Stanford University, in progress.

Kyriakides, M.A. and S.A. Billington (2008). "Seismic retrofit of masonry-infilled non-ductile reinforced concrete frames using sprayable ECC." *Proceedings of the 14th World Conference on Earthquake Engineering*, Beijing, China.

Liauw T.C. and K.H Kwan (1983). "Plastic theory of infilled frames with finite interface shear strength." *Proc. Inst. Civ. Engrs*, Part 2, 1983, 75, Dec 707-723

Lotfi, H.R. (1992). "Finite element analysis of fracture of concrete and masonry structures." *Doctoral Dissertation*, University of Colorado at Boulder.

Lotfi, H.R. and P.B. Shing (1991). "An appraisal of smeared crack models for masonry shear wall analysis." *J. Computers Struct.*, ASCE, Vol. 120(1), 63-80.

Lotfi, H.R. and P.B. Shing (1994). "An interface model applied to fracture of masonry structures." *J. Struct. Eng.*, ASCE, 120(1): 63-80.

Lourenco, P.B. (1996). "Computational Strategies for masonry structures." *Doctoral Dissertation*, Delft University, Delft, The Netherlands.

MacGregor, J.G and J.K. Wight (2005). "Reinforced Concrete Mechanics and Design." Pearson Prentice Hall, Upper Saddle River, NJ.

Madan, A., A.M. Reinhorn, J.B. Mander, and R.E. Valles (1997). "Modeling of Masonry Infill Panels for Structural Analysis." *ASCE Journal of Structural Engineering*, 123 (10), 1295–1302.

Maffei J., J. Kariotis, D. Breiholz, G. Kingsley, R. Mayes, P. Murray, and M. Valley (2006). *Personal Communication.*

Mainstone, R.J. and G.A. Weeks (1970). "The influence of bounding frame on the racking stiffness and strength of brick walls." *Proceedings of the 2nd International Conference on Brick Masonry*, Stoke-on-Trent, United Kingdom, 165-171.

Marini, A and E. Spacone (2006). "Analysis of reinforced concrete elements including shear effects." *ACI Structural Journal*. Vol 103(5), 645-655.

Mander J. B., L. E. Aycardi, and D. K. Kim (1994), "Physical and analytical modeling of brick infilled steel frames." *Proceedings from NCEER Workshop on Seismic of Masonry Infills.* D.P. Abrams (ed), *Technical Report No NCEER-94-0004*, National Center for Earthquake Engineering Research, State University of New York, Buffalo, NY.

Manzuri, T. (1995). "Nonlinear finite element analysis and experimental evaluation of retrofitting techniques for unreinforced masonry structures." *Doctoral Dissertation*, University of Colorado at Boulder.

McKenna F., G.L. Fenves (2000). An Object-oriented software design for parallel structural analysis. *Proceedings of the SEI/ASCE Structures Congress*, Philadelphia, PA.

Mehrabi, A.B. and P. B. Shing (1997). "Finite element modeling of masonry-infilled RC frames." *J. Struct. Eng.*, ASCE, Vol. 123(5), 604-613.

Mehrabi, A.B., P.B. Shing, M.P. Schuller, and J.L. Noland (1994). "Performance of masonry-infilled R/C frames under in-plane lateral loads." *Report No. CU/SR-94/6*, University of Colorado at Boulder.

Menegotto M., P.E. Pinto (1973). "Method of analysis for cyclically loaded reinforced concrete plane frames including changes in geometry and nonelastic behavior of elements under combined normal force and bending." *IASBE Symposium on Resistance and Ultimate Deformability of structures Acted on by Well-Defined Repeated Loads*, Final Report, Lisbon, 1973.

Moaveni, B., X. He, J.P. Conte, and J.I. Restrepo (2009) "System identification study of a seven-story full-scale building slice tested on the UCSD-NEES shake table." *Journal of Structural Engineering, ASCE*, under review.

Moaveni, B., A. Stavridis, and P.B. Shing (2010). "System identification of a three-story infilled RC frame tested on the UCSD-NEES shake table." *Proc. of 28th International Conference on Modal Analysis (IMAC-XXVIII)*, Jacksonville, FL.

Masonry Standards Joints Committee (2008). *Building Code Requirements and Specifications for Masonry Structures*. The Masonry Society, Boulder, CO.

Ozcelik, O. (2008). *A Mechanics-based virtual model of NEES-UCSD shake table: theoretical development and experimental validation.* Ph.D. Dissertation, Department of Structural Engineering, University of California, San Diego, CA.

Ozcelik, O., E.J Luco, J.P. Conte, T.L. Trombetti, and J.I. Restrepo (2008). "Experimental characterization, modeling and identification of the UCSD-NEES shake table mechanical system." Earthquake Engineering and Structural Dynamics, Volume 37(2), pp. 243-264, doi: 10.1002/eqe.754.

Papadrakakis M., V. Papadopoulos, M. Georgioudakis, G. Hofstetter, and C. Feist (2005). "Reliability analysis of a plain concrete beam." *IALAD Project Report*, Verbund - Austrian Hydro Power, Austria.

Paulay, T and M.J.N. Priestley (1992) *Seismic Design of Reinforced Concrete and Masonry Buildings*, John Wiley & Sons, Inc, Hoboken, New Jersey, pp 768.

Pluijm, R.v.d. (1992). "Material properties of masonry and its components under tension and shear." *6th Canadian Masonry Symposium*. Saskatchewan, Canada, 675-686.

Restrepo, J.I., J.P. Conte, F. Seible, and L. Van Den Einde (2005). "The NEES@UCSD Large High Performance Outdoor Shake Table." *Proceedings of Geofrontiers Conference,* ASCE, Austin, Texas.

Rots J.G. (1988). "Computational modeling of concrete fracture." Doctoral Thesis, Delft University of Technology, Netherlands.

Shing P.B. and B. Spencer (1999). "Modeling of Shear Behavior of RC Bridge Structures." *Proc. of the US-Japan Seminar on Post-Peak Behavior of RC Structures Subjected to Seismic Loads – Recent Advances and Challenges of Analysis and Design*, NSF-JSPS-JCI, Tokyo, Japan, 315-333.

Spacone E., F.C. Filippou, F.F. Taucer. (1996). "Fibre beam-column model for nonlinear analysis of R/C frames: Part I. Formulation." *Journal of Earthquake Engineering and Structural Dynamics* 1996; 25, 711-725.

Stafford Smith, B. (1962). "Lateral stiffness of infilled frames." *Journal of Structural Division*, ASCE. Vol. 88(6), 183-199.

Stafford Smith, B. (1966). "Behavior of square infilled frames." *Journal of Structural Division.* ASCE, 381-403.

Syrmakezis, C.A. and V. Y. Vratsanou (1986). "Influence of infill walls to R.C frames response." *Proceedings of the eighth European conference on Earthquake Engineering*, Lisbon, Portugal. Vol 3, pp. 6.5/47-53.

Tasios Th.P. (1992). *Mechanics of Masonry*. Symmetria Publishing, Athens, Greece. [in Greek].

Taylor, R. L (2007). "FEAP - A Finite Element Analysis Program - Version 8.1." *Manual.* Dept. of Civil and Environmental Engineering, University of California at Berkeley, Berkeley, California.

Thoen, B. K. (2004). *469D seismic digital control software*, MTS Corporation.

Willam, K., B. Blackard, and C. Citto (2008). "Performance evaluation of masonry infills subjected to axial and in-plane shear: meso- and macro experiments and simulations." *5th European Congress on Computational Methods in Applied Sciences and Engineering*, Venice, Italy.

Wittmann, F.H. (2002). "Crack formation and fracture energy of high strength concrete." *Sadhana*, Vol. 27, Part 4, 413-423.

Zarnic, R., S. Gostic, A.J. Crewe, and C.A. Taylor (2001). "Shaking table tests of 1:4 reduced-scale models of masonry infilled RC frame buildings." *J. Earthquake Eng. Struct. Dyn.*, Vol. 30, 819-834.

Zarnic, R. and M. Tomazevic (1985). "Study on the behavior of masonry infilled reinforced concrete frames subjected to seismic loading." Proceedings of the seventh International Brick Masonry Conference, Melbourne, Australia. Vol. 2, pp. 13315-1325.

Zeris C. (2006). *Personal Communication.*